On the calibration and use of Adaptive Optics systems: RAVEN observations of metal-poor stars in the Galactic Bulge and the application of focal plane wavefront sensing techniques

by

Masen Lamb
B.Sc., University of British Columbia, 2011

A Dissertation Submitted in Partial Fulfillment of the
Requirements for the Degree of

DOCTOR OF PHILOSOPHY

in the Department of Physics and Astronomy

On the calibration and use of Adaptive Optics systems: RAVEN observations of metal-poor stars in the Galactic Bulge and the application of focal plane wavefront sensing techniques

by

Masen Lamb
B.Sc., University of British Columbia, 2011

Supervisory Committee

Dr. Kim Venn, Co-Supervisor
(Department of Physics and Astronomy)

Dr. David Andersen, Co-Supervisor
(Department of Physics and Astronomy)

Dr. Patrick Côté, Member
(Department of Physics and Astronomy)

Dr. Colin Bradley, Outside Member
(Department of Mechanical Engineering)

Supervisory Committee

Dr. Kim Venn, Co-Supervisor
(Department of Physics and Astronomy)

Dr. David Andersen, Co-Supervisor
(Department of Physics and Astronomy)

Dr. Patrick Côté, Member
(Department of Physics and Astronomy)

Dr. Colin Bradley, Outside Member
(Department of Mechanical Engineering)

ABSTRACT

Adaptive optics holds a fundamental role in the era of thirty meter class telescopes; this technology has gained such import that is incorporated into all first light instruments of both the upcoming E-ELT and TMT telescopes. Moreover, each of these telescopes are planning to use advanced forms of adaptive optics to exploit unprecedented scientific niches, such as Multi-Conjugate Adaptive Optics and Multi-Object Adaptive Optics. The complexity of these systems requires careful preliminary considerations, such as demonstration of the technology on existing telescopes and effective calibration procedures. In this thesis I address these two considerations through two different approaches. First, I demonstrate the use of the Multi-Object Adaptive Optics demonstrator RAVEN to gather high-resolution spectroscopy for the first time with this technology, and I identify some of the most metal-poor stars in the Galactic bulge to date. Secondly, I develop two focal plane wavefront sensing techniques to calibrate the internal aberrations of RAVEN and explore their applications to other adaptive optics systems.

I analyze spectra of individual stars in two Globular Clusters to establish infrared techniques that can be used with the RAVEN instrument. Detailed chemical abundances for five stars in NGC 5466 and NGC 5024, are presented from high-resolution optical (from the Hobby-Eberley Telescope) and infrared spectra (from the SDSS-III APOGEE survey). I find [Fe/H] = -1.97 ± 0.13 dex for NGC 5466, and [Fe/H] = -2.06 ± 0.13 dex for NGC 5024, and the typical abundance pattern for globular clusters for the remaining elements, e.g. both show evidence for mixing in their light element abundance ratios (C, N), and asymptotic giant branch contributions in their heavy element abundances (Y, Ba, and Eu). These clusters were selected to examine chemical trends that may correlate them with the Sgr dwarf galaxy remnant, but at these low metallicities no obvious differences from the Galactic abundance pattern are found. Regardless, I compare my results from the optical and infrared analyses to find that oxygen and silicon abundances determined from the infrared spectral lines are in better agreement with the other α-element ratios and with smaller random errors.

Using the aforementioned infrared techniques, I derive the chemical abundances for five metal-poor stars in and towards the Galactic bulge from the H-band spectroscopy taken with RAVEN at the Subaru 8.2-m telescope. Three of these stars are in the Galactic bulge and have metallicities between -2.1 < [Fe/H] < -1.5, and high [α/Fe] $\sim$ +0.3, typical of Galactic disc and bulge stars in this metallicity range; [Al/Fe] and [N/Fe] are also high, whereas [C/Fe] < +0.3. An examination of their orbits suggests that two of these stars may be confined to the Galactic bulge and one is a halo trespasser, though proper motion values used to calculate orbits are quite uncertain. An additional two stars in the globular cluster M22 show [Fe/H] values consistent to within 1σ , although one of these two stars has [Fe/H] = -2.01 ± 0.09, which is on the low end for this cluster. The [α/Fe] and [Ni/Fe] values differ by 2, with the most metal-poor star showing significantly higher values for these elements. M22 is known to show element abundance variations, consistent with a multipopulation scenario though our results cannot discriminate this clearly given our abundance uncertainties. This is the first science demonstration of multi-object adaptive optics with high-resolution infrared spectroscopy, and we also discuss the feasibility of this technique for use in the upcoming era of 30-m class telescope facilities.

Lastly, I develop two focal plane wavefront sensing techniques to calibrate the non-common path aberrations (NCPA) in adaptive optics systems. I first demonstrate these techniques in a detailed simulation of the future TMT instrument NFIRAOS.

I then validate these techniques on an experimental bench subject to NFIRAOS-like wavefront errors. The two techniques are subsequently used to identify and correct the NCPA on both RAVEN and the NFIRAOS test-bench knowns as HeNOS. The application of these techniques is also explored on the VLT/SPHERE system to identify what is known as the 'Low Wind Effect' (LWE). I first quantify the LWE in simulation and then validate the technique on an experimental bench. I then estimate the LWE from on-sky data taken with the VLT/SPHERE adaptive optics system. Lastly, I apply my focal plane wavefront sensing techniques to estimate residual mirror co-phasing errors seen on Keck with the NIRC2 adaptive optics system data. I first demonstrate the ability of my techniques to quantify these errors in a simulation of Keck/NIRC2 data. I then apply their capabilities to estimate the mirror co-phasing errors of Keck with on-sky data.

Contents

List of Tables

List of Figures

ACKNOWLEDGEMENTS

Firstly, I wish to thank my advisors Kim Venn and David Andersen for their support, guidance and perhaps more important - patience with me - over the years. When they first approached me with the possibility of studying both instrumentation and astronomy I was ecstatic. I am extremely grateful that they made this work so well all the way through to the end of my PhD. I would also like to thank them for the opportunity to be a part of the RAVEN engineering runs. I was able to go to Hawaii more times than I feel I deserved and during those trips I had more fun that I could've possibly imagined (even through hurricanes, earthquakes and protestors).

I would like to thank Jean-Pierre Véran for all of his guidance and long discussions, where I used up way too much of his time. I would like to thank all of the people in the adaptive optics group at the HIA for the help and support I've received throughout the years, in particular Glen Herriot, Paolo Turri, Matthias Rosentsteiner, among many others. I would like to thank Carlos Corriea, not only for his support with my instrumentation work but also for allowing the amazing opportunity to work in Marseille for 3 months - this experience was incredible for both my academic and personal growth. I would also like to thank Jean-François Sauvage and Matthew Shetrone.

Special thanks to the many amazing people I've encountered throughout the UVic department: Ben Hendrix for too many reasons to count, Charli Sakari, Jean-Claude Passy, Razzi Movassaghi, Mike Palmer and many other outstanding people at UVic.

More personally, thank you to my close friends Nathan and Jock who helped keep me sane with numerous adventures and hilarity over the years. Unlimited thanks to my parents who have always provided incredible love and support. And finally I would particulary like to thank my fiancé, Leah, who in addition to being a wonderful and supportive person has also managed to put up with me throughout my degree.

DEDICATION

For my parents and for Leah.

Chapter 1

Introduction

My goal is to explore and understand astronomical instrumentation, astronomical observation, and contribute in a scientifically meaningful way to the astronomical community. I aim to achieve these goals through the thesis statements below:

- **(i)** Develop spectroscopic data-analysis techniques in the near-infrared (NIR), show they are robust, and use them to observe metal-poor stars in Milky Way globular clusters.
- **(ii)** Use these infrared techniques along with Adaptive Optics (AO) technology to observe metal-poor stars in the Galactic Centre.
- **(iii)** Develop and apply methods to correct the internal aberrations in the AO system used to make the aforementioned observations, and explore the applications of these methods to current and future AO systems.

1.1 NIR data-analysis techniques: robustness and scientific applications

Globular Clusters (GCs) are an incredibly important feature within our universe that can reveal a wealth of information about the Milky Way (MW). For example, the relatively simple nature of their stellar populations can lead to age constraints of the MW, and their spatial distribution about the Galactic Centre can reveal our radial location within the Galactic plane, R_0 (Harris, 2001). Equally intriguing is tracing the history of GCs in order to determine the evolutionary history of the MW. Their spatio-kinematic features can reveal if a GC was perhaps captured by the MW as opposed to

forming in situ; such an example is M54, both kinematically and spatially associated with the Sagitarius dwarf remnant within the MW (Carretta et al., 2010). Turning to their chemical properties can also reveal important evolutionary information. The age-metallicity relationship, for example, has been used to distill MW GCs that have formed in situ from those that have been captured (i.e. Leaman et al. 2013; Forbes & Bridges 2010). Moreover, detailed chemical properties of stars within GCs can be compared with extragalactic features such as tidal streams to try and identify the origins of the GC (e.g., Sakari et al. 2015).

Therefore, chemical properties are an excellent tool for understanding the evolution of the MW in terms of GC history. As such, the spectroscopic observations of stars within GCs play an integral role. These observations are traditionally done at optical wavelengths, where standard analysis techniques and detector technology is well developed. However, the infrared counterpart of these observations can allow access to complementary spectral information; when this is combined with optical studies it can lead to a wealth of chemical information on GCs and allow us to further constrain their origins. Up until recently infrared analysis techniques (and technology) has been significantly more primative than its optical counterpart. However, with projects such as APOGEE[1], and recent advances in detector technology (Finger et al., 2010), it has opened up the capabilities in the NIR.

A direct chemical analysis comparison between the optical and infrared wavelengths on the same astronomical targets is a healthy exercise to ensure consistency and identify any systematic errors between the two regimes. Furthermore, if this is done simultaneously to scientifically important targets then the exercise is significantly more valuable. As such, this thesis demonstrates an optical and infrared analysis on two GCs - both without prior detailed chemical analyses - thought to be associated with interesting galactic features (such as tidal streams). I determine the chemical composition of individual stars in each of these GCs and discuss their scientific importance in Chapter 2. Abundances are determined from both optical and infrared spectroscopic data gathered from the Hobbey Eberly Telescope and the APOGEE survey, respectively. This larger wavelength coverage allows us to determine the abundances of more spectral lines and more elements (e.g., CN, CO, OH, Si, and Al are ubiquitous in the IR yet rare in the optical). I also compare the accuracy of the abundance results between the two wavelength regions. As previously men-

[1]APOGEE is an H-band, high-resolution, high signal-to-noise spectroscopic survey of thousands of Milky Way stars, carried out at the Apache point observatory.

tioned, comparing the stellar abundances derived from observations of the same stars from the two different wavelengths is useful, with the ultimate goal being to show the newer, younger infrared technique is a robust and complementary tool to optical spectroscopy. This robustness is particularly critical for the infrared observations discussed on in Chapter 3, as we use these infrared techinques to observe metal-poor stars in the Galactic Centre. Furthermore, the stars we will observe in the Galactic Centre are around the same metallicity and type as the stars found in the GCs mentioned here (i.e. red giant branch stars (RGB) with [Fe/H] $\sim$ -2), allowing for a very easy application of our infrared analysis technique.

1.2 Using RAVEN to search for Metal-Poor stars in the Galactic Centre

Metal-poor stars within the MW are another extremely important tool used to understand the nature of the MW. These stars can tell us about the information of the Galaxy at early evolutionary stages and can yield constraints on population III (i.e. first) stars (Beers & Christlieb, 2005). The majority of metal-poor stars are found in the Galactic Halo, where the metal-poor tail of the metallicity distribution function (MDF) can extend down to [Fe/H]<-5 (i.e. Yong et al. 2013). Simulations have shown that a population of metal-poor stars should exist at the Galactic Centre as well (i.e. Diemand et al. 2005; Gao et al. 2010), with possible links to the first stars, however the MDF of large Galactic bulge surveys does not support this information (Hill et al., 2011; Ness et al., 2013). This is mainly due to the overwhelming metal-rich population in the Galactic bulge, and identifying single, metal-poor stars in this region can be a difficult task. Nonetheless, a small sample of metal-poor stars has been observed in the bulge (i.e., see Howes et al. 2016) and appears to show relatively little carbon compared to metal-poor halo stars at the same metallicity. Therefore investigating the chemical properties of these stars can help discern important characteristics of the underlying population. One of the main limitations faced when using traditional observing techniques (i.e. optical spectroscopy from large ground-based telescopes) to chemically identify stars in the Galactic bulge is the heavy dust obscuration and the extreme stellar crowding. The former limitation can be significantly mitigated by observing in the NIR, a region which has excellent access to chemical features somewhat difficult to ascertain in the optical, such as oxygen or more importantly in

this context - carbon. However, the latter limitation must turn to the technology of AO to reduce the effects of stellar crowding.

AO counteracts the atmospheric effects on the telescope image of an astronomical object by use of a deformable mirror (more information is provided in Section 1.3), and can allow for ground-based images to exceed the resolution of the Hubble Space Telescope. However, at NIR wavelengths such as H-band, the correctible diameter of an AO system is only on the order of 10-20 arcseconds; recent advances in AO (e.g., see Davies & Kasper 2012) have significantly improved on this limitation such as multi-conjugate adaptive optics (MCAO) and multi-object adaptive optics (MOAO). MOAO in particular allows for multiple regions of AO correction over a wide field of regard (1-2 arcminutes); this becomes particularly powerful when considering multi-object, high-resolution spectroscopy. For example, high-resolution spectroscopic observations of RGB stars within the dust-obscured bulge require significant integration times in the NIR (i.e. 10+ hours for H=15 on the Subaru Telescope). Therefore any multiplexing of stellar observations is unquestionably desirable. Mutliplexed observations where each target has an AO correction has never been possible until the introduction of MOAO. RAVEN is a recent demonstator of this technology for the ELT era, where it was designed and installed on the Subaru Telescope to demonstrate the technical feasibility of MOAO on an 8m class telescope.

In this thesis, I use RAVEN to demonstrate the first science acquired at high-resolution with MOAO by observing metal-poor stars in and towards the Galactic Centre. The infrared analysis techniques developed in Chapter 2 are used to derive the chemical abundances of these stars and their analysis is discussed in Chapter 3. I also address the lessons learned in using this new technology such that future observations with MOAO can be improved. It should be mentioned that these observations could be achievable with individual AO observations with conventional facilities (such as Keck/NIRSPEC) and that the main purpose of using RAVEN was to demonstrate the technology.

1.3 Sensing and correcting internal aberrations in AO systems

As previously mentioned, AO in astronomy works to remove the atmospheric effects on extra-terrestial light received by a telescope. These effects are caused by turbulent

regions in the atmosphere where there is mixing of hot and cold pockets of air - each with a different index of refraction - thus causing a distorted image. This effect can be avoided if telescopes are launched into space, however this can be very expensive, technically challenging, and the telescopes are limited in physical size; the latter point is particularly crucial considering that increasing the diameter of a telescope allows for an significant gain in light collecting area and resolution. Therefore it is desirable to build very large telescopes from the ground which can correct atmospheric distortion (instead of avoiding it). AO achieves this by utilizing a mirror that can change to the opposite shape of the phase imprinted by the atmosphere, known as a deformable mirror (DM); ideally this mirror adapts its shape at the same rate the atmosphere is changing to provide a full correction. Another important component to an AO system is a wavefront sensor (WFS), which tells the system what shape the mirror needs to be to compensate for the atmosphere. A typical WFS is a grid of lenses called a Shack-Hartmann WFS (SHWFS), where a flat wavefront would cause an image of the pupil to create an equally spaced grid of 'spots', each spot coming from one of the lenses in the WFS. If there is any deviation to the wavefront, the grid will be imperfect and the control system will calculate the appropriate DM shape to cause the spots to return to their reference grid. This system works in a closed loop process for a typical AO system such as the one shown in Figure 1.1.

Optical elements in AO systems such as lenses and mirrors can suffer from imperfections in polishing or coating processes; therefore if these elements exist after the beamsplitter in a simple AO system (in either the WFS path or the Science path) they induce what are known as Non-Common Path Aberrations (NCPA) since one path 'sees' the aberration and the other path does not. These aberrations ultimately cause a degradation in the image quality of an AO system. In the classic AO system the only major NCPA can be characterized by relatively few optical elements, such as the single lens marked by '*' in Figure 1.1). However, contemporary AO systems using more advanced techniques such as multi-object AO (MOAO) (i.e. RAVEN, see Section 3 for a description) host a variety of non common optical elements between the WFS and camera arms. In such systems the NCPA can be quite significant, as is shown on the left of Figure 1.2 where the NCPA of NFIRAOS[2] are simulated in the depicted phase map. The impact of such a phase error can have a considerable effect on the closed loop PSF as is shown in the right panel of Figure 1.2, where an optical

[2]Narrow Field Infrared Adaptive Optics System (NFIRAOS) is the multi-conjugate adaptive optics system that will operate at first light on the Thirty Meter Telescope.

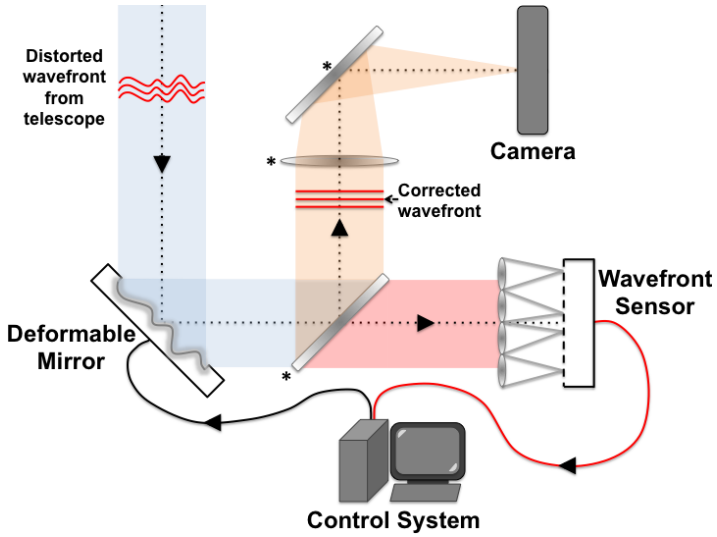

Figure 1.1: A classic AO system consisting of a deformable mirror (DM) and a wavefront sensor (WFS). The non-common path errors in this system arise from the single lens located in-between the beam splitter and the science camera (denoted by a '*'; imperfect polishing errors cause aberrations on the science image that are not 'seen' by the WFS.

star has been simulated subject to these effects. The Strehl ratio of this image is ∼40% and the wavelength is 655 nm; an equivalent Strehl in H-band is ∼87%, which is significantly higher than the optical, but must be corrected nonetheless to achieve optimal AO performance.

To correct for these errors an AO system's NCPA must first be quantified and then applied as an offset on the deformable mirror. There are a variety of different ways to determine the NCPA in an AO system, two of which will be investigated and discussed in throughout this thesis. In Chapter 4 these two methods are introduced and used in simulation to quantify a reasonable application to the TMT/NFIRAOS system. Subsequently, the techniques are validated on an experimental bench in the presence of a custom phase screen representative of NFIRAOS-like NCPA. Finally, these techniques are used to correct the NCPA on two real AO systems: the MOAO system RAVEN on the Subaru telescope, and the NFIRAOS test-bench HeNOS at NRC Herzberg in Victoria. In Chapter 5, we explore these techniques in simulation to try and quantify their abilities to estimate two real-life scenarios where pupil discontinuities severely limit the perfomance of an AO system. The first of these scenarios involves the VLT/SPHERE AO system, where nights with low wind and

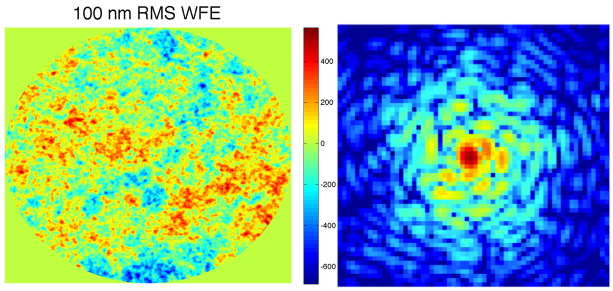

Figure 1.2: Left: typical NCPA polishing errors represented by a contemporary AO system (NFIRAOS); the wavefront error is ∼100 nm RMS. Throughout the remainder of the thesis such a phase map is always expressed in units of nm. Right: the impact such a phase aberration has on a diffraction limited PSF; the Strehl ratio reduces to ∼40% for wavelengths at 655 nm, however this is only reduced to ∼87% in H-band. Contemporary AO systems must be capable of overcoming such errors in order to achieve optimal image quality. As such, quantification and correction of NCPA on any AO system is of utmost importance if these errors are sufficiently large.

good seeing disrupt the PSF in what is known as the 'Low Wind Effect' (see Sauvage et al. 2016b). The second scenario involves mirror-segment piston errors unseen by the NIRC2 AO system on Keck, which negatively impact the PSF. We subsequently use data taken from an experimental bench with a phase screen representative of the Low Wind Effect on SPHERE mentioned above to validate our techniques. We then apply these methods to on-sky data acquired during a night subject to a strong Low Wind Effect and show they are an effective method to quantify this effect over time. Finally, we briefly summarizes the applications of our techniques developed in 5 to estimate the co-phasing effects on-sky with Keck/NIRC2 data subject to a night dominated by this effect.

1.4 Summary

Therefore, to summarize:

- Thesis statement (i) is addressed in Chapter 2 and summarizes the use of near-infrared spectroscopic techniques to chemically identify metal-poor stars; the work follows the publication Lamb et al. (2015).

- Using these developed infrared techniques, thesis statement (ii) is achieved in Chapter 3 by using high-resolution spectroscopy with MOAO for the first

time ever to observe metal-poor stars in and towards the Galactic Centre with RAVEN. The results of this work follow the publication Lamb et al. (2017)

- In Chapter 4, two techniques are developed to calibrate the internal aberrations of an adaptive optics system and validated in both simulation and experimental bench; they are then successfully used on two real AO systems RAVEN and HeNOS, therefore fulfilling a portion of thesis statement (iii). Chapter 4.1 follows the publication Lamb et al. (2016a) and Chapter 4.2 is a publication that will be submitted to MNRAS shortly.

- Finally, the remainder of thesis statement (iii) is addressed in Chapter 5 by using the techniques developed in Chapter 4 to validate in both simulation and with real data the estimation of two significant AO problems on VLT and Keck. The simulated aspects of this Chapter are taken from a publication submitted to JATIS (recently accepted for publication) and the results pertaining to real data are part of a publication to be submitted to the Journal of Astronomical Telescopes and Instrumentation (JATIS) in the near future.

Chapter 2

Chemical abundances in the globular clusters NGC 5024 and NGC 5466 from optical and infrared spectroscopy

Important note: the work in this Chapter is taken directly from the paper titled *Chemical abundances in the globular clusters NGC 5024 and NGC 5466 from optical and infrared spectroscopy* (Lamb, M. P., Venn, K. A., Shetrone, M. D., Sakari, C. M., & Pritzl, B. J. 2015, MNRAS, 448, 42).

2.1 Introduction

The discovery of the accretion of globular clusters (GCs) from the Sagittarius dwarf galaxy (Da Costa & Armandroff, 1995), has led to the question as to how many globular clusters have been captured by the Milky Way. Multiple studies have looked at the globular cluster systems of the Milky Way to derive an age-metallicity relationship and have come to different conclusions as to which clusters have likely been accreted (Mackey & van den Bergh, 2005; Forbes & Bridges, 2010; Dotter et al., 2011; Leaman et al., 2013). The question is still open as to which type of clusters are accreted and which form in situ; and furthermore what the fraction of each type is within the Milky Way.

GCs formed in dwarf galaxies may differ from those found in the Galactic halo,

depending on their age and metallicity. Dwarf galaxies show a wide variety of star formation histories (Hidalgo et al., 2011, 2013; Weisz et al., 2014) that are predicted to lead to variations in their metallicity distribution functions and chemical abundances. It has also been suggested these variations could be attributed to differences in the IMFs of these galaxies (McWilliam et al., 2013). If the IMFs are the root cause of these differences then this would also lead to differences in the age-metallicity relationship, which is observed by both Forbes & Bridges (2010) and Leaman et al. (2013). From observations, field stars in dwarf galaxies do exhibit different abundance ratios from Milky Way (MW) field stars, e.g., lower [α/Fe] ratios and variations in neutron capture element ratios at intermediate metallicities. However these typically do not show up until [Fe/H] ~ -1.5 (Shetrone et al., 1998, 2001, 2003; Venn et al., 2004; Okamoto et al., 2012; Tolstoy et al., 2009; Frebel, 2010). At metallicities below [Fe/H] $= -1.5$ the abundance variations between field and GC stars become less pronounced in dwarfs and the MW (Hill et al., 2000; Pritzl et al., 2005; Carretta et al., 2010; Letarte et al., 2010); a good example of this is M54, located at the heart of the Sagittarius (Sgr) dwarf accretion remnant. M54 has a much lower metallicity than the Sgr field stars (e.g., Carretta et al. 2010) and the [α/Fe] ratios resemble the field stars in the MW halo and its detailed chemical abundance ratios resemble the patterns seen in other globular cluster systems (e.g., the Na-O anti-correlation; Carretta et al. 2009). Therefore, other than its physical association with the Sgr remnant, M54 does not stand out from other GCs in terms of its chemical abundance patterns, similar to the metal-poor GCs Terzan 8 and Arp 2 (both also kinematically and spatial associated with the Sgr stream (Mottini et al. 2008). On the other hand, Hodge 11 in the LMC at [Fe/H] = -2.0 does have lower [α/Fe] than MW field and GC stars (Mateluna et al., 2012); and Ruprecht 106 has an anomalously low [α/Fe] ratio for a MW GC (Villanova et al., 2013).

Two metal-poor clusters that have been associated with the Sgr stream are NGC 5024 (M53) and NGC 5466 (Bellazzini et al., 2003; Martínez-Delgado et al., 2004). Both of these clusters are more metal-poor than M54 (each at [Fe/H] ~ -2, Harris 2010), which means that detailed chemistry could be inconclusive as to their origins in the Sgr dwarf galaxy. We have opted to study the chemistry in these GCs regardless though because (1) there are few published chemistries for these clusters and (2) they are both associated with other interesting dynamical structures. NGC 5466 has a large tidal tail (Grillmair & Johnson, 2006). However it appears to have no association with the Sgr stream, and knowing the chemistry of this GC can help identify

members in the tidal feature. It is also worth nothing that NGC 5466 has a retrograde orbit, suggestive of an extragalactic origin (Allen et al., 2006; Forbes & Bridges, 2010). NGC 5024 may be linked by a stellar bridge to NGC 5053 (Bellazzini et al., 2003; Chun et al., 2010), although no bridge was seen by Jordi & Grebel (2010), and detailed chemical abundances of stars in these two clusters can be used to study if their formation was coeval.

Detailed chemical abundances have been determined for a few stars in these clusters; one star in NGC 5024 and two stars in NGC 5466 by Pilachowski et al. (1983), and one anomalous cepheid in NGC 5466 by McCarthy & Nemec (1997). Iron abundances for several stars in NGC 5024 have also been estimated from photometry by Dékány & Kovács (2009). All of these analyses confirm the metallicities of [Fe/H] ~ -2 dex (Harris, 2010). Carbon abundances have been derived from CN and CH band strengths for over a dozen stars in both NGC 5024 and NGC 5466 from Martell et al. (2008) and Shetrone et al. (2010), respectively. In both clusters, large variations in the [C/Fe] ratios are found, typical of stars that have undergone deep mixing on the red giant branch (RGB).

In this paper, we determine the chemical composition of individual stars in each GC. Abundances are determined from both optical and infrared spectroscopic data. This larger wavelength coverage allows us to determine the abundances of more spectral lines and more elmeents (e.g., CN, CO, OH, Si, and Al are ubiquitous in the IR yet rare in the optical). We also compare the accuracy of the abundance results between the two wavelength regions (similar to Smith et al. 2013).

2.2 Observations and Data Reduction

2.2.1 Observing Program

Five red giant branch (RGB) stars have been selected in the outer regions of two globular clusters, NGC 5024 and NGC 5466, for detailed spectral analyses. The locations of these objects are shown in Fig. 2.1 and their fundamental properties are listed in Table 1. Targets were chosen based on their V magnitudes, and V-I colours from the Harris catalogue (Harris, 2010). Foreground contamination is minimal.

Optical spectra were gathered with the High Resolution Spectrograph (HRS, Tull et al. 1998) on the HET[1]. The HRS was configured at resolution R = 30,000 with

[1]Observing time was allocated through NOAO program number 05 A-330, via the predecessor of

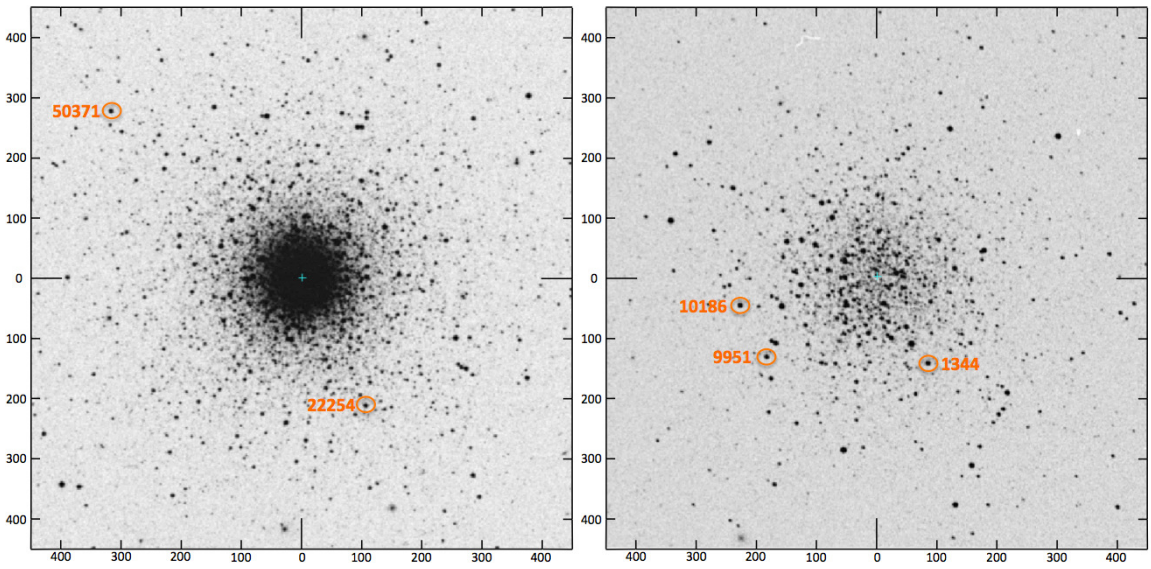

Figure 2.1: Positions of our science targets in NGC 5024 (left) and NGC 5466 (right). Axes are in arc seconds from the cluster centre (the centre is noted by the cyan cross in each image). North is up and East is left. Images taken from the SDSS survey.

2x2 pixel binning using the 2 arcsecond fibre. The HRS splits the incoming beam onto two CCD chips, from which the spectral regions regions 6000 - 7000 Å (red chip) and 4800 - 5900 Å (blue chip) were extracted for this work. Two standard stars were also observed, RGB stars with previously published spectral analyses in each of the globular clusters M3 and M13. The signal to noise (S/N) for these seven targets ranged from 40 - 120 (see Table 3.1).

IR spectra for four of the five targets in NGC 5466 and NGC 5024 are available in the APOGEE DR10 release[2]. APOGEE provides H-band spectra, ranging from 15000-17000Å at a resolution R $\sim$ 20,000 with S/N $\geq$ 100. These spectra expand our analysis of our main science targets to features at longer wavelengths. We have not analysed the APOGEE spectra of our M3 and M13 standard stars since there are no published results of their infrared spectral features for a comparison.

The HET-HRS data were reduced using standard IRAF[3] packages. Some data was taken over multiple nights, therefore data was reduced per night and coadded in those circumstances (see Table 1).

the TSIP program, i.e., the NSF Facilities Instrumentation Program

[2]https://www.sdss3.org/dr10/

[3]IRAF (Image Reduction and Analysis Facility) is distributed by the National Optical Astronomy Observatory, which is operated by the Association of Universities for Research in Astronomy, Inc., under cooperative agreement with the National Science Foundation.

Table 2.1: The sample of stars observed in the optical with the HET

Star	R.A. (J2000)	Dec. (J2000)	Date Obs.	Exp. Time (s)[a]	Red SNR @6250Å	Blue SNR @5500Å	$V_{hel.}$ (km/s)
NGC 5024-22254	13 12 47.94	+18 06 32.1	May 2005	2700(1)	50	40	-57.57 ± 0.50
NGC 5024-50371	13 13 17.36	+18 14 46.4	March 2007	3387(1)	75	55	-62.69 ± 0.24
NGC 5466-9951	14 05 41.08	+28 29 48.2	June 2005	6350(2)	60	55	126.53 ± 1.10
NGC 5466-1344	14 05 20.73	+28 29 42.0	June 2006	6600(3)	70	60	129.29 ± 0.81
NGC 5466-10186	14 05 44.53	+28 31 13.5	July 2006	3300(1)	70	60	107.33 ± 0.48
M3-C41303-2217	13 41 30.30	+28 29 42.0	March 2008	3000(1)	50	40	-145.25 ± 0.37
M13-III-18	16 41 24.64	+36 25 45.0	March 2008	3000(1)	85	75	-233.64 ± 0.23

[a]Total exposure time is listed, including the number of nights that observations were taken.

For each science observation, bias images (5), flat field images (5), a wavelength calibration, and a telluric standard star (a rapidly-rotating hot star) were also obtained. A medianed bias was subtracted from the red CCD images, but not the blue CCD images at the suggestion of the HET data reduction manuals[4] as this CCD is very clean and bias subtracting can add noise. Three science exposures from 2005 were taken with an older red CCD that suffered from hot pixels and bad columns - these exposures were corrected in IRAF (using *fixpix*). Images were divided by a medianed flat field, and scattered light was removed before aperture extraction. Spectra were extracted with variance weighting (to reduce cosmic ray contamination), and wavelength calibrated using a standard thorium-argon lamp. The telluric standards were reduced by the same methods, and divided into the science spectra to remove atmospheric features. The sky fibre on the HRS was not used because our science targets are quite bright.

Samples of the final spectra are shown in Fig. 2.2. Radial velocities were calculated using the IRAF task *fxcor*, and cross-correlating the heliocentric-corrected spectrum of Arcturus (Hinkle & Wallace, 2005). These values are listed in Table 3.1. The velocities in NGC 5466 are in excellent agreement with those calculated per star by Shetrone et al. (2010), thus this cluster shows a significant dispersion (Shetrone et al. 2010 finds a velocity dispersion of $\sim$17 km/s from 67 stars).

Post-pipeline processed APOGEE spectra are available in the SDSS DR10 database, where they have been reduced and coadded when multiple exposures were taken, and then continuum normalized. We took an additional step and shifted these spectra from the vacuum rest frame to the air rest frame.

2.3 Equivalent Width Analysis of Optical Spectra

Optical abundances are determined from an equivalent width (EW) analysis. All equivalent widths were initially measured using DAOSPEC Stetson & Pancino (2008)[5]. The atomic lines used with DAOSPEC comprises a list taken from several sources: Shetrone et al. (2003), Aoki et al. (2007), Cohen et al. (2008), Letarte et al. (2009), Tafelmeyer et al. (2010), Frebel et al. (2010), and Venn et al. (2012). EWs greater

[4]http://hydra.as.utexas.edu/?a=help&h=29#HRS

[5]DAOSPEC is a program that is capable of measuring equivalent widths and radial velocities of spectra. It was written by P.B. Stetson for the Dominion Astrophysical Observatory, National Research Council, Canada.

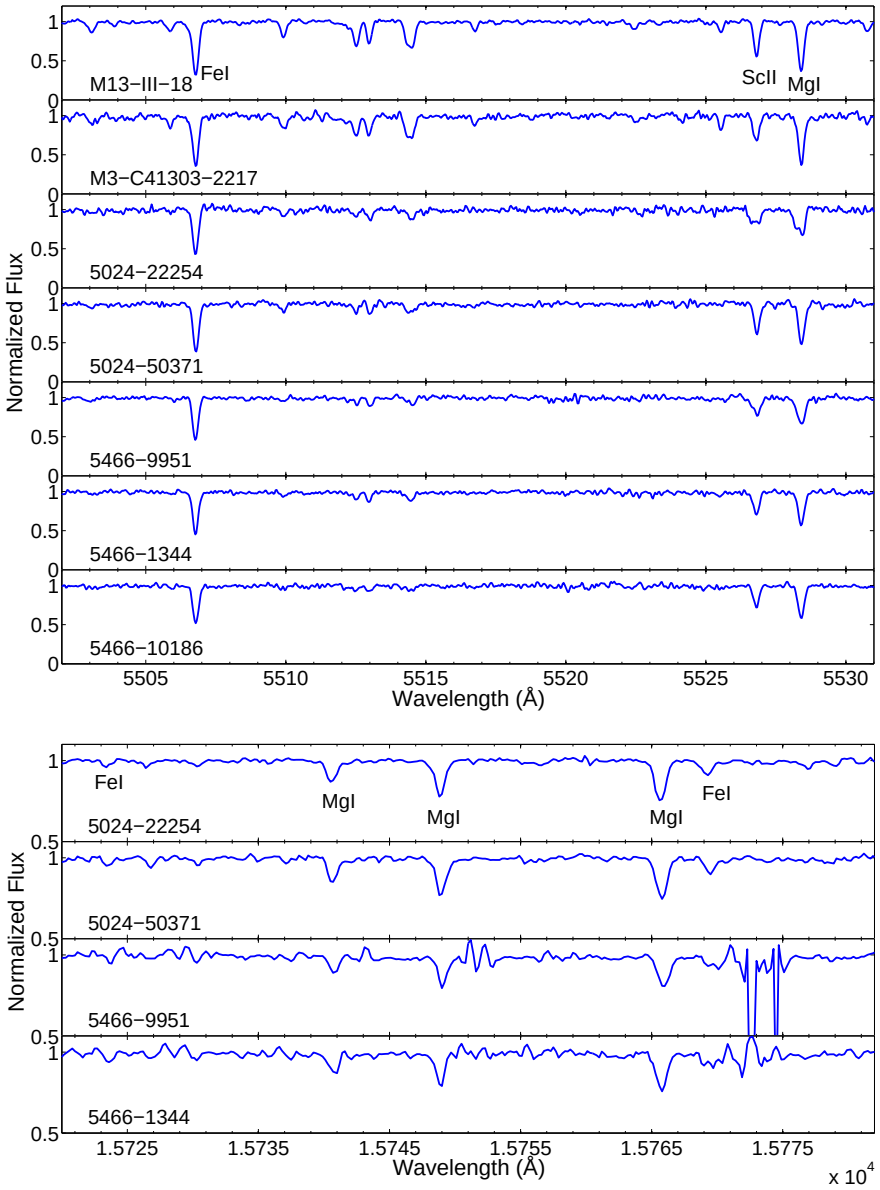

Figure 2.2: Sample spectral regions in the optical (blue chip, top), and infrared (bottom) showing magnesium, scandium, and iron lines that were used in the abundance analysis.

Table 2.2: Equivalent Widths and Atomic Data

				NGC 5024		NGC 5466			M3	M13
	λ	χ		22254	50371	1344	9951	10186	C41303-2217	III-18
Ion	(Å)	(eV)	log gf	(mÅ)	(mÅ)	(mÅ)	(mÅ)	(mÅ)	(mÅ)	(mÅ)
Fe I	5302.302	3.28	-0.880	78.4	94.9	83.4	78.5	75.5	109.0	123.7
Fe I	5307.370	1.61	-2.912	68.8	93.3	91.1	83.7	74.5	123.1	122.2
Fe I	5324.190	3.21	-0.100	123.3	123.9	111.8	123.8	111.5	158.4	158.2
Fe I	5339.930	3.27	-0.720	95.9	92.7	79.3	75.3	77.1	123.8	127.3
Fe I	5364.860	4.45	0.228	54.4	56.8	57.3	61.7	54.3	86.8	93.3
...										

*Full table available online

than 100 mÅ are offset between DAOSPEC Gaussian fitting profiles and area measurements with the IRAF task *splot*; the IRAF measurements were adopted for lines $>$ 100 mÅ. Lines were also examined by eye for unrecognized blends or other mismeasurements (i.e. contaminated with noise spikes, etc.), using the spectrum of Arcturus and the Sun as references. Lines with EWs $>$ 200 mÅ were not analysed since they tend to be very sensitive to small uncertainties in the model atmospheres.

2.3.1 ΔEW

The uncertainty in EW measurements can be estimated from the revised Cayrel formula Cayrel (1988); Battaglia et al. (2008),

$$\Delta(EW) \sim \frac{\sqrt{1.5 \cdot FWHM \cdot \Delta x}}{S/N} \tag{2.1}$$

where FWHM is the measured full width at half maximum of a particular line in Å, Δ x is the dispersion of the spectra in Å/pixel (37.9 mÅ for the Blue chip and 50.89 mÅ for the Red), and S/N is the signal-to-noise measured in the wavelength region of the particular line being measured. For a stronger line (EW $\sim$ 100 mÅ) then Δ(EW) $\sim$ 3% whereas weaker lines (EW $\sim$ 20 mÅ) yield a value closer to 10%, thus we conservatively adopt 10 % as the uncertainty in EW measurements for each line.

2.3.2 EW comparison with standard stars

To test the validity of the analysis procedure, two standard stars are analysed using the same method as the target stars: M3-C41303-2217 and M13-III-18. Figure 2.3 shows a comparison of EW measurements (this work) compared with those from Cohen & Meléndez (2005) (hereafter referred to as CM05). A mean difference (This Study - Literature) of -0.819 mÅ ($\sigma = 5.836$ mÅ) is found in M13-III-18 (from 127 lines) and a difference of -1.599 mÅ ($\sigma = 5.967$ mÅ) is found for M3-C41303-2217 (from 115 lines). This agreement is reasonable and these measurement methods are applied to the new targets in NGC 5024 and NGC 5466.

2.4 Model Atmosphere and Abundance Analysis of Optical Data

The optical abundances are computed by using the radiative transfer code MOOG (Sneden, 1973), which uses stellar model atmospheres and atomic data to synthesize spectra. The new MARCS spherical models have been adapted (Gustafsson et al. 1975, 2008, also see Mészáros et al. 2012) assuming [α/Fe] enhancement since the science targets and standard stars are relatively metal-poor ([Fe/H] < -1 dex). This combination of spherical model atmospheres and MOOG's plane parallel radiative transfer is appropriate for analyzing red giants (e.g. see Heiter & Eriksson 2006 and additional tests by Venn et al. 2012).

2.4.1 Photometric Stellar parameters

The stellar parameter T_{eff} is computed using the infrared flux method (IRFM, described by Ramírez & Meléndez 2005), which requires precision photometry, reddening, distance modulus, metallicity, and stellar mass. Using this T_{eff} and an estimate of the stellar mass, the surface gravity can be determined.

Optical photometry comes from the Stetson database[6] and the infrared photometry comes from 2MASS (Skrutskie et al., 2006) (see Table 3.3). Typical errors for both photometric sources are ~ 0.02 mag. Reddening values are from the Harris catalogue; typical reddening errors are 10%. Distance moduli are from the Harris catalogue as determined from the horizontal branch magnitude (taken from Kopacki 2000 for NGC

[6]http://www4.cadc-ccda.hia-iha.nrc-cnrc.gc.ca/community/STETSON/standards/

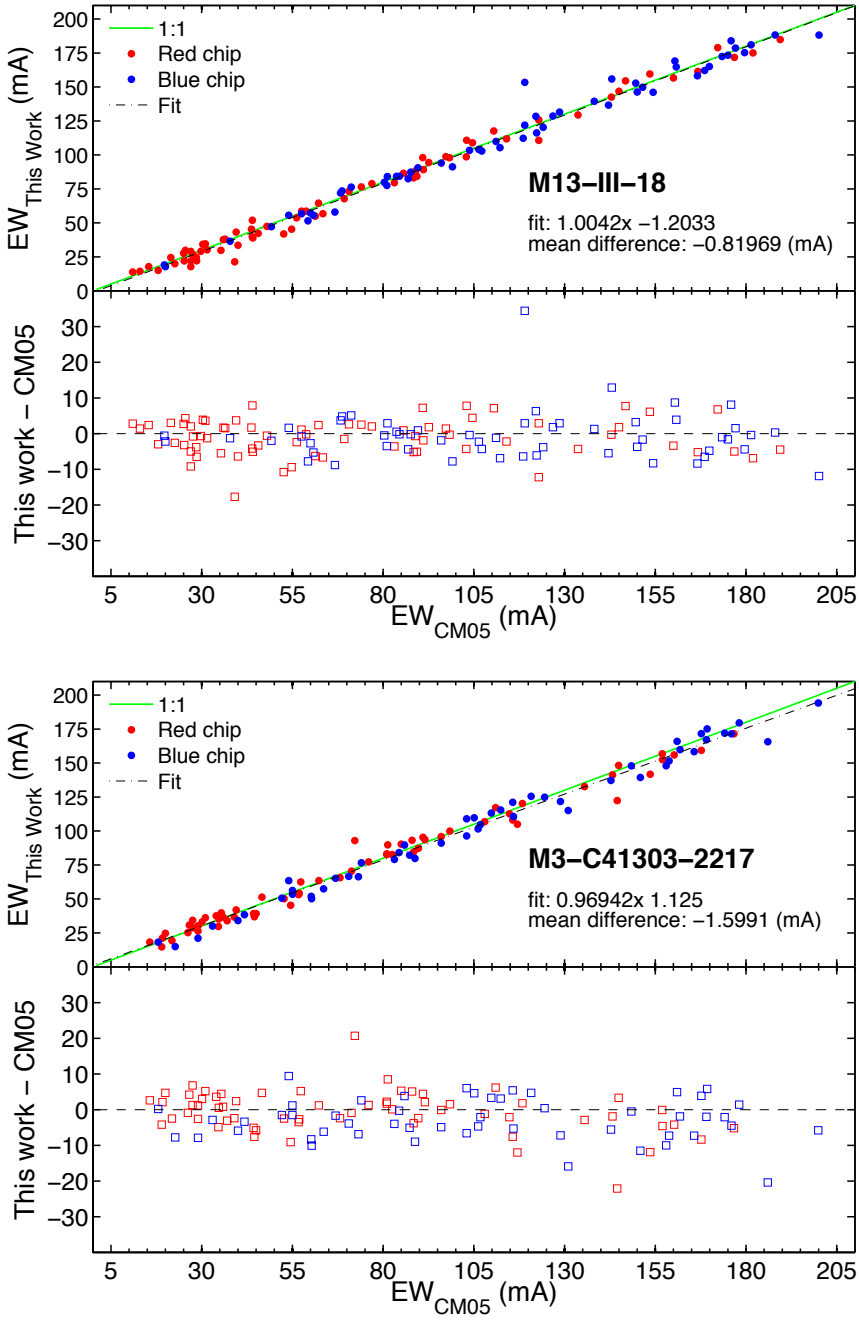

Figure 2.3: Top: measured equivalent widths with DAOSPEC vs. CM05 for M13. Bottom: measured equivalent widths with DAOSPEC vs. CM05 for M3.

5024 and from Fekadu et al. 2007 for NGC 5466). The uncertainty in the distance moduli are 0.1 mag. Input metallicities are taken from the literature: either from direct Fe measurements or from the average cluster metallicity (see Table 3.3). Assuming the RGB mass is roughly equivalent to the main sequence turnoff (MSTO) mass, an input stellar mass of $0.8M_{\odot}$ is taken from the MSTO of the isochrone fits of NGC 5024/5466 (Dotter et al., 2010)[7]. The isochrone with the larger age uncertainty is NGC 5466 ($\sigma = 0.75$ Gyr, reflecting a larger intrinsic scatter in its CMD), resulting in a maximum turnoff mass uncertainty of $\Delta M_{\rm turnoff} = 3\%$.

2.4.2 Spectroscopic stellar parameters

Stellar model atmospheres were created with the initial parameters described in Section 2.4.1. These models were run with MOOG to compute initial line abundances from EW measurements. Revised values of $T_{\rm eff}$ and Fe, and new microturbulence values were found. $T_{\rm eff}$ is adjusted in small increments to find the best fit to the Fe I line abundances when plotted against the excitation potential (χ). Simultaneously the microturbulence is adjusted such that there is no dependence between $\log\epsilon$(Fe I) and the reduced EWs. This process is repeated until the final slopes in Fe I vs χ and reduced EW were < 0.004. These spectroscopic parameters are listed in Table 2.4. Also included in the table are the derived stellar parameters from the APOGEE Stellar Parameters and Chemical Abundance Pipeline (ASPCAP[8] García Pérez et al. 2016) for Fe, C and N.

2.4.3 Stellar parameter uncertainties

The uncertainties in $T_{\rm eff}$ were found by assuming the derived individual Fe I line abundances are distributed randomly about the mean; thus the standard deviation ($\sigma_{\rm Fe}$) in the mean abundance measures the scatter in the data. If $T_{\rm eff}$ is adjusted such that the slope of the log(Fe) vs χ spans $\pm 1\sigma$ over the range in excitation potentials (χ), then $\Delta T_{\rm eff}$ is found to be $\sim$100 K for both standard stars, and this is adopted for the five science targets given the similarity in S/N and $T_{\rm eff}$ in our sample.

The Δv_t is found by allowing the slope logϵ(Fe I) vs. reduced EW to vary such that the range of logϵ(Fe I) values span 1 σ over the range of reduced EWs, similar

[7]the actual isochrones corresponding to the GC parameters in Dotter et al. (2010) can be downloaded from The Dartmouth Stellar Evolution Database (http://stellar.dartmouth.edu/models/) and manually searched for a turn-off mass.

[8]ASPCAP parameters were retrieved online at http://data.sdss3.org/sas/dr10/apogee/spectro/redux/r3/fields.htr

Table 2.3: Photometric magnitudes and cluster properties

	Photometry[a]						Cluster parameters[b,c]		
Star	B	V	I	J	H	K	$(m-M)_V$	$E(B-V)$	Initial [Fe/H] (dex)
NGC 5024-22254	15.92	14.88	13.74	12.932	12.367	12.230	16.32	0.02	-2.10
NGC 5024-50371	15.64	14.56	13.35	12.574	11.973	11.878	16.32	0.02	-2.10
NGC 5466-9951	15.90	14.97	13.92	13.092	12.551	12.472	16.02	0.00	-1.98
NGC 5466-1344	15.67	14.67	13.58	12.725	12.153	12.056	16.02	0.00	-1.98
NGC 5466-10186	15.56	14.62	13.55	12.712	12.137	12.107	16.02	0.00	-1.98
M3-C41303-2217	14.86	13.75	12.58	11.698	11.118	10.969	15.07	0.01	-1.37±0.05
M13-III-18	13.94	12.74	11.51	10.601	9.928	9.830	14.33	0.02	-1.43±0.05

[a]All B, V, and I values taken from the Stetson database (Stetson, 2000). All J, H, K values taken from the 2MASS survey.

[b]Distance modulus and reddening taken from Harris (2010)

[c]NGC 5024/5466 metallicity taken from the cluster metallicity itself Harris (2010), M3 and M13 metallicities taken from CM05. These metallicities are used as input to determine initial stellar parameters.

Table 2.4: Derived Temperatures and Gravity

Star	This Study			CM05			ASPCAP[a] (APOGEE)		
	T_{eff} ($\pm$100 K)	log(g) ($\pm$0.2 dex)	v_t ($\pm$0.2 km s^{-1})	T_{eff} ($\pm$75 K)	log(g) ($\pm$0.2 dex)	v_t ($^{+0.4}_{-0.2}$km s^{-1})	T_{eff} (K)	log(g) dex)	v_t (km s^{-1})
NGC 5024-22254	4410	1.21	1.60	-	-	-	4409	1.37	1.83
NGC 5024-50371	4425	1.06	1.80	-	-	-	4391	1.26	1.86
NGC 5466-9951	4595	1.44	1.55	-	-	-	4512	1.75	1.71
NGC 5466-1344	4499	1.27	1.40	-	-	-	4469	1.62	1.75
NGC 5466-10186	4585	1.29	1.75	-	-	-	-	-	-
M3-C41303-2217	4538	1.19	1.55	4436	1.20	1.60	4319	1.69	1.73
M13-III-18	4397	1.02	1.75	4350	1.00	1.65	4498	2.25	1.56

[a]The uncertainties in these stellar parameters are very small and are therefore not included here.

to the method used to find ΔT_{eff}. The $\Delta v_t = 0.2 kms^{-1}$ for both standard stars and is adopted for the five science targets.

Physical gravities are adopted from the IRFM, thus log(g) depends on the distance to the star (or cluster), reddening, T_{eff} value, turn-off mass, and photometry; an estimate in the uncertainty of log(g) is calculated by quantifying and propagating the errors in these parameters. After calculating log(g) and varying these parameters by the errors described in this Section, $\Delta log(g) = 0.2$ dex (assuming no covariance).

2.4.4 Comparison of stellar parameters and iron with the standard stars

To test the validity of this abundance analysis technique the procedure is applied to the standard stars in M3 and M13 using the model atmospheres and EWs of this work and comparing the Fe I abundance with CM05. The model atmosphere parameters of CM05 agree within the uncertainties of this work (see Table 2.4) and so the Fe comparison should yield consistent results. The derived M13 standard star [Fe/H] abundance from this work is -1.57 ± 0.05 whereas that of CM05 is -1.48 ± 0.05 and that of Sneden et al. (2004) is -1.50 ± 0.05 (after correcting both for different solar Fe abundances). The derived M3 standard star [Fe/H] abundance is -1.33 ± 0.05 whereas that of CM05 is -1.42 ± 0.05 (again correcting for different solar Fe abundances). We consider these results in good agreement (see Section 2.6.2 for an abundance comparison of all determined elements).

2.5 Abundance Analysis of Infrared Data

Chemical abundances in the IR are determined via spectrum synthesis, and not EWs. EWs are not practical in the IR due to the presence of molecular lines and blends across the entire spectrum. Synthetic spectra are calculated with MOOG using the model atmospheres described in Section 2.4 and the DR10 line list from Matthew Shetrone (Shetrone et al. 2015). A $^{12}C/^{13}C$ ratio of 6 is adopted following Shetrone et al. (2010). However, at low metallicities the spectral features sensitive to this ratio (i.e. $^{13}C^{16}O$) show no observable change when altering this ratio from 6 to 50. There is also no observable change in overall cabon abundance after altering the ratio by this amount. Therefore, the choice of this value over this range is not critical.

To find the iron abundance a preliminary selection of the most prominent iron

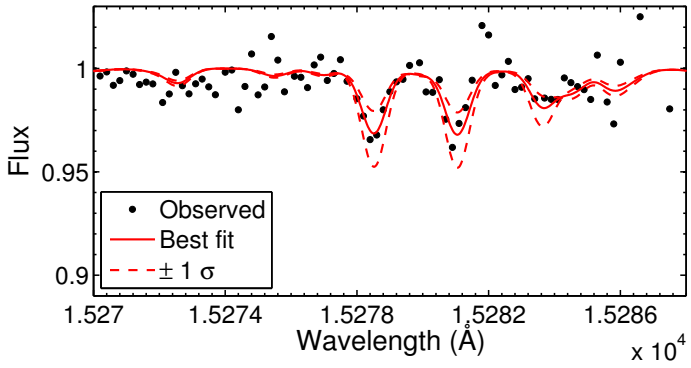

Figure 2.4: Example of a typical OH line measured in the infrared. This particular line is taken from NGC 5466 1344. The two dotted lines represent 1 σ abundance errors.

lines ($\sim$20) is chosen over the spectral range 15100-16900 Å. The spectral region around each of these lines is synthesized with an iron abundance of zero to ensure the feature of interest vanishes and that no other elements or molecules contribute to the spectral line. The resulting sample of iron lines is typically reduced to $\sim$12. The uncertainty for each measured iron line is determined by examining the residual between the synthetic and actual spectrum and finding the abundance which causes the residual to differ visually from the noise. The weighted average is computed for all of the individually examined iron lines and then set as the iron abundance for the synthesis of the rest of the elements. The error of the weighted mean is taken to be the final abundance uncertainty; this method is used to compute the uncertainties in all infrared abundance calculations except in the case of oxygen.

Oxygen has a slight dependance on the carbon abundance through CO formation, therefore an initial carbon abundance is determined from the analysis of a single atomic CI line and several CO features, where carbon is much more sensitive than oxygen. With carbon fixed, the oxygen is then determined by synthesizing OH lines (see Fig. 2.4). The new oxygen abundance is fixed, and the carbon redetermined. This iteration is repeated until the carbon and oxygen abundances converge (typically two iterations). The oxygen uncertainty is first determined exactly as described above with iron, then it is added in quadrature to the value found from re-deriving the oxygen abundance after fluctuating carbon by its maximum error. Finally, nitrogen is found from CN regions using the final carbon abundance (see section 3.5.2 for the regions). The rest of the elements are then synthesized and their abundances determined. The final abundances are shown in Tables 2.7 and 2.8.

2.6 Abundance Results

In this section, the abundance errors and standard star comparison are first addressed before comparing our results with the Galactic sample. The abundances with respect to Fe I from both wavelength regions are then compared with the literature in Section 2.6.3. The reported abundances are with respect to solar, according to Asplund et al. (2009). Galactic comparison stars are taken from Venn et al. (2004), Frebel (2010) (metal-poor stars), and Reddy et al. (2006) (thick disk stars) and comparison MW clusters are taken from Pritzl et al. (2005). Additional comparison stars for Cu and Zn are included from Mishenina et al. (2002). These comparison stars were chosen because their abundances were determined from high-resolution, high S/N spectra. For each element the specific spectral lines used to compute the abundances are discussed as well as any additional effects or corrections (i.e. hyperfine structure, NLTE, 3D effects, etc.). Hyperfine structure corrections are applied to the elements Sc, V, Mn, Co, Cu, Ba, and La; the isotopic data used to compute the corrections were collected from a variety of sources (Sc, V, Mn, and Co from Prochaska et al. 2000, additional Mn from Booth et al. 1983, Cu from McWilliam 1998, Ba from Lawler et al. 2001a, Eu and La from Lawler et al. 2001b), and the corrections are only found to be significant (>0.05 dex) for V and Mn. The abundance errors and standard star comparisons are also discussed in this section.

2.6.1 Abundance errors

The abundance errors are determined by combining intrinsic random errors in the sample with the errors associated with the stellar parameter uncertainties. The intrinsic errors in the sample are determined by computing the error in the mean (i.e. σ_X / $\sqrt{N_{\rm X}}$) except in the case where there were fewer than 5 lines of element X, in which case $\sigma_{\rm Fe}$ / $\sqrt{N_{\rm X}}$ is used. The abundance sensitivities due to stellar parameter uncertainties are calculated and summarized for a sample star (NGC 5024-22254) in Table 2.5. The final errors used with the Galactic comparison are determined by adding the random and stellar parameter uncertainties in quadrature (ignoring the covariant terms between temperature and microturbulence).

Table 2.5: Abundance Sensitivities for NGC 5024-22254

Species	$\Delta T_{\rm eff}$ (+ 100K)	Δ log g (+ 0.2 dex)	Δv_t (+ 0.2 km/s)	Total[a]
		Optical Data		
Fe I	-0.15	0.00	0.10	0.18
Fe II	0.06	-0.07	0.05	0.10
O I	-0.01	-0.04	0.01	0.04
Na I	-0.15	0.04	0.06	0.17
Mg I	-0.09	0.03	0.05	0.11
Al I	...	...	...	...
Si I	-0.01	-0.01	0.01	0.02
Ca I	-0.12	0.01	0.05	0.13
Sc II	0.01	-0.07	0.04	0.08
Ti I	-0.21	-0.01	0.05	0.22
Ti II	0.01	-0.06	0.08	0.10
V I	-0.21	-0.01	0.00	0.21
Cr I	-0.21	-0.01	0.08	0.22
Cr II	0.06	-0.06	0.03	0.09
Mn I	-0.15	0.02	0.08	0.17
Co I	-0.15	-0.01	0.01	0.15
Ni I	-0.13	-0.01	0.03	0.13
Cu I	-0.15	-0.01	0.01	0.01
Zn I	0.04	-0.03	0.04	0.06
Y II	-0.01	-0.07	0.10	0.10
Ba II	-0.05	-0.07	0.12	0.15
La II	-0.03	-0.08	0.01	0.09
Nd II	-0.03	-0.08	0.01	0.09
Eu II	...	...	...	
		Infrared Data		
Fe I	-0.07	0.01	0.00	0.07
C I	-0.01	-0.08	-0.05	0.09
N I	-0.15	0.09	0.06	0.18
O I	-0.18	0.00	-0.01	0.18
Mg I	-0.13	-0.01	-0.02	0.14
Al I	-0.11	-0.01	-0.04	0.12
Si I	-0.12	-0.03	-0.03	0.12
Ca I	-0.19	-0.10	-0.14	0.26
Ti I	-0.20	-0.05	-0.05	0.21

[a]All errors added in quadrature.

2.6.2 Standard star comparison

The standard star abundances are compared to CM05 in detail here. The EWs and stellar parameters between this work and CM05 are in good agreement, as summarized in Sections 2.3.2 and 2.4.4; thus the remaining elemental abundances are now compared. The standard star abundances are shown in Table 2.6; the average abundance difference ($\pm\sigma$) between this work and CM05 is 0.08 $\pm$ 0.13 and 0.14 $\pm$ 0.11 for M3-C41303-2217 and M13-III-18 respectively which we consider good agreement. In the case where there are derived abundances for both the neutral and ionized species (except for the case of Fe), the weighted mean and error between the two is reported and compared with CM05. As opposed to the other elemental abundances, oxygen was determined with respect to Fe II in order to keep consistent with CM05.

For the M3 star most of the elements agree within the errors with the exception of Sc, V, Ni, and La (which lie within 2 σ of each other), of Ca (3 σ), and of Zn (4 σ). Sneden et al. (2004) find Sc to be -0.11 dex lower than CM05 and we also find Sc to be lower (by -0.16 dex). The V abundance in this work has only 3 overlapping lines with CM05, all with different log(gf) values ($\sim$0.05 dex difference). The Ni abundances in this work are derived with log(gf) values that are quite different than CM05, with all 8 of the overlapping lines showing differences up to 0.24 dex. La is derived from 2 lines in this work with similar EWs and log(gf) values to CM05, and from one additional La line; after taking into account the differences in adopted solar values between this work and CM05 the La abundances agree within the errors. The M3 Ca abundance derived by Sneden et al. (2004) differs from CM05 by -0.13 dex, and the difference between this work and CM05 is also found to be lower (by -0.17 dex). There is only one common Zn line between this work and CM05; this line differs in both EW (by 17%) and in log(gf) value (by 0.05 dex).

The M13 star also shows most elements agree within the errors with the exception of Na, and V (which lie within 2 σ), of Ti, Ni, and Y (3 σ), and of Al, and Ca (4 σ). The Na abundances are computed from log(gf) values that differ with CM05 by up to 0.05 dex and with excitation potentials that differ by up to 0.10 ev. V, Ni, Ca, and La derived abundances share the same discrepancies discussed above with the M3 standard star. The Ti abundance is calculated from an average between TiI and TiII and in this work there are many more TiII lines than with CM05. The NLTE effects on TiI are well known and result in a lower TiI abundance compared to TiII (see Section 2.6.3), thus an average computed with more TiI lines than TiII (such

as CM05) will inevitably ensure an overall lower Ti abundance as is shown for both standard stars. The Y abundance is derived from 4 lines, 3 of which are in common with CM05; the line that is not in common with CM05 yields a higher abundance by ~ 0.2 dex. The Al abundance is derived from entirely different lines than CM05. For La there are only two out of four lines that overlap with CM05 and there are $\sim 15\%$ discrepancies in EW for the common lines; furthermore if [La/Fe I] is calculated using the solar values and Fe I parameters of CM05 then the La abundances agree.

Overall, the standard star comparison is within good agreement and we consider the methods used both here and with the target stars sound. The target star abundances are discussed in detail in the following section.

2.6.3 NGC 5024/5466 stars

The final optical and infrared stellar abundances of the target stars are reported in Tables 2.7, 2.8, and 2.9. For all of the comparisons with the Galactic sample, the abundance uncertainties reflect both the errors from the stellar parameters and intrinsic errors reported in these Tables; the two errors are added in quadrature.

Iron

The Fe I and Fe II abundance derived from the optical data are noticeably different in all stars, with differences ranging from 0.18 to 0.33 dex. It is well known that this is caused by NLTE effects on the Fe I lines, e.g., Bergemann et al. (2012); Lind et al. (2012) find that metal-poor RGB stars have Fe I abundances that are underestimated due to the overionization of iron by the radiation field (effects on Fe II are negligible). NLTE corrections[9] for NGC 5466-9951 (the star with the largest Fe I - Fe II discrepancy) are typically +0.1 dex for a sample of 24 lines. Assuming this is representative of our samples (>100 Fe I lines per star in the optical), then we apply a global correction to our results (see Table 2.7). All elements from all ionization states are computed with respect to Fe I.

The iron abundances of the individual stars in both clusters agree with the cluster metallicities (see Table 3). We note the iron abundance spread in NGC 5466 is larger than the 1 σ measurement uncertainties, with one star at [Fe/H] = -2.19 $\pm$ 0.05 dex. This star will be discussed further in Section 2.7.4.

[9]Taken from the online database at http://inspect-stars.net/

Table 2.6: Standard star abundance comparison

Species[a]	Abundance	σ	N	Abundance	σ	N	Δ[b]
	This work			CM05			
M3-C41303-2217 comparison with CM05							
[Fe I/H]	-1.33	0.05	103	-1.37	0.05	126	0.04
[Fe II/H]	-1.33	0.05	14	-1.34	0.05	14	0.01
[O/Fe]	0.49	0.10	2	0.33	0.05	2	0.10
[Na/Fe]	-0.27	0.05	2	-0.39	0.09	3	0.12
[Mg/Fe]	0.33	0.13	2	0.40	0.11	3	-0.07
[Al/Fe]	0.32	0.20	2	...	...	...	...
[Si/Fe]	0.16	0.08	2	0.20	0.05	9	-0.04
[Ca/Fe]	0.25	0.05	16	0.08	0.05	15	0.17
[Sc/Fe]	-0.01	0.05	3	0.15	0.05	7	-0.16
[Ti/Fe]	0.17	0.05	29	0.10	0.05	25	0.07
[V/Fe]	0.05	0.10	12	-0.18	0.06	8	0.23
[Cr/Fe]	0.08	0.05	7	0.01	0.06	9	0.07
[Mn/Fe]	-0.25	0.13	6	-0.27	0.14	4	0.02
[Co/Fe]	0.10	0.30	2	-0.11	0.03	3	0.21
[Ni/Fe]	0.03	0.08	16	-0.16	0.05	15	0.19
[Cu/Fe]	-0.44	0.09	3	-0.56	0.21	2	0.12
[Zn/Fe]	0.24	0.08	2	-0.10	0.05	2	0.34
[Y/Fe]	-0.21	0.08	4	-0.15	0.10	4	-0.06
[Ba/Fe]	0.12	0.08	4	0.16	0.05	3	-0.04
[La/Fe]	0.23	0.05	3	-0.02	0.15	2	0.25
[Nd/Fe]	0.25	0.07	4	0.28	0.06	5	-0.03
[Eu/Fe]	0.65	0.10	1	0.51	0.10	1	0.14
				mean $\pm$ st. dev.			$\overline{\Delta} = 0.08 \pm 0.13$
M13-III-18 comparison with CM05							
[Fe I/H]	-1.57	0.05	118	-1.43	0.05	123	-0.14
[Fe II/H]	-1.34	0.05	23	-1.46	0.05	13	0.12
[O/Fe]	...	...	...	0.35	0.10	1	...
[Na/Fe]	0.57	0.08	4	0.36	0.06	4	0.21
[Mg/Fe]	0.39	0.13	3	0.29	0.14	3	0.10
[Al/Fe]	1.07	0.06	2	0.74	0.10	1	0.33
[Si/Fe]	0.41	0.05	6	0.36	0.05	13	0.05
[Ca/Fe]	0.32	0.05	15	0.10	0.05	13	0.22
[Sc/Fe]	0.31	0.20	5	0.21	0.05	7	0.10
[Ti/Fe]	0.27	0.05	46	0.09	0.05	22	0.18
[V/Fe]	0.04	0.07	11	-0.11	0.05	8	0.15
[Cr/Fe]	0.11	0.07	8	-0.01	0.05	7	0.12
[Mn/Fe]	-0.25	0.09	7	-0.25	0.08	4	0.00
[Co/Fe]	0.16	0.27	2	-0.02	0.06	4	0.18
[Ni/Fe]	0.08	0.05	11	-0.09	0.05	18	0.17
[Cu/Fe]	-0.45	0.08	3	-0.61	0.13	2	0.16
[Zn/Fe]	0.09	0.10	1	-0.05	0.05	2	0.14
[Y/Fe]	0.01	0.09	5	-0.26	0.06	5	0.27
[Ba/Fe]	0.39	0.05	4	0.36	0.05	3	0.03
[La/Fe]	0.41	0.06	4	0.09	0.09	3	0.32
[Nd/Fe]	0.40	0.05	3	0.31	0.06	7	0.09
[Eu/Fe]	0.70	0.10	1	0.58	0.10	1	0.12
				mean $\pm$ st. dev.			$\overline{\Delta} = 0.14 \pm 0.11$

[a] A line weighted average is calculated for species with more than one ionization state to stay consistent with CM05. The [Ab/Fe] is calculated with respect to Fe I except for with O which is calculated with Fe II to match CM05.

[b] Δ = (This Work - CM05)

Table 2.7: Derived abundances for NGC5466 and NGC5024: Fe I, C, N, O

Species[d]	Data source	Abundance ([X/Fe])[a] $\pm\sigma/\sqrt{N}$ (#)[b,c] NGC5024-22254	NGC5024-50371	NGC5466-9951	NGC5466-1344	NGC5466-10186
Fe I	Optical	-2.17 ± 0.05 (105)	-2.15 ± 0.05 (114)	-1.98 ± 0.05 (114)	-2.02 ± 0.05 (114)	-2.19 ± 0.05 (110)
	Infrared	-2.19 ± 0.07 (12)	-2.12 ± 0.07 (12)	-2.00 ± 0.07 (16)	-2.06 ± 0.06 (11)	...
	Ave. NLTE[e]	-2.08 ± 0.09	-2.04 ± 0.09	-1.89 ± 0.09	-1.94 ± 0.08	-2.09 ± 0.05
	ASPCAP	-2.07 ± 0.01	-1.99 ± 0.01	-1.89 ± 0.05	-1.94 ± 0.01	...
C I	Optical	...	...	...	...	...
	Infrared	-0.12 ± 0.37 (*)	-0.28 ± 0.33 (*)	-0.33 ± 0.35 (*)	-0.20 ± 0.20 (*)	...
	ASPCAP	-0.02 ± 0.03	-0.15 ± 0.05	-0.35 ± 0.17	-0.17 ± 0.08	...
N I	Optical	...	...	...	...	...
	Infrared	0.21 ± 0.32 (*)	0.46 ± 0.38 (*)	0.70 ± 0.30 (*)	0.58 ± 0.21 (*)	...
	ASPCAP	0.49 ± 0.04	0.57 ± 0.05	0.87 ± 0.17	0.76 ± 0.10	...
O I	Optical	0.74 ± 0.18 (1)	0.89 ± 0.17 (1)	0.38 ± 0.19 (1)	0.59 ± 0.16 (1)	< 0.40
	Infrared	0.16 ± 0.12 (12)	0.29 ± 0.11 (12)	0.32 ± 0.12 (12)	0.27 ± 0.11 (12)	...
	ASPCAP	...	...	...	...	...

[a] [X/H] is given for Fe I instead.

[b] For elements where N < 5 and σ is less than $\sigma_{\rm FeI}$, the error is reported as $\pm\sigma_{\rm FeI}/\sqrt{N}$; this is also applied to Tables 2.8 and 2.9.

[c] A * indicates the case where there was a synthetic fit to a molecular band.

[d] All abundances ratios computed with respect to NLTE corrected Fe I.

[e] Average [Fe I/H] between optical and infrared (where applicable), corrected for NLTE.

Table 2.8: Derived abundances for NGC5466 and NGC5024: Elements in common between Optical and IR

Species[a]	Data source	Abundance ([X/Fe])$\pm\sigma/\sqrt{N}$ (#) NGC5024-22254	NGC5024-50371	NGC5466-9951	NGC5466-1344	NGC5466-10186
Mg I	Optical	0.16 ± 0.27 (3)	0.50 ± 0.14 (3)	0.24 ± 0.14 (3)	0.27 ± 0.15 (3)	0.32 ± 0.13 (3)
	Infrared	0.23 ± 0.12 (3)	0.25 ± 0.12 (3)	-0.09 ± 0.16 (3)	0.09 ± 0.13 (3)	-
Al I	Optical	...	...	...	...	...
	Infrared	-0.03 ± 0.14 (2)	-0.18 ± 0.21 (2)	0.25 ± 0.16 (3)	-0.36 ± 0.21 (2)	...
Si I	Optical	0.68 ± 0.18 (1)	0.34 ± 0.17 (1)	0.34 ± 0.14 (1)	0.36 ± 0.16 (1)	0.41 ± 0.17 (1)
	Infrared	0.23 ± 0.06 (11)	0.34 ± 0.07 (11)	0.12 ± 0.08 (11)	0.12 ± 0.08 (11)	...
Ca I	Optical	0.31 ± 0.11 (14)	0.26 ± 0.07 (15)	0.17 ± 0.08 (17)	0.18 ± 0.07 (15)	0.19 ± 0.07 (14)
	Infrared	0.23 ± 0.19 (2)	0.25 ± 0.42 (2)	0.12 ± 0.31 (2)	0.15 ± 0.25 (1)	...
Ti I	Optical	-0.14 ± 0.09 (17)	-0.09 ± 0.12 (17)	-0.24 ± 0.07 (15)	0.12 ± 0.11 (16)	0.13 ± 0.11 (14)
	Infrared	0.15 ± 0.20 (1)	< 0.30	0.15 ± 0.28 (2)	< 0.40	...

[a]All abundances ratios computed with respect to NLTE corrected Fe I.

Table 2.9: Derived abundances for NGC5466 and NGC5024: Additional elements from optical data

		Abundance ([X/Fe])[a] $\pm\sigma/\sqrt{N}$ (#)				
Species[b]	Correction	NGC5024-22254	NGC5024-50371	NGC5466-9951	NGC5466-1344	NGC5466-10186
Fe II	None	-1.88 ± 0.13 (18)	-1.90 ± 0.09 (23)	-1.65 ± 0.05 (28)	-1.84 ± 0.10 (18)	-1.89 ± 0.08 (24)
Na I	None	-0.38 ± 0.11 (3)	-0.58 ± 0.17 (2)	-0.28 ± 0.19 (1)	-0.67 ± 0.16 (1)	-0.65 ± 0.12 (2)
Na I	NLTE	-0.38 ± 0.11 (3)	-0.58 ± 0.17 (2)	-0.28 ± 0.19 (1)	-0.67 ± 0.16 (1)	-0.65 ± 0.12 (2)
Sc II	None	0.03 ± 0.14 (5)	0.33 ± 0.14 (4)	-0.01 ± 0.08 (6)	0.19 ± 0.17 (5)	-0.01 ± 0.11 (3)
Ti II	None	0.52 ± 0.09 (17)	0.56 ± 0.10 (20)	0.29 ± 0.09 (34)	0.37 ± 0.09 (18)	0.40 ± 0.07 (23)
V I	None	0.07 ± 0.14 (5)	0.27 ± 0.17 (1)	-0.10 ± 0.19 (1)	...	0.41 ± 0.17 (1)
V I	HFS	0.14 ± 0.09 (5)	0.22 ± 0.17 (1)	-0.17 ± 0.19 (1)	...	0.34 ± 0.17 (1)
Cr I	None	-0.79 ± 0.33 (5)	-0.33 ± 0.11 (3)	-0.34 ± 0.17 (5)	-0.18 ± 0.10 (3)	-0.27 ± 0.11 (3)
Cr I	NLTE	-0.57 ± 0.32 (5)	-0.11 ± 0.11 (3)	-0.12 ± 0.17 (5)	0.04 ± 0.10 (3)	-0.05 ± 0.11 (3)
Cr II	None	0.50 ± 0.25 (3)	0.32 ± 0.25 (3)	0.55 ± 0.15 (4)	0.36 ± 0.18 (3)	0.17 ± 0.11 (4)
Cr II	NLTE	0.55 ± 0.25 (3)	0.37 ± 0.25 (3)	0.59 ± 0.15 (4)	0.40 ± 0.18 (3)	0.22 ± 0.11 (4)
Mn I	None	-0.21 ± 0.13 (2)	-0.59 ± 0.15 (5)	-0.26 ± 0.20 (6)	-0.68 ± 0.09 (4)	-0.58 ± 0.11 (3)
Mn I	HFS	-0.39 ± 0.13 (2)	-0.65 ± 0.14 (5)	-0.36 ± 0.20 (6)	-0.24 ± 0.09 (4)	-0.52 ± 0.11 (3)
Co I	None	0.02 ± 0.33 (2)	...	-0.38 ± 0.19 (1)	-0.22 ± 0.16 (1)	...
Ni I	None	-0.31 ± 0.20 (6)	-0.14 ± 0.09 (6)	0.00 ± 0.21 (8)	-0.18 ± 0.09 (7)	-0.05 ± 0.13 (5)
Cu I	None	...	-0.52 ± 0.17 (1)	...	...	...
Zn I	None	0.25 ± 0.18 (1)	0.30 ± 0.17 (1)	-033 ± 0.19 (1)	-0.07 ± 0.16 (1)	0.01 ± 0.17 (1)
Y II	None	0.00 ± 0.21 (4)	-0.11 ± 0.13 (4)	-0.43 ± 0.12 (3)	-0.48 ± 0.10 (3)	-0.36 ± 0.11 (3)
Ba II	None	0.17 ± 0.28 (4)	0.25 ± 0.09 (4)	0.02 ± 0.24 (5)	0.04 ± 0.09 (3)	0.11 ± 0.14 (4)
La II	None	0.63 ± 0.15 (2)	0.52 ± 0.17 (1)	0.56 ± 0.19 (1)	...	...
Nd II	None	0.16 ± 0.21 (2)	0.11 ± 0.17 (1)	0.09 ± 0.14 (2)	0.21 ± 0.16 (1)	0.18 ± 0.12 (2)
Eu II	None	...	0.74 ± 0.17 (1)	0.71 ± 0.19 (1)	...	0.70 ± 0.17 (1)

[a] [X/H] is given for Fe II instead.

[b] All abundances ratios computed with respect to NLTE corrected Fe I.

The iron abundances of the individual stars in both clusters generally agree with the cluster metallicities quoted in the literature. NGC 5024 has an observed global metallicity of -2.10 (Harris, 1996, 2010) and the average found in this work (after NLTE correction) is -2.06 ± 0.13, which we consider in good agreement. NGC 5466 has an observed metallicity of -1.98 (Harris, 1996, 2010) and the average abundance of this work (after NLTE correction) is -1.96 ± 0.13, also in good agreement.

Carbon and Nitrogen

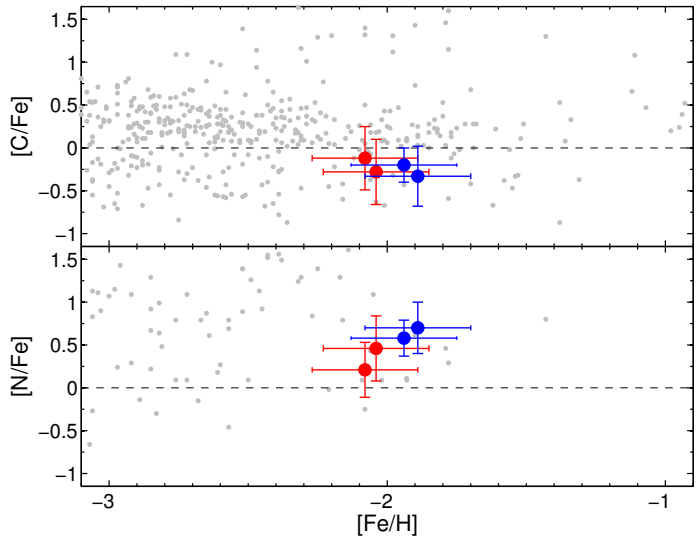

Figure 2.5: C and N abundances of stars in NGC 5024 and NGC 5466 plotted as a function of Fe I, compared with Galactic stars from Frebel (2010) and Reddy et al. (2006) (grey points). Red and blue circles represent NGC 5024 and NGC 5466 stars, respectively.

Carbon abundances are determined by fitting synthetic spectra to CO lines in the IR (formed by vibration-rotation lines throughout the spectral range 15570 - 16200 Å) and to the atomic C I line at 16890 Å. Since the C abundances are relatively low, the molecular lines suffer greatly from noise contamination as their line strengths are small. Thus, large uncertainties are shown in the final abundance. The C abundances of this work (derived from 4 of the 5 stars as there was no IR data for NGC 5466-10186) agree with both the ASPCAP results and Shetrone et al. (2010); see Table 7. The C abundances are compared with a Galactic sample in Fig. 3.7 and appear to be similar to other Galactic stars at the same metallicity.

Nitrogen abundances can be found by fitting synthetic spectra to the CN electronic

transition lines located through the IR spectral range 15200 - 15600Å. The abundances must be determined *after* the C and O abundances are set (refer to section 2.5) because of the C dependance of the molecular lines. The derived N abundances agree with the ASPCAP values (Table 7) and are consistent with Galactic stars of similar metallicity (see Fig. 3.7). Similar to C, the somewhat large uncertainty is due to relatively weak CN lines suffering from noise contamination.

α-elements

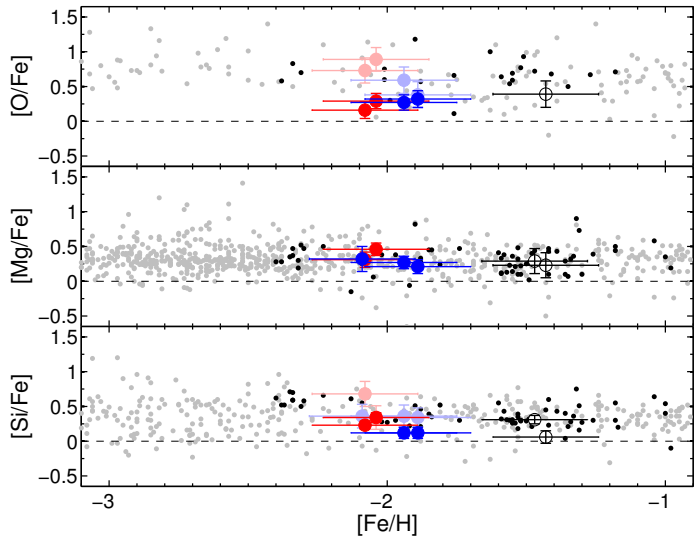

Figure 2.6: O, Mg, and Si alpha element abundances of stars in NGC 5024/5466 plotted as a function of Fe I, compared with Galactic stars from the literature. Red circles represent NGC 5024 stars while blue circles are those of NGC 5466 - O and Si abundances come from IR measurements while Mg abundances come from a weighted average between optical and IR (see text). Light gray points represent Galactic distributions of field stars summarized by Venn et al. (2004), Frebel (2010), and Reddy et al. (2006). Black points represent Galactic GCs, assembled by Pritzl et al. (2005). The hollow black points are abundances derived from the standard stars in M3 and M13. The transparent points in the O and Si plots are abundances derived in the optical where only 1 line was available for abundance determination (one transparent point is hidden behind its infrared data point in the Si plot and there is one additional transparent Si point as there is no IR data for that star).

Alpha elements (O, Mg, Si, and Ca) are constructed via the capture of α particles (^{4}He nuclei) during the hydrostatic burning phase of massive stars and α-rich explosive nucleosynthesis during Type II supernovae (SN II). Ti is also included as an alpha element as it resembles the other alpha elements in the distribution of [α/Fe] ratios in

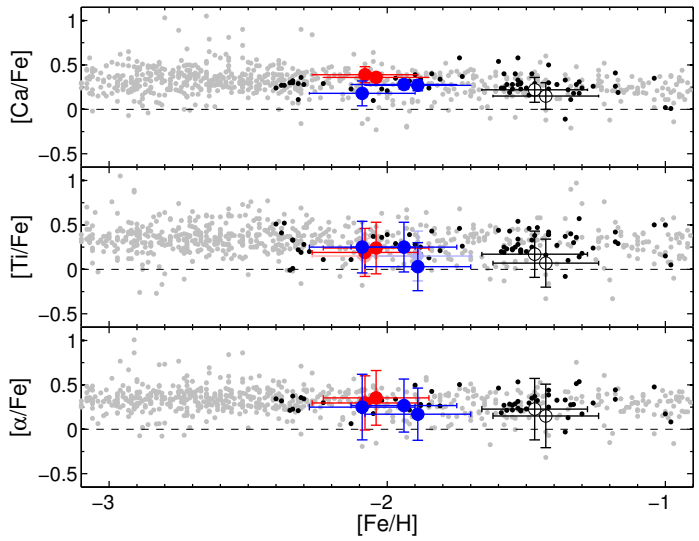

Figure 2.7: Ca, Ti, and α abundances of stars in NGC 5024/5466 plotted as a function of Fe I, compared with Galactic stars from the literature as described in Fig. 3.8. Only the optical Ti abundance is included, and it is computed as a weighted average between TiI and TiII.

Galactic metal-poor field stars. Comparing the alpha elements to Fe (which dominates the yields from Type Ia SN) then the [α/Fe] ratios can inform us on the relative contributions from each type of supernova to the interstellar medium.

Oxygen: O abundances are derived from both the optical and the IR. The only line measured in the optical is the forbidden line (6300 Å, generally quite weak, spanning 13 $<$ EW $<$ 32 Å) while O derived from the IR comes from $\sim$12 OH vibration-rotation lines spanning the spectral range 15260 - 16710 Å. The O abundance derived in 5466-10186 is an upper limit determined from spectrum synthesis. The derived optical and IR O abundances are discrepant (see Table 7), which is not uncommon (e.g., see Israelian et al. 2004; García Pérez et al. 2006). The discrepancy is partially due to a Ni I blend with the forbidden O I line in the optical and that there are a small number of optical O I lines compared to the numerous IR OH lines. Also, large systematic effects are found for the OH lines due to temperature uncertainties in model atmospheres (García Pérez et al. 2006, 2013), and 3D and NLTE effects are not expected to have a major effect on the optical forbidden line (Kiselman 1993; García Pérez et al. 2006), but may play a role in the line formation of the infrared OH lines. Smith et al. (2013) have reproduced the optical abundances from IR spectra of several nearby field giants using 1D and LTE atmospheres in the same spectral windows and line lists used here. In this paper, the IR measurements are adopted for

oxygen, as shown in Fig. 3.8.

Magnesium: Mg abundances are derived from both the optical and IR spectra. The optical abundances are mostly determined from three MgI lines at 4703, 5528, and 5711 Å; the first two lines are generally strong (100 < EW < 140 mÅ) and the third is generally weak (EW∼40 mÅ) while the IR abundances are determined from the three strong lines (EW > 140 mÅ) at 15740, 15748, and 15765 Å. A weighted average between the optical and IR abundances is computed and shown in Fig. 3.8: the resulting abundances agree with most of the other Galactic stars at the same metallicity.

Silicon: Only a single weak Si line (EW ∼ 20 mÅ) is available in the optical (at 6155 Å) and is not in very good agreement with the IR Si abundance(see Table 8). Therefore the final reported Si abundance is only from the ∼ 11 lines found in the IR (spanning 15370-16380 Å, where the lines have varied strength). Fig. 3.8 shows that the four target stars (those with IR spectra) have Si abundances which are consistent with other Galactic stars at the same metallicity.

Calcium: Ca abundances are determined from both optical and IR lines. Although there are significantly more available lines in the optical (∼15, found over the spectral range 5588-6717 Å, of varied strength) than compared with the IR (2 relatively weak features at 16150 and 16196 Å) the abundances are found to be in good agreement (see Table 8). The weighted average abundance between the two wavelength regions (computed when both data sets are available) shows Ca in the target stars is comparable to other stars in the Galactic sample at roughly the same metallicity (see Fig. 3.9).

Titanium: There are numerous TiI and TiII lines available in the optical, spanning the entire wavelength range and of varied line strength; conversely there are very few lines in the IR. Final Ti abundances are determined from the average between TiI and TiII lines (30-40) in the optical while the single TiI line in the IR (at 15335 Å) is omitted as it may be less reliable due to line blending with Fe I. The errors from the abundances of both ionization states are added in quadrature and reported here. Table 8 indicates the IR Ti abundances are in excellent agreement with the optical. Fig. 3.9 reveals the Ti in the target stars behaves in a similar manner to stars of similar metallicity in the Milky Way. The abundance discrepancy found between Ti I and Ti II (typically ∼ 0.2 dex) is a feature which is seen in other work (Letarte et al. 2010; Lemasle et al. 2012), but not found here. This discrepancy could be explained by NLTE effects associated with Ti I, described by Bergemann (2011), however the

stellar parameters were outside the range of the target stars in this work and so NLTE corrections are not applied.

Alpha: In this work, an α-element abundance is defined as the average of Ca, Mg, and Ti, and is calculated for both the target stars and Galactic distributions taken from the literature. The results are shown in Fig. 3.9. Results for the target stars are consistent with the Galactic distribution. Ca and Mg abundances are derived from both optical and infrared data, and their weighted averages are shown here. Ti is reported here as the average between Ti I and Ti II, and their respective errors are added in quadrature.

Sodium and Aluminum: Sodium abundances are derived in the optical from the D1 and D2 lines (if the D lines are the only available measurements then lines above 200 mÅ are kept) and the line at 5688 Å (which is generally weak, $\sim$ 20 mÅ). Sodium is known to have a range of NLTE effects that are line dependent, but also depend on the Fe and T_{eff} of the models. Corrections have been applied following Lind et al. (2011)[10], where NLTE corrections ranged from -0.05 dex (for the 5688 Å line) up to -0.29 for the D lines. Abundance measurements are shown in Fig. 3.10, almost all of which are relatively low compared to the Galactic GCs. The GC abundance average would include the second-generation Na-enhanced stars.

Aluminum lines were only found in the higher metallicity standard stars at optical wavelengths. Conversely, there are three strong (EW > 100mÅ) Al I lines in the IR at 16718, 16750, and 16760 Å. The Galactic distribution of Al in stars around this metallicity is quite dispersed and the NGC 5466/5024 stars fall more or less within the Galactic field star distribution.

Iron-peak Elements

Scandium, *vanadium*, and *manganese* are derived exclusively from optical data, using 1-6 spectral lines (per element) and are shown in Fig. 2.9. Scandium is found entirely from singly ionized lines and two of the five target stars have slightly high Sc abundances. As noted in Section 2.6, HFS corrections were negligible for Sc. V was derived for two stars from each target cluster from generally weak lines (EW $\sim$ 20 mÅ). Hyper fine structure corrections for V were calculated and applied to each individual star (typically -0.07 dex, following the references discussed in Section 2.6). The V abundance appears consistent with the Galactic sample although there is a

[10]Adopted from the online database at http://inspect-stars.net/

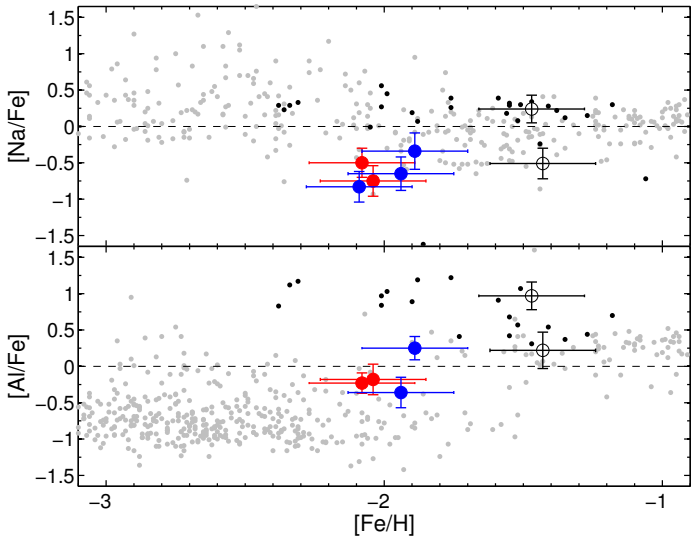

Figure 2.8: Na and Al abundances of stars in NGC 5024/5466 plotted as a function of Fe I, compared with Galactic stars from the literature as described in Fig. 3.8. Na abundances were determined from optical data (with NLTE corrections) while the Al abundances are from infrared data (explaining why there are only 4 data points).

significant scatter in V for the NGC 5466 stars; these NGC 5466 abundances are measured from a single V line in each star and the scatter agrees within the errors therefore this scatter may not be real. The Mn lines varied in strength and were found to have significant hyperfine structure corrections (ranging from -0.06 to -0.21 dex, depending on the star); after applying these corrections (again following the references in Section 2.6) the Mn in the target stars appears to follow the Galactic distribution at their respective metallicities. Bergemann & Gehren (2008) show that a metal-poor star ([Fe/H]∼-2.5) with similar stellar parameters to the targets in this work and has a *total* NLTE correction of +0.44 dex, however there are no stars in their sample that share the same parameter space as our standard stars. We do not apply this correction because this would not allow a comparison with our standard stars and it is unclear whether the correction of Bergemann & Gehren (2008) applies to the same lines of this work. However, it should be noted that NLTE effects are strong for Mn lines within the stellar parameters of our sample.

Chromium, *cobalt*, and *nickel* are also derived exclusively in the optical. The Cr abundance is reported as a line weighted average between 6-10 Cr I and Cr II lines found over the spectral range 4550-6330 Å and of varying line strength. The discrepancy between Cr I and Cr II is apparent, which can be attributed to NLTE

effects of Cr I, e.g. Bergemann & Cescutti (2010). NLTE corrections were found by locating stars of a similar metallicity to this sample, looking at common chromium lines between the two datasets, and then extracting the NLTE abundance correction. The NLTE correction was applied line by line to the abundances in this sample, with corrections typically found to be 0.22 dex for target stars and 0.10 dex for the standard stars; the Cr II correction also applied in the same manner and was generally found to be much smaller ($\sim$ 0.05 dex). The Cr abundance in the NGC 5024/5466 stars is slightly higher than the Galactic distribution (see Fig. 2.10), however given the NLTE corrections and 1-σ uncertainties then we consider our results in good agreement with the other Galactic globular cluster data. Co is found in both cluster stars from weak lines (EW $\sim$ 20 mÅ). In NGC 5024 Co is found in one of the stars, specifically from 2 lines at 5483 and 5647 Å and agrees with the Galactic distribution (see Fig. 2.10). In both the NGC 5466 stars Co is determined from 1 line at 5483 Å. Bergemann et al. (2010) find Co NLTE corrections for the same star used to find Mn NLTE corrections in Bergemann & Gehren (2008). They find Co has high NLTE corrections at low metallicities, similar to Mn, and find corrections of 0.64 dex for the star that shares the same parameter space with this work. Co NLTE corrections are not applied to this work for the same reasons discussed with Mn. Finally, Ni abundances are derived from 5-8 optical lines of varied strength and are in good agreement with other Galactic stars at this metallicity.

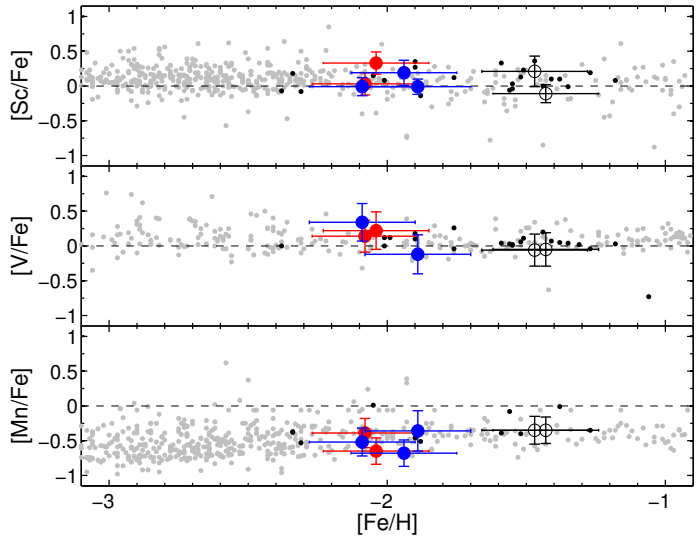

Figure 2.9: Sc, V, and Mn abundances of stars in NGC 5024/5466 plotted as a function of Fe I, compared with Galactic stars from the literature as described in Fig. 3.8.

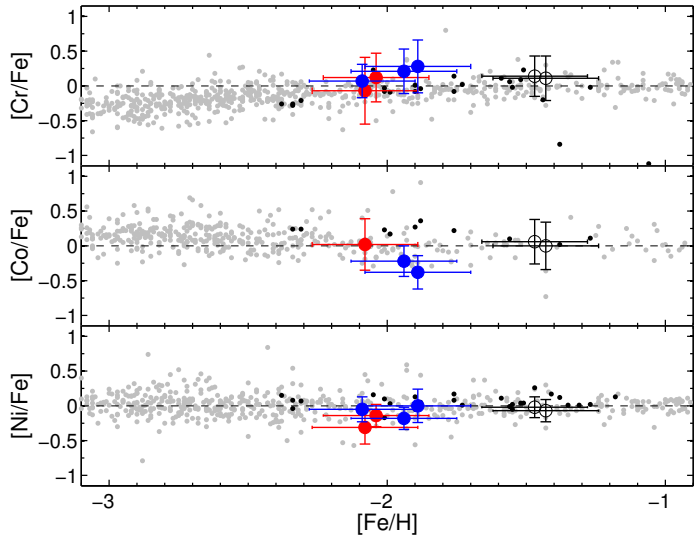

Figure 2.10: Cr, Co, and Ni abundances of stars in NGC 5024/5466 plotted as a function of Fe I, compared with Galactic stars from the literature as described in Fig. 3.8. The Cr abundance is reported as a weighted average between Cr I and Cr II, where NLTE corrections have been applied to each ionization state.

Copper and Zinc

Copper and *zinc* measurements are relatively scarce in the literature, thus an additional source is added (Mishenina et al., 2002) for comparison. Copper is only detected in one of the NGC 5024 stars (from the single weak line at 5105 Å) and not in NGC 5466. Zinc is measured in all the target stars from the neutral line at 4722 Å(typically with an EW of 40 mÅ); the NGC 5466 stars show a trend slightly lower (see Fig. 2.11). The NGC 5466 Zn abundance was noted to be significantly low in a detailed abundance analysis of a single anomalous cepheid star reported by McCarthy & Nemec (1997). They argue that since the low [Zn/Fe] ratio should reflect the primordial abundance of their target star and predicted other stars would also be low in Zn.

Neutron-capture Elements

The neutron-capture elements come from one of two processes: either the slow process (or s-process) via AGB stellar winds or through the rapid process (r-process) during SNe II nucleosynthesis. Burris et al. (2000) have shown that in the Sun 97 % of the Eu abundance originates from the r-process, whereas at least 72% of the Y, Ba, and

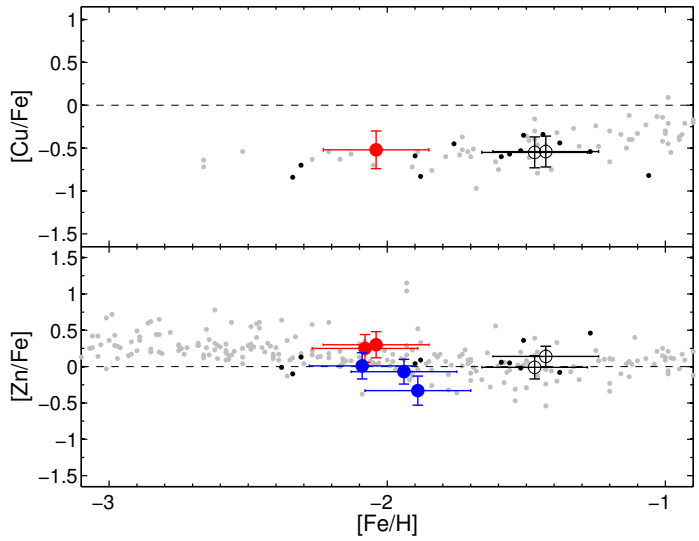

Figure 2.11: Cu and Zn abundances of stars in NGC 5024/5466 plotted as a function of Fe I, compared with Galactic stars from the literature as described in Fig. 3.8. Also included are Cu and Zn abundances from Mishenina et al. (2002), also plotted as light gray points. The Cu line used to compute the Cu abundance is quite weak and only detectable in NGC 5024-50371.

La in the Sun come from the s-process. Thus these elements are excellent indicators as to which of these two types of processes have been involved within the environment of the cluster.

Yttrium is detected in all five target stars from 3-4 singly ionized lines of varied strength in the optical data. Y in both clusters is consistent with the Galactic comparison sample. The abundance in the two NGC 5024 stars is higher than those in NGC 5466 (see Fig. 2.12). The Y can be seen to have little star to star variations within each cluster and is also in agreement with the standard stars in M3 and M13.

Barium is detected in all five target stars from 3-5 strong (EW $>$ 100 mÅ) singly ionized lines in the optical. Fig. 2.12 shows the small star to star dispersion of Ba within each cluster and it also shows the Ba is in good agreement with the M3/M13 standard stars.

Lanthanum is detected from only 1-2 weak, singly ionized optical lines in the NGC 5024 stars and one NGC 5466 star. These La abundances appear to be slightly higher than our M3/M13 stars and the Galactic distribution (see Fig. 2.12).

Neodymium abundances are measured from 1-2 weak lines from the optical data (at 5249 and 5319 Å) for all five of the target stars. Nd measurements show very little star to star variation within each cluster and also agree with our standard stars

(see Fig. 2.13).

Europium is only detected in three stars (two in NGC 5466 and one in NGC 5024) from the weak 6645 Å line in the optical (EW $\sim$ 15 mÅfor all three stars). Fig. 2.13 shows the measured Eu abundance in both clusters is relatively higher than the Galactic distribution.

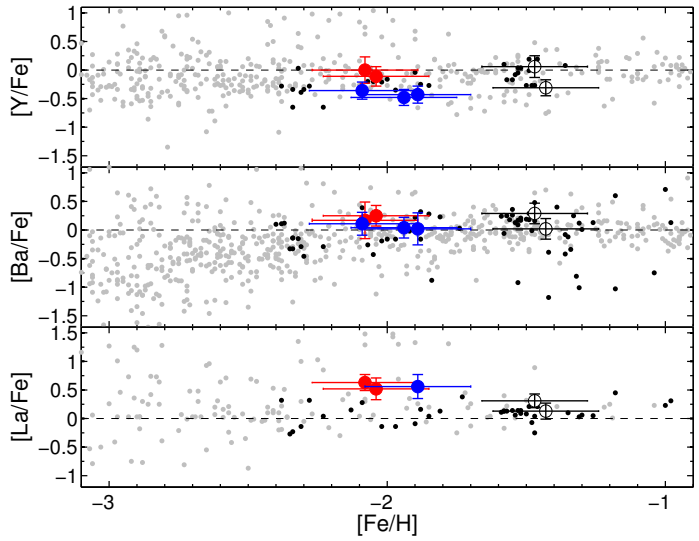

Figure 2.12: Y, Ba, and La abundances of stars in NGC 5024/5466 plotted as a function of Fe I, compared with Galactic stars from the literature as described in Fig. 3.8.

To validate the accuracy of the Eu abundance derived from the EW analysis we synthesize the weak line at 6645 Å for a single star (NGC 5466-9951) and compare. Fig. 2.14 shows a synthetic spectrum for the EW Eu abundance with 1 sigma errors. Also shown is the synthetic fit to the weak La line in the same star, where the synthetic spectrum is created with the EW La abundance (also with 1 sigma errors).

2.7 Discussion

2.7.1 Infrared Abundance Comparison with Optical and Literature Abundances

There are 7 elements from the sample of stars in this work (including standard stars) which have abundances derived from both the optical and the IR: Fe, O, Mg, Al, Si, Ca, and Ti. Tables 2.7 and 2.8 summarize the reported abundances and show the

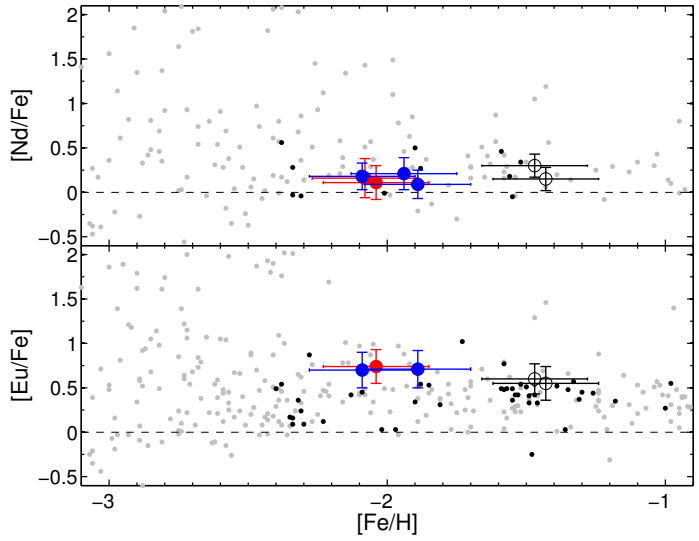

Figure 2.13: Nd and Eu abundances of stars in NGC 5024/5466 plotted as a function of Fe I, compared with Galactic stars from the literature as described in Fig. 3.8.

excellent agreement of Fe derived from the optical and the IR. The ASPCAP (see Section 2.4.2) Fe abundances are also in excellent agreement, even though the model atmospheres used to compute the abundances in this work have different parameters (although within the errors, see Table 2.4). In Fig. 2.15, we compare the optical and IR abundance results for the remaining six elements that are found in both wavelength regions (Fe is excluded as the abundances are shown as [X/Fe]), as well as C and N. There are reported abundances for C and N from ASPCAP and for C from Shetrone et al. (2010) and Martell et al. (2008). The IR C abundance in NGC 5024 is in excellent agreement with ASPCAP and Martell et al. (2008). Similarly the IR C abundance in NGC 5466 is consistent both with ASPCAP and Shetrone et al. (2010). The N abundance in both clusters also shows consistency with ASPCAP. The O abundance derived in the IR is much lower than that of the optical for the two stars in NGC 5024; this discrepancy is discussed in section 3.5.3 and we favour the IR results. The rest of the element abundances are consistent, with the exception of Si in one star; we favour the IR abundances for Si since there are only 1-2 measured lines in the optical but many more lines in the IR.

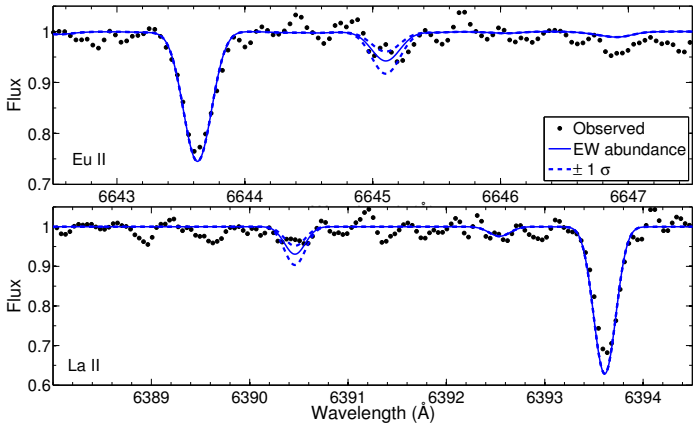

Figure 2.14: Top: synthetic abundance fit to the single Eu line in NGC 5466-9951; the 1 sigma errors here are 0.19 dex. The spectrum synthesis agrees with the EW analysis abundance. Bottom: synthetic fit to the weak La line in the same star, along with 1 sigma errors (0.19 dex); the synthetic abundance agrees with the EW abundance.

2.7.2 r and s-process contributions

Europium is a used as proxy for the r-process (based on an analysis of the solar system distribution of the heavy elements, e.g., Arlandini et al. (1999); Burris et al. (2000)), whereas Y, La, and Ba are formed in a number of nucleosynthetic sites ranging from core collapse SN to the s-process during the thermal pulsing in AGB stars. Gallino et al. (1990) and Busso et al. (1999) showed that the s-process yields in AGB stars are metallicity dependent, such that low metallicity AGB stars will bypass the first s-process peak elements in favour of the second and third peak elements due to a lack of iron seed nuclei. In Galactic field stars, the increase in these elements from the s-process can be seen between metallicities of $-3 <$ [Fe/H] < -2 (e.g., McWilliam et al. 1995; McWilliam 1998). Fig. 2.16 shows [Ba/Eu] and [Ba/Y] as a function of metallicity in Galactic globular clusters and field stars; the r-process yield in [Ba/Eu] from Burris et al. (2000) is also shown. The slightly elevated [Ba/Eu] values in our two globular clusters are consistent with a mild s-process contribution, and the [Ba/Y] values suggest those contributions are from metal poor AGB stars.

2.7.3 Evidence for Mixing

The locations of the target stars on their colour-magnitude diagrams (CMDs) are shown in Fig. 2.17; photometry is from Sarajedini et al. (2007); Anderson et al.

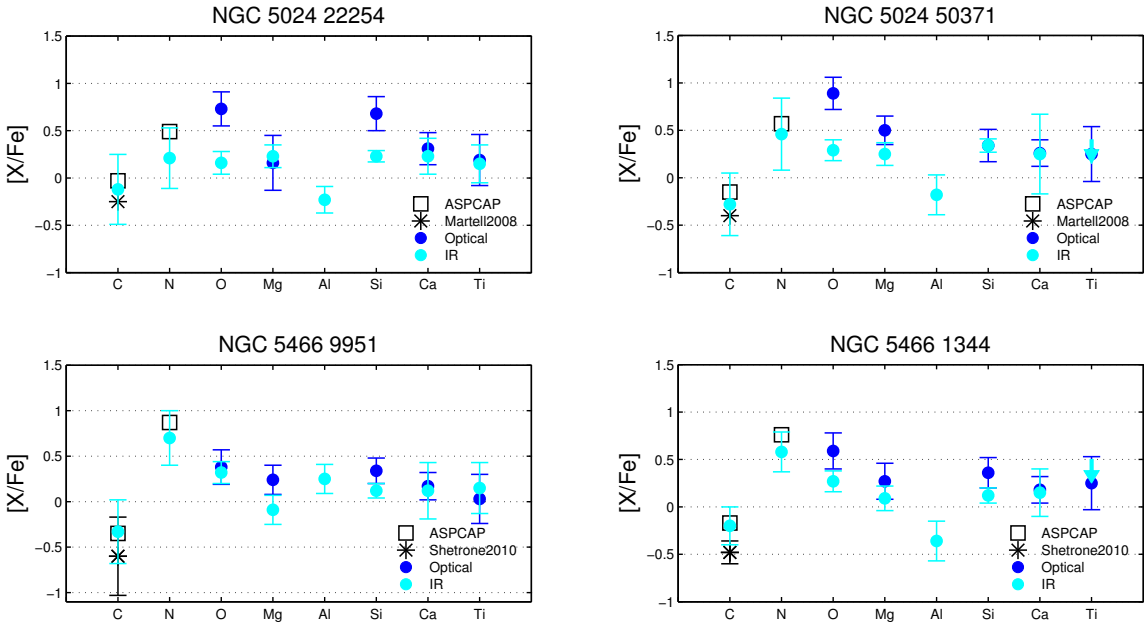

Figure 2.15: Abundance comparison of overlapping elements between target stars. The blue points are from the optical observations of this work, the cyan points from infrared APOGEE observations, the square points from APOGEE's abundance pipeline ASPCAP, and the asterisk points from Martell et al. (2008) (NGC 5024), Shetrone et al. (2010) (NGC 5466). The ASPCAP points and the points of Martell et al. (2008) are plotted without errors, as the reported values in each case are negligibly small and perhaps do not reflect the true spread in the measurements. In general, the results are consistent except for O and Si in NGC 5024-22254 and for O in NGC 5024-50371.

(2008). All of our targets are bright stars located near the tip of the red giant branch, above the RGB bump, where mixing of CNO-cycled H-burning gas is expected (e.g., Suntzeff & Smith 1991; Smith & Martell 2003; Smith & Briley 2006, Charbonnel et al. 1998, Sweigart & Mengel 1979; Charbonnel 1995; Bellman et al. 2001; Denissenkov & VandenBerg 2003; Carretta et al. 2005). This will have the effect of elevated N (by $\sim$ 0.5 dex), slightly depleted C (by $\sim$0.2 dex), and even slighter depletions of oxygen ($<$ 0.1 dex) from their initial abundances (Carretta et al., 2005). Assuming the globular clusters started with solar C and N, then the [(C+N)/Fe] abundances will remain $\sim$solar (we ignore the very small change in oxygen that is expected from its enhanced, Galactic plateau, initial value). The [(C+N)/Fe] values are shown in Fig. 19, and are consistent with standard mixing as the sums remain near solar. NGC5466-9951 also shows slight enhancements in Na and Al suggestive of primordial variations or pollution within the cluster (e.g., Gratton et al. 2004; Carretta et al.

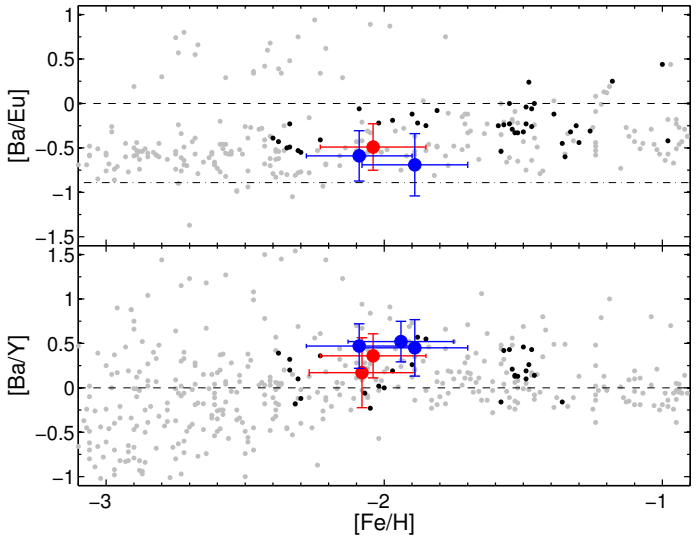

Figure 2.16: [Ba/Eu] vs [Fe/H] and [Ba/Y] for the NGC 5024/5466 stars with available abundances. The lower dashed-dotted line in the top plot represents the lowest [Ba/Eu] ratio possible, where only the r-process contributes to these elements (Burris et al., 2000).

2009). This suggests that NGC 5466-9951 may be a member of a second generation population in this cluster.

2.7.4 NGC 5024/5466 origins

NGC 5024 and NGC 5466 do not show any distinct abundance differences with GC and field stars within the MW, although at these low metallicities it is difficult to discern whether the abundances of these clusters would show extra-galactic signatures. As previously described, this is because at low metallicities GCs like M54 do not show chemical abundance patterns that stand out with GCs in the MW, even though it has physical associations with a dwarf remnant. However, M54 and ω Cen *do* show an Fe metallicity spread (i.e. 0.19 dex rms scatter for M54), and are among the few GCs known to show such a spread Carretta et al. (2010); where it is also argued this spread could be caused by large and repeated bursts of star formation. Interestingly, NGC 5466 also shows a spread in Fe abundance found from the three stars in this work (0.09 dex rms scatter). The velocity dispersion is relatively large in this sample (12 km/s), which is also seen to be large by Shetrone et al. (2010) (17 km/s, although from low resolution spectra). It is possible that the one star NGC 5466-10186 that causes most of this velocity dispersion is a non-member, however the position of this star on the

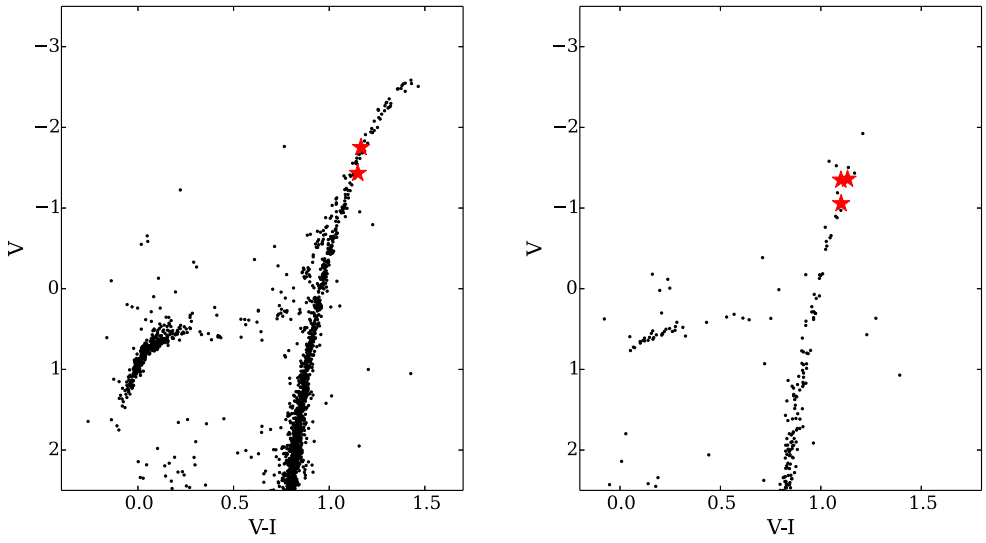

Figure 2.17: Colour-magnitude diagrams for the globular clusters NGC 5024 (left) and NGC 5466 (right), with photometry taken from Sarajedini et al. (2007); Anderson et al. (2008), respectively.

CMD and lack of foreground contamination towards this cluster makes this unlikely. It is also possible that NGC 5466-10186 is in a binary system which may have affected its apparent radial velocity and could also explain the slightly lower metallicity we have found if the binary companion has artificially increased its continuum flux levels. Before interpreting the velocity and Fe dispersions in NGC5466 in terms of its origins or physical mass, more stars should be examined in this cluster.

2.8 Summary and Conclusions

A detailed chemical abundance analysis has been performed for two RGB stars in NGC 5024 and three RGB stars in NGC 5466. In this analysis, we have found:

1. The optical and infrared abundances are in good agreement for the elements Fe, Mg, Si, Ca, and Ti. There is a discrepancy in the oxygen abundances, which has been seen before in the literature. We favour our IR oxygen abundances, determined from several OH features.

2. The neutron-capture elements are mildly enriched in s-process yields from metal-poor AGB stars.

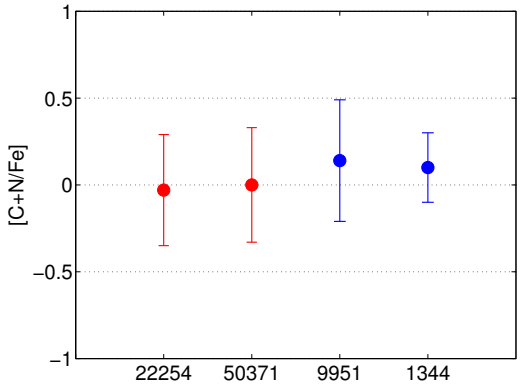

Figure 2.18: [C+N/Fe] abundances to the NGC 5024/5466 stars where the data was available. The red and blue points are those of NGC 5024 and NGC 5466, respectively.

3. The stars in both clusters exhibit CNO mixing, as evidenced from the enhanced N, depleted C, and solar [(C+N)/Fe] ratios. One star NGC5466-9951 shows slight enhancements in Na and Al as well, which suggests it may be a member of a second generation population.

4. Both globular clusters show element ratios that are similar to other Galactic clusters at this metallicity, however NGC5466 may have a larger spread in the iron abundances and a larger velocity distribution. This may be due to one star (NGC5466-10186) in a binary system, or it may represent a physical property of this cluster. Other clusters with metallicity and velocity dispersions similar to this include Omega Cen and M54, both accreted from the Sgr dwarf galaxy.

We conclude that abundances derived from both the optical and infrared regions complement each other in a stellar atmospheres analysis, and that NGC5024 and NGC5466 appear to be similar to the majority of Galactic globular clusters. Further spectroscopic analysis of NGC5466 is needed to confirm its apparent metallicity and velocity dispersion. The infrared techniques developed in this analysis are robust and can be confidently applied to other infrared spectroscopic data (such as the MOAO instrument RAVEN).

Chapter 3

Using the multi-object adaptive optics demonstrator RAVEN to observe metal-poor stars in and towards the Galactic Centre

Important note: the work in this Chapter is taken directly from the paper titled *Using the multi-object adaptive optics demonstrator RAVEN to observe metal-poor stars in and towards the Galactic Centre* (Lamb, M., Venn, K., Andersen, D., et al. 2017, MNRAS, 465, 3536).

3.1 Introduction

The metallicity distribution function (MDF) of the Milky Way (MW) Galaxy is varied and can differ drastically from one Galactic component to the next. Prime examples of this are the differences in the mean and metal-poor extension of the MDF of the Galactic halo (Schörck et al., 2009; Yong et al., 2013) compared to that of the Galactic bulge (Hill et al., 2011; Ness et al., 2013; Bensby et al., 2013; Howes et al., 2014). The metal-poor stars in both components are important and can reveal a wealth of information about these environments, i.e. characterization of the Galaxy at earlier stages in its evolution, and constraints on Population III stellar models and chemical yields (Beers & Christlieb, 2005; Salvadori et al., 2007; Ekström et al., 2008). Even though most metal-poor stars are found in the halo, it has been proposed that evidence

of the most metal-poor stars (even the First Stars) could in fact be located within the Galactic bulge (Diemand et al., 2005; Salvadori et al., 2010; Tumlinson, 2010; Gao et al., 2010). Furthermore, the bulge exhibits evidence of multiple components (Babusiaux et al., 2010; Hill et al., 2011; Ness et al., 2013), chemically distinct from one another, thus in this paper we have used a new method to search for and examine metal-poor stars in the Galactic bulge, and investigate their locations and orbits.

The discovery and characterization of metal-poor stars in the bulge has been approached through a variety of techniques. Bensby et al. (2013) discovered a [Fe/H] = -1.9 dex star based on high resolution spectroscopy from a gravitational microlensing event. García Pérez et al. (2013) found two stars at [Fe/H] $\sim$ -2.1 dex from near-infrared (NIR) APOGEE[1] spectroscopy. More recently, the EMBLA Survey (Howes et al., 2014, 2015, 2016), Casey & Schlaufman (2015), and Koch et al. (2016) have used photometric indices as metallicity indicators to identify and spectroscopically observe bulge metal-poor stars at high resolution; as a result they have shown the metal-poor tail end of the bulge MDF extends much further than has previously been observed, showing a sample of 23 stars with -2.3 < [Fe/H] < -4.0. In addition, the ARGOS survey (Ness et al., 2013) have identified $\sim$20 stars with [Fe/H] < -2 at medium resolution.

There have been two notably unique features regarding bulge metal-poor stars to date. The first is that out of the 23 stars observed by Howes et al. (2015), *none* of the stars were observed to be significantly enhanced in carbon, which is contrary to that found by Placco et al. (2014) in the halo at these metallicities. Second, is a sample of stars observed in NGC 6522 - a bulge cluster with one of the oldest known ages in the Galaxy - show anomalously high s-process elements given their metallicities ([Fe/H] $\sim$ -1.0), a feature only seen in halo stars with [Fe/H] < -3.0 (this feature however has been argued to be a false detection, e.g. see Ness et al. 2014). Discovering and accounting for these unique features within bulge metal-poor stars is inherently interesting; Howes et al. (2015) and Chiappini et al. (2011) draw links between these unique features and First Star remnants. As such, filling in the metallicity gap between these two works (i.e. -1.0 < [Fe/H] < -2.3) with a sample of bulge stars with detailed chemical abundances is compelling.

To date, detailed spectroscopic observations of metal-poor bulge stars have been observationally difficult due to (i) the stellar obscuration from dust, (ii) the stellar

[1]APOGEE is an H-band, high-resolution, high signal-to-noise spectroscopic survey of thousands of Milky Way stars, carried out at the Apache point observatory.

crowding of the highly dense region, and (iii) the rare nature of metal-poor stars within the entire sample ($\sim$1 in 5000 Ness et al. 2013). The aforementioned observing techniques (i.e. Bensby et al. 2013; García Pérez et al. 2013; Howes et al. 2015, amongst others) hold advantages and disadvantages over one another, with each technique mitigating one or two of the issues, however none capable of simultaneously correcting all three. In this paper, we employ a new approach that can significantly mitigate all three issues simultaneously; this method uses the new RAVEN multi-object adaptive optics (MOAO) instrument (Lardière et al., 2014; Ono et al., 2016) with the Infrared Camera and Spectrograph (IRCS, Kobayashi et al. 2000) at the Subaru 8.2-m telescope.

RAVEN employs the technology of MOAO - a flavour of adaptive optics (AO) that allows for multiple windows of correction over a wide field of regard (i.e. on the order of arcminutes). Each window is provided by a mirror on a 'pick-off' arm, which patrols the astronomical field and is placed over scientifically interesting objects. Bright stars within the field of regard act as guide stars (including a laser guide star), which is then used to reconstruct the volume of turbulence above the telescope.

RAVEN demonstrates this technology with 2 pick-off arms on an 8-m class telescope, however there may be many more arms on future extremely large telescope (ELT) instruments. ELTs will also employ MOAO to a greater effect; a larger diameter pupil will in turn have a meta-pupil that does not de-correlate as quickly as an 8-m class telescope as a function of altitude. This results in the capability of a larger field of regard for ELTs, which in turn allows for a larger availability of guide stars (and therefore sky coverage). In addition, ELT-MOAO will use many laser guide stars and will only rely on natural guide stars for tip/tilt/focus measurements; these measurements can use the full aperture of the telescope and therefore sensitivity (and sky coverage) is increased for an ELT compared to an 8-m telescope. However, demonstrating MOAO on a telescope such as Subaru is important to gain technological insight and test scientific observing strategies for these future MOAO applications.

The RAVEN instrument operates in the near-infrared, allowing relief from dust obscuration. In addition, AO performance improves with respect to increasing wavelengths, allowing for higher Strehl ratios compared to the optical. Traditional stellar spectroscopy is usually practiced in optical regions, however the near-infrared has shown to be an excellent complementary resource to optical stellar abundances, (e.g. Mészáros et al. 2015; Holtzman et al. 2015; Cunha et al. 2015; Smith et al. 2013;

Lamb et al. 2015). This wavelength region is spectroscopically accessible to many of the light elements, with more numerous C, N, and O features than the optical, where the continuum is formed in the deepest layers of the stellar atmosphere (Alves-Brito et al., 2012). Furthermore, the near-infrared is an excellent regime to examine Fe features, where typical Fe lines have high excitation potential and are thus less sensitive to variations in Teff (e.g., see Alves-Brito et al. 2012). Finally, light elements such as Si are readily available in the infrared, whereas they can be more elusive in the optical (e.g., see Lamb et al. 2015).

In this paper, we use the AO instrument RAVEN coupled with IR spectroscopy to determine stellar abundances. Thus, the goals of this paper are to demonstrate MOAO, discuss its unique observing strategies for future applications, and to observe metal-poor stars in and towards the centre of our Galaxy.

3.2 Observations and data reduction

3.2.1 RAVEN technical details

RAVEN features two pick off arms, each selecting a 4"x4" region over a field of regard, which can be up to $\sim$ 3.5 arcminutes in diameter. The field of regard is defined by an asterism of three guide stars: either 3 natural or 2 natural and 1 laser (using the existing sodium LGS at the Subaru facility, Hayano et al. 2010). The limiting magnitudes on the guide stars are R$\sim$13[2]. Each guide star utilizes a wavefront sensor (WFS), from which a tomographic representation of the atmosphere is constructed within the asterism (for more details see Jackson et al. 2014; Correia et al. 2015). Any region selected by a pick off arm within the asterism can project this tomographic model onto its own deformable mirror (DM), thus providing an AO correction. The two deformable mirrors are custom 145 actuator ALPAO DMs, with 11 actuators spanning the pupil. MOAO features open-loop control as opposed to the closed-loop control of a classic AO system (otherwise known as SCAO), meaning the system will command the DM using WFS data of the full turbulence as opposed to the residual turbulence. In other words, the WFS does not see the DM correction, because the DM is located after the WFS. However, RAVEN is also capable of employing SCAO

[2]The limiting magnitude could reach R$\sim$14 during dark time, however the moon contaminated they sky during most of our engineering time, and the limiting magnitude depended on its phase and location on the sky

and ground layer adaptive optics (GLAO). GLAO is a technique that corrects for ground layer turbulence only, and is employed by averaging the measurements of all three WFSs to drive the DMs. GLAO can be particularly useful when the RAVEN Slope Detection and Ranging (SLODAR) measurements showed the majority of the turbulence to be in the ground layer. Figure 3.2 shows a typical asterism, defined by the green dashed boundary, as well as two potential science targets within the asterism shown in red.

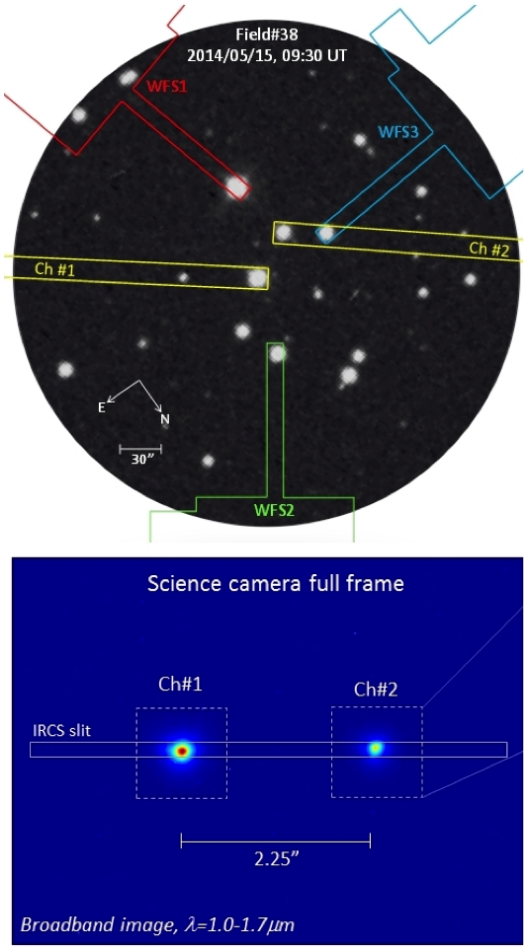

Figure 3.1: Example configuration of RAVEN's WFS and science channel pick off arms on a field used during an engineering run. The 3 WFS arms are outlined in red, green, and blue while the science channels are outlined in yellow. Also shown is the arrangement of the two channel targets on the IRCS slit.

RAVEN re-images the two channels onto the slit of the IRCS on the Subaru Telescope. The IRCS includes two 1024^2 ALADDIN III arrays side by side with a wavelength coverage of 0.9-5.6 µm. With one target in each pick off arm, then both

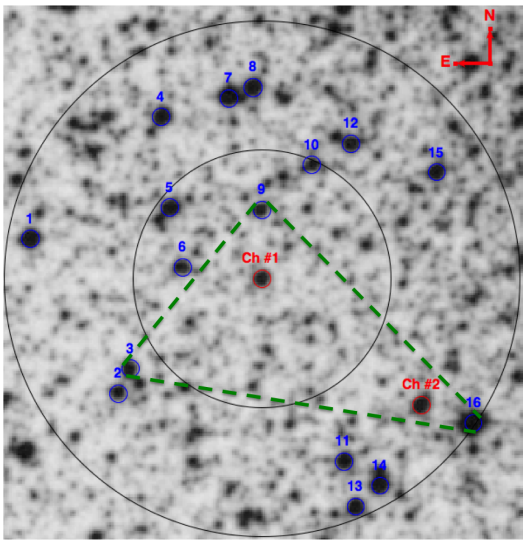

Figure 3.2: An image of the M22 field used in this work showing the arrangement of suitable guide stars (blue), the adopted asterism (green dashed) and the two science targets (red). The two black circles correspond to 60 and 120 arcseconds. This image was taken from the DSS survey archive (http://archive.eso.org/dss/dss).

stars are directed to opposite sides of the IRCS slit, such that two spectra are gathered simultaneously. All observations were obtained using the echelle mode of the IRCS with the 0.14 arcsec slit, yielding R $\sim$ 20000 spectra. The H-band wavelength region was chosen (H+ filter[3]), with intermittent coverage from 15000 - 17000 Å. This region was selected to take advantage of the linelist and techniques for analysing this region developed by the SDSS-III APOGEE project (Smith et al. 2013; García Pérez et al. 2013; Shetrone et al. 2015).

3.2.2 Performance and science observations

Three engineering runs took place between May 2014 and June 2015 at the Subaru Telescope, during which several AO tests were carried out, and the observations of our metal-poor star candidates. The details of the observations are summarized in Table 3.1. Over the four nights where the science observations were taken, the mean seeing of no-AO, SCAO, GLAO, and MOAO was 0.47", 0.09", 0.26", and 0.26" respectively; this shows a general improvement of at least 0.20" in FWHM and demonstrates the AO performance of the instrument. As a result, 2-3 times more flux passed through the slit of our observations, depending on the night and observing mode (MOAO or

[3]www.naoj.org/Observing/Instruments/IRCS/echelle/orders.html

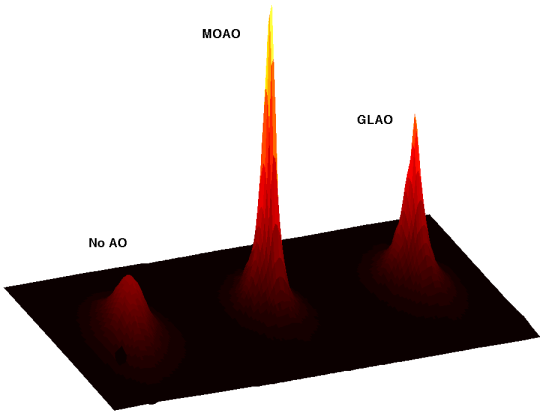

Figure 3.3: The PSF of MA8 with no AO (left), and with MOAO and GLAO corrections (middle, and right respectively). MOAO is shown to outperform GLAO, however there is substantial improvement from the two corrections. The ensquared energy of the PSFs are 7.29%, 24.4%, and 16.19% for no-AO, MOAO, and GLAO respectively, which was calculated over an aperture equvilant to the slit-width squared.

GLAO). Figure 3.3 demonstrates the quality of the Point Spread Function (PSF) for MA8 (prior to incidence on the slit) with no AO correction, and with MOAO and GLAO correction.

3.2.3 Target selection

Galactic Centre targets

Three RGB stars were selected for their low metallicity and proximity to the Galactic Centre, based on both SkyMapper photometry and low resolution spectroscopy (from the EMBLA survey, Howes et al. 2014, 2016). When targeting metal-poor stars in the Galactic Centre, pre-selection is necessary considering that the vast majority of the stars in this region are metal-rich (i.e. Hill et al. 2011). Furthermore, observations of these targets in the infrared with AO exploits the issues involved with a crowded and dust-ridden field. These pre-selected targets were observed with RAVEN during two engineering runs (in August 2014, and June 2015). Each pointing involved a simultaneous observation of an additional star of similar brightness to demonstrate the multiplexing capabilities of RAVEN; these additional stars were found to be relatively metal-rich and will be presented in a companion paper. The targets were observed in different AO modes (i.e. MOAO, GLAO, SCAO) depending on the turbulence profile of the evening (further described in Section 3.2.4).

M22 targets

Two metal-poor stars in the globular cluster M22 were selected for our program. This cluster is directly in front of the Galactic bulge but still subject to crowding, with reddening variations of 0.10 mag in *E(B-V)* across the face of the cluster (Marino et al., 2011), thus an ideal target for our MOAO demonstrations. This cluster also has evidence for a spread in iron, a characteristic found in only a few globular clusters within the Milky Way (i.e. M54, Omega Cen, etc.). It has been argued that M22 is host to multiple stellar populations, with one of the key indicating factors being a significant spread in iron, calcium, A(C+N+O), and s-process elements between stars (e.g. Marino et al. 2009, 2011; Alves-Brito et al. 2012). However there is also evidence claiming the contrary (Mucciarelli et al., 2015), where it is argued the Fe spread can be explained by the large systematics involved with deriving surface gravities spectroscopically. We have selected two targets in M22 from Lane et al. (2011), who determined Fe abundances for stars in M22 from low resolution spectra (part of the RAVE survey). Our targets include a relatively metal-poor and a metal-rich RGB star from this sample; the spread in Fe between the two stars is $\Delta \sim 0.3$ dex. In addition, we required the stars exist within a 3.5' vicinity of each other. Our goal is to determine detailed abundances of the two stars and search for element abundance differences. This demonstration can show the advantage of the multiplexing capabilities of RAVEN and the AO correction available in a crowded field, provide homogeneous observations mitigating potential systematic differences in derived abundances, and utilize the infrared to overcome extinction from scattering by dust. An image of the M22 field used in this work, along with a footprint of the asterism, is shown in Figure 3.2.

Standard star

One standard RGB star in M15 with known low metallicity ([Fe/H] $\sim$ -2.3, Mészáros et al. 2015) was observed to track the precision and accuracy of our methods. This star is well described in the literature (Carretta et al., 2009; Sobeck et al., 2011; Mészáros et al., 2015), providing a comparison sample for all of the the light-element abundances derived in this work. Furthermore, the comparison sample is derived from both optical and infrared spectroscopic methods, providing an excellent framework to determine the validity of our methods. The comparison is drawn in Section 3.4.1.

Table 3.1: The sample of stars observed

2MASS ID (alternate name[a])	R.A. (J2000)	Dec. (J2000)	b	l	Date Obs.	Exp. (s)	S/N[b]	$V_{hel.}$ (km/s)	Obs. mode	AO seeing (")	No AO seeing (")[c]
J21295492+1213225 (M15 K341)	21 29 54.928	+12 13 22.55	-27.27	65.05	Aug. 2014	2400	80	-109.59 ± 1.09	SCAO[d]	0.06	0.46
J18364826-2357135 (M22-MA4)	18 36 48.267	-23 57 13.56	-7.66	9.89	June 2015	5600	100	-142.34 ± 0.60	MOAO	0.36	0.53
J18364279-2358110 (M22-MA4.1)	18 36 42.792	-23 58 11.07	-7.64	9.86	June 2015	5600	130	-152.48 ± 0.59	MOAO	0.36	0.53
J18154190-2749464 (MA8)	18 15 41.872	-27 49 45.40	-5.20	4.24	Aug. 2014	3200	80	-215.59 ± 0.98	MOAO	0.19	0.46
J16572220-2840402 (MA11)	16 57 22.207	-28 40 40.36	8.85	-5.79	June 2015	6400	110	113.06 ± 0.45	GLAO	0.24	0.47
J18260509-2536479 (MA14)	18 26 05.095	-25 36 47.93	-6.23	7.29	June 2015	3600	125	-136.66 ± 0.58	GLAO	0.24	0.41

[a]For the rest of this paper we adopt this alternate name when referencing these target stars.

[b]Measured at $\sim$ 12-16 different featureless regions across the entire H-band spectrum and reported as a straight average.

[c]The median seeing for the entire night.

[d]This mode was used solely to demonstrate the SCAO capabilities of RAVEN and was otherwise unnecessary. A detailed description of the observing modes is in the text.

3.2.4 Observing strategies with MOAO

Given that RAVEN observations are made with both a new instrument *and* a new technology, we had to develop unique observing strategies prior to the engineering runs to manage the complexity of MOAO. In some circumstances, it was necessary to adjust observation strategies on the fly, while in others we found adjustments had to be made aftewards, for future observing runs. Since this paper is also intended to provide insight for future MOAO developments, we discuss these observing strategies here.

Pick-off arm limitations and arm swapping

Although the telescope tracks the sidereal rotation, the beam delivered to the Nasmyth focus has a rotating field of view, and was not corrected by Subaru's derotator for several reasons (i.e. degraded image quality). Therefore the field rotation was tracked by the pick-off arms of RAVEN. As a pick-off arm tracks an object across the field of regard, the optical path length of its respective channel is altered; to conserve this path length, a trombone in the channel translates along the optical axis to compensate for optical path differences created by the varying pick-off arm positions. During the M22 observation, one of the pick-off arms moved beyond the allowable travel of the trombone as it tracked a target throughout the observation. For this reason, we were forced to switch the two targets (and thus pick-off arms) mid observation. Fortunately, this was trivial given that there are two pick off arms, however when an instrument has many pick off arms (such as the TMT IRMOS design), this could be more complicated and something to consider for more complex MOAO systems.

ABBA nodding

To alleviate sky emission lines, dark current and bias effects, spectral data were gathered at two positional configurations projected onto the IRCS slit (referred to as A and B positions), and then subsequent A minus B image pairs are computed. Although this technique is fairly standard for traditional spectroscopic observations, extra care was needed when determining the A and B positions because of the MOAO techniques. For example, typical ABBA nodding involves moving the telescope itself to provide the A and B offset positions. With RAVEN, moving the telescope may disrupt the loop by disturbing a WFS, and so the nodding was achieved by moving the

pick-off arms instead. When only one star is fed to the spectrograph slit, a subsequent (A - B) image will produce alternating 'bright' and 'dark' lines corresponding to the positive and negative residual dispersion signals, and the separation between these lines is determined by the size of the nod. However, with RAVEN there are two targets fed to the slit (see the bottom of Figure 3.1), resulting in a much more crowded (A - B) residual dispersion signal image as can be seen by Figure 3.4 (bottom image). The total slit length is 5.17", and the typical FWHM of the AO-corrected PSFs are 0.2-0.35" (see Table 3.1); considering the ABBA nodding should be sufficiently large such that signals do not overlap (i.e. ∼1-2") and that *two* PSFs occupy the slit (taking ∼2" in total when considering the signal beyond the FWHM), very little slit space is leftover.

During our first engineering run (May 2015), even after pre-determining suitable A and B nodding configurations, there was slight overlap between signals where the spectra are more closely packed; these spectra were subsequently trimmed where there was signal overlap. From the experience of our first run we were able to improve on the (A - B) configurations for our future engineering runs. (A - B) positioning needs careful consideration in more complex MOAO systems, unless such systems send each channel to an independent IFU.

Choice of GLAO

Maunakea is known to have most of its turbulence confined to the ground layer (i.e. Chun et al. 2009). Averaging the WFS measurements from all 3 guide stars during MOAO allowed us to estimate the ground layer turbulence, and we found the performance of GLAO was nearly as good as this averaged MOAO mode when most of the turbulence was observed in the ground layer (through SLODAR measurements). Thus during the nights where we observed MA11 and MA14, there was a significant level of ground layer turbulence and we chose to observe these targets in GLAO mode only.

Acquisition

During our first two engineering runs, we had problems setting the tracking offsets of the ABBA nodding sequence, which resulted in a significant amount of overhead time (∼20-30 min.). Since RAVEN's primary purpose is to demonstrate MOAO our science observations were not optimized and the limited testing of the AO system

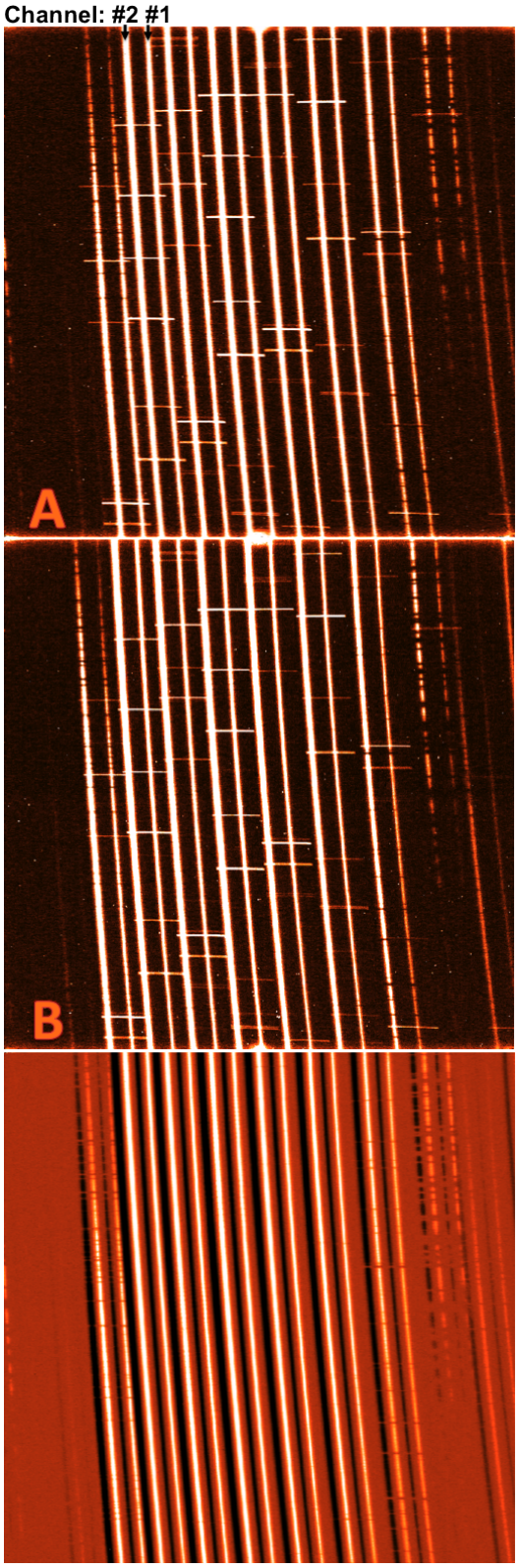

Figure 3.4: ABBA nodding for M22 MOAO spectra: MOAO allows multiple targets in the cluster to be projected onto the same slit and cross-dispersed side-by-side (labelled as channel #1 and #2 on the top-most image above) over several orders. Bottom: Subtracting the top two images from each other yields spectra free of sky lines, dark current and bias; A and B configurations with MOAO were carefully pre-determined to ensure their subtraction did not contain overlapping signals.

(once installed on the telescope) was dedicated to engineering items. As a result, the overheads were progressively reduced as we became more familiar with the science observation requirements. By the third engineering run the target acquisition times were reduced to ∼10 minutes (similar to standard AO acquisition times on workhorse instruments such as ALTAIR on Gemini North). This problem can also be translated to future ELT MOAO systems, where careful foresight will undoubtedly be required to accommodate the increased complexity of more pick off arms when trying to track many simultaneous targets. A field de-rotator may help improve this issue.

Guide star strategies

Scientific observations with MOAO are tightly restricted to the availability of guide stars in the field. The guide star asterisms required careful planning a priori, including back-up asterisms in case any NGSs are unrecognized binary systems. A back-up asterism was used during our observations of the bulge target MA11, where the LGS proved to be too faint on one particular night (this could have been due to the beam output power, the particular sodium profile that evening, or a combination of factors). The back-up asterism included fainter NGSs (R>14.5, which is technically within the limits of RAVEN's capabilities but reduces the AO correction and performance). We further note that during the first two engineering runs, we had difficulty guiding at R∼14.5, however we had no such problem during the third engineering run. We attribute this to two factors: i) the Moon was not in the sky, as opposed to the first two runs, reducing the background signal on all of the WFSs, and ii) a newly developed centroid correlation technique for the WFSs (see Andersen et al. 2014). The latter point effectively reduces the photon noise by correlating the well-sampled PSF with a reference image. These points summarize the importance of quality (i.e. bright) asterisms, and the necessity of having a back-up asterism (or multiple back-ups), even though this requirement greatly limits the total observable targets on the sky. This can be alleviated if an asterism of LGSs are used. Future ELT MOAO systems will employ multiple LGSs, and thus allow for much greater sky coverage; this is made possible because of the availability of NGSs for Tip/Tilt/Focus correction due to the wide field.

Telluric standard

Telluric standard stars are used to divide out the spectral imprint of the atmosphere. These observations did not require AO, since the targets are bright and isolated. Nevertheless, *both* MOAO pick off arms were used; one arm for the telluric standard star and the other on a region of sky only. This observing strategy alleviated the need for ABBA nodding.

3.2.5 Data reduction

ABBA nodding (as described in Section 3.2.4) was used to obtain the spectra of our targets. Equal exposures of the targets were taken at alternating A and B slit positions, producing a set of N A/B pairs, where N was the number of images required to obtain a final spectrum with signal to noise of ~ 100. The A and B positions were selected such that subtraction of one from the other would remove the thermal and sky emission lines, bias, and dark current, but not contain overlapping target signals. Exposures were taken in 200 second intervals to avoid saturation of the detector. Each image subtraction creates an 'A - B' pair (B *subtracted* from A) from which the pairs were then median combined using IRAF[4]. We chose median combining in order to reduce cosmic ray incidents on the images. The median combined image was fixed for bad pixels using a bad pixel mask (located on Subaru's echelle website as *cam_badpix.coo*), an example of such an image is shown at the bottom of Figure 3.4. Flat fields were created each night with a uniform lamp set to 'on' and 'off'; the flat 'off' images were subtracted from the 'on' images and then median combined. This flat image was normalized using the IRAF task *apnormalize*. Each science image was divided by the normalized flat and the A spectra were extracted separate from the B spectra. The remaining reduction steps were applied to the A and B spectra separately.

The wavelength solution was determined from the OH lines and using IRAF's *ecid*. To find accurate OH lines covering the full spectral range of each aperture, an observation of the sky was used (one of our observations had a misplaced slit alignment where *no* stars fell on the slit, thus it contained only sky lines such as OH). An OH atlas (Rousselot et al., 2000) was used, and the sky spectrum was fit with a

[4]IRAF (Image Reduction and Analysis Facility) is distributed by the National Optical Astronomy Observatory, which is operated by the Association of Universities for Research in Astronomy, Inc., under cooperative agreement with the National Science Foundation.

Table 3.2: Telluric standards

Star	RA	Dec	Star(s) Corrected
Sag 4	17 59 47.55	-23 48 58.09	MA 11, MA 8, MA 11
HR 7355	19 24 30.18	-27 51 57.40	M22-MA 4, M22-MA 4.1
HD 192425	20 14 16.61	+15 11 51.39	M15K341

high-order Chebyshev polynomial (x=5, y=3). The OH atlas reports spectral lines with vacuum wavelengths, which we shifted to air wavelengths for the remainder of the analysis. In certain cases the OH emission lines were unresolved doublets, and for these we adopted the brighter of the two lines.

Telluric subtraction was done with the spectrum of a hot star (late B-type or early A-type) with broad spectral lines (*vsini* >100 km/s) observed at roughly the same airmass as our targets (within 0.1 air masses). The specific stars used are listed in Table 3.2.

Radial velocities were determined from a cross-correlating with the H-band, zero-shifted spectrum of Arcturus (Hinkle & Wallace, 2005). The final A and B spectra were combined to increase the total signal-to-noise ratio. Figure 3.5 shows all of the metal-poor spectra plotted in a region with multiple spectral features used in this analysis.

3.3 Model atmospheres analysis

Spherically-symmetric, LTE model atmospheres generated by OSMARCS (Gustafsson et al. 1975, 2008, also see Mészáros et al. 2012) are adopted. These models are used with the LTE radiative transfer code MOOG (Sneden, 1973), along with the DR10 APOGEE line list (Shetrone et al., 2015). This abundance analysis follows that in our previous work (Lamb et al., 2015).

3.3.1 Stellar parameters

The stellar parameters (T_{eff}, log g) of the standard star in M15 were determined through the infrared flux method (IRFM) using calibrations by Ramírez & Meléndez (2005) along with standard stellar structure equations. This method requires optical and infrared photometry of the star, as well as the distance modulus, reddening, and metallicity of the cluster. Microturbulence was determined following the methodology of Gratton et al. (1996) for K-type stars. A consistency check shows that the derived

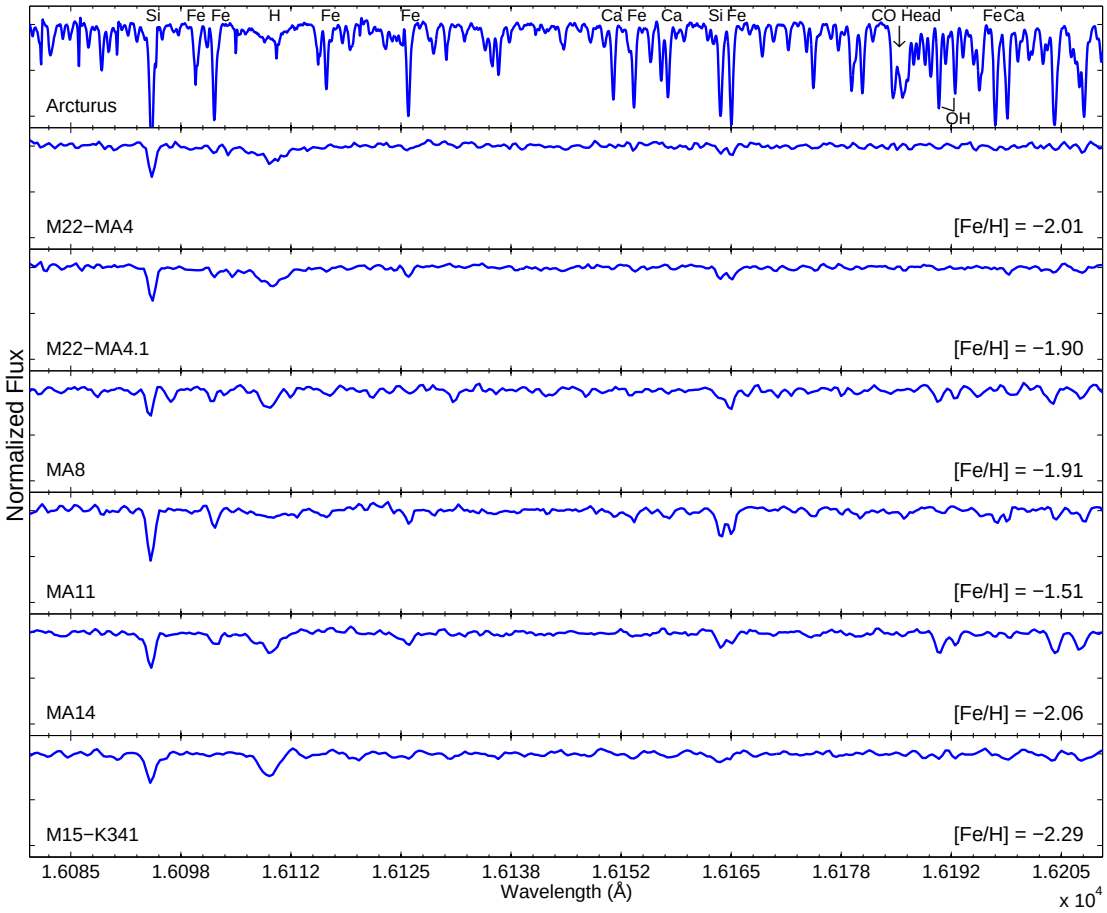

Figure 3.5: Sample spectral regions Si and Fe lines that were used in the abundance analysis. The derivation of the Fe abundances shown here are discussed in Section 3.4. Also shown is the higher-resolution spectrum of Arcturus for comparison purposes only, taken from Hinkle & Wallace (2005).

M15 stellar parameters agree well with those of the literature (see Table 3.4). Stellar parameters for the two M22 targets were also computed with the IRFM. A discrepancy in log(g) of $\sim$ 1 dex was found for M22-MA4 compared to Lane et al. (2011) (RAVE pipeline), however our gravity value is in good agreement with that from the EMBLA survey (Howes et al., 2014, 2016). For the three Galactic bulge targets, we adopt stellar parameters from the EMBLA survey, which infers stellar parameters from the tool known as *sick* (The Spectroscopic Inference Crank; Casey 2016). This tool minimizes over all parameters using a Markov chain Monte Carlo approach, sampling the posterior probability distributions to yield best fit stellar parameters along with their uncertainties. We note that for M22-MA4, the parameters from the EMBLA

survey and our IRFM results were in good agreement (although this would not take into account significant reddening effects for the bulge stars). Table 3.4 summarizes the final stellar parameters for all stars used in this paper.

3.3.2 Stellar parameter uncertainties

Stellar parameter uncertainties for our M15 and M22 targets were determined by altering the input variables associated with the IRFM (reddening, distance modulus to cluster, stellar mass, photometry and metallicity). Results for one star, M22-MA4.1 are shown in Table 6, and adopted for the rest of the M15 and M22 targets. The reddening error was taken as the total reddening variation (0.10 mag) across the face of M22 from Marino et al. (2011), an error in the distance modulus of 0.2 mag is taken from Monaco et al. (2004), the stellar mass uncertainty was taken as 3%, and the metallicity uncertainty as 0.10 dex, following Lamb et al. (2015). Photometric errors are typically 0.2 mag (following errors reported in the 2MASS survey), however these had negligible impact on the stellar parameter determinations. The mean uncertainties, ΔT_{eff} and $\Delta\log(g)$, were determined to be $\pm$ 123 K and $\pm$ 0.15 respectively; we conservatively adopt $\Delta T_{eff} = \pm$ 150 K and $\Delta\log(g) = \pm$ 0.20 dex to include systematic uncertainties in the calibrations themselves. We adopt an uncertainty in microturbulence of $\Delta\xi = 0.5$ km/s. For the Galactic bulge targets, we adopt the uncertainties from the EMBLA survey (Howes et al., 2014, 2016). The survey inferred stellar parameter uncertainties calculated with the tool *sick*, as discussed in Section 3.3.1. All stellar parameter uncertainties are presented in Table 3.4.

3.4 Abundance analysis

Elemental abundances are determined using the LTE 1D radiative transfer code MOOG[5]. The first step in the infrared spectral analysis of a red giant is to determine its Fe and CNO abundances, and potentially refine the model atmosphere adopted.

Iron has been determined from the spectrum syntheses of 23-50 relatively isolated Fe I lines (see Appendix A). Measurement errors were estimated from each synthetic fit by visual inspection. Spectral broadening parameters were determined from the instrumental resolution, where we adopted Gaussian broadening with FWHM = 0.85

[5]MOOG was originally written by Chris Sneden (1973), and has been updated and maintained (see Sneden et al. 2012), with the current versions available at http://www.as.utexas.edu/ chris/moog.html.

Table 3.3: Photometry and stellar parameters

	Photometry [a]								Cluster parameters[b]		Metallicity estimate [c]
Star	B	V	I	Ref.	(BVI)[d]	J	H	K	$(m-M)_V$	$E(B-V)$	[Fe/H] (dex)
M15 K341	13.72	12.54	11.22		A	10.455	9.796	9.695	15.39	0.10	-2.53
M22-MA4	14.83	13.60	12.09		B	11.107	10.514	10.363	13.60	0.34	-2.46
M22-MA4.1	14.38	13.01	11.46		B	10.467	9.803	9.644	13.60	0.34	-2.26
MA8	14.42	13.12	12.16		C,D	10.576	9.910	9.711	-	-	-2.28
MA11	14.13	13.12	11.98		C,D	11.246	10.75	10.658	-	-	-2.41
MA14	14.99	13.35	10.84		C,D	10.155	9.387	9.181	-	-	-2.35

[a]B, V, I photometry taken from the sources described in the Ref. column. J, H, and K photometry taken from 2MASS survey.

[b]Taken from Harris (2010).

[c]All metallicities estimates are from the EMBLA survey, except for M15 K341 (metallicity taken from Carretta et al. (2009)) and MA4.1 (Lane et al. 2011 provide [m/H], which we scale by the MA4 difference: $[Fe/H]_{EMBLA}$ - $[m/H]_{Lane2011}$).

[d]A - Kirby et al. (2008), B - Libralato et al. (2014), C - Girard et al. (2011), D - Monet et al. (2003).

Table 3.4: Stellar Parameters

	EMBLA[a]		Other sources[b]			This study[c]	
Star	T_{eff} (K)	log(g)	T_{eff} (K)	log(g)		T_{eff} (K)	log(g)
M15 K341	-	-	4324 ± 50	0.69 ± 0.20	A	4282± 150	0.52 ± 0.20
M22 MA4	4756 ± 124	1.68± 0.34	4514 ± 276.5	0.26 ± 0.60	B	4685± 150	1.47 ± 0.20
M22 MA4.1	-	-	4646 ± 276.5	0.99 ± 0.60	B	4577± 150	1.18 ± 0.20
MA8	4495 ± 127	0.84 ± 0.35	-	-	-	-	-
MA11	4514 ± 122	0.31 ± 0.30	-	-	-	-	-
MA14	4267 ± 125	0.74 ± 0.32	-	-	-	-	-

[a]Stellar parameters obtained from the EMBLA Survey (Howes et al., 2014, 2016)

[b]A - Carretta et al. (2009), B - Lane et al. (2011)

[c]Calculated following Ramírez & Meléndez (2005); photometry taken from Table 3.3 and errors are discussed in Sec 3.3.2

Å, and made slight adjustments to the local continuum (typically $< 1\%$) for the best fits. The mean Fe abundance is determined, and its measurement error is the weighted mean of the individual measurements. This measurement error technique is applied for every element and throughout this paper.

The C and O abundances were determined by following the procedures in Lamb et al. (2015) and Smith et al. (2013). C was determined from CO features (which are weakly sensitive to O), mainly from features in the band heads starting at 15578, 15775, 15978, 16185, 16398, 16613, and 16835 Å. In most cases C features at these metallicities are difficult to discern from the continuum, and while upper errors are not difficult to determine the lower errors in some cases are not possible. Therefore we adopt upper limits for C; however to determine O and N, a C value must still be adopted (since OH and CN features depend on C) and so we set the C abundance to its upper limit value.

O was determined (using the same method as Fe) from a large sample of OH lines; typically 30-40 features which spanned the entire spectrum and had no CN contamination. With the new O abundance, C was re-determined from the CO features, although our stars are sufficiently metal-poor that the CO features are weak. With this new C abundance (upper limit), then O was re-calculated from the OH lines. This procedure usually required only 1 iteration before the C and O abundances converged. Nitrogen was determined from the CN features between 15100-16100 Å, although the metal-poor stars in this analysis have relatively weak CN features.

To test the impact of adopting the upper limit value of C on the derived O and N abundances, we perform a simple analysis. Using MA14 (chosen arbitrarily), we decrease the upper limit C abundance by it's *upper error* (0.25 dex); as previously stated the upper error can easily be determined while the lower error is extremely difficult. We re-compute the O and N abundances using this shifted C value and we find O is unchanged while N is *increased* by 0.22 dex (approximately the value of how much C was decreased). We therefore caution the values of our N abundances may be higher than what is reported here, and for this reason our final N abundances are derived as lower limits. We note however, any [(C+N)/Fe] or [(C+N+O)/Fe] calculations should remain relatively unchanged, regardless of these upper and lower limit variations.

New model atmospheres were interpolated from the OSMARCS atmosphere grid given the new CNO and Fe abudances for each star and the analysis repeated. With the Fe, C, N, and O fixed, the abundances of the remaining elements were determined

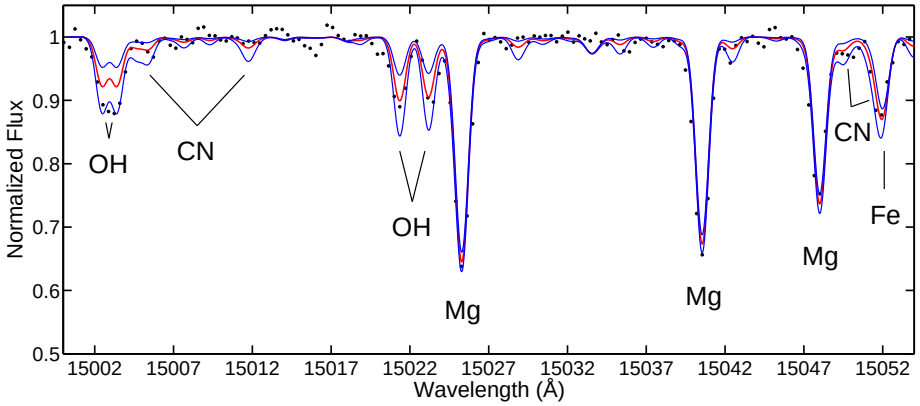

Figure 3.6: Sample spectral region for MA14; observed spectra are shown as black data points. Also shown is the synthetic spectra computed with the final adopted abundances for this star (solid red line). The syntheses from shifting each element by its adopted upper and lower error is also plotted for reference (shown in blue); the description of how these errors are computed is in Section 3.4. For C, the upper error is adopted as the lower error as well (also see Section 3.4) for visual purposes.

from individual line syntheses (summarized in Appendix A, and discussed in Section 3.5). A spectral region of MA14 is shown in Figure 3.6 along with a best fit spectrum synthesis, and $\pm 1\sigma$ total errors (in the case of C we use its upper error for both upper/lower errors). The abundance errors due to the stellar parameter uncertainties are reported in Table 3.7.

3.4.1 Standard star comparison

A red giant in the metal-poor globular cluster M15 was observed and analyzed as a standard star. This star has been analyzed by the APOGEE survey Mészáros et al. (2015), therefore a similar analysis of the H-band infrared spectral region, but from fitting of template spectra through the ASPCAP pipeline. As seen in Table 5, our stellar temperature and gravity are slightly lower than from the APOGEE analysis, however the differences are within 1σ. The metallicity and element abundances are in good agreement, with only Si showing a difference of up to 2σ.

This star has also been analyzed from optical spectra by Sobeck et al. (2011) and Carretta et al. (2009). The stellar parameters from these optical analyses are in better agreement with our results, although the Fe and C abundances determined by Sobeck et al. (2011) are significantly lower than ours, and this may imply our C

Table 3.5: Standard star M15-K341: parameters and abundances

Stellar Properties	This study	Sobeck[a] et al. 2009	Carretta et al. 2009	Mészáros et al. 2015
T_{eff} (K)	4282 ± 150	4375 ± 100	4324 ± 50	4494 ± 100
log(g)	0.52 ± 0.20	0.30 ± 0.20	0.69 ± 0.20	0.82 ± 0.30
Fe	5.21 ± 0.10	4.99 ± 0.05	5.32 ± 0.03	5.20 ± 0.12
C	< 6.11	5.51 ± N/A	...	5.72 ± 0.22
N	> 6.27	...	...	6.13 ± 0.32
O	6.96 ± 0.13	7.02 ± 0.05	7.08 ± 0.11	7.07 ± 0.13
Mg	5.53 ± 0.19	5.59 ± 0.10	5.69 ± 0.08	5.63 ± 0.09
Al	4.01 ± 0.21	4.05 ± 0.13	...	4.02 ± 0.17
Si	5.45 ± 0.09	5.30 ± 0.10	5.78 ± 0.08	5.66 ± 0.13
Ti	< 2.98	2.71 ± 0.05	...	2.68 ± 0.28

[a]The abundances were retrieved using their online data table and adopting a $\sigma/\sqrt{N}$ error, except in the case where the error was below 0.05 dex, in which case 0.05 dex was adopted.

abundance should be lower than it's upper limit. Their C result is from a synthetic fit of the 4300 Å, G-band, with little discussion of the errors. Throughout their analysis, Sobeck et al. (2011) report line abundances, from which we infer their mean abundances and error by adopting $\sigma/\sqrt{N}$ (unless the error was below 0.05 dex, in which case 0.05 dex was adopted). The Fe result from Carretta et al. (2009) is in good agreement with ours, however their [α/Fe] ratios are larger by 1σ (O) to 4σ(Si). To ensure a uniform comparison, we convert the results from each of these works to absolute log abundances.

3.4.2 Abundance uncertainties

The sensitivities of the elemental abundances (including elements other than Fe, C, N, and O) are shown in Table 3.6. While M15-K341 is the standard star for this analysis, we computed these abundance sensitivities for M22-MA4.1 because this star has a temperature and metallicity that is more representative of our sample. The surface gravity of M22-MA4.1 is slightly higher than the mean of our sample, however this has a smaller impact on the precision in the elemental abundances.

The abundances in M22-MA4.1 were derived using our best model atmosphere parameters, and again with models that vary by ± 1σ in temperature, gravity, and metallicity. The mean errors in each of the element abundances have been determined per parameter, and adopted for the other stars in this paper, as reported in Table

3.6. The errors in metallicity show negligible effects on the other element abundances (<0.2 dex), and are thus not reported here. The total errors for each species are calculated per star by combining these in quadrature with the measurement errors in Table 3.6.

Table 3.6: Abundance Uncertainties for M22-MA4.1

Species	$\Delta T_{\rm eff}$ (+150K)	Δ log g (+0.2 dex)	Δv_t (+0.5 km/s)	Total Error[a]
[Fe/H]	-0.08	0.01	0.00	0.08
[C/Fe]	0.21	0.00	-0.02	0.21
[N/Fe]	0.04	-0.05	-0.01	0.06
[O/Fe]	0.19	-0.02	0.00	0.19
[Mg/Fe]	-0.03	0.02	-0.05	0.06
[Al/Fe]	0.01	-0.02	0.01	0.02
[Si/Fe]	0.01	0.00	-0.03	0.03
[Ca/Fe]	-0.04	-0.07	0.00	0.08
[Ti/Fe]	0.12	0.01	0.00	0.12
[Mn/Fe][b]	0.03	-0.06	0.00	0.07
[Ni/Fe]	-0.07	0.02	0.00	0.07

[a]Both errors added in quadrature. Model atmosphere input metallicity sensitivities were found to be negligible and were not included here.

[b]Since Mn was derived as an upper limit for this star, the Mn sensitivity was computed for MA11.

3.5 Abundance results

Elemental abundances have been determined from H-band infrared spectra for three stars in the Galactic bulge and two stars in M22, as a scientific demonstration of the new RAVEN instrument and MOAO methodologies. Through the analysis of a standard star in M15, we have demonstrated that the quality of our spectra and analysis methods do reproduce previous published results. Here we discuss the abundance results for our main science targets, also summarized in Table 3.7. The results for M22 are compared with those from the optical analyses by Marino et al. (2011); Kacharov et al. (2015); Roederer et al. (2011); Mucciarelli et al. (2015), and infrared analysis by Alves-Brito et al. (2012); the two studies by Marino et al. (2011); Alves-Brito et al. (2012) find a large dispersion in Fe, with two rough groups spanning roughly -2 <

Table 3.7: Target abundances

Species	M22-MA4	N[a]	M22-MA4.1	N	MA8	N	MA11	N	MA14	N	M15-K341	N
[Fe/H]	-2.01 ± 0.10	23	-1.90 ± 0.10	35	-1.93 ± 0.12	17	-1.51 ± 0.09	49	-2.06 ± 0.09	38	-2.29 ± 0.11	17
[C/Fe]	< 0.10	3	< 0.22	6	< 0.35	7	< -0.35	6	< -0.38	6	< -0.03	4
[N/Fe]	> 0.85	4	> 0.54	15	> 0.64	9	> 0.57	14	> 1.03	14	> 0.73	8
[O/Fe]	0.68 ± 0.22	11	0.49 ± 0.20	38	0.83 ± 0.20	36	0.27 ± 0.20	30	0.64 ± 0.20	40	0.56 ± 0.20	39
[Mg/Fe]	0.32 ± 0.15	4	0.15 ± 0.12	7	0.16 ± 0.16	3	0.42 ± 0.10	10	0.28 ± 0.11	6	0.22 ± 0.19	3
[Al/Fe]	-0.28 ± 0.23	2	-0.26 ± 0.16	3	-0.18 ± 0.18	2	0.23 ± 0.15	3	-0.35 ± 0.18	2	-0.15 ± 0.21	2
[Si/Fe]	0.21 ± 0.09	12	0.18 ± 0.08	12	0.13 ± 0.09	10	0.26 ± 0.07	13	0.30 ± 0.09	11	0.23 ± 0.09	11
[S/Fe]	0.64 ± 0.33	3	0.47 ± 0.35	2	0.60 ± 0.31	2	0.41 ± 0.32	2	-	-	-	-
[Ca/Fe]	0.28 ± 0.28	3	0.05 ± 0.33	3	0.29 ± 0.28	3	0.28 ± 0.17	4	0.27 ± 0.32	3	-	-
[Ti/Fe]	0.65 ± 0.33	2	0.30 ± 0.28	2	0.26 ± 0.30	2	< 0.22	-	< 0.27	-	-	-
[Mn/Fe]	< 0.24	-	< -0.05	-	-	-	0.01 ± 0.32	3	< -0.06	-	< -0.06	-
[Ni/Fe]	0.33 ± 0.21	5	-0.06 ± 0.19	3	0.36 ± 0.25	2	0.03 ± 0.16	6	-0.03 ± 0.25	5	0.02 ± 0.34	3
[α/Fe][b]	0.36 ± 0.12	-	0.16 ± 0.10	-	0.20 ± 0.12	-	0.38 ± 0.09	-	0.28 ± 0.11	-	0.22 ± 0.34[c]	-
[(C+N+O)/Fe][d]	0.58 ±0.61	-	0.42±0.58	-	0.73±0.40	-	0.19±0.42	-	0.55±0.46	-	0.46±0.52	-
A(C+N+O)	7.49±0.61	-	7.44±0.58	-	7.71±0.40	-	7.60±0.42	-	7.41±0.46	-	7.09±0.52	-

[a]Number of lines or features (i.e. band heads or molecular features) used to determine abundance.

[b]Taken as a weighted average between Mg, Ca, and Ti.

[c]In this case α was adopted as the weighted average between Mg and Ca only.

[d]Error derived by adding C, N, and O abundance errors in quadrature. C is adopted here as the upper limit and its error taken as its *upper* error (see Section 3.4). For simplicity we adopt this as the A(C+N+O) error as well.

[Fe/H] < -1.4 dex. Our Galactic bulge candidates are compared with bulge survey results by Koch et al. (2016); Howes et al. (2014, 2015); Johnson et al. (2014); García Pérez et al. (2013); Ruchti et al. (2010); Casey & Schlaufman (2015).

3.5.1 Iron

M22: The mean Fe abundances for our two M22 targets is [Fe/H] = -1.95 ± 0.05. This is ~ 0.2 dex lower than the cluster average determined from the optical analyses of larger numbers of stars by Marino et al. (2011) and Mucciarelli et al. (2015). M22 has been found to have a spread in Fe (Marino et al., 2011; Alves-Brito et al., 2012), though the cause of this spread is debated; Mucciarelli et al. (2015) reproduce the spread only when deriving abundances from spectroscopic gravities, and show that the use of photometric gravities erases the signature. Mucciarelli et al. (2015) also argue that photometric gravities are less sensitive to systematic effects, and suggest that the spread in Fe in this cluster is not astrophysical, but a systematic effect. In this paper, we adopt photometric gravities, which would be consistent with our finding of no spread in the Fe abundance.

Galactic Centre candidates: Based on the classifications by Beers & Christlieb (2005), our sample includes two metal-poor and one very metal-poor star. Before considering whether these targets are *bonafide* bulge members (see orbit calculations in Section 3.6), we note that they fall on the metal-poor tail of the bulge MDF (i.e., Ness et al. 2013). Furthermore, these stars have metallicities between those studied by Howes et al. (2015) and those by Chiappini et al. (2011), where each study suggests that the stars at these metallicities can provide links to the First Stars. Our bulge candidates also fall within the metallicity range of two other works (García Pérez et al., 2013; Koch et al., 2016), contributing to the total sample of metal-poor stars studied in/towards the bulge. We note the discrepancy from the original EMBLA Fe abundances (determined from low resolution optical spectroscopy), which may be due to the different resolution and wavelengths between the two works; however we are confident in our abundances based on the results of our standard star comparison.

3.5.2 Carbon and nitrogen

The C and N abundances were determined from the best synthetic fits to the features as described in Section 3.4 and are derived as upper and lower limits, respectively.

M22: Both stars in M22 show elevated N abundances coupled with slightly enhanced C relative to scaled-solar abundances. It is evident from Figure 3.7 the derived C abundances are slightly elevated with respect to Marino et al. (2011) while the N abundances between the two works agree. These abundances are consistent with mixing of CN-cycled gas if the initial abundances were slightly elevated and not simply scaled-solar (see Table 3.7); e.g., if the initial [C/Fe] $\sim$ [N/Fe] $\sim$ +0.3 in M22 in general, then a small N enrichment is observed in our two stars with a small C depletion. This is discussed further in Section 3.7.1.

Galactic Centre candidates: The C abundances in our metal-poor bulge candidates show [C/Fe] $<$ +0.35, relative to scaled-solar abundances. C has been determined in other metal-poor bulge candidates by (Howes et al., 2015; Koch et al., 2016; Casey & Schlaufman, 2015). Similar to Howes et al. (2015) and Casey & Schlaufman (2015), none of our bulge candidates are very carbon-rich, which is a common feature seen in metal-poor halo stars Placco et al. (2014). Only one bulge candidate star has been found which satisfies the CEMP criteria, as well as one that is above the halo average (Koch et al. 2016; see Figure 3.7). The average C abundance of the metal-poor stars from Howes et al. (2015) and Casey & Schlaufman (2015) appears to be similar to scaled-solar ([C/Fe] $\sim$ 0), slightly lower than the mean C abundance in the halo stars at similar metallicities (see Figure 3.7).

We report the first N abundances in metal-poor bulge candidates. They appear to be enhanced, consistent with mixing of CN-cycled gas on the RGB. Since one of these stars has a slightly elevated C abundance, then it is unclear if they all share the same initial C and N abundances before mixing. This is discussed further in Section 3.7.

3.5.3 α-elements

The individual elements that form through α capture processes during hydrostatic He-core burning or subsequent α-rich freeze out in He-rich burning layers include O, Mg, Si, S, Ca, and Ti. The results from our infrared H-band analysis are shown in Table 7, where it can be seen that measurement errors for Mg and Si are much smaller than the other elements primarily due to the larger number of lines available. We calculate a mean $<$[α/Fe]$>$ as a weighted average of Mg, Si, Ca, and Ti. Our [O/Fe] measurements are also sufficiently precise, however we do not average it into our α

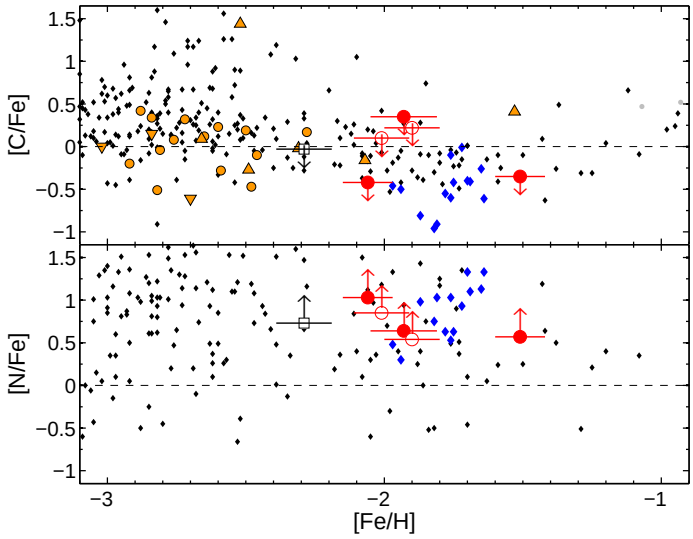

Figure 3.7: C and N abundances of our target stars as a function of Fe compared with the Galactic sample: thick disk taken stars from Reddy et al. (2006) are shown as grey points while halo stars are shown in black (taken from Roederer et al. 2014). Orange circles, triangles, and inverted triangles are metal-poor bulge stars from Howes et al. (2015), Koch et al. (2016) and Casey & Schlaufman (2015), respectively. Blue diamonds are the abundances of 35 M22 stars, taken from Marino et al. (2011) (several of their stars report multiple abundances from different observations of the same star - for these cases we adopt a straight average). The hollow and solid red points represent our M22 and Galactic Centre stars, respectively. Shown also is our standard star in M15, plotted as a hollow black square.

index.[6]

The average α abundances for our target stars are compared with the galactic sample in Figure 3.9. For the comparison sources, [α/Fe] was computed as an unweighted average of Mg, Si, Ca, and Ti except in the cases of García Pérez et al. (2013); Howes et al. (2014); Johnson et al. (2013) where each source contained only 3 out of 4 of these elements, and the alpha abundance was computed as the average of these 3. Our M22 target abundances are consistent with those of Marino et al. (2011), with a slightly lower average of $<[\alpha/\mathrm{Fe}]> = 0.22 \pm 0.10$ compared to their $<[\alpha/\mathrm{Fe}]> = 0.33 \pm 0.04$. For the three Galactic bulge stars, we report $<[\alpha/\mathrm{Fe}]> = 0.25 \pm 0.11$, which is in excellent agreement with the mean abundances $<[\alpha/\mathrm{Fe}]> = 0.27 \pm 0.13$ from Howes et al. (2014, 2015), also in agreement with García Pérez et al. (2013) who find

[6]We note that Mg can also be affected through other processes in globular clusters, however our two stars in M22 have identical Al, implying that deep mixing has not affected Mg and so we keep Mg in our computation of α.

$<[\alpha/\mathrm{Fe}]> = 0.26$ (no reported error). Inspection of Figure 3.9 reveals this is in slight contrast to the higher α abundances reported by Casey & Schlaufman (2015); Koch et al. (2016), and the metal-poor stars taken from Johnson et al. (2014).

Oxygen:

Most O abundances derived in the literature have been inferred from optical spectroscopy, usually from either the forbidden line (∼6300 Å) or from the triplet region between 7770-7777 Å. These lines are notoriously difficult to analyse at low [Fe/H] due to 3D effects, departures from LTE, small line strengths and/or blends (e.g. Asplund 2005; Amarsi et al. 2016). Relatively few O abundance determinations are thus available for our comparison sample (Fig. 6). Since the H-band is host to a plethora of OH lines, it is an excellent wavelength region to determine stellar O abundances. We have derived O abundances from a selection of 58 OH lines of varying line strengths.

From two stars in M22, we find [O/Fe] = 0.68 ± 0.22 and 0.49 ± 0.20, which is significantly higher than Marino et al. (2011) and Alves-Brito et al. (2012), where <[O/Fe]> = 0.34 ± 0.03 (from the single forbidden line at 6300 Å) and 0.40 (no reported error), respectively. Alves-Brito et al. (2012) also report a large spread in O ($\Delta\log(\mathrm{O/Fe})$=0.74); such a spread in globular clusters has been explained as proton capture reactions which impact O and Mg (Marino et al., 2011). A strong Na-O anticorrelation has been determined in this cluster Marino et al. (2011); our high O abundances relative to the sample of M22 stars (see Figure 3.8) suggest that our two M22 stars represent primordial stars within the cluster.

Oxygen abundances for bulge stars have been rarely determined in this metallicity range (as seen in Figure 3.8). For our three bulge candidates we find <[O/Fe]> = 0.58 ±0.20. This is in excellent agreement with both García Pérez et al. (2013) (<[O/Fe]> =0.54 ± 0.07 from 5 stars) and Johnson et al. (2014) (<[O/Fe]> = 0.61 ± 0.07, from 3 metal-poor stars with [Fe/H] < -1 dex). Similar to previous results, this averaged value is higher than metal-poor stars in the halo, but in good agreement with the thick disk stars (e.g. Roederer et al. 2014; Johnson et al. 2014; we caution however that the thick disk stars should generally agree with the halo stars, and the offset between the two in Figure 3.8 may merely be a systematic effect).

Magnesium:

Magnesium is measured from several prominent lines in the IR, the most notable of which are the 3 at 15025-15050Å, and the 3 at 15740-15770Å, and several weaker lines spread throughout the H-band. We find <[Mg/Fe]> = 0.24 ±0.14 for our two M22 targets. Figure 3.8 shows these abundances relative to Galactic globular clusters and results from the optical analysis of stars in M22 by Marino et al. (2011). Our results are slightly lower than the average from Marino et al. (2011), where <[Mg/Fe]> = 0.39 ± 0.02 dex. Our three Galactic Centre candidates have <[Mg/Fe]> = 0.29 ± 0.13 (see Figure 3.8). Like García Pérez et al. (2013) and Howes et al. (2015), these Mg abundances are lower than the optical results for stars of similar metallicity in the halo. This is also in contrast to results by Koch et al. (2016) and Johnson et al. (2014), who found higher [Mg/Fe] from optical analyses of stars in the bulge and thick disk. Howes et al. (2014) report a large spread of Mg Δ[Mg/Fe] = 0.69, while Casey & Schlaufman (2015) find little to no Mg variation in their sample. Our data would support a dispersion in the bulge star Mg abundances.

Silicon:

We derive Si abundances from numerous lines of varying strength (≥10 lines per star). The average <[Si/Fe]> = 0.20 ±0.09 for our two M22 stars which, similar to oxygen, is lower than Marino et al. (2011) (where <[Si/Fe]> = 0.44 ± 0.01 dex); this is readily seen by inspection of Figure 3.8. Our M22 Si abundances agree with other Galactic globular clusters at this metallicity (see Figure 3.8). We find <[Si/Fe]> = 0.23 ±0.09 for our three bulge candidates, in agreement with most other bulge studies (García Pérez et al. 2013, Johnson et al. 2013, and Howes et al. 2015); only Koch et al. 2016 and Casey & Schlaufman 2015 find higher Si results (see Figure 3.8).

Calcium:

Calcium is measured from the 4 features located between 16150-16200 Å. It is clear from Table 7 that our infrared Ca abundances have large uncertainties, due to a large line-to-line scatter. We were unable to measure the Ca lines in the M15 standard star, thus it is difficult to critically evaluate the 4 individual spectral lines used in this analysis. The resulting abundances are plotted in Figure 3.9 along with our comparison sample. The average Ca for our two stars in M22 is <[Ca/Fe]> = 0.17 ±0.30. This is in fair agreement with results from Marino et al. (2011) (<[Ca/Fe]> = 0.30 ± 0.01)

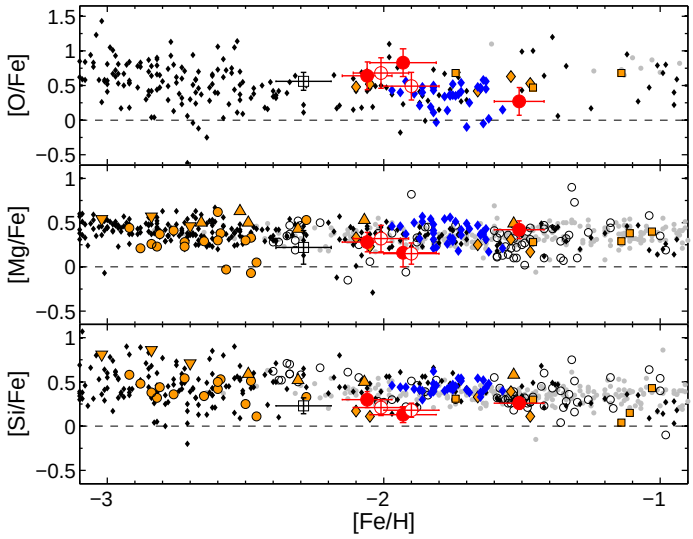

Figure 3.8: The light elements O, Mg, and Si plotted as a function of Fe compared with the Galactic sample. The grey points are thick disk stars from Reddy et al. (2006) and Ruchti et al. (2010) while the black points (solid) represent halo stars (taken from Roederer et al. 2014 and Reddy et al. 2006). Also shown are Galactic GCs as hollow black circles, assembled by Pritzl et al. (2005) and metal-poor bulge stars in orange (diamonds García Pérez et al. 2013, squares Johnson et al. 2014, triangles Koch et al. 2016, inverted triangles Casey & Schlaufman 2015 and circles Howes et al. 2014, 2015). Blue diamonds are the abundances of 35 M22 stars, taken from Marino et al. (2011) (several of their stars report multiple abundances from different observations of the same star - for these cases we adopt a straight average). The M22 and Galactic Centre targets from this work red open and filled circles, respectively while the standard star in M15 is represented by a hollow black square.

given our large uncertainties. The mean Ca abundance in our sample of bulge stars is $<$[Ca/Fe]$>$ = 0.28 $\pm$0.26, which is consistent with the 26 bulge stars in Howes et al. (2015) ($<$[Ca/Fe]$>$ = 0.23 $\pm$ 0.12). Johnson et al. (2014), Koch et al. (2016), and Casey & Schlaufman (2015) find slightly higher Ca for bulge stars ($<$[Ca/Fe]$>\sim$ 0.4), though all of these analyses are within 1σ errors. We note that Howes et al. (2015) find lower Ca in their bulge sample than halo stars at the same metallicities, though the source of this discrepancy is unclear.

Titanium:

Titanium is measured from two features in our IR spectra, 15335 Å(which is very close to a strong Fe feature) and a weak line at 15544 Å. Inspection of Figure 3.9 indicates that our Ti abundances for the two M22 stars are quite high, with $<$[Ti/Fe]$>$ = 0.48

±0.31, compared with Marino et al. (2011), however with a large uncertainty. These results are also consistent with the Galactic sample of globular clusters. Ti is measured in only one Galactic bulge candidate (MA8), and determined with upper limits for the other two. The abundances we report in Table 3.7 are consistent with those for other bulge stars, as well as the thick disk and halo stars which overlap at this metallicity (see Figure 3.9).

Sulphur:

We examine three S I features that span the range 15400-15480 Å. These three features yield significantly different results, and without detections of these lines in our M15 standard star then it is difficult to critically evaluate these results. We report the mean abundance for [S/Fe] here, however the unrecognized blends or poor atomic data could be affecting these infrared S I abundances. We calculate <[S/Fe]> = 0.56 ± 0.48 dex from two stars in M22; this is similar to Kacharov et al. (2015), who find <[S/Fe]> = 0.57 ±0.21 from an average of 6 stars in the same cluster (also with comparably large errors).

Sulphur is measured in 2 out of 3 of our Galactic bulge candidates, where <[S/Fe]> = 0.51 ±0.32. These are the first S I abundances reported for Galactic bulge candidates, but the uncertainties are too high to discuss the nucleosynthesis or S I compared with Galactic halo stars. Detailed analyses of S I measurements have been carried out by Nissen et al. (2007); Jönsson et al. (2011) and find <[S/Fe]> = 0.20 ± 0.07, and 0.40 ± 0.11 respectively, which is within the 1σ errors of our S I abundances.

3.5.4 Other elements

Three more elements are available in our H-band spectra: the odd-elements Al and Mn, and Ni. Odd-elements typically are affected by hyperfine splitting, which is not yet available for these IR lines. Elemental abundances for these three elements are shown in Figure 8.

Aluminum:

In the H-band, there are three prominent Al features, located between 16718 - 16765 Å, from which we derive our Al abundances. Shetrone et al. (2015); Smith et al. (2013) chose to not include the strongest feature at 16750 Å, because of potential HFS effects. However we found no significantly large abundance difference with the

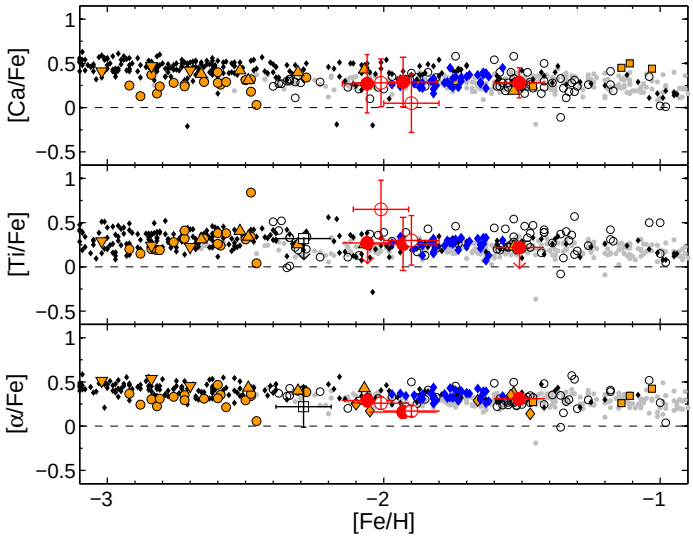

Figure 3.9: The light elements Ca, Ti, and α plotted as a function of Fe compared with the Galactic sample. Data points are labelled the same as in Figure 3.8. The Ti abundances from Roederer et al. (2014) (solid black points), Koch et al. (2016) (orange triangles), and Ruchti et al. (2010) (light gray circles) are taken as an average between Ti I and Ti II.

weaker Al features. In M22, we search for a Mg-Al anti-correlation in the discussion. We find <[Al/Fe]> = -0.27 ± 0.20, which may be anti-correlated with our slightly elevated [Mg/Fe] results. High Al was found in Marino et al. (2011) which we do not reproduce, and we attribute our low Al abundances as evidence of these stars being of the first generation in the cluster. Inspection of Figure 3.10 reveals that the galactic sample at these low metallicities is slightly lower than the abundances of both our M22 and Galactic bulge targets. We report <[Al/Fe]> = -0.10 ± 0.29 for our three Galactic Centre candidates, where most of the spread is attributed to the higher Al abundance in MA11 (however MA11 agrees with the Al trends of other stars at its metallicity). Only Johnson et al. (2013) have measured Al in a galactic bulge star at our target metallicities, for which we find excellent agreement (see Figure 3.10).

Manganese:

Three Mn I features are examined, at 15159, 15218, and 15262 Å, and primarily used to determine [Mn/Fe] upper limits. These upper limits for our two M22 targets, show [Mn/Fe] $\leq$ 0.2. This is consistent with Roederer et al. (2011), who derive <[Mn/Fe]> = -0.52 ± 0.05 dex from 6 RGB stars in M22 (we computed the error

from a weighted average of their reported abundances). For the Galactic bulge targets, the upper limits and one detection result in scaled-solar abundances, with [Mn/Fe] $\leq$ 0. Casey & Schlaufman (2015) find underabundant [Mn/Fe] for their bulge star sample; we do not reproduce this feature, similar to Howes et al. (2016).

Nickel:

There are several Ni features in the H-band. We determine Ni abundances from $\leq$6 lines spanning across the spectrum (from 15555 - 16996 Å). In M22, our two stars yield very different [Ni/Fe] results, but with large uncertainties; <[Ni/Fe]> = 0.14 $\pm$0.28. This is consistent with Marino et al. (2009) (<[Ni/Fe]> = -0.07 $\pm$0.04). In our three Galactic bulge candidates, two stars show scaled-solar nickel, with [Ni/Fe] $\sim$ 0, while the third appears Ni rich with [Ni/Fe] = 0.36 $\pm$0.25; this star clearly stands out from the Galactic comparison stars in Figure 8.

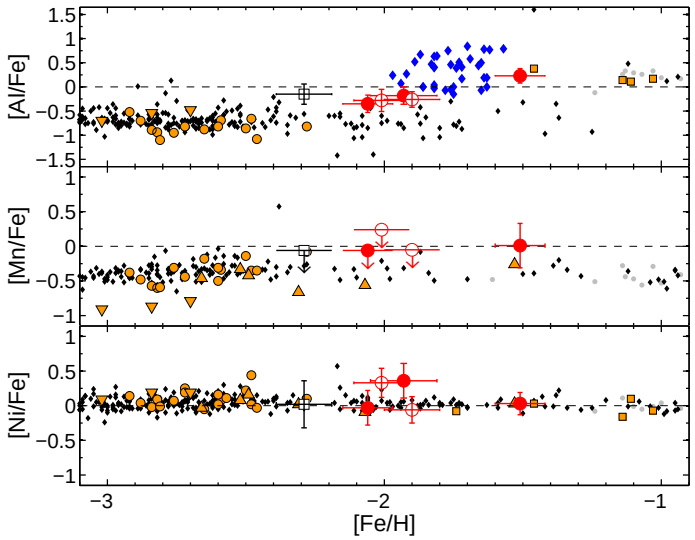

Figure 3.10: The light elements Al, Mn, and Ni plotted as a function of Fe compared with the Galactic sample. Data points are labelled the same as in Figure 3.8.

3.6 Stellar orbits

The Galactic bulge candidate stars may be transient in nature (i.e. foreground disk/halo, or halo stars with orbits that pass through the bulge); therefore they need to be identified as *bonafide* bulge members if they are to be used to study the

evolution of the bulge stellar population. To affirm their bulge membership, we determine their orbital parameters by calculating orbits from stellar distances, proper motions, positions on the sky, and radial velocities.

3.6.1 Distances

The distances to our target stars are determined from the absolute magnitudes of each star, based on their stellar parameters ($T_{\rm eff}$ and log g), bolometric magnitudes, and bolometric corrections (BC_V), following Buzzoni et al. (2010). The bolometric magnitudes were calculated assuming a stellar mass of 0.8 $M_{\odot}$. These distances are corrected for reddening using the maps of Schlegel et al. (1998); the computed heliocentric distances are listed in Table 3.8. Upper and lower errors on the calculated distances are determined by varying the uncertainties in both the stellar parameters and the reddening values; we adopt the absolute lowest and highest values as our errors. As a comparison, the distance to M22 is determined from the distance modulus of Monaco et al. (2004), $D_{M22} = 3251^{+313}_{-286}$ pc. This is consistent with our two stars, $D_{\rm MA4} = 3479^{+1314}_{-978}$ and $D_{\rm MA4.1} = 3432^{+1328}_{-987}$ pc. The final derived distances and errors for all target stars are summarized in Table 3.8.

3.6.2 Proper Motions and Stellar Kinematics

Assuming a Milky Way potential, the stellar kinematics of the bulge candidates can be calculated from their distances, radial velocities, proper motions, and positions on the sky. Using the distances and radial velocities derived in this work, along with the positions of the stars, we examine the proper motions from both UCAC4 (Zacharias et al., 2012) and SPM4 (Girard et al., 2011), and orbits are represented by their apocentre and pericentre distances. For this calculation, heliocentric parameters are transformed to Galactocentric distances and velocities assuming the LSR circular motion of 220 km/s, the Sun location of 8.5 kpc from the Galactic centre, and $(U_{\odot},V_{\odot},W_{\odot})$[7]=(10.1,4.0,6.7) km/s (Hogg et al., 2005) for peculiar motion of the Sun. Uncertainties in the LSR and solar motion measurements are negligible compared to the uncertainties in the distance and velocities of our stars. It should be noted that the error bars on the proper motions can be quite large, and can differ significantly from one catalogue to the next (see Table 3.8). These discrepancies translate

[7](U,V,W) is a right handed system, with U pointing towards Galacticcentre, V to the direction of Galactic rotation, and W to the North Galactic Pole.

to large orbit uncertainties, and highlight the need for more reliable proper motion measurements (i.e. GAIA), and we caution the reader about the orbits calculated with these proper motions. The apocentre and pericentre of each star are computed using both proper motion catalogues, using two different methods; each method is described below.

Method 1: APOSTLE Potential Models

For the potential of the Milky Way, we adopt *spherically averaged* potentials of Milky Way-size haloes from the APOSTLE[8] project (Fattahi et al., 2016; Sawala et al., 2016), a suite of high resolution hydrodynamical zoom-in simulations of twelve volumes resembling the Local Group. The simulations were performed using the EAGLE galaxy formation code (Schaye et al., 2015; Crain et al., 2015). The interested reader is referred to Fattahi et al. (2016) and Sawala et al. (2016) for the details of the runs and the selection of Local Group candidates. Simulations have been set up at three different resolutions. In this paper, we use six Milky Way-size haloes from the three highest resolution simulations (AP-1, AP-4, and AP-11 in Fattahi et al. (2016) of APOSTLE). No other haloes were simulated at this resolution and so only these six were used in this study.

Given the potentials and Galactocentric distances and velocities of bulge candidate stars, we compute the apocentre and pericentre of their orbits. Uncertainties in apocentre and pericentre were obtained using 1000 Monte Carlo experiments, assuming Gaussian errors in observed heliocentric distances and velocities. For distance measurements with asymmetric errors, we assume Gaussians of different widths on either side of the mean value. Table 3.9 summarizes the results, where 6 rows for each star correspond to 6 Milky Way analog hosts, and lower/upper errors represent $\pm 1\sigma$ errors.

Method 2: Galpy

Bulge candidate orbits were also computed using Galpy, a python and c-based code made freely available[9] by Jo Bovy. We adopt the standard Milky Way potential described in Bovy (2015), consisting of a power-law profile bulge, Miyamoto-Nagai disk, and Navarro-Frenk-White halo (Miyamoto & Nagai, 1975; Navarro et al., 1996).

[8] A Project Of Simulating The Local Environment

[9] https://github.com/jobovy/galpy

Table 3.8: Bulge Candidate Observed Parameters

			SPM4 (Girard et al., 2011)		UCAC4 (Zacharias et al., 2012)	
Star	$r_\odot$	V_{hel}	$\mu_\alpha \cos\delta$	μ_δ	$\mu_\alpha \cos\delta$	μ_δ
	(kpc)	km/s	(mas/yr)	(mas/yr)	(mas/yr)	(mas/yr)
MA8	$4.5^{+1.8}_{-1.3}$	-215.59 ± 0.98	-3.93 ± 3.96	-10.86 ± 3.98	-13.9 ± 2.5	-4.0 ± 3.4
MA11	$11.0^{+4.3}_{-3.2}$	113.06 ± 0.45	-5.22 ± 2.62	-7.86 ± -2.64	-3.4 ± 2.1	-13.6 ± 2.1
MA14	$4.5^{+1.9}_{-1.4}$	-136.66 ± 0.58	-1.23 ± 4.08	-5.67 ± 4.11	0.1 ± 4.5	-2.9 ± 4.6

Median apocentres and pericentres of each star are computed by integrating their orbits using the aforementioned 3D potential model and orbital parameters in Table 3.8; these results assume the same galactic circular velocity, radius, and (U,V,W) as in our APOSTLE calculations (see Section 3.6.2). The results are presented in Table 3.10. Finally, 1000 orbits were computed (following Howes et al. 2015), using a Monte Carlo simulation along with the uncertainties from Table 3.8 to determine 1-sigma errors. These orbital errors are in Table 3.8.

3.6.3 Orbits

A recent study using 2MASS data (Robin et al., 2012) find a two component model best fits the shape of the Galactic bulge: one component is physically smaller and more metal rich, with a major-axis scale length of 1.46± 0.25 kpc, while the second component is less massive, more metal-poor, and physically larger, with scale length of 4.44 ± 0.25 kpc. While the first component is attributed to the main boxy bar of the Galactic Centre, they suggest the second component may represent a flattened classical bulge, driven to this shape by the potential of the bar. If we consider our bulge candidates as potential members of the latter metal-poor component (given their metallicities) and we find their orbit apocentres are within one scale length, or 4.44 ± 0.25 kpc, then they can be safely assumed as bulge members. Robin et al. (2012) also find the bulge cutoff radius of $\sim$ 6 kpc.

- *MA8:* In no calculation does the bulge candidate MA8 show an orbit constrained to the Galactic bulge; this suggests MA8 is a transient halo member temporarily passing through the centre of the Milky Way.

- *MA11:* Lower bound apocentres calculated using both the SPM4 proper motions and Method 2 (using Galpy) show an apocentre of 3.2 kpc - well within the Galactic bulge. The smallest lower bound apocentres for Method 1 (MW1 and MW4 potentials), yields 4.8 and 5.5 kpc (respectively) - marginally outside one scale length yet still within the bulge cutoff radius. Neither method yields realistic bulge orbits when considering the UCAC4 proper motions, emphasizing the need for high quality proper motions to alleviate this discrepancy (e.g. soon to be available from GAIA; Perryman 2012). We conclude the kinematics of MA11 suggest it may be a potential bulge member, however the majority of the orbit calculations do not support this.

- *MA14:* Using SPM4 proper motions, a lower bound apocentre is found within one scale length using Method 1 (MW1 potential) and Method 2 (found to be 4.5 and 3.6 kpc, respectively). Lower bound apocentres for five out of the six MW-like potentials are found to be < 6 kpc - within the bulge cutoff radius. Method 2 calculated with the UCAC4 proper motions suggests MA14 is a bulge member, with a lower bound apocentre of 4 kpc; however Method 1 produces a larger lower bound apocentre of 5.5 kpc (but still within the bulge cutoff radius). Therefore, the kinematics of MA14 show roughly half of the calculated orbits have lower bound apocentres consistent with bulge membership, and we conclude this star is a potential bulge member.

3.6.4 Comparison of the two methods

The two methods used here to compute orbits are complementary, and we briefly comment here which method may be better suited for this work. The potential chosen in Galpy is fit to the observations of the MW, which works well for small to intermediate Galactic radii and beyond large radii (i.e. 50 kpc), the potential is less well known. The method using APOSTLE haloes, however, is less sensitive to the inner regions of the Galactic Centre, where multiple stellar components can influence the local potential. Therefore, when computing orbits within the inner regions of the Galaxy, a method such as Galpy might be more desirable. For this work we consider each method equally reliable for the MA8 halo trespasser due to the large orbital radius, however we believe MA11 and MA14 are better represented by orbits calculated with Galpy.

3.7 Discussion

3.7.1 M22

CNO mixing

Stars above the RGB bump exhibit signs of mixing with CN-cycled material from the hydrogen burning shell, as has been seen in many globular clusters, e.g. Sweigart & Mengel (1979); Suntzeff & Smith (1991); Charbonnel (1995); Charbonnel et al. (1998); Bellman et al. (2001); Denissenkov & VandenBerg (2003); Smith & Martell (2003);

Table 3.9: Bulge Candidate Orbits using APOSTLE MW-like Potentials

		SPM4 proper motions		UCAC4 proper motions	
		Median	Median	Median	Median
	Potential[a]	apocentre (kpc)	pericentre (kpc)	apocentre (kpc)	pericentre (kpc)
MA8	MW1	$15.3\ ^{+12.1}_{-5.4}$	$1.8\ ^{+0.8}_{-0.9}$	$18.5\ ^{+17.3}_{-5.6}$	$3.1\ ^{+0.6}_{+0.9}$
	MW2	$41.6\ ^{+99.6}_{-20.6}$	$1.9\ ^{+0.9}_{-0.9}$	$62.2\ ^{+191.9}_{-30.2}$	$3.2\ ^{+0.7}_{+0.9}$
	MW3	$20.2\ ^{+23.2}_{-7.5}$	$1.8\ ^{+0.9}_{-0.8}$	$25.9\ ^{+38.0}_{-9.0}$	$3.2\ ^{+0.6}_{+1.0}$
	MW4	$23.1\ ^{+38.8}_{-10.3}$	$1.8\ ^{+0.9}_{-0.9}$	$32.2\ ^{+66.7}_{-13.6}$	$3.1\ ^{+0.7}_{+0.9}$
	MW5	$23.6\ ^{+40.5}_{-9.9}$	$1.8\ ^{+0.9}_{-0.8}$	$32.6\ ^{+75.6}_{-13.5}$	$3.2\ ^{+0.6}_{+1.0}$
	MW6	$28.1\ ^{+50.4}_{-11.9}$	$1.9\ ^{+0.9}_{-0.9}$	$39.1\ ^{+100.9}_{-16.4}$	$3.2\ ^{+0.7}_{+0.9}$
MA11	MW1	$18.8\ ^{+>300}_{-14.0}$	$2.9\ ^{+3.9}_{-1.8}$	$246.4\ ^{+>300}_{-233.8}$	$3.1\ ^{+3.9}_{+1.5}$
	MW2	$75.2\ ^{+>300}_{-66.5}$	$2.9\ ^{+4.0}_{-1.7}$	$> 300^{+>300}_{->300}$	$3.1\ ^{+3.9}_{+1.5}$
	MW3	$28.1\ ^{+>300}_{-22.0}$	$2.9\ ^{+3.9}_{-1.7}$	$> 300^{+>300}_{->300}$	$3.1\ ^{+3.9}_{+1.5}$
	MW4	$34.2\ ^{+>300}_{-28.7}$	$2.9\ ^{+3.9}_{-1.8}$	$> 300^{+>300}_{->300}$	$3.1\ ^{+3.9}_{+1.5}$
	MW5	$36.4\ ^{+>300}_{-30.1}$	$2.9\ ^{+3.9}_{-1.7}$	$> 300^{+>300}_{->300}$	$3.1\ ^{+3.9}_{+1.5}$
	MW6	$45.0\ ^{+>300}_{-37.5}$	$2.9\ ^{+3.9}_{-1.7}$	$> 300^{+>300}_{->300}$	$3.1\ ^{+3.9}_{+1.5}$
MA14	MW1	$7.2\ ^{+4.6}_{-2.7}$	$1.9\ ^{+1.4}_{-1.0}$	$9.7\ ^{+8.8}_{-4.2}$	$2.4\ ^{+1.5}_{+1.2}$
	MW2	$12.3\ ^{+16.0}_{-5.7}$	$2.2\ ^{+1.5}_{-1.1}$	$21.1\ ^{+42.2}_{-12.7}$	$2.7\ ^{+1.4}_{+1.4}$
	MW3	$8.6\ ^{+6.8}_{-3.3}$	$2.1\ ^{+1.4}_{-1.1}$	$12.4\ ^{+13.6}_{-6.0}$	$2.6\ ^{+1.4}_{+1.3}$
	MW4	$8.4\ ^{+8.1}_{-3.5}$	$2.0\ ^{+1.4}_{-1.1}$	$12.7\ ^{+19.8}_{-6.6}$	$2.5\ ^{+1.5}_{+1.3}$
	MW5	$9.0\ ^{+8.1}_{-3.6}$	$2.1\ ^{+1.4}_{-1.1}$	$13.5\ ^{+19.3}_{-6.9}$	$2.6\ ^{+1.4}_{+1.3}$
	MW6	$10.3\ ^{+10.1}_{-4.3}$	$2.1\ ^{+1.5}_{-1.0}$	$16.0\ ^{+23.6}_{-8.5}$	$2.7\ ^{+1.4}_{+1.4}$

[a]Each potential is a MW-like, taken from the APOSTLE project. See Section 3.6.2 for a more detailed description.

Table 3.10: Bulge Candidate Orbits using Galpy

	PM[a] source	Median apocentre (kpc)	Median pericentre (kpc)	Median ecc.	Median Z_{max}
MA8	SPM4	$9.22^{+5.51}_{-3.02}$	$1.08^{+0.95}_{-0.65}$	$0.79^{+0.12}_{-0.11}$	$2.91^{+6.16}_{-2.08}$
	UCAC4	$9.93^{+5.72}_{-2.62}$	$2.06^{+0.84}_{-1.03}$	$0.66^{+0.17}_{-0.07}$	$7.93^{+5.39}_{-3.55}$
MA11	SPM4	$9.22^{+492.94}_{-6.02}$	$2.09^{+3.98}_{-1.53}$	$0.77^{+0.21}_{-0.28}$	$4.89^{+80.46}_{-3.21}$
	UCAC4	$585.98^{+2083.26}_{-579.54}$	$3.34^{+3.76}_{-2.33}$	$0.99^{+0.01}_{-0.28}$	$274.38^{+1028.85}_{-271.03}$
MA14	SPM4	$5.50^{+2.46}_{-1.89}$	$1.30^{+1.31}_{-0.86}$	$0.60^{+0.22}_{-0.14}$	$0.89^{+1.30}_{-0.39}$
	UCAC4	$6.51^{+4.00}_{-2.44}$	$1.89^{+1.43}_{-1.29}$	$0.57^{+0.21}_{-0.12}$	$1.11^{+1.58}_{-0.56}$

[a]Proper Motion sources: Girard et al. (2011) (SPM4) and Zacharias et al. (2012) (UCAC4).

Carretta et al. (2005); Smith & Briley (2006). Both of the stars in M22 analysed in this paper are above the RGB bump (see Figure 3.11), and do show enhancements of N; however, this is also accompanied by enhancements in C and O. While both may be AGB stars (having also undergone the third dredge-up of gas from the H and He burning shells), it is also possible that the initial abundances of CNO are simply not scaled-solar. The higher [O/Fe] value is consistent with halo stars at this metallicity, indicating initial abundances primarily from SNe II, unlike scaled-solar values which would include yields from SNeIa from a more extended galactic chemical evolution history. If the initial C and N are also more pristine, then possibly $[C/Fe]_i \sim [N/Fe]_i \sim +0.1$ would be consistent then with mixing of CN-cycled gas; this is confirmed with CN-cycle calculator[10] as described in Placco et al. (2014). Marino et al. (2011) and Alves-Brito et al. (2012) find two groups of stars in M22; one group that has A(C+N+O) $\sim$ 7.9 (and enhancements in s-process elements by [s/Fe]$\sim$0.35) and a second group that has A(C+N+O) $\sim$ 7.5 (and no s-process enrichment, thus [s/Fe]$\sim$0). The two M22 stars in this paper have $<$A(C+N+O)$>$ = 7.46 ($\pm$ 0.25 for MA4, and $\pm$ 0.16 for MA4.1), consistent with the lower A(C+N+O) value. Note here the sum of C, N and O should be unaffected by the upper limit of C as discussed in Section 3.4. This would imply that both are s-poor; unfortunately, there are no s-process element spectral features in our H-band spectra.

[10]http://www3.nd.edu/$\sim$vplacco/carbon-cor.html

Anti-correlations

The Mg-Al anti-correlation in M22 may be evident in our stars, where we find enriched Mg and depleted Al relative to scaled-solar abundances. This anti-correlation was not evident in the work of Marino et al. (2011). However, they do find a strong Na-O anti-correlation; this implies our M22 targets (with enhanced O abundances) are primordial, suggesting Al should be also be low since the Mg-Al cycle has not yet initiated. Indeed we find low Al (with enhanced O); this agrees with Marino et al. (2011), who also find a strong Al-Na correlation, consequently implying an Al-O anti-correlation.

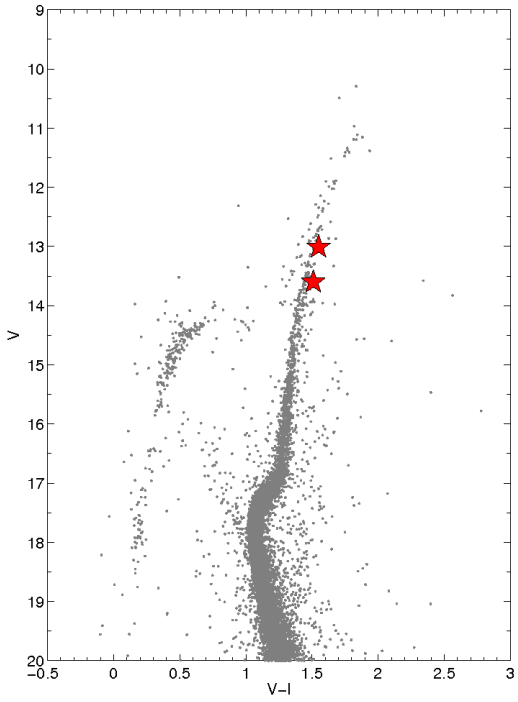

Figure 3.11: CMD of M22; photometry taken from the Hubble ACS Globular Cluster Survey Sarajedini et al. (2007). Both target stars are above the RGB bump as indicated by their positions on the CMD (red stars).

3.7.2 The Bulge Candidates

CNO-cycling

The physical gravities of our three bulge candidates would place them above the RGB bump on a stellar evolution track, and therefore they are likely to have undergone

mixing with CN-cycled gas. As discussed in Section 3.7.1 for our M22 targets, their high [O/Fe] implies that these stars do not simply have scaled-solar abundances for their metallicities, consistent with Galactic chemical evolution models. Similarly with MA8, we find elevated C and N values that imply that each of [(C,N,O)/Fe] are above scaled-solar values. However, for MA11 and MA14, the elevated [N/Fe] and reduced [C/Fe] are consistent with scaled-solar CN-cycled gas (e.g., as found[11] with the interactive CN-cycling calculator as described in Section 3.7.1).

MA8: [Fe/H] = -1.9, r_{apo} > 6.5 kpc, likely halo transient

MA8 appears to be only $4.5^{+1.8}_{-1.3}$ kpc from the Sun towards the Galactic Centre; at b = -5.2^o. A recent comprehensive review of the Galactic Centre distance by Bland-Hawthorn & Gerhard (2016) considers 8.1 ± 0.1 kpc as the best distance estimate; MA8 is then 3.6 kpc from the Galactic Centre. Uncertainties in its proper motion result in orbits with a wide range in $r_{\rm apo}$ values as shown in Tables 3.9 and 3.10, but all are larger than the size of the bulge. This would imply that it is a halo star that is just passing through the Galactic bulge at this time.

The elemental abundances of MA8 are interesting when compared to halo stars, since the C, N, O, and Al abundances are slightly enhanced, while Mg and Si appear to be slightly depleted (see Figures 3.7 and 3.8). The Ni abundance is also unusual, although it has a large uncertainty. These unusual chemical abundances may suggest that it is associated with a disrupted dwarf galaxy, that had a unique chemical evolution history (e.g. Tolstoy et al. 2009; Venn et al. 2004), particularly when given the low [Mg/Ca] (e.g. Lemasle et al. 2012; Venn et al. 2012; Jablonka et al. 2015).

MA11: [Fe/H] = -1.5, r_{apo} > 3.2 kpc, possible bulge member

The stellar parameters for MA11 imply that it is currently $11.0^{+4.3}_{-3.2}$ kpc from the Sun towards the Galactic Centre; at b = 8.9^o, it would be directly above the Galactic Centre at a height of ∼ 5 kpc (consulting z_{max} in Table 3.10 computed with SPM4 proper motions); given its metallicity, it is possible MA11 may be a disc star, however this vertical orbital distance suggests this may not be the case. The lowest permitted apocenter value places MA11 in a bound orbit, however the majority of orbit calculations suggest it is a halo trespasser.

[11]The carbon correction yields Δ[C/Fe] = +0.51, +0.65 for MA11 and MA14 (respectively).

Its elemental abundances are consistent with halo, thick disk stars, and bulge stars in the literature, with the exception of perhaps Al. Al appears to be $\sim 2\sigma$ higher than the halo stars, although there are very few halo stars at this metallicity (see Figure 3.10). Our Al is entirely consistent, however, with a bulge star from Johnson et al. (2013) at its metallicity. From these abundances and orbital kinematics, we argue that it is possible MA11 may be a bulge member.

MA14: [Fe/H] = -2.1, r_{apo} > 3.6 kpc, possible bulge member

MA14 appears to be $4.5^{+1.9}_{-1.4}$ kpc from the Sun towards the Galactic Centre; at b = -6.2^o; this places the object is 3.6 kpc from the Galactic Centre (again using the distance adopted in Bland-Hawthorn & Gerhard 2016). As previously discussed in Section 3.6.3, the orbit is sufficiently small that this could be a bulge member.

The elemental abundances for MA14 are consistent with those of halo stars, thick disk stars, and bulge stars at its respective metallicity, as indicated by Figures 3.8-3.10. This is consistent with Meléndez et al. (2008); Alves-Brito et al. (2010); Bensby et al. (2010, 2011); Ryde et al. (2010); Gonzalez et al. (2011); Hill et al. (2011); Johnson et al. (2013, 2014), who suggest that the thick and metal-poor bulge populations have alpha-element abundances that are very similar and that the homogeneity between the two may indicate the bulge and the disk formed in situ. Based on these kinematic and elemental findings, we suggest that MA14 is a potential bulge member.

3.8 Summary and Conclusions

A detailed chemical abundance analysis has been performed on the H band IR spectra for metal-poor stars in and towards the Galactic Centre. These spectra were taken with the newly developed technology of MOAO, using the RAVEN science demonstrator and IRCS detector at the Subaru 8.2-m telescope. In this analysis, we have found:

1. The technical feasibility of MOAO on an 8-m telescope has been a success for high resolution spectroscopy. We report the first use of MOAO with high resolution spectroscopy, which is a crucial step in the science demonstration of this technology for the future ELT era. We demonstrate the benefits of MOAO and GLAO on the uncorrected PSF, yielding an on-average improvement of 0.2" in seeing, along with a 2-3 times flux gain through the spectroscopic slit.

We also demonstrate these observations are successful when observing dusty, crowded regions within the MW.

2. Five metal-poor stars in and towards the Galactic Centre have been identified and their chemical abundances were derived for 12 elements. Two of these stars belong to the globular cluster M22, while three of these stars are currently situated in the bulge.

3. The two M22 stars have metallicities and element abundance ratios in common with other spectroscopic analyses (Marino et al., 2011; Alves-Brito et al., 2012). Our CNO abundances are in common with the more metal-poor subpopulation in M22 and CNO-mixing, although we suggest the initial abundances may have been slightly higher than scaled-solar.

4. The three metal-poor bulge candidates in this paper are in a metallicity regime with little to no previous high-resolution measurements (-1 $<$ [Fe/H] $<$ -2.5 dex). One out of three of our bulge candidates (MA8) has an orbit that suggests it's a transiting halo object; its chemistry shows some unique abundance characteristics that could imply it was captured from an accreted dwarf galaxy. Our two other stars (MA11 and MA14) may be bulge members based on both their kinematic and elemental properties. We note the large variation in orbit calculations when using two different proper motion catalogues. Future work on bulge members will benefit from the improved precision in the GAIA proper motions.

5. The future of MOAO, and even GLAO, can benefit from the strategies developed for our observations, and from the lessons learned; we have summarized these strategies in order to facilitate the future use of this technology, which to date - other than a demonstration by the MOAO system CANARY (Gendron et al., 2011) - has had very little demonstration on-sky. We anticipate that in the coming ELT-era many interesting science cases will be developed specifically for the use of MOAO.

Chapter 4

NCPA calibration methods: validation and application to RAVEN

4.1 Characterization of NFIRAOS-like NCPA in simulation

4.1.1 Introduction

In adaptive optics (AO) systems non-common path aberrations (NCPA) arise from the inability of the wavefront sensor (WFS) to detect static phase aberrations introduced on the separate science camera path; these static aberrations typically arise from the surface errors of each optical element in the non-common path. As AO systems become more and more complex the impact of these NCPA becomes more and more significant, requiring the use of calibration techniques to mitigate these aberrations. There are a variety of different ways to estimate the NCPA in an AO system, such as the well known technique of Phase Diversity (Gonsalves, 1982; Paxman et al., 1992); however, other approaches have been explored such as Focal Plane Sharpening (Lamb et al., 2014) and using the Zernike mask sensor (N'Diaye et al., 2013). The technique of Focal Plane Sharpening does not depend on any sort of model of the PSF while Phase Diversity requires the generation of synthetic images - therefore any errors in the parameters that define the synthetic images (such as pupil, etc.) will hinder the optimal performance of Phase Diversity. As such, a reasonable hypothesis is that

Focal Plane sharpening may work well in tandem with Phase Diversity to achieve the optimal solution.

The TMT/NFIRAOS AO system is expected to host ~ 100 nm RMS NCPA and it is a base-level requirement that a portion of these errors be compensated on the real system. The goal of this chapter is to explore two different types of NCPA techniques (Phase Diversity and Focal Plane Sharpening) and how they might be able to correct the NCPA in a system such as NFIRAOS. We then explore the operational parameters of Phase Diversity in a noiseless scenario and assess which flavours of Phase Diversity work best. Two different modal bases are also considered in this work: Zernike modes and Disk Harmonics, with the goal to characterize which basis might best be suited for NFIRAOS NCPA estimation/compensation. Finally, we use the insight of these approaches to simulate the estimation of NCPA in a NFIRAOS like scenario, where considerations such as detector requirements, wavelength, pupil, SNR, etc. are taken into account.

4.1.2 Estimation methods

Phase Diversity

We adopt a Phase Diversity routine that uses the aberration-dependent objective/gradient functions of Paxman et al. (1992), and feed these functions to the well established non-linear optimization technique known as the Broyden-Fletcher-Goldfarb-Shanno (BFGS) algorithm. This code is written as a class for the MATLAB AO simulation tool OOMAO (Conan & Correia, 2014). The Phase Diversity estimate is in the form of aberration coefficients of the basis of the user's choice (i.e. Zernikes, etc.). The input requires both the diversity images and the diversity information, such that synthetic images can be created. The real and synthetic images are minimized in OTF space, again following Paxman et al. (1992). There is a termination tolerance parameter for the BFGS algorithm that we typically take as 10^{-9}, which was found by finding the minimum tolerance required to estimate a known phase map for noiseless images. The functionality exists in our code to estimate the object simultaneously with the phase, in which case the objective and gradient likelihood functions are (respectively):

$$L_M(\alpha) = \sum_{u\in\chi_1} \frac{\left|\sum_{j=1}^{K} D_j(u) S_j^*(u)\right|^2}{\sum_{l=1}^{K} |S_l(u)|^2} - \sum_{u\in\chi} \sum_{k=1}^{K} |D_k(u)|^2 , \tag{4.1}$$

$$\frac{\partial}{\partial \alpha_n} L_M = -\frac{4}{N^2} \phi_n(u) \mathrm{Im} \left[\sum_{k=1}^{K} H_k(u) (Z_k * H_k^*)(u) \right], \tag{4.2}$$

where

$$Z_k(u) \equiv \left\{ \left[\sum_l |S_l|^2 (\sum_j D_j S_j^*) D_k^* - \left| \sum_j D_j S_j^* \right|^2 S_k^* \right] \right\} \Big/ \left(\sum_l |S_l|^2 \right)^2. \tag{4.3}$$

Here α are the coefficients of the basis being estimated, $D(u)$ is the optical transfer function (OTF) of the detected image (u is an element of X, where X is all x,y pixel positions), N is number of pixels on a side of the detected image, S is the OTF of the synthetic images created from the known parameters of the system, ϕ is the set of basis functions being estimated, H is the generalized pupil function of the system, and K is the number of images used in the Phase Diversity.

We also have the ability to disregard the object estimation (by assuming a point source), in order to simplify the above equations (and thus increase computation speed) by using the following objective function (again, taken from Paxman et al. 1992):

$$L_M(\alpha) = -\sum_{u \in \chi} \frac{|D_1(u) S_2(u) - D_2(u) S_1(u)|^2}{|S_1(u)|^2 + |S_2(u)|^2}. \tag{4.4}$$

For an excellent review on the technique we refer the reader to Mugnier et al. (2006).

Focal Plane Sharpening

Focal Plane Sharpening (Lamb et al., 2014) (FPS) optimizes the PSF based on varying deformable mirror (DM) shapes, using the downhill simplex approach of Lagarias et al. (1998). The DM shapes are broken down into a projection of a set of modes (i.e. Zernikes, although the modes need not be orthogonal), as using individual influence functions can be very time consuming in the case of a NFIRAOS-like DM (with thousands of actuators). At each step in the optimization the PSF is assessed for a particular criterion, and then a new set of DM commands (from the de-projection of the modal set) is computed based on the optimization algorithm. We have developed a FPS class for OOMAO, and the PSF criteria options are summarized as follows:

- Peak of the PSF
- Encircled energy
- Amplitude of 2D Gaussian fit

In addition to the criteria options, the code also includes several other options:

- Applying noise filters (useful when dealing with low SNR images)
- PSF oversampling (useful when the criteria is either the peak of the PSF or the encircled energy)
- Boundary conditions - boundaries beyond which the estimated modal coefficients are not allowed to vary

If the system is stable (i.e. no vibrations and little noise) then measuring the peak value of the PSF is a suitable criterion in terms of speed and accuracy. This is further improved when using a noise filter (i.e. a median filter with a box size equal to 2 x the FWHM of the PSF) and oversampling the PSF at each iteration. Using the encircled energy with the same noise/oversampling application yields very comparable results to using the peak of the PSF. We find the most robust performance, however, is when the noise filter is used along with a fit of a 2D Gaussian, and the amplitude of the Gaussian is optimized. To do this efficiently the PSF is truncated such that it only contains 2 x FWHM pixels on each side. We also always induce boundary conditions consistent with the peak to valley (PV) of the error being estimated; we understand this may be difficult in a real scenario where the phase error is unknown. For the sake of this work the boundaries are always set to 1.5 x the maximum modal coefficient of the phase being estimated; this coefficient is found by projecting the known phase map onto the modal basis in question. This combination allows the estimation of extremely low SNR situations in a very robust manner (PSFs with a SNR of 10 could be efficiently estimated in Lamb et al. 2016b).

NCPA phase map generation

Several examples in this paper require the generation of realistic NCPA profiles. We create phase maps with a power spectrum following a $1/\nu^2$ profile, following what was found for realistic optical surfaces (Dohlen et al., 2011). The phase maps are generated by first creating a map of spatial frequencies, distributed between 0 and 2

π (denoted as k). A subsequent circular amplitude map, A, is constructed, with a radial power law corresponding to $1/\nu^2$. The phase map ϕ, is created by:

$$\phi = \mathbb{R}\{\mathcal{F}\{Ae^{-ik}\}\} \tag{4.5}$$

An example of one of these phase maps - corresponding to ∼100 nm rms on a TMT pupil, along with its power spectrum - is shown in Figure 4.11.

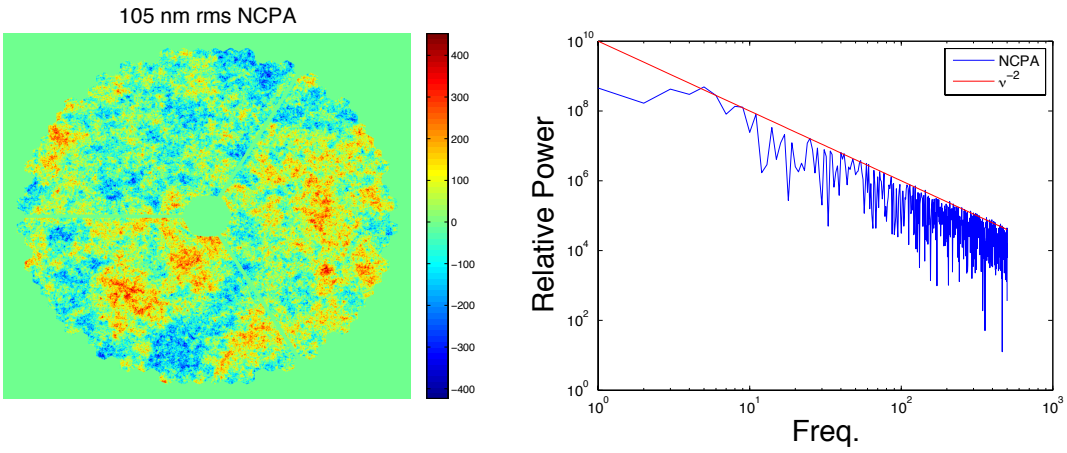

Figure 4.1: Phase map and power spectrum of NCPA profile showing $1/\nu^2$ power law (in units of nm). The TMT pupil is shown here. Global tip/tilt is removed.

Phase Diversity Techniques

A better understanding of the variations on the Phase Diversity parameters will allow us to more efficiently use the algorithm in a real scenario. Therefore we opt to explore Phase Diversity in a more detailed simulation, starting with a simple circular telescope pupil in the presence of no noise. The goal is to explore a range of Phase Diversity parameters (no. of images, obj./no obj. estimation, etc.) to assess their impact on the quality of estimation.

We simulate ∼ 70 nm rms NCPA, and attempt to estimate the first 7 radial orders of Zernike modes using the variety of Phase Diversity flavours shown in Table 4.1. One example showing an estimate on this table is shown in Figure 4.2. This Table summarizes our experimental results and we draw the following conclusions:

- When estimating the object, an in-focus image always improves the estimate

- When not estimating the object (i.e. assuming a point source), excluding an in-focus image always improves the estimate (even in the case where using only 1 diverse image). When there is only one image we call this 'single image Phase Diversity'.

- The best estimate was found when using multiple images on either side of the focal plane at asymmetric focal positions, and assuming the object was a point source.

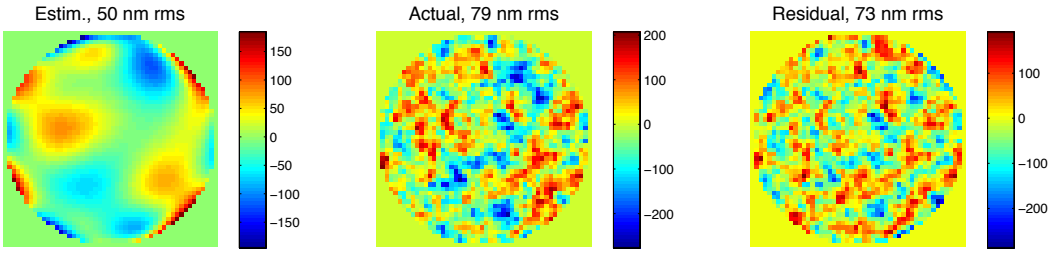

Figure 4.2: Sample estimation of the phase (left, with WFE noted on the top), using the case from Table 4.1 where 1 image was used (with 1 wave of focus) to estimate the phase. The Actual phase map being estimated is shown in the center and the residual is shown on the right. The first 7 radial orders of Zernike modes were estimated in this example.

The explanation of why the in-focus image does not work when assuming a point-source is currently under investigation. It seems only one diverse image will do and we will explore this on our experimental bench.

Single Image Phase Diversity

One immediate result of Section 4.1.2 is the implications of single image phase diversity (also known as *phase-diverse phase retrieval* Ellerbroek et al. 1997). When considering on-sky Phase Diversity it has been shown in the past (Jolissaint et al., 2012) that the evolution between two sequential images (i.e. due to AO residual errors, changing seeing, etc.) can have a large negative impact when trying to estimate the phase. This impact can be greatly mitigated if using only one image. It is worth noting similar work has been done investigating single image Phase Diversity (Meimon et al., 2010) in developing the LIFT technique, and it is not an entirely new concept. We explore this effect by means of simulating real telescope images in Lamb et al. (2016b) and refer the reader to this paper for more information. In

Table 4.1: Estimating NCPA with $Z_{1:36}$ for different types of Phase Diversity

Diversity images (units of waves of focus)	Object Estimation?	rms Residual WF (Estimate - Actual NCPA*) (nm rms)	Strehl (Marechal)
[0, 1]	yes	73.3	92.5
[0, 1]	no	88.8	89.2
[1]	no	72.8	92.6
[2]	no	72.5	92.7
[0, 2]	yes	72.7	92.7
[-1, 0, 1]	yes	71.8	92.8
[-2, 0, 1]	yes	70.4	93.1
[-2, 1]	yes	74.1	92.4
[-2, 1]	no	70.1	93.2
[-2, 0, 1]	no	86.0	89.9

*Actual NCPA: 79.2 nm rms

the context of this paper, however, we we consider a noiseless scenario with a ciruclar pupil; it is thus desirable to explore some immediate capabilities of single image Phase Diversity in this scenario. We propose a simple test: given a typical NCPA profile, how well can the phase be estimated (with 7 radial orders of Zernikes) with single image Phase Diversity for a range of focus values. Table 4.2 summarizes our results. In this table different focus diversities are explored (column 1), and their estimated phase is subtracted from the actual NCPA phase and the residual WFE is expressed (column 2). It is immediately clear that for images below roughly a 1/2 wave PV of focus, the estimation breaks down, as indicated by the residual WFE in column 2. Given this information, if using single image Phase Diversity it is always worth investigating diversities of at minimum 1/2 wave PV. In Section 4.1.4 we explore single image Phase Diversity on a TMT/NFIRAOS like simulation, and we therefore use diversities greater than 1/2 wave PV.

4.1.3 Zernike Modes vs Disk Harmonics

Traditionally, Zernike modes are the most commonly used basis used to represent the wavefront modes. The wavefront variations in high order Zernike modes become more and more restricted to the outer ring of the wavefront with increasing orders. DMs become more and more restricted in making these high order Zernike shapes when they reach the threshold of their inter-actuator spacing.

Table 4.2: Estimating 87.9 nm rms NCPA with $Z_{1:36}$ for single image Phase Diversity

Diversity images (units of waves of focus)	rms Residual WF (Estimate - Actual NCPA*) (nm rms)
[3]	83.7
[2]	82.5
[1]	82.7
[0.5]	83.2
[0.40]	87.1
[0.33]	104.3
[0.25]	108.9

*Actual NCPA: 87.9 nm rms

There are alternate wavefront bases that do not restrict their high orders to the outer edges of the wavefront, such as Disk Harmonics (Verrall & Kakarala, 1998). Disk harmonics are similar in form to Zernike modes (see Figure 4.3), however they tend to spread the wavefront amplitude variations more evenly across the wavefront. This becomes particularly interesting when trying to reproduce high order modes. For example, a situation can be imagined where a high-order Disk Harmonic mode can be made with a DM of a particular pitch and stroke, while the Zernike mode of that order will not be made as accurately with the same DM. We therefore investigate the capabilities of estimating Disk-Harmonic modes in comparison with Zernike modes. In particular we would like to show we have the framework to estimate Disk Harmonics to the same efficiency as Zernikes. This will be useful when applying the *correction* of estimated NCPA, where creating higher-order shapes will be less difficult for a DM if using Disk Harmonics. We have developed an OOMAO implementation of Disk Harmonics, following their description in Verrall & Kakarala (1998).

Next we employ Phase Diversity on a circular pupil with $\sim$ 70 nm rms simulated NCPA. We use two, noiseless, H-band diverse images, with 2 waves (PV) of focus as our diversity and the object is estimated. The first 20 radial orders of Zernike Modes and Disk Harmonics are subsequently estimated and are shown in Figure 4.4.

4.1.4 NFIRAOS example

The NFIRAOS AO system on TMT will have a calibration source which can be used to estimate the NCPA, and we wish to consider calibrating such a system in simulation.

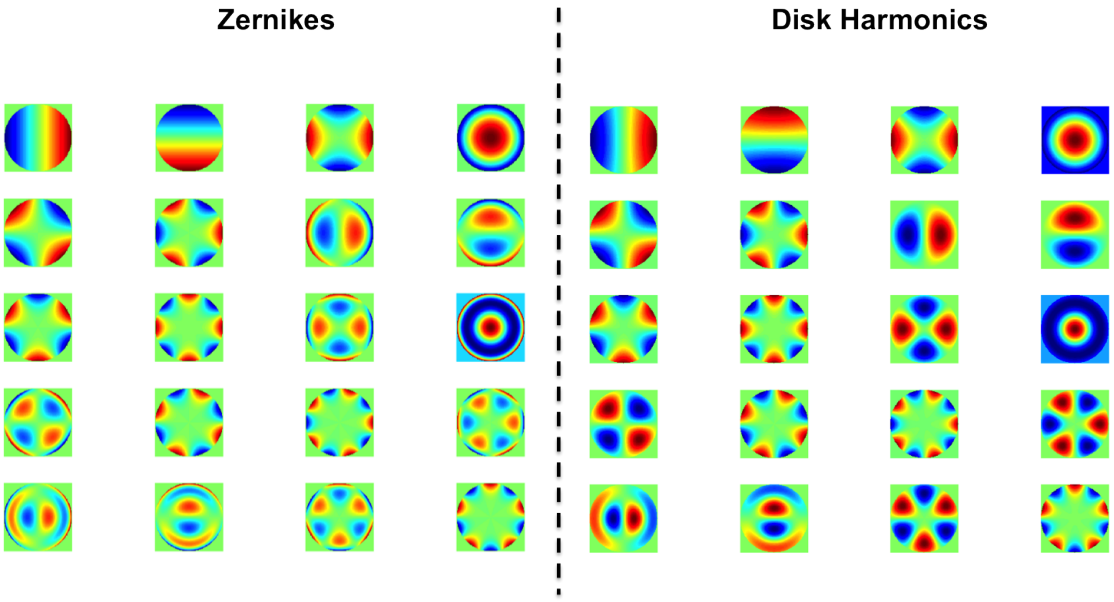

Figure 4.3: Zernike modes (left) vs. Disk Harmonics (right). The modes are similar in form with the exception that disk harmonics spread their wavefront variations throughout the pupil more so than their high-order Zernike counterparts. We wish to validate the framework of phase estimation using Disk Harmonics and compare them with the more traditional Zernike estimation. A DM will have less difficulties creating higher modes estimated from Disk Harmonics than Zernikes, and therefore having a tool that can estimate the NCPA in the form of Disk Harmonics is useful.

We consider an AO system with ∼100 nm rms WFE NCPA and aim to correct 105 modes (13 radial orders) using phase diversity - this is in accordance with a realistic scenario. Our goal is to explore: 1) a variety of different estimation parameters, and 2) performance as a function of signal-to-noise. The estimation parameters we choose to explore are: Zernike vs Disk Harmonic bases, the combination of phase diversity plus Focal Plane Sharpening, number of images, and different types of diversity. The detector on NFIRAOS becomes non-linear above 100,000 ADU and therefore we choose to assess this family of estimation parameters over images with peak signals spanning 1000 to 100,000 ADU (in logarithmic increments). Our images are created assuming the dominant noise is photon and read-out noise; the read-out noise is taken to be $10e^{-}$ following a typical Hawaii I detector. The images are created in H-band, assuming the NFIRAOS calibration source will be at this wavelength. It is noted that the calibration source will be resolved (and therefore have a measurable width), however we choose not to model this in our study. As a side note, our experimental bench has a measurable width and we were able to estimate the phase quite well -

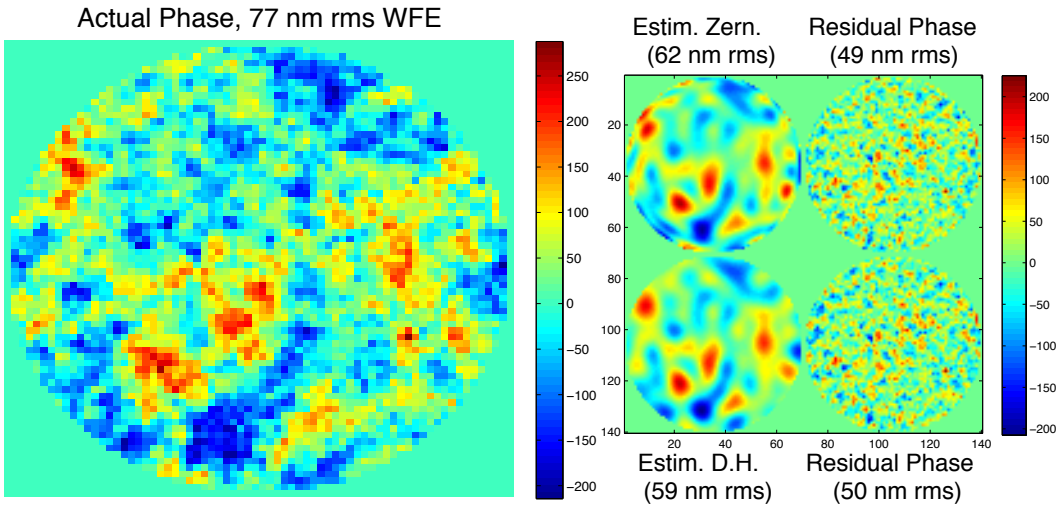

Figure 4.4: Zernike vs Disk Harmonics. Left: actual phase before correction. Right: residual phase maps after correction using both Zernike modes and Disk Harmonics.

even when assuming a point source - therefore we believe the exclusion of this in our study will not have a large effect. The results from our simulations are shown in Table 4.3.

Important Notes

To create images corresponding to peak signals of 100000, 10000, and 1000 adu, we selected magnitude values for our simulated star that produced these values after an average of 10 measurements. The useful information here is the resulting signal to noise of the in-focus image for each Phase Diversity scenario, which we compute and tabulate in Table 4.3. Furthermore, the peak of the 1000 adu data point was consistently too faint to make reliable measurements, and so the magnitude on the simulated star was slightly increased - this value is reflected in the final signal to noise recorded in the Table.

To simulate Phase Diversity while estimating the object, we took the best scenario from Table 4.1, where 3 images are used. Estimating the object for 105 modes takes considerable computation time, as indicated by Table 4.3. Therefore we opted to only simulate the highest signal to noise case for both Zernike and Disk Harmonic modes - fainter signal to noise images always take a longer time to compute. Regardless, we found that estimating the object yielded the best results when estimating both Zernikes and Disk Harmonics - albeit only slightly better than some of the other

Phase Diversity scenarios.

Focal Plane Sharpening would also take a considerable amount of time if estimating all 13 radial orders in this example. We therefore opted to estimate the first 11 radial orders with Phase Diversity, and assess whether Focal Plane Sharpening can estimate the remaining 2 radial orders better than the Phase Diversity estimates of all 13 radial orders. We did this in the case where Phase Diversity used two images, both asymmetrically placed on either side of the focal plane, and assumed a point source.

We also chose to explore a $1/\nu^2$ diversity profile, as this is the phase pattern we are trying to estimate. We made this diversity over the first 4 radial orders of Zernike modes by dividing the amplitude of each mode by its radial order - this roughly creates a $1/\nu^2$ profile. These Zernike modes were globally scaled such that their PV wavefront was around 5 microns and therefore within the capabilities of the NFIRAOS DM. We evaluated a higher mode, specifically Z_{66}, to see if it outperforms traditional focus. We chose this mode based on our findings in Phase Diversity simulation to estimate the 'low wind effect' on the VLT/SPHERE system (Lamb et al., 2016b).

Finally, we explored the effects of using multiple images in the scenario of non-object estimation. We used the two best examples from Table 4.1 and also consider a situation with six images at asymmetric positions on either side of the focal plane. We specifically chose this scenario because of our findings on the experimental bench - with the exception that we do not use an in-focus image as we found in Section 4.1.2 this degrades the performance.

Results

We find that there is a threshold in how well we can estimate the phase based on the common level of residual wavefront error, which we interpret as the limit to which the 105 modes can fit the NCPA. As a whole, it seems Disk Harmonic functions improve the estimation when compared with Zernike modes. This is promising considering the correction of these estimated modes will be less strenuous using the Disk Harmonic estimation. It also appears that estimating the object does yield the best result, although the computation time is considerably large. We find using a single image with 2 waves of focus and no object estimation will do almost as well as the object estimated case. Furthermore, increasing the number of images allows this estimation to work equally well *at all signal to noise ratios* considered in this example. Assuming

Table 4.3: Estimating 105 modes of NCPA using different Phase Diversity methods.

Diversity images (in units of waves)	Object Est.?	Diversity	rms(Res, WF) (Est. - NCPA*) (nm rms)	SNR of in-focus image	Iterations (# mini-mizations)	Comp. time (s)
Estimating 105 Zernike Modes						
			82.8	9218	873	134
[2]	No	Focus	86.3	1041	818	129
			95.8	274	826	129
			77.8	8579	499	104
[-2, 1]	No	Focus	78.0	1028	501	112
			79.6	317	512	106
			-	-	-	-
[-2, 0, 1]**	Yes	Focus	77.6	8785	506	3193
			-	-	-	-
			83.2	7788	822	133
[1]***	No	$1/f^2$	86.6	1084	839	132
			113.3	299	741	121
			83.2	8970	767	149
[-2, 1]	No	Z_{66}	86.6	1041	776	152
			121.8	304	750	203
[-2.5, -1.5,			79.0	9689	469	236
-0.5, 0.25	No	Focus	79.4	1061	449	220
1.25, 2.25]			79.5	276	475	243
			-	-	-	-
[-2, 1]+FPS****	No	Focus	81.2	9137	169	405
			-	-	-	-
Estimating 105 Disk Harmonic Modes						
			81.5	9343	856	186
[2]	No	Focus	81.3	1029	855	155
			92.9	304	857	173
			77.0	9467	655	153
[-2, 1]	No	Focus	77.3	983	657	162
			79.7	289	647	167
			-	-	-	-
[-2, 0, 1]**	Yes	Focus	76.7	9439	597	3986
			-	-	-	-
			81.4	9777	957	210
[1]***	No	$1/f^2$	85.5	1047	963	218
			136.6	359	971	244
			81.4	9895	964	246
[-2, 1]	No	Z_{66}	85.7	983	1016	260
			93.7	344	1031	247
[-2.5, -1.5,			77.8	8527	610	324
-0.5, 0.25	No	Focus	77.7	1024	608	311
1.25, 2.25]			77.6	315	557	242
			-	-	-	-
[-2, 1]+FPS****	No	Focus	78.8	10260	145	411
			-	-	-	-

*Actual NCPA: 97 nm rms; **The corresponding lower SNR cases were not simulated considering the length of the computation time in this example; ***The scale was selected such that the $1/f^2$ power law yielded a wavefront $\sim$5 micron PV (therefore within the limits of the NFIRAOS DM); ****Phase Diversity performed on first 11 radial orders and then followed up with 2 radial orders of FPS correction.

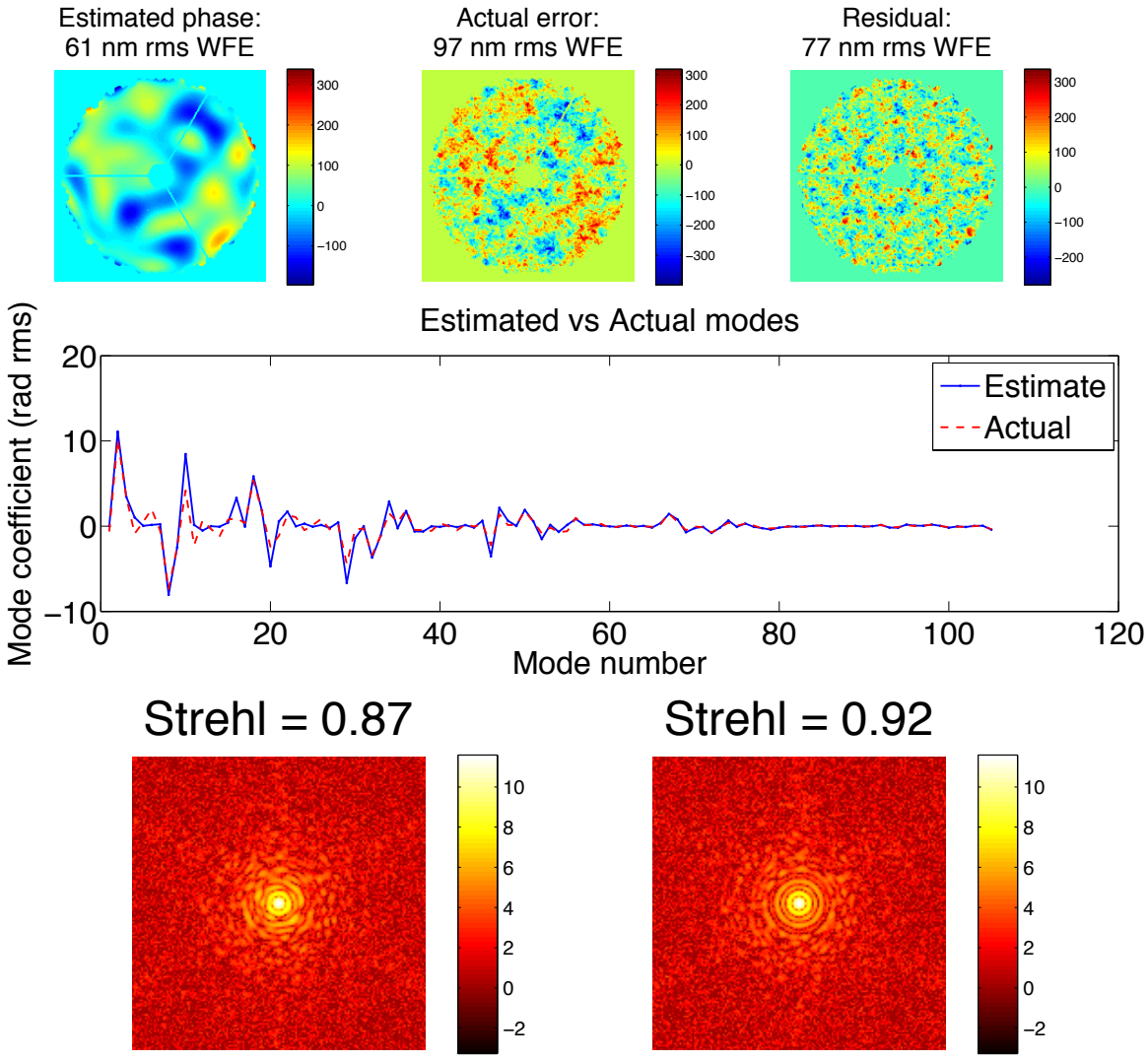

Figure 4.5: Simulating the estimation of NFIRAOS NCPA: estimating 105 modes for 100 nm rms NCPA. This result here shows the estimation of Disk Harmonics, taken as the best result from Table 4.3 (the third case in the Disk Harmonic portion of the Table). The top phase maps show the estimate, acutal, and residual phase maps. The middle plot shows the estimated Disk Harmonic modes compared with the actual modes. The bottom figure shows a simulated PSF before and after correction.

the object is a point source may not be entirely realistic, as the calibration source will most likely be resolved, however we find on our experimental bench that this does not seem to be an issue. The combination of Phase Diversity and Focal Plane Sharpening did not outperform our best Phase Diversity scenarios, contrary to our hypothesis. With real images, however, there may be more errors involved with creating the

model used for our Phase Diversity images and the model-independent Focal Plane Sharpening may indeed prove promising. Figure 4.5 shows the example from Table 4.3 with the best result - which is the case with both Disk Harmonic modes and object estimation.

4.1.5 Simulated NFIRAOS NCPA discussion

The operational effects of Phase Diversity and Focal Plane Sharpening has been explored in simulation, and we draw the following conclusions:

- Single image Phase Diversity was shown to be effective in a noiseless scenario. We show the range of diversity over which the technique is successful. This technique will be applied to realistic on-sky images in Section 5 to both successfully estimate the low wind effect on SPHERE and the low order segment piston errors on Keck.

- We explore the estimation of both Zernike modes and Disk Harmonics in a simple NCPA estimation scenario and show that both are comparable. This is important considering high order Disk Harmonic modes are more easily formed on a DM than their Zernike counterparts, thus leading us to conclude that if you can estimate Disk Harmonics to the same accuracy of Zernikes then they are a superior means to characterize the NCPA.

- We show that when estimating the first 13 radial orders of modes on a NFRIAOS-like system, we appear to achieve a threshold performance of the bases we are using and that estimations using Disk Harmonics outperforms Zernike modes. Furthermore, estimating the object along with the phase yields the best results, however it takes a perhaps unrealistic amount of computation time on our machine. When considering the assumption of a point source and multiple diverse images, the performance is almost as comparable as the object-estimation case and runs in a much shorter amount of time; specifically for the case of estimating Disk Harmonics it took 26 times longer to estimate the object than to use use two diverse images and assume a point source. We explore a range of diversities and combination of images and conclude that using focus is the best choice, along with several images at asymmetric positions on either side of the focal plane. When these considerations are met the estimation is accurate regardless of the signal to noise. Finally, we find that estimating the first 11 radial orders

with Phase Diversity and then the remaining 2 with Focal Plane Sharpening did not do as well as our best Phase Diversity cases. However, based on the visualization of the estimated modes (see Figure 4.5) it seems the best approach might be to use FPS on the first 4 radial orders, and then follow up with Phase Diversity for the higher modes; this will be considered in future studies.

Important note: the work in this Section is taken directly from the paper titled *Exploring the Operational Effects of Phase Diversity for the Calibration of Non-Common Path Errors on NFIRAOS* (Lamb, M., Correia, C., Sauvage, J.-F., Andersen, D., & Veran, J.-P. 2016a, in Proc. SPIE, Vol. 9909, Society of Photo-Optical Instrumentation Engineers (SPIE) Conference Series, 99096E).

4.2 Characterization of NFIRAOS-like NCPA on an experimental bench

4.2.1 Introduction

In this Section the two techniques developed in Section 4.1 are explored with an experimental bench subject to NFIRAOS-like NCPA. The goal is to experimentally validate the performance of each method and see if they can be used in conjunction with each other to yield the best corrected PSF. The NFIRAOS-like NCPA are introduced to the system by a custom made phase screen. Two figures of merit in this work are: (i) the RMS residual between the estimated phase of the phase screen (i.e. by Phase Diversity or Focal Plane Sharpening) and that measured by a SHWFS, and (ii) the Strehl ratio of the corrected image from Phase Diversity, Focal Plane Sharpening, and the SHWFS. We then recommend a suitable approach to correct the NCPA in terms of the actual NFIRAOS system.

Imporant note - this work is in preparation for submission, and may potentially be submitted by the time of the defense. There are repetitions of the description of Phase Diversity and Focal Plane Sharpening that are seen in Section 4.1 of this chapter. Therefore the two techniques are briefly mentioned here, along with minor side notes describing parameters unique to this Section.

4.2.2 Methods and observations

Phase Diversity

The Phase Diversity method used in this section is described in Section 4.1 of this chapter. The diversity images are acquired in closed loop with the SHWFS by providing offset slopes representing the diversity focus. The images are reduced to Nyquist sampling to increase the computational speed of the algorithm. The parameters for the algorithm (i.e. number of images, how much focus, object estimation, etc.) are outlined in Section 4.2.3.

Focal Plane Sharpening

The Focal Plane Sharpening method is also described in detail in Section 4.1 of this chapter. At each iteration in the algorithm, the new shape in question is converted to offset slopes and applied to the SHWFS. After a sufficient number of iterations (it will be shown that $\sim$6 is enough) the shape will converge and its image can be recorded. This ensures that any 'drifting' or 'creep' effects of the DM are mitigated (i.e. Bitenc et al. 2014), as will be discussed in Section 4.2.2. The parameters used with Focal Plane Sharpening in this Section adopt the following procedure: the PSF is subject to a median filter (3x3 pixels) to mitigate noise, oversampled by a factor of 8 to yield an image where a single pixel can represent the peak value, from which the new set of Zernike modes is computed and the process is repeated.

Experimental bench observations

The experimental bench used in this work consists of the following major components:

- 32x40 subaperture Shack-Hartmann Wavefront Sensor (SHWFS) from Imagine Optic
- 11x11 Deformable Mirror (DM) by Alpao
- 655 nm Fiber Source by Imagine Optic
- CMOS Camera with 6.5 micron pixels by Andor (Zyla 5.5 sCMOS)
- Phase Screen by Lexitek (a custom turbulence phase plate with a 150 nm RMS polishing error profile over a 100 mm disk)

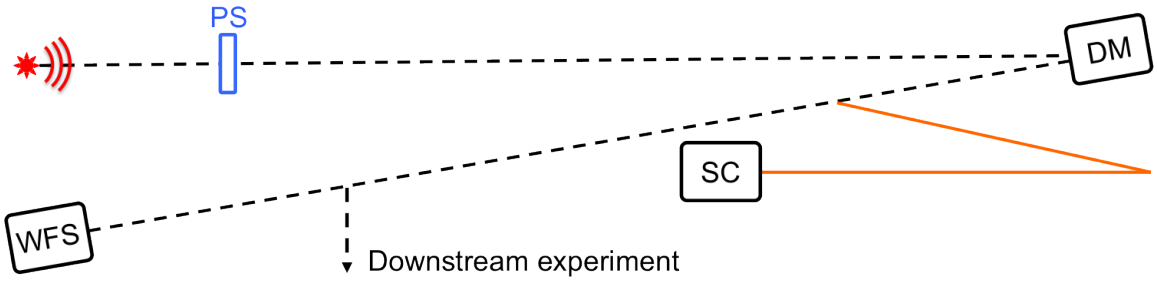

Figure 4.6: Illustrative diagram of the experimental bench used in this work. The non-common path is shown in orange. The particularly compact design of this bench is to additionally accommodate two down stream experiments, where the optical path leading to these projects is shown in between the science camera beam splitter and the WFS. A phase screen is inserted into the common path of this system (at a plane conjugate to the DM pupil) and is denoted in this diagram in blue.

PSF artifacts

The bench SHWFS and DM are controlled in closed loop with software developed in MATLAB. Figure 4.6 illustrates the experimental setup. The Alpao DMs have been shown to 'creep' over time if operated in open loop (Bitenc et al. 2014; Bitenc et al. 2017, in prep.) which can result in significant wavefront error contributions over the course of an extended measurement of the PSF. Therefore all images acquired in this work are done with the AO loop closed to mitigate this effect. All science camera images used in this experiment are taken as the average of 50 single millisecond exposures, unless otherwise indicated. In addition, a background frame taken as the average of 1000 single millisecond exposures is subtracted off each science image. A sample of the closed loop PSF is shown in the left panel of Figure 4.7. We note here the asymmetry of the PSF, which we believe is the result of an interference between an un-correctable sinusoidal pattern and the diffraction rings of the PSF. Supporting evidence for this is the 'dark hole' seen in the third diffraction ring, which also has a symmetric over-intensity on the opposite side of the PSF. Indeed, a closer look at the residual wavefront in closed loop displays a sinusoidal feature in the vertical direction, with a total WFE of 10 nm RMS (see Figure 4.8). The frequency of this sinusoid appears to be ~ 5 cycles across the pupil, which is in line with the maximum correctable frequency given by a 11x11 DM. While this feature seems technically correctable with this actuator density, this is only true when the actuator pitch aligns with the 'peak' and 'trough' of the sinusoid; any phase shift of the sinusoid with

respect to this alignment will reduce the ability of the DM to correct this shape and this may be indicative of the scenario at hand. The origin of such a sinusoidal feature may be due to gravity pulling down on each row of actuators (the direction of the sinusoid is indeed in the vertical plane of the bench), but understanding this feature falls outside the scope of this work. We note this will affect the focal plane wavefront sensing capabilities of Phase Diversity, as will be discussed in Section 4.2.3.

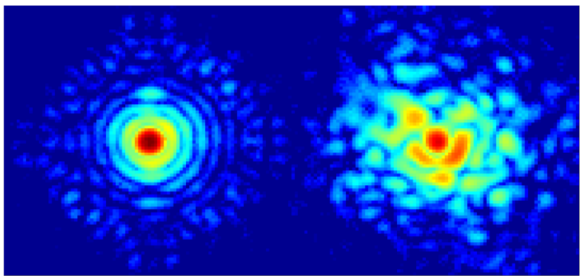

Figure 4.7: Log scale science camera image with and without the common path phase screen (left and right panels, respectively), produced in closed loop with the SHWFS. The latter image is generated by using the full wavefront measurement as reference slopes in the closed loop, while the former is generated from a null reference slope vector (i.e., a vector of zeros). The Strehl ratios are found to be 88.6% and 36.6%, respectively.

Strehl ratio computations

To calculate the Strehl ratio, the curve of growth is first computed for a sample image and a cut-off radius, r is identified (approximately where the slope of the curve begins to level off). The image is then cropped to an nxn square, where $n = 2r$. A synethetic, diffraction-limited PSF is then computed with the same sampling and size of the previous nxn image (assuming a uniform, circular pupil); this synthetic image is then normalized to a maximum value of 1. The actual image is normalized to the total sum of the synthetic image and its peak value is taken as the Strehl ratio. The validation of this procedure is performed in Section 4.2.4.

Closed loop PSFs

The closed loop PSF shown in 4.7 shows a reasonably high image quality, with a Strehl Ratio of $\sim$ 88%; the mean rms WFE over 530 iterations of the loop is 11.8 nm and is plotted in Figure 4.8. In this work we wish to assess the robustness of

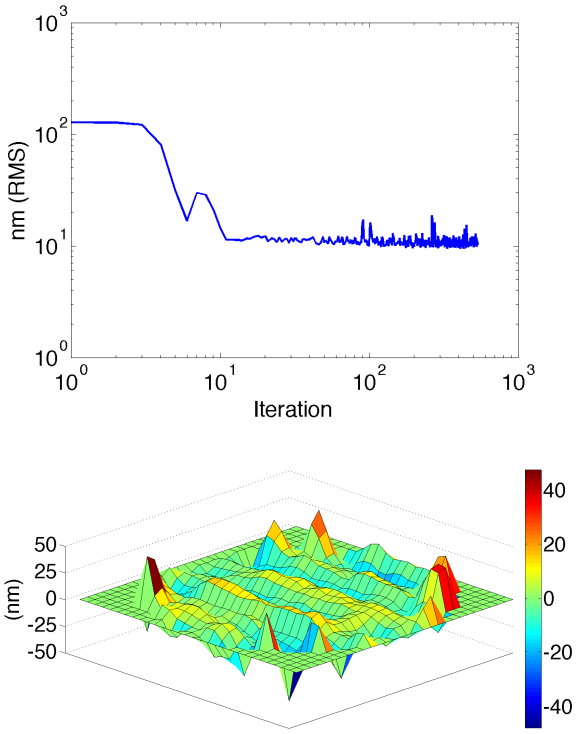

Figure 4.8: Top: closed loop WFE as a function of iteration number (no phase screen in the system, loglog scale); the mean RMS WFE is 11.8 nm over the entire sequence. Bottom: a sample wavefront taken during the closed loop, displaying a sinusoidal frequency of ~ 5 cycles across the pupil. This feature is likely the culprit for the PSF over/under intensity artifact shown in Figure 4.7 and discussed in Section 4.2.2.

two focal plane wavefront sensing techniques in the presence of NFIRAOS-like NCPA ($\sim$100 nm RMS mainly due to polishing errors). Therefore we purposely aberrate the system with a phase screen manufactured[1] with 150 nm RMS WFE which follows a $1/f^2$ power law, typical of optical polishing errors (Dohlen et al. 2011, see Figure 4.9). The phase screen is inserted at a pupil-plane in the common path of the AO system as indicated in blue in Figure 4.6. The beam size at this location is approximately 6.5 mm, which roughly translates to $\sim$100 nm RMS WFE on the phase screen (and therefore is a reasonable approximation of NFIRAOS-like NCPA, although we do note at H-band the impact on the image quality will be much less with this WFE). To statistically confirm the WFE produced from a 6.5 mm beam, we sample 100 random realizations of the prescribed phase shown in Figure 4.9 and compute the mean and

[1]The actual phase imprint of the system is achieved via *near index-matching* (Ebstein, 1996), where two machined surfaces differing in diffractive index are sandwiched together.

standard deviation of the RMS WFE to be 104 and 14 nm RMS, respectively. A PSF demonstrating the impact of this phase screen is shown in Figure 4.7, where the image is created in closed-loop using the full measured wavefront as reference slopes, thereby generating an un-corrected closed-loop image. The Strehl Ratio of this image is measured to be 36.6%, which corresponds to 104.5 nm RMS WFE (from the Maréchal approximation) and is in excellent agreement with the expected 104 nm RMS.

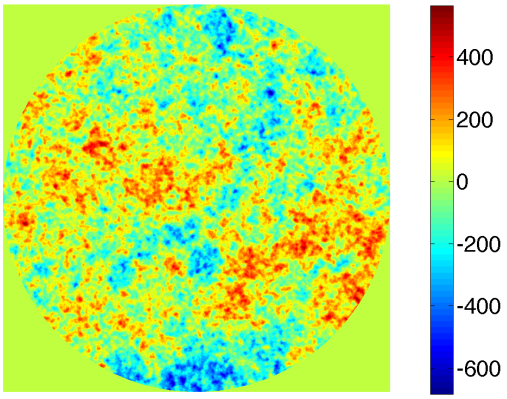

Figure 4.9: Phase prescription of the manufactured phase screen used in this experiment. The total WFE across the face of the screen is 150 nm RMS, and follows a $1/f^2$ power law (typical of polishing errors).

4.2.3 Method evaluation

Phase screen estimation

To measure the wavefront error induced by the phase screen we choose to aberrate the system in the common path at a pupil plane prior to the DM (see Figure 4.6). We wish to isolate the measurement of the phase screen, Φ_{PS} in the context of the diagram shown in Figure 4.10; to do this we propose three measurements, the first of which, Φ_1, is done at the focal plane and without the phase screen in the system:

$$\Phi_1 = \Phi_{\text{CP}} + \Phi_{\text{DM}} + \Phi_{\text{SC}} \tag{4.6}$$

This measurement is taken while the system is in closed loop, and therefore:

$$\Phi_{\mathrm{CP}} + \Phi_{\mathrm{DM}} + \Phi_{\mathrm{WFS}} = 0 \tag{4.7}$$

Combining these two equations yields the focal plane measurement achieved by either Phase Diversity or Focal Plane Sharpening:

$$\Phi_1 = -\Phi_{\mathrm{WFS}} + \Phi_{\mathrm{SC}} \tag{4.8}$$

The second measurement is of the phase screen itself using the SHWFS; this can be achieved by the following steps:

1. Closing the loop of the system without the phase screen
2. After convergence, open the loop and freeze the DM commands
3. Subsequently insert the phase screen into the common path and immediately record the measured wavefront on the SHWFS, denoted as $\Phi_2 = \Phi_{\mathrm{PS}}$

The third measurement is nearly identical to the first, with two major exceptions: (i) the phase screen is introduced in the common path, and (ii) the slopes of the full wavefront are recorded prior to closing the loop and then subsequently used as reference slopes such that the SHWFS does *not* correct the phase screen during the closed loop. This ensures a focal plane image subject to the errors of the phase screen while still retaining the closed loop functionality; the latter point is important so that any measurement of the focal plane wavefront can be injected as reference slopes in the closed loop and therefore provide a correction of the PSF. Therefore a phase measurement at the focal plane is:

$$\Phi_3 = \Phi_{\mathrm{CP}} + \Phi_{\mathrm{PS}} + \Phi_{\mathrm{DM}} + \Phi_{\mathrm{SC}} \tag{4.9}$$

and when in closed loop (using the full measured wavefront as reference slopes),

$$\Phi_{\mathrm{CP}} + \Phi_{\mathrm{PS}} - \Phi_{\mathrm{PS}} + \Phi_{\mathrm{DM}} + \Phi_{\mathrm{WFS}} = 0 \tag{4.10}$$

which leads to:

$$\Phi_3 = -\Phi_{\mathrm{WFS}} + \Phi_{\mathrm{SC}} + \Phi_{\mathrm{PS}} \tag{4.11}$$

From these three measurements, a direct comparison can now be drawn from the measurement of the phase screen using both PD/FPS and the SHWFS:

$$\Phi_3 - \Phi_1 = \Phi_{\mathrm{PS}} = \Phi_2 \tag{4.12}$$

Therefore a useful metric in the context of this paper is

$$\Phi_{\mathrm{Res}} = \Phi_3 - \Phi_1 - \Phi_2 \tag{4.13}$$

which quantifies the quality of the focal plane wavefront estimation with respect to the SHWFS measured wavefront. We consider this approach reasonable if the SHWFS is providing an accurate measurement of the wavefront induced by the phase screen. Furthermore, the number of modes estimated in the modal basis of the focal plane wavefront must not greatly exceed the sensing resolution of the SHWFS; we discuss this concept further in Section 4.2.4.

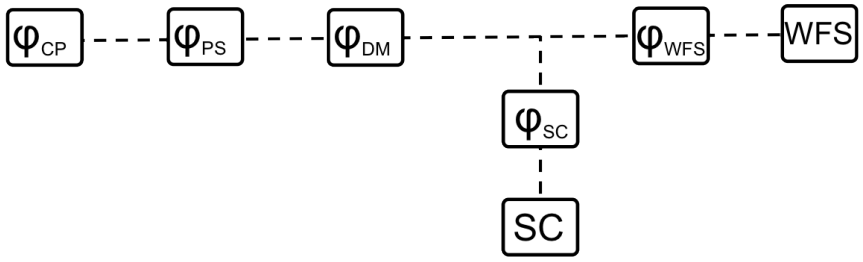

Figure 4.10: Diagram tracking the phase contributions of the common, phase screen, WFS and science camera paths. In this work we aim to measure and compare Φ_{PS} using the SHWFS, Phase Diversity and Focal Plane Sharpening.

Mitigation of the PSF artifacts

We note that estimating more than 4 radial orders of Zernike modes (i.e. > 2 diffraction rings of the PSF) introduces undesired wavefront estimations of the uncorrected sinusoidal interference effects introduced by the surface of the DM (the over/under intensity PSF features discussed in Section 4.2.2, also see Figure 4.7). A direct result of this effect is that an NCPA estimation of Φ_1 and its correction to the PSF will actually *degrade* the Strehl ratio of the closed loop PSF (from 88% to 85%) if 12 radial orders of Zernike modes are estimated; when the same correction is applied from the estimation of 4 radial orders the Strehl is *increased* from 88% to 90%. The

estimate of Φ_1 from Phase Diversity, along with the NCPA corrected PSF is shown in Figure 4.11. The three images used in this estimation were +/-λ out of focus and in-focus (and the object was estimated); the reasoning for the use of these particular parameters is discussed in Section 4.2.3.

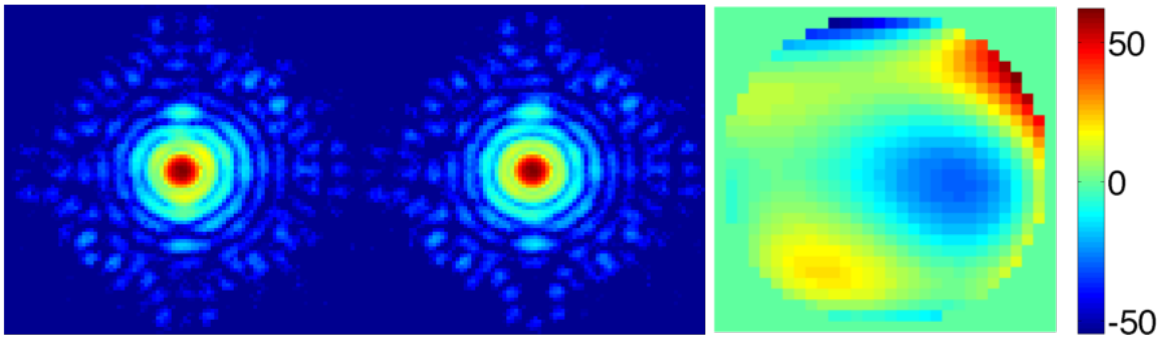

Figure 4.11: Left: closed loop PSFs before and after the correction of the NCPA (shown in log scale), where the correction was applied by updating the closed loop system with a reference vector representative of the phase shown above. The Strehl ratios before and after correction are 88.6% and 90.1%, respectively. Right: NCPA phase as measured by Phase Diversity with no phase screen in the common path; the WFE is 16 nm RMS.

In the presence of the phase screen these over/under intensity features in the PSF are dominated by the phase screen aberrations and are not visibly apparent in Figure 4.7. However an estimate of many more radial orders will inherently contain these undesired effects. Nonetheless, when the phase screen is in the optical path more than 4 radial orders of Zernike modes must be estimated because (i) we wish to compare the estimated wavefront aberration of the phase screen with that of the SHWFS, a device which in our system uses 29 subapertures to sample the wavefront and is therefore capable of measuring more than 4 radial orders of Zernike modes; and (ii) aliasing effects are mitigated when the estimated modal set contains more elements than are actually being corrected for. For these reasons, when the phase screen is in the optical path we choose to estimate at minimum 12 radial orders of Zernikes modes in order to determine our well-functioning set of Phase Diversity parameters. The highest correctable radial order of Zernike modes for 11 actuators across the pupil is 10, therefore by using 12 radial orders we can eliminate most errors associated with aliasing.

Choice of diversity and object

As previously discussed, Phase Diversity requires images subject to some know wavefront aberration, which is typically taken to be focus (Gonsalves, 1982; Paxman et al., 1992; Jolissaint et al., 2012, for example). We wish to briefly address the quality of wavefront estimation as a function of focus diversity magnitude, number of images, and whether or not the object is assumed to be a point source. The scope of this assessment can encompass many forms of exploration and for the sake of this work we provide a very limited determination of an ideal scenario. The following sequence of steps represents how we determined a useful set of Phase Diversity parameters (i.e. diversities, number of images and treatment of the object).

First, a single diversity image with +200 nm RMS focus was used to estimate the phase in question, assuming the object is a point source; this technique is also known as *phase-diverse phase retrieval* (Ellerbroek et al., 1997) and was the same method used to determine the Hubble Space Telescope aberrations (Roddier & Roddier, 1991, 1993; Fienup et al., 1993). At the wavelength of our system, this diversity amplitude is $\sim$1 wave peak-to-valley (P-V), which is within the recommended $\lambda \pm 1/2\lambda$ (Mugnier et al. 2008, see also Meynadier et al. 1999). Using these Phase Diversity parameters, Φ_3 was estimated at the focal plane using 12 radial orders of Zernike Polynomials (as discussed in Section 4.2.3). Prior to this, the phase screen was inserted in the common path and Φ_2 was measured. Using this information and Φ_1 from Section 4.2.3, Φ_{Res} (see Eq. 4.12) was determined to be $\sim$ 47 nm RMS; all three wavefronts from this scenario are shown in Figure 4.12.

Using the same procedure, we determined the estimated wavefront residual, Φ_{Res} when altering the +200 nm RMS focus and re-estimating Φ_3 (Φ_1 was kept from the previous calculation and will be adopted for all future calculations of Φ_{Res} for consistency). Extending the diversity $>$ 200 nm RMS resulted in a degradation of the estimation (in part due to the loss in signal-to-noise as the intensity spreads to larger λ/D) and therefore we chose only to explore smaller diversities. Repeating the calculation of Φ_{Res} for +100 nm RMS focus diversity also produced a significantly worse result ($\Phi_{\text{Res}} \sim 86$ nm RMS); therefore we explored a range of diversities between 100 and 200 nm RMS that yielded the lowest Φ_{Res}, which we found to be +175 nm RMS focus (with $\Phi_{\text{Res}} \sim 41$ nm RMS).

We also wished to try and improve the estimation by including multiple diversity images (as was first suggested by Paxman et al. 1992). We consider a diversity vector

of [0 and +175] nm RMS focus, where each element in the vector represents an image with a different amount of diversity. The residual WFE, Φ_{Res} is found to be significantly worse (148 nm RMS); this result was also shown in simulation (Lamb et al., 2016a) when estimating the phase with *both* an assumed object and including an in-focus image. Therefore the in-focus image was changed to -175 nm RMS focus, and the result improved significantly ($\Phi_{\text{Res}} \sim 35$ nm RMS). We now consider the inclusion of object estimation (instead of assuming a point source). Section 4.1 showed that if the object is estimated then an in-focus image must be used as one of the images. Therefore we consider a diversity vector of [-175 0 +175] nm RMS focus, which results in $\Phi_{\text{Res}} \sim 33$ nm RMS. This set of diversity parameters gives the best phase estimate from our parameter set and no manipulation (i.e. increase in the number of images) improved the results; Table 4.4 summarizes the results. For the remainder of this work we use this set of parameters with Phase Diversity. Figure 4.13 shows the diversity images (degraded to Nyquist sampling for ease of computation in the algorithm) for the cases of no phase screen (top), synthetic images used in the algorithm (middle) and with the phase screen (bottom).

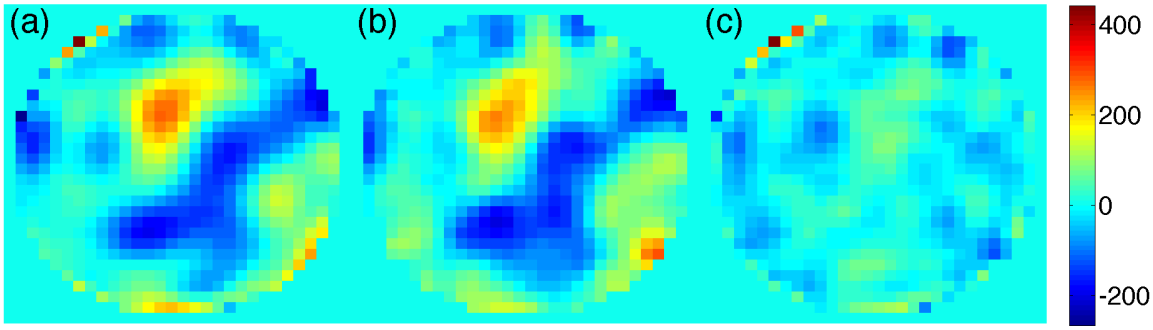

Figure 4.12: (a) - A sample determination of Φ_{Res} (see Eq. 4.12), where both wavefronts (Phi_1 and Phi_2) are estimated with Phase Diversity using a single image with +200 nm RMS focus (assuming the object is a point source); the wavefront error is 116 nm RMS. (b) - The wavefront as measured by the SHWFS (Φ_2); the wavefront error is 100 nm RMS. (c) - The residual between the two, measured to be 47 nm RMS. This example is also shown in the first row of Table 4.4.

Table 4.4: Estimate of the phase screen wavefront using Phase Diversity with different diversities.

Diversity Vector* (nm RMS focus)	Object Estimated?	Φ_{Res} (Eq. 4.13) (nm RMS WFE)
[200]	no	47
[100]	no	86
[175]	no	41
[0 175]	no	148
[-175 175]	no	35
[-175 0 175]	yes	33

*Each component represents a diversity image (0 is in-focus).

4.2.4 Phase screen estimation and correction results

Determination of the phase screen wavefront

In the context of Eq. 4.13, Phase Diversity and Focal Plane Sharpening are used to derive Φ_3 in the presence of the phase screen, and Φ_{Res} is determined using the Φ_1 and Φ_2 values derived in Sections 4.2.3 and 4.2.3, respectively. In both estimation methods, multiple iterations are explored in an attempt to quantify the best performing scenario. The results are summarized in Table 4.5.

The SHWFS is capable of measuring 30 radial orders (29 subapertures span the pupil) while the DM is only capable of correcting 10 (see 4.2.3). Therefore we wish to estimate as many radial orders as possible with Phase Diversity, up to a maximum of 30 to stay consistent with the SHWFS. However, increasing the estimated modes beyond 20 becomes impractical for two reasons: (i) the time required to make the estimation and correction approaches 10 minutes; and (ii) there is not enough focal plane information available to provide a reliable estimation of the higher order modes without being dominated by noise. Both of these issues could be mitigated by using both faster computers and higher signal-to-noise images (or a higher quality detector), but this remains beyond the scope of this work. Therefore we initially estimate 18 radial orders of Zernike Modes with Phase Diversity when estimating Φ_3. In addition, we perform a second iteration of Phase Diversity using 20 radial orders (shown as row 4 in Table 4.5). Examples of the residual wavefront (Φ_{PS}) for the first four scenarios of Table 4.5 are shown in Figure 4.14.

Focal Plane Sharpening limits the maximum number of correctable radial orders to that which the DM is capable of correcting. Again, this is due to the nature of the algorithm, which explores a basis-set by means of the DM surface projection (in

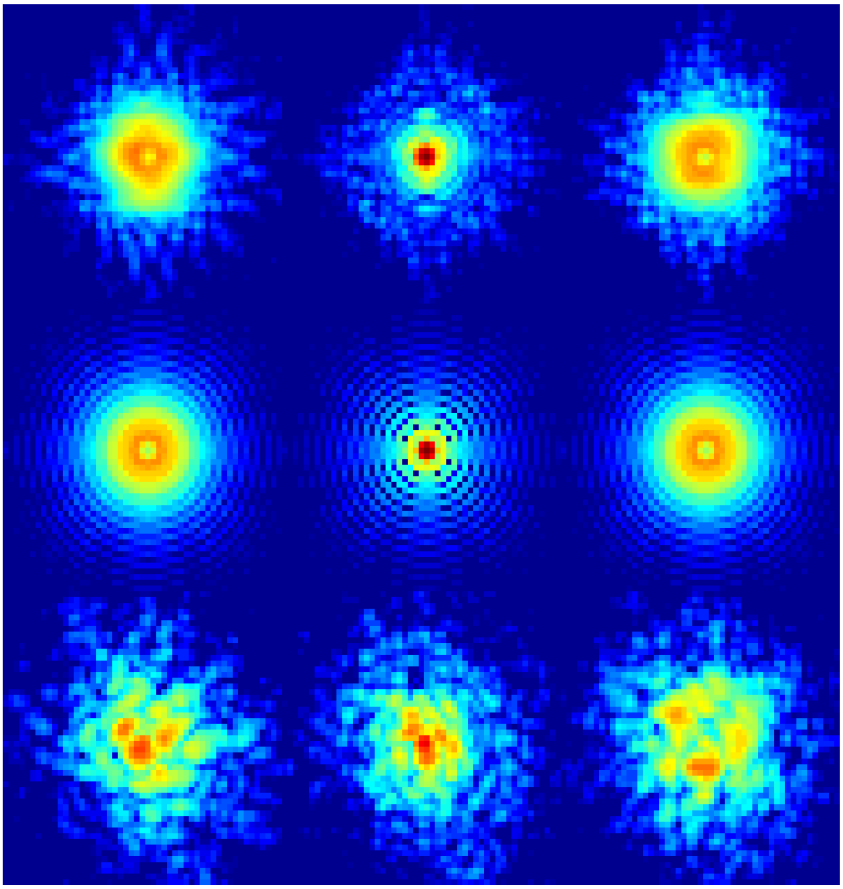

Figure 4.13: Images used with Phase Diversity for the phase estimation in this work (shown in log scale). The top row displays three images at -175, 0 and 175 nm RMS focus diversity. The middle row shows the synthetic diversity images subject to the same diversity. The bottom row displays the same diversity images with the phase screen inserted into the path.

this case via offset slopes with the SHWFS). Here we assess the performance of Focal Plane Sharpening for both 8 and 10 radial orders, which allow correction up to the fourth and fifth diffraction rings, respectively. The typical number of iterations before convergence using 8 radial orders of correction is ∼750 while 10 radial orders is ∼1300. In the context of our AO system, 1300 iterations (with 5 images averaged at each iteration, see Section 4.2.2) takes about thirty minutes. When the algorithm converges the corrected Zernike coefficients and corrected PSF are recorded; the coefficients are expressed in a wavefront, Φ_3, which can be compared with the phase screen measurement of the SHWFS (Φ_2).

Table 4.5: Estimation of the phase screen wavefront using phase diversity and focal plane sharpening

First iteration method	Estim. modes (rad. ord.)	Second iteration method	Estim. modes (rad. ord.)	Figure label	Φ_{Res} (nm RMS)	Corrected PSF Strehl
PD	18	-	-	4.14-(a)	27.1	79.2
PD	18	PD	18	4.14-(b)	25.7	80.8
PD*	18	PD*	18	4.14-(c)	25.7	81.8
PD	18	PD	20	4.14-(d)	26.4	82.6
FPS	8	-	-	4.15-(a)	39.4	74.9
FPS	8	FPS	8	4.15-(b)	40.3	74.3
FPS*	8	FPS*	8	4.15-(c)	40.2	75.7
PD	18	FPS	10	4.15-(d)	34.0	76.7

*This case is a third iteration (starting from the PSF of the last iteration).

PSF correction

Strehl ratio validation: To ensure the calculation of our Strehl ratios yield reasonable results a synthetic and actual PSF shown in Figure 4.16 for the phase estimated (Φ_3) with Phase Diversity in the first row of Table 4.5. The synthetic PSF was constructed assuming a uniform, circular pupil, a pixel sampling of 2.22 pixels/FWHM, and using the aforementioned estimate of Φ_3. The actual PSF was obtained by transforming Φ_3 to a reference slope vector and updating the reference slopes of the closed loop, aberrated AO system. Their Strehl ratios are computed to be 37.6% for the model PSF and 36.4% for the actual PSF (following the method outlined in Section 4.2.2). This result shows good agreement and we therefore use this method for the calculation of all Strehl ratios in this work.

Corrected PSFs: As previously discussed, the correction for the Phase Diversity estimate is applied by converting the estimated wavefront to reference slopes and feeding them as offsets to the closed loop AO system. The corrected images from four different cases of Phase Diversity are shown in Figure 4.17. Focal Plane Sharpening is slightly different in the sense that the correction is 'active', and when the algorithm converges the set of Zernike modes is recorded and subsequently converted to reference slopes. Updating the loop with these reference slopes yields the corrected PSFs shown in Figure 4.18 (following the same format as the Phase Diversity correted PSFs). The

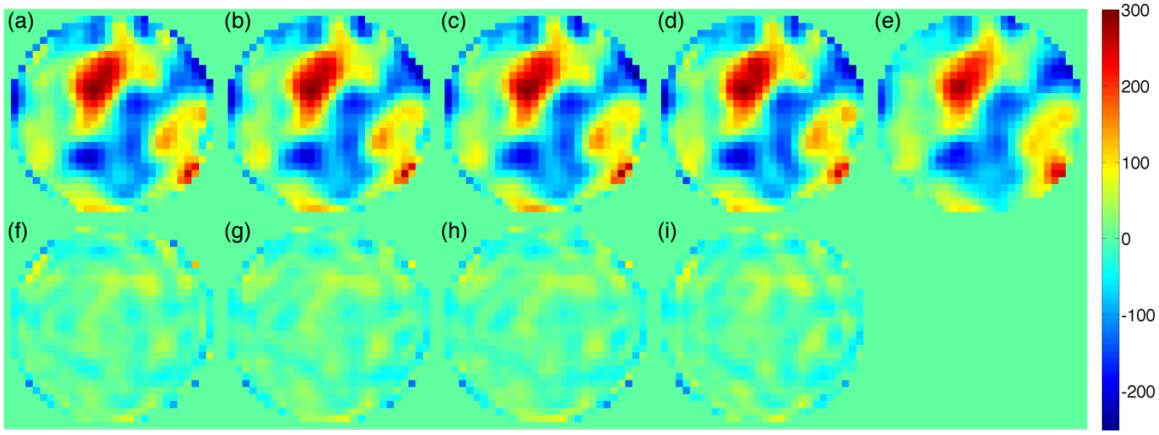

Figure 4.14: Phase Diversity estimates of Φ_{PS} (Eq. 4.12), shown in panels (a) through (d) on a nm scale; the description of these estimates is shown in Table 4.5 where each case is identified in column 5. Shown in panel (e) is Φ_{PS} as measured by the SHWFS for comparison. The residual between the Phase Diversity estimates and SHWFS measurement (Φ_{Res}) are shown in panels (f) through (i); the rms WFE of these residuals are shown in Table 4.5 in column 6.

Strehl ratios of all corrected images (Phase Diversity and Focal Plane Sharpening) are summarized in the last column of Table 4.5.

4.2.5 Experimental NFIRAOS NCPA discussion

Phase Diversity

The lowest residual between the Phase Diversity and SHWFS measurement of the phase screen (Φ_{Res}) is found by a second iteration of Phase Diversity, (as indicated in Table 4.5). Performing a third iteration yielded the same residual, and we conclude there is no major benefit (in terms of wavefront estimation) to include more than two iterations of Phase Diversity. It is worth noting that the difference between the four different estimations is 1.4 nm RMS and could be smaller than the measurement error, thereby yielding the same result for all four cases. Given that the sensitivity of the SHWFS is 30 radial orders (as discussed in Section 4.2.4) and that we are estimating at most 20 radial orders with Phase Diversity, we expect the magnitude of Φ_{Res} could be reduced if one were capable of sensing 30 radial orders with Phase Diversity. However, the difference in RMS WFE between the full measured SHWFS and one that has been projected onto 20 radial orders of Zernike modes is < 1 nm. This leads us to conclude the majority of Φ_{Res} is indeed limited to the ability of Phase

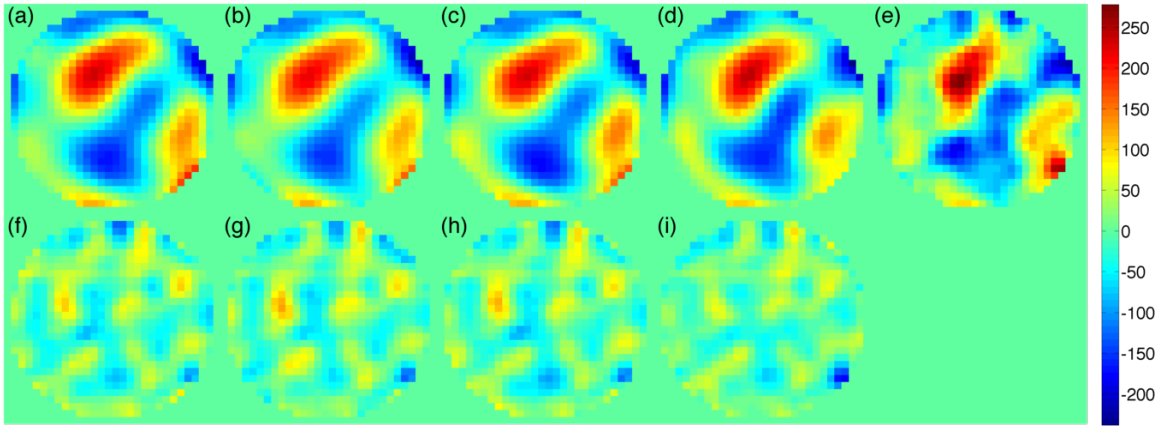

Figure 4.15: Focal Plane Sharpening estimates of Φ_{PS} (Eq. 4.12), identical to Figure 4.14 with the exeption that Φ_{PS} in panels (a), (b), and (c) are estimated from 8 radial orders while (d) is from 10 radial orders. Panel (e) is the SHWFS measurement of Φ_{PS} and panels (f), (g), (h) and (i) are the residuals between (a)/(b)/(c)/(d) and (e).

Diversity to estimate the first 20 radial orders of Zernike modes, and could possibly be improved by increasing the signal to noise of the diversity images (either through increased exposure time, a higher quality detector, or perhaps an increase in diversity strength).

Nonetheless, the Strehl ratio of the image corrected in closed loop with the SHWFS *with* the NCPA correction found in Section 4.2.3 is 85.9%, which through the Marechal approximation yields 40.5 nm RMS of WFE. If we sum (in quadrature) this WFE with that of the best Phase Diversity estimate (Φ_{Res} = 25.7 nm RMS), we obtain 48.0 nm RMS WFE (and therefore a Strehl ratio of 80.9% at 655 nm throught the Maréchal approximation). Indeed, as shown in Table 4.5 the actual measured Strehl in this scenario is 80.8%, which shows the consistency between the measured phase screen wavefront and the correction applied through Phase Diversity. Interestingly, the Strehl ratio appeared to improve for every scenario where we used an additional iteration of Phase Diversity; this does not follow the trend of Φ_{Res}, which was lowest after just the second iteration. However, the uncertainty in both Φ_{Res} and Strehl ratio may encompass the range of variation seen here. We can conclude that one iteration of Phase Diversity can reduce the WFE of a system subject to NFIRAOS-like NCPA from 104 to 48.7 nm RMS; this is not quite as high as the 40.5 nm RMS of the SHWFS, but a very promising improvement given the only hardware needed for this measurement was the science camera.

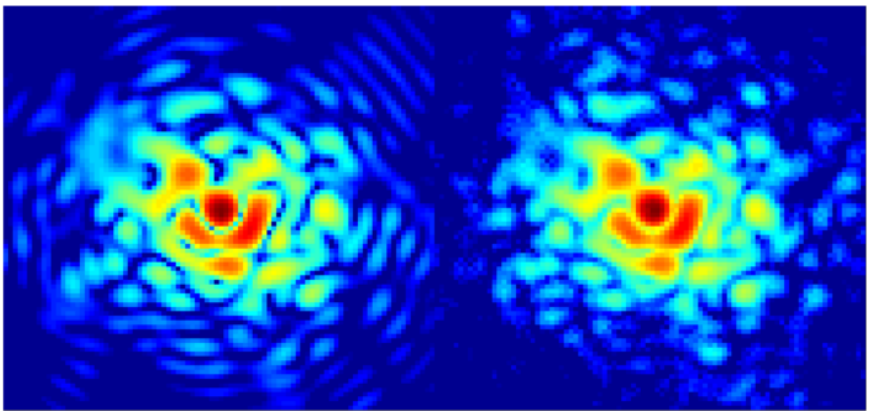

Figure 4.16: Demonstration of Strehl calculation on a synthetic and real image. Left panel: synthetic PSF of the aberrated system as seen at the focal plane (shown in log scale). The PSF was generated using the phase estimated from Phase Diversity and the known parameters of the system. Right panel: actual PSF measured at the focal plane after updating the closed loop with the Phase Diversity reference slopes (also shown in log scale). The Strehl ratio of both images was computed as described in Section 4.2.2 and found to be 37.6% and 36.4%, respectively.

Focal Plane Sharpening

In terms of Focal Plane Sharpening, the lowest residual wavefront (Φ_{Res}) was achieved after the second iteration where 10 radial orders were estimated (shown as the last column in Table 4.5). A second iteration on a corrected image did not improve the residual wavefront when estimating only 8 radial orders. Similarly, a third iteration further did not improve the residual wavefront and the result remained almost identical to the previous iteration. The Strehl ratios from the corrected images were all very similar (see the last column of Table 4.5), and the highest Strehl was found when estimating 10 radial orders. This improvement is not surprising given the correctable region should encompass 10 radial orders, as discussed in Section 4.2.3. To get a better sense of how well the Phase Diversity and Focal Plane Sharpening are quantifying the phase screen, the Zernike modes for the first 10 radial orders are shown in Figure 4.19. The black curve representing the SHWFS measurement was created by projecting Φ_2 onto the first 10 radial orders of Zernike modes. The root sum squared value of the residual between the Phase Diversity modes and the SHWFS modes is 20.8 nm RMS while the Focal Plane Sharpening equivalent is 26.0 nm RMS, further exemplifying that Focal Plane Sharpening is not quantifying the wavefront to the same effectiveness as Phase Diversity within this scenario.

Our interpretation of this discrepancy is that when creating an individual shape

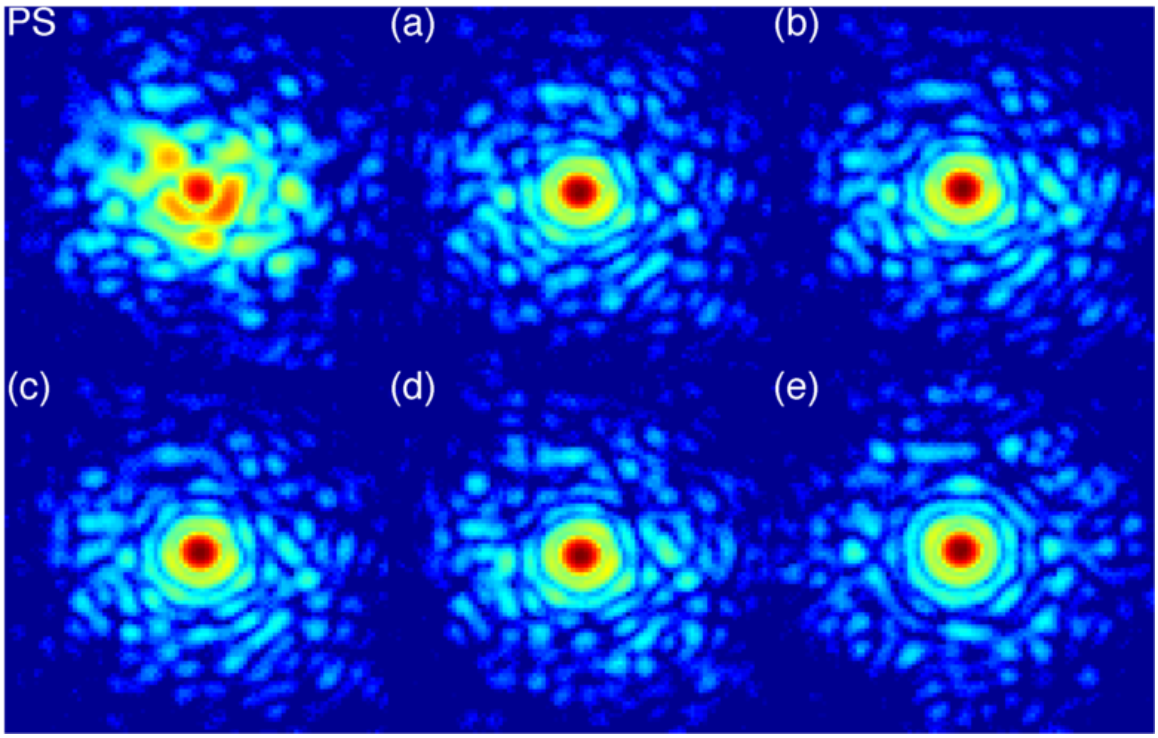

Figure 4.17: Uncorrected PSF (first panel) and Phase Diversity corrected PSFs (panels a through d, as described according to column 5 of Table 4.5). Also shown is the PSF corrected with the SHWFS in closed loop (compensated for the NCPA estimated with Phase Diversity Φ_1; see Section 4.2.3) in panel (e) for comparison (with Strehl ratio of 85.9%). All images shown in log scale.

during an iteration of Focal Plane Sharpening, the system will be limited to the ability of the AO system to close the loop on that shape. Any closed loop errors (fitting, aliasing, etc.) will propagate with each iteration of the Focal Plane Sharpening algorithm and if they are significant, they will affect the performance of the method. Operating in open-loop will bypass these closed loop errors, but will in turn subject the system to the DM 'creep' (see Section 4.2.2); which has a significant impact on timescales of minutes (i.e. on the same time scales as Focal Plane Sharpening, which can take up to 30 minutes on our bench). Therefore Focal Plane Sharpening is perhaps not ideally suited to our bench, but may be considered useful in other scenarios where either the closed loop errors are sufficiently small, or the DM is more stable in open loop control. Given the fact that Focal Plane Sharpening does not rely on a model of the PSF (unlike our Phase Diversity algorithm), and that it is much easier to implement than Phase Diversity, it remains a focal plane WFS tool well worth exploring.

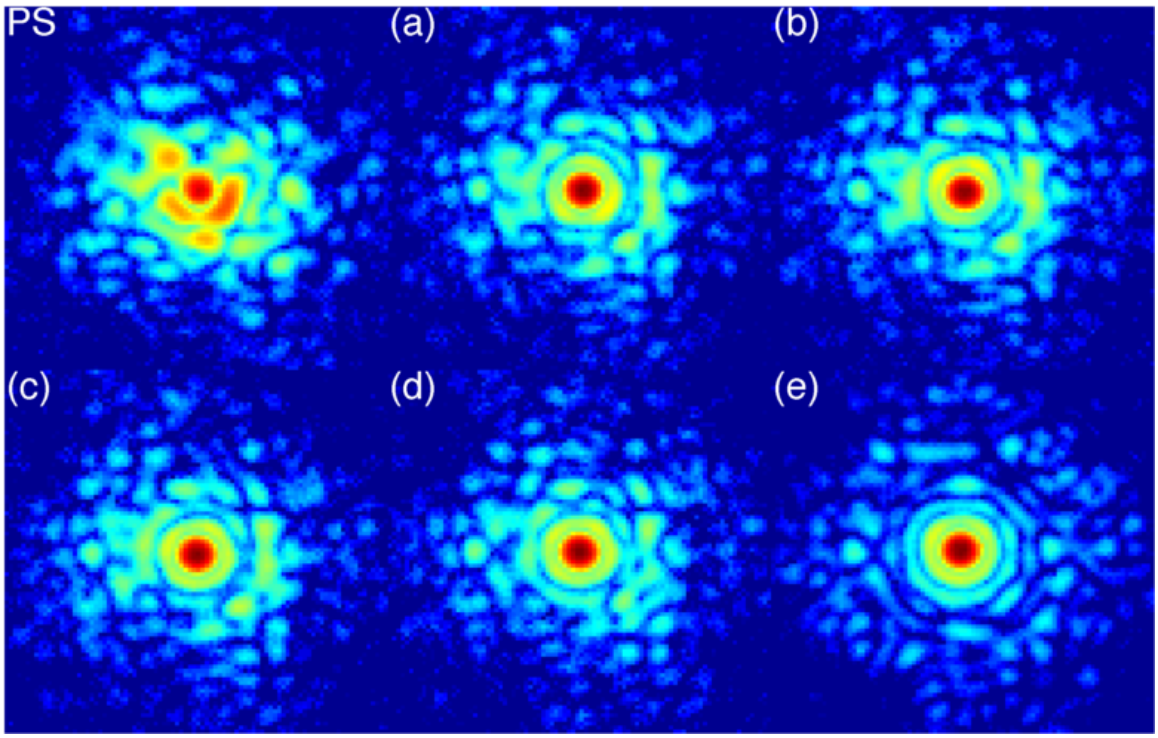

Figure 4.18: Identical to Figure 4.17, except the panels (a) through (d) are corrected with Focal Plane Sharpening. Again, the details pertaining to each of these panels is described in Table 4.5.

Conclusions

In this Section, we compare the ability of two focal plane wavefront sensing techniques to estimate and correct NFIRAOS-like non-common path aberrations on an experimental bench. Using the SHWFS as a reference wavefront sensor, we conclude the following:

- Between the two methods, we found that Phase Diversity provides the best PSF correction to the phase screen, improving the Strehl ratio from ∼36% to ∼81%; Focal Plane Sharpening improves the Strehl to ∼75% while the SHWFS can achieve a Strehl of ∼ 85% in closed loop after appling an NCPA correction. It is worth noting that the SHWFS represents the ideal correction and could never realistically be applied as an NCPA estimator.

- When examining the first 10 radial orders (the maximum correctable modes by the DM), the wavefront of the phase screen (as measured by the SHWFS) is better characterized by Phase Diversity than Focal Plane Sharpening. We

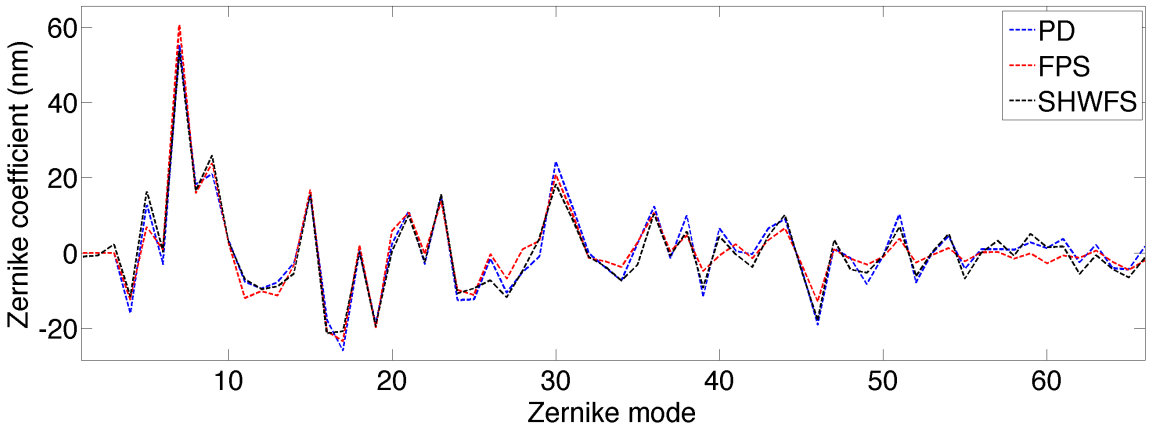

Figure 4.19: The first 10 radial orders of Zernike modes quantified by Phase Diversity (blue), Focal Plane Sharpening (red) and the SHWFS (black). Visually it can be seen that Phase Diversity shows a better estimation of the SHWFS measured wavefront than Focal Plane Sharpening. Quantitatively the root sum squared value of the difference between the Phase Diversity modes and the SHWFS modes is 20.8 nm RMS, while that of Focal Plane Sharpening is 26.0 nm RMS.

consider that Focal Plane Sharpening may work better in an AO system with smaller residual AO loop errors or in a reliable open loop scenario where the DM does not significantly drift in shape over time. Given the fact that Focal Plane Sharpening is not model dependent, unlike the Phase Diversity algorithm used here, we believe Focal Plane Sharpening should be explored for instruments to determine wither this simple approach would meet NCPA estimation requirements.

- In the context of correcting the NFIRAOS NCPA, we recommend two iterations of Phase Diversity based on the results of this work. In addition, we also find that multiple diverse images improve the estimation, where each is subject to at minimum *one wave* λ P-V focus error.

4.3 Characterizing the NCPA on two AO systems: RAVEN and HeNOS

In this Section, the NCPA techniques described in Sections 4.1 and 4.2 are applied to two real AO systems. Unlike most of this work, it is not based on a publication and simply serves to show the application of the two techniques. Both examples shown

here were performed in the nascense of the techniques and more complex applications are explored in Chapter 5, both in simulation and with real data.

4.3.1 RAVEN NCPA correction

The first system to which we applied NCPA corrections was RAVEN (see Section 3 for a detailed description of the instrument). At the time of the second engineering run (June 2014), Focal Plane Sharpening was robust and had been demonstrated in both simulation and on our experimental bench, however it was still unproven on an on-sky AO system. Phase Diversity, however was only successfully demonstrated in simulation up to this point. As such, only Focal Plane Sharpening was applied to RAVEN to correct its NCPA. It should be noted that a relatively short window of time was available during this engineering run to explore NCPA correction by this technique, therefore only minimal data was acquired showing the results of this correction. After roughly two days of on and off trouble shooting while at the summit of Mauna Kea, the technique was shown to work on both science arms of RAVEN. The first science arm contained very minimal NCPA and essentially no correction was achieved. The second arm however, contained significant NCPA and Focal Plane Sharpening was able to improve the Strehl ratio of the calibration source from 50% to 79% (see Figure 4.20). As a result, the delivered performance of the the second science arm was significantly increased. Therefore Focal Plane Sharpening was run multiple times per night, every night, for the remainder of the second engineering run and for all of the third engineering run. These runs included three different science programs, all of which benefitted from the correction provided by Focal Plane Sharpening.

4.3.2 HeNOS NCPA characterization

The multi-conjugate adaptive optics (MCAO) system NFIRAOS for the TMT will deliver an AO-corrected beam over a 30" field of view at first light. The system will be constructed in Victoria at NRC Herzberg. In support of this flagship project, a test bench has been constructed to mimic a scaled-down version of the instrument to develop the appropriate techniques and calibrations needed for the development of the actual instrument. The test bench is known as HeNOS (Herzberg Nfiraos Optical Simulator; Rosensteiner et al. 2016) and employs four fiber sources to simulate the laser guide stars (LGS) required for the operation in MCAO mode. Interestingly, temporal variations of the NCPA over the course of the day appears to be an issue;

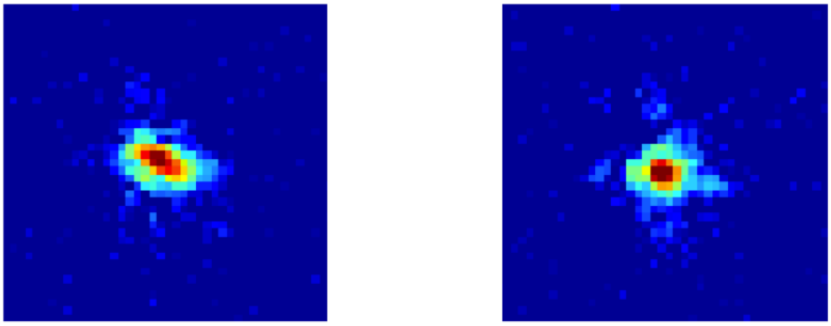

Figure 4.20: The second science arm PSF of RAVEN before and after NCPA correction using Focal Plane Sharpening. The images are 1"x1" in size. The Strehl ratio improves from 50% to 79% and signicantly enhances the throughput of this science arm. This technique was used to calibrate the NCPA on RAVEN several times a night, every night for the second and third engineering runs.

if the AO system is held in closed loop throughout the course of the day there is shown to be a significant 'drift' in the PSF - mainly in the form of focus. The opto-mechanics of the AO system are based on a set of four rods, which hold each optical element in place through a hole at each corner of each mount. It was proposed that the temperature variations within the lab, due to a lack of any form of thermal stabilizer (i.e. air conditioning, etc.) would cause these rods to expand when the lab was active, thereby shifting an optical element in the x/y *and* z planes. A shift of an optical element in the z plane in the non-common path will cause the AO system to exhibit focus on the closed loop PSF. Therefore it is desirable to quantify the NCPA of each LGS as a function of time, while simultaneously tracking the temperature of the bench. This will help establish a relation between the temperature and individual Zernike modes of the NCPA and perhaps lead to a calibration method to alleviate its effect.

Here I demonstrate in and out of focus images of *each* LGS used with Phase Diversity to estimate the NCPA every 15 minutes over the course of 14 hours. The out of focus images were acquired by providing focus offset slopes of 200 nm RMS WFE to the AO system in closed loop (with a SHWFS). Simultaneously, I installed a separate temperature sensor located midway between the WFS and science camera arm (therefore the location of where we expect the NCPA to originate) to track

temperature changes at each timestamp of the Phase Diversity measurements. Figure 4.21 displays the actual closed loop PSFs of each LGS seen on the science camera (top) and the reconstructed PSFs for each LGS using the Phase Diversity estimates (bottom). This figure demonstrates the ability of the algorithm to reasonably estimate the main features of the PSF.

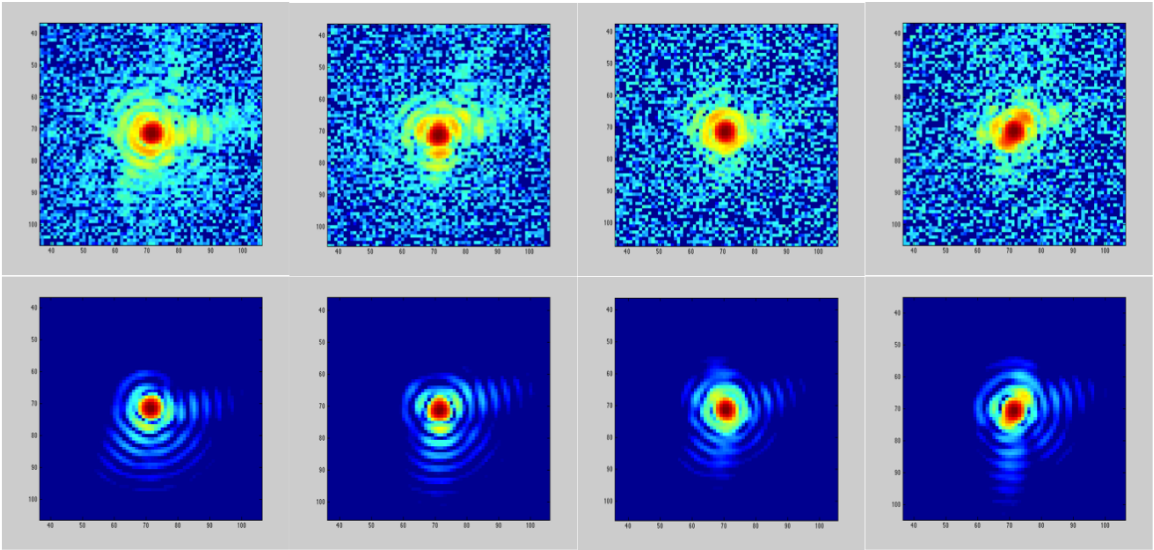

Figure 4.21: Top: recorded PSFs of the four LGS during closed loop of the AO system. Bottom: reconstructed PSFs from the Phase Diversity estimates of each LGS in/out of focus image pair.

Figure 4.22 shows the results from tracking the NCPA over the course of 14 hours using Phase Diversity to estimate the first 36 Zernike modes on one of the LGS (this was done for each LGS, but only one is shown here). The top plot in the Figure shows Z_4 (focus) to Z_8 (coma 2) measurements (in absolute value of nm RMS) as a function of time; at approximately 4 am a strong variation in Focus is observed, changing in magnitude by $\sim$ 20 nm RMS. This feature is in very good agreement with the temperature 'drop' seen in the middle plot, which also occurs at 4 am. We confirmed that the building's ventilation system turns on at exactly this time. Therefore temperature variations such as these significantly impact the performance of the AO system, and either temperature stabilization or post-calibration is required to mitigate this effect. Currently, an air conditioning unit has been installed and preliminary results have shown a vast improvement in bench temperature stability, and we hope this will significantly mitigate this effect. We find that the higher order NCPA modes seem to be unaffected by this temperature variation as observed in

the bottom plot of Figure 4.22, where the mean of each mode (box magnitude) and standard deviation (error bar) over the entire 14 hours of measurements is shown. It is worth noting the other three LGS show the same general trend where Focus is the pre-dominate NCPA mode to show variation, followed by astigmatism. This makes sense considering focus and astigmatism are errors directly resulting from an x/y/z displacement of an optical element in the non-common path.

4.3.3 Discussion

Both Focal Plane Sharpening and Phase Diversity have been demonstrated with two real AO systems to characterize the NCPA. In this Section, these two techniques were demonstrated as simple focal plane wavefront sensors, and it is worthwhile to investigate their capabilities for larger magnitude telescope applications. In Chapter 5 the techniques are explored first in simulation, then with on-sky data to characterize two significant problems with two large telescopes: VLT and Keck.

4.4 Summary and Conclusions

This chapter has summarized two independent methods used to characterize and correct the NCPA on AO systems: Phase Diversity and Focal Plane Sharpening. The methods were shown in Section 4.1 to be effective in the characterization of NCPA for a NFIRAOS-like system under the context of simulation. Section 4.2 extended these two techniques to an experimental bench, where they were also proven to be efficient in the characterization and correction of NFIRAOS-like NCPA in the presence of a custom made phase screen. Finally, Section 4.3 successfully demonstrated these techniques on two real AO systems: RAVEN and HeNOS. The remainder of this thesis focuses on the application of these two techniques to characterize two current major problems affiliated with the VLT and Keck AO systems.

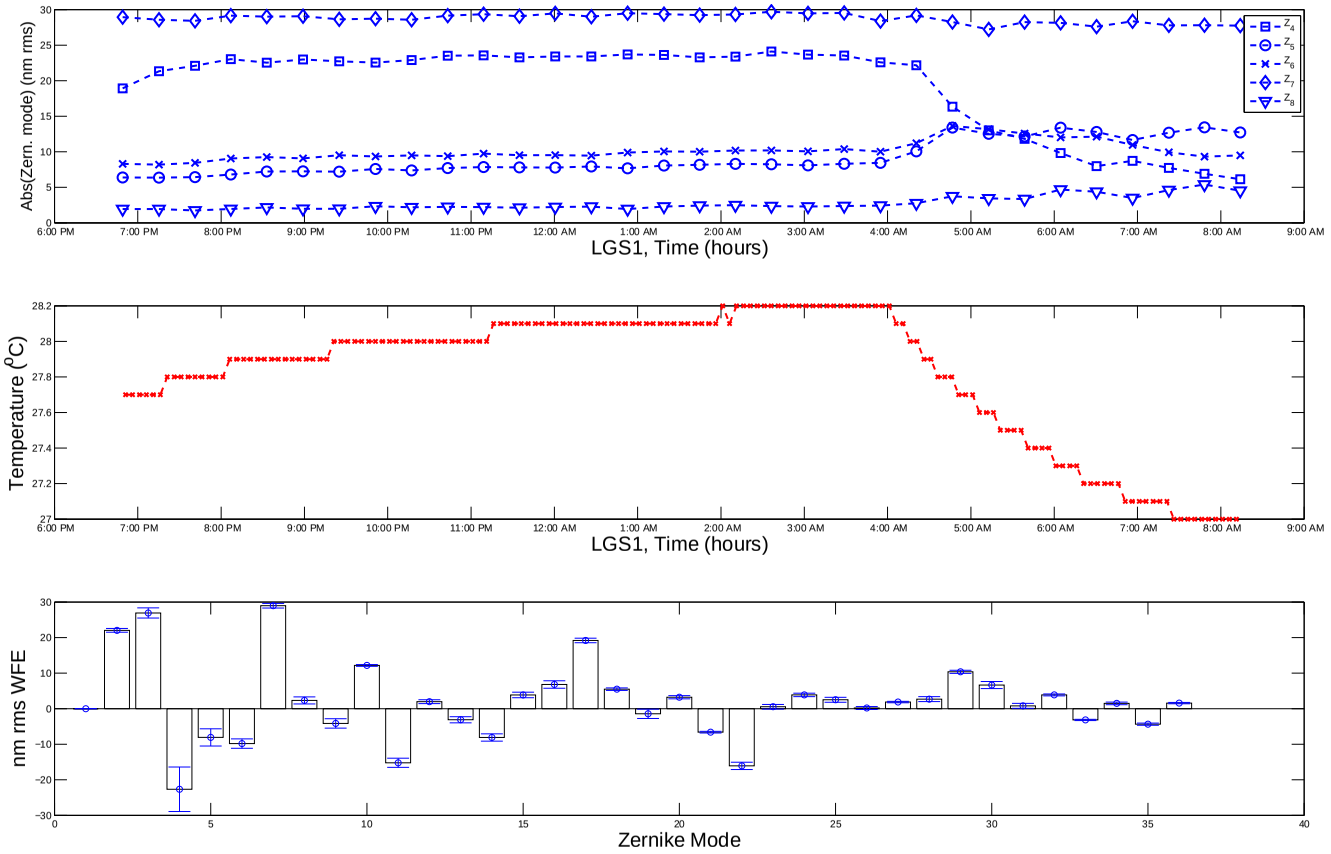

Figure 4.22: Top: LGS1 Phase Diversity estimates of Zernike modes Z_4-Z_8 as a function of time, over the course of 14 hours. At 4 am, a strong NCPA variation is observed in Z_4 (focus). Middle: temperature sensor measurements over time, showing that at 4 am a strong drop in temperature is observed, coinciding exactly with when the focus NCPA start to show variation. Upon further investigation this time coincides with when the ventilation system is turned on at NRC Herzberg. Bottom: the mean (box height) and standard deviation (error bars) of each Zernike mode over the course of the 14 hour data sequence. The strongest variation (i.e. largest standard deviation) is seen by focus and astigmatism (Z_{4-6}), which makes sense considering these two modes can be caused by an x/y/z shift of an optical element in the non-common path.

Chapter 5

Applications of Phase Diversity and Focal Plane Sharpening to VLT and Keck

5.1 Introduction

Piston discontinuities in segmented pupils are difficult to quantify when considering traditional AO systems, which originates from the inability of the Shack-Hartmann wavefront sensor to measure differential piston. A prime example of this is the 'low wind effect' (LWE) on the VLT/SPHERE system, where nights with good seeing and a relative lack of wind surprisingly yield focal plane images of poor quality. This effect has been interpreted to be a result from temperature discontinuities across the VLT pupil (Sauvage et al., 2015; Sauvage et al., 2016b). Conceptually these temperature discontinuities are thought to be defined by the secondary mirror spiders, which act as thermal barriers between quadrants (or segments) of the pupil. Airflow simulations of the spiders have been shown to reproduce these thermal effects, and for more information we refer the reader to Sauvage et al. (2016b). Sharp differentials in temperature may translate to a differential piston effect, which is due to the index of refraction of air having a dependency on temperature. The Shack-Hartmann WFS is simply unable to detect differential piston and the resulting PSF reveals features akin to 'Mickey Mouse Ears' (Sauvage et al. 2015, see Figures 5.1 and 5.9); correcting this effect is crucial considering the purpose of SPHERE is to achieve the highest contrast possible, which is clearly contaminated by this effect. The target contrast of

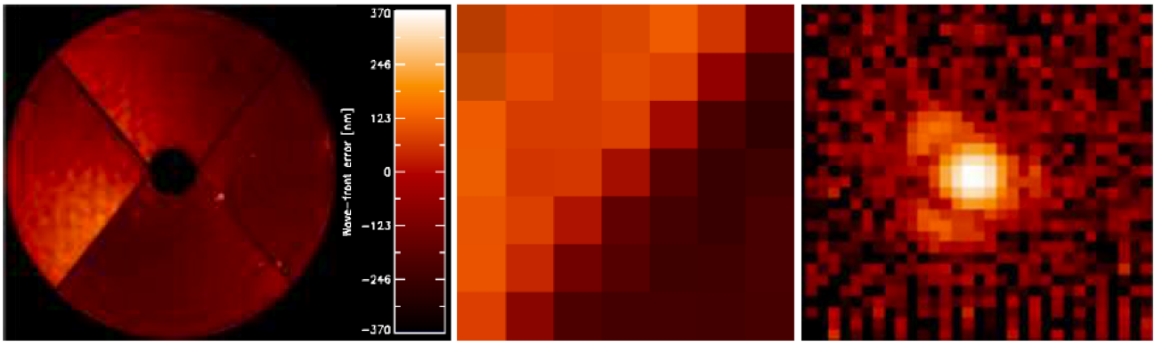

Figure 5.1: Example of phase measured with Zelda (left) during the LWE and its corresponding PSF on the DTTS imager (right).

SPHERE is 10^{-6} at 0.5" (Beuzit et al., 2008), which is achievable if the non-common path aberrations (NCPA) in the system are under 50 nm RMS WFE (wavefront error) (Sauvage et al., 2016b). The internal NCPA of SPHERE were initially quantified at 25 nm RMS (Sauvage et al., 2016a), however this value is thought to have grown to ∼40 nm RMS and will be quantified in the near future (Fusco et al., in prep.). Assuming this latter value to be true, this leaves a maximum of only 30 nm RMS (the quadratic sum) from other contributions such as the LWE to achieve SPHERE's target contrast. The LWE is observed to occur when nights have sub meter per second speeds ($\sim 1/5$ of the nights at Cerro Paranal) and therefore such a method to quantify and correct this effect could be extremely valuable for future SPHERE observations. This effect drives the operation of the observatory to disable the SPHERE instrument and re-organize the observations program, when the conditions are otherwise optimal. Developing the ability to estimate and correct the LWE to within 30 nm RMS is therefore critical for the success of the SPHERE project.

Piston discontinuities also impact the performance of segmented telescopes such as the Keck telescopes. Artifacts of the PSF due to differential piston (and potentially other sources) on the Keck/NIRC2 AO system have been observed and identified as 'low order residual errors' (Rampy et al. 2014; Ragland et al. 2014, see Figure 5.9). These errors typically result in a PSF with a deviation in the first diffraction ring and a reduced Strehl ratio, and are shown to be stable on relatively long time scales (i.e. $>$ 30 minutes; van Dam 2016). Some (but not all) of these errors (i.e. van Dam 2016) arise from the inability of the SHWFS to detect differential piston. Any correction of this effect requires a reliable estimation; applying such a correction will increase the Strehl ratio and allow the AO system to achieve its full potential. Estimating this effect will also provide essential information for PSF reconstruction, which is vital for

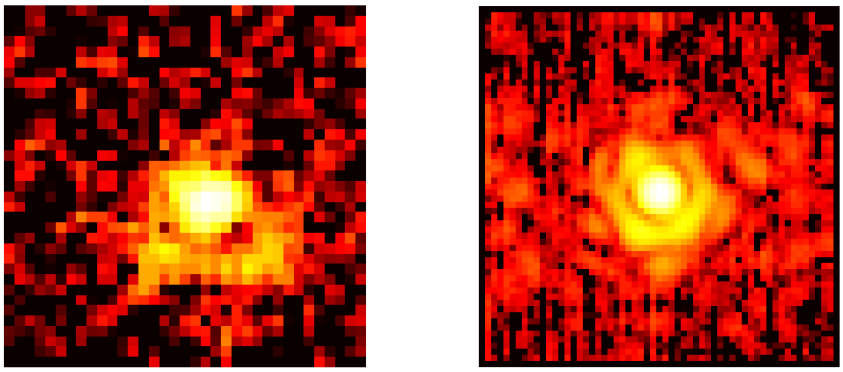

Figure 5.2: Left: An image acquired by the DTTS imager on SPHERE during a night with a strong low wind effect, shown in log-scale (courtesy of J.F. Sauvage). The asymmetric 'ear' like features on the PSF shown here are an example of the PSF contamination experienced throughout the course of the entire night, and restricted use of the instrument. Right: A K-band, short exposure Keck/NIRC2 image (also shown in log-scale) displaying typical features of 'low order residuals', which are persistent throughout the duration of the closed AO loop (courtesy of S. Ragland).

a variety of astronomical applications (Ragland et al., 2016).

These two pupil effects have been investigated using a variety of different approaches. For example, recent studies (see N'Diaye et al. 2016) have explored the use of a Zernike WFS (ZELDA; N'Diaye et al. 2013), capable of detecting these piston variations on VLT/SPHERE (see Figure 5.1). In the case of the Keck low order residuals, the approaches of both the Gerchberg-Saxton algorithm and Phase Diversity have been used to estimate these residuals both in simulation and on-sky (van Dam, 2016; Ragland et al., 2016).

In this Chapter we explore two different methods for estimating these pupil-discontinuity effects for simulated and real data. The first method is the well established approach of Phase Diversity, where images with known diversity are compared to their synthetic counterpart to estimate the phase of an optical system (Gonsalves, 1982). The second method is the technique of Focal Plane Sharpening (FPS; Lamb et al. 2014), where the PSF in the focal plane is optimized using only a deformable mirror. We simulate realistic images on both the VLT/SPHERE system and the Keck/NIRC2 system and investigate the feasibility of these methods to estimate the respective errors in question. We also explore the concept of single image Phase Diversity (also known as Phase Diverse Phase Retrieval Ellerbroek et al. 1997), which could

be very useful in avoiding the evolution of turbulence therefore freezing AO residuals for a set of on-sky images. We then explore the application of these methods to real data with VLT and Keck.

5.2 Estimation methods

5.2.1 Phase Diversity

We employ a Phase Diversity code that follows the formulation of Paxman et al. (1992), where an aberration-only objective function and its gradient are fed through a non-linear optimization algorithm to minimize the quadratic difference between synthetic and observed images. The aberration-only objective function consists of the coefficients of the basis to be estimated (i.e. Zernikes, or other type of basis). The completion criterion is triggered (see Chapter 4) when the quadratic difference between the images is below a tolerance parameter. The synthetic and real data are typically in and out of focus images, although the code can incorporate any number of images or type of diversity. The optimization technique we employ is the well established quasi-Newton Broyden-Fletcher-Goldfarb-Shanno (BFGS) algorithm. The code has the ability to either jointly estimate the object along with the phase, or to just estimate the phase itself and assume the object is known (which we simplify as a point source). This code has been developed as a class for the AO MATLAB software OOMAO (Conan & Correia, 2014); more details of the algorithm is described in Chapter 4. For an overview of the Phase Diversity technique we refer the reader to Mugnier et al. (2006).

5.2.2 Focal Plane Sharpening

The results in this work use a MATLAB based Focal Plane Sharpening code, which has also been developed as a class for OOMAO, and has cross-compatibility with its Phase Diversity counterpart. The algorithm receives the focal plane PSF as input and optimizes on a variety of criteria (chosen by the user) using the Nelder-Mead downhill-simplex method (Lagarias et al., 1998); the input parameters to the optimization method are the basis used to create the PSF (which can be DM influence functions, Zernike Modes, or any combination of modes chosen by the user). This method, along with a description of different criteria choices are explained in more detail in Chapter

4. The results in this work use the following criteria: at each step in the optimization a small region centred on the PSF is extracted and subsequently median-filtered with a 2xFWHM kernel (i.e. two times the number of pixels across the FWHM of the theoretical diffraction limited PSF) to reduce noise; a 2D-Gaussian is fit to this image, from which the amplitude is measured. The amplitude of the fit is the metric that is optimized, changing at each iteration as the set of basis coefficients evolve.

5.3 Estimating the Low Wind Effect on SPHERE in simulation

5.3.1 Basis and simulated images

To estimate the low wind effect on SPHERE we propose a basis roughly defining the pupil plane phase variations that occur at each quadrant of the VLT pupil (see Figure 5.3). The basic principle of our analysis is as follows: estimate the coefficients of this modal basis using both Phase Diversity and focal plane sharpening and assess the performance of each method. The amplitude of the piston/tip/tilt errors we use to artificially produce the LWE are $\sim$ 1200 nm peak-to-valley (PV) WFE and are shown in Figure 5.4 (right); this LWE error is conservatively high, as typical LWE errors are estimated to be in the range of 600-800 nm PV WFE (Sauvage et al., 2015). The objective of this work is to estimate this error to within 30 nm RMS, so in the future SPHERE can correct the error and eliminate the LWE. We adopt a representative NCPA of the SPHERE system, specifically 45 nm RMS WFE following a $1/\nu^2$ power law that is also shown in Figure 5.4. As described in Section 5.1, the magnitude of the SPHERE NCPA are estimated to be $\sim$40 nm RMS, and our choice of 45 nm RMS is chosen to reflect a conservative over-estimate of the error. This over-estimate increases the error budget to 54 nm RMS, and we still aim to quantify the LWE to within 30 nm RMS WFE.

Phase Diversity and FPS require focal plane images of the PSF in order to estimate the coefficients of this selected basis; these images are created as simulations of the SPHERE differential tip tilt sensor (DTTS) imager. The DTTS imager exists directly before the coronograph on SPHERE and therefore shares most of the common internal aberrations with the science image optics. Using the DTTS images for the LWE characterization is much less complicated than using the coronographic

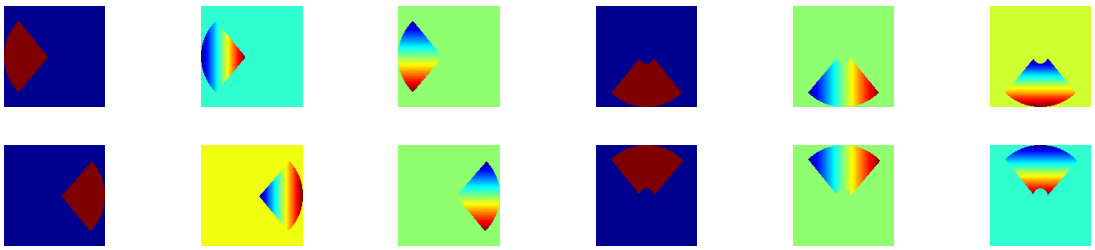

Figure 5.3: Piston, tip, and tilt basis used to recreate the PSF variations seen during the low wind effect on SPHERE. Each mode is normalized to 1 rad RMS (except the pistons). For the remainder of this paper, mode '1' of this basis corresponds to the top left mode shown here (piston on the left segment). The remaining modes numerically follow from left to right, ending with mode '12' shown in the bottom right of this figure (tip on the top segment).

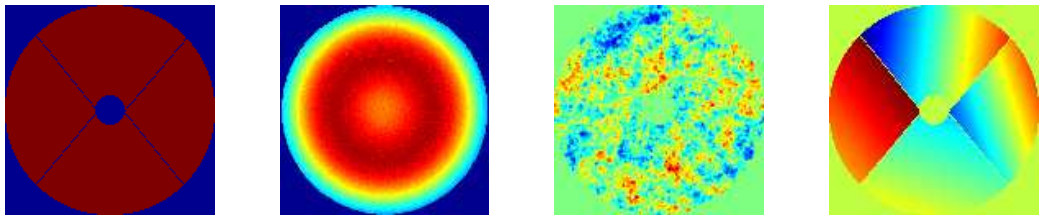

Figure 5.4: From left to right: VLT pupil, SPHERE apodization mask, assumed NCPA corresponding to 45 nm RMS WFE, and 1200 nm PV WFE low wind effect errors.

images, even though the latter can be used for the estimation of aberrations (Paul, B. et al., 2014; Herscovici-Schiller et al., 2017). We therefore aim to show the DTTS imager is sufficient for the LWE estimation and create synthetic DTTS H-band images dominated by photon and read noise.

Images are created using the adaptive optics simulation tool OOMAO with a 32x32 pupil sampling. Adding photon and read-noise is straightforward with this software, and we adopt a read-noise of 10e-, which is typical for a Hawaii I detector. We simulate a DM with 41 actuators across the pupil. Images are created with a sampling as close to the DTTS imager as possible ($\sim$ 4 pixels across the FWHM). We subject the image to a turbulence profile (generated assuming an r_0 of 11 cm at 550 nm, and that all the turbulence occurs at the ground layer), and subsequently apply an AO correction using the simulated DM. The turbulence evolves according to a sampling rate of 500 Hz, and with a windspeed of 15 m/s; long exposure images are created by stepping the turbulence over the appropriate number of sampling steps

pertaining to the total integration time of the image. This is particularly important since the DTTS imager typically acquires ∼1 second exposures. We note however that no residual AO phase errors are incorporated in the generation of these long exposure images (i.e. lag, aliasing, etc.) but we will add functionality in the near future. However we are currently able to apply these residual phase errors to instantaneous images, and we generate these in a different analysis of Keck images in this paper. Finally, the images used with both Phase Diversity and FPS contain a field of view within the correctable region of the DM. This is not extremely important for focal plane sharpening, but for Phase Diversity it is extremely important: we find we have serious errors otherwise, increasing in effect as more of the uncorrected halo contaminates the image. Furthermore, the diversity we choose (i.e. focus) is always aimed to have its intensity distribution contained within the 'dark' correctable region.

5.3.2 Estimation methods

Phase Diversity

We first consider the estimation of the LWE modal coefficients by means of Phase Diversity; in particular we employ what we consider 'Classic' Phase Diversity i.e. when two images are used with focus diversity and the object is simultaneously estimated. Due to the combination of 45 nm RMS NCPA and the relatively large PV amplitude of the LWE (∼1200 PV nm), we consider two waves PV of focus to ensure the diversity is larger than the phase to be estimated.

It is important to simulate images with realistic DTTS signal-to-noise ratios (SNR), and so we consider the on sky data shown in Figure 5.5. We simulate a star with a typical SNR from this plot and run Phase Diversity with the aforementioned parameters. We found that we have difficulty reaching convergence, where half the time the solution will 'run away' in tip and tilt and converge on an erroneous result. We consider 3 approaches to solving this issue:

1. Increase the SNR of the image (i.e. increasing the exposure time of the image), however on the real system this will integrate residual AO effects such as lag error, etc. We find this solution increases the Strehl from 0.47 to 0.96 (see Figure 5.6), however we do not simulate these long exposure errors and caution that these errors need to be considered for a more in-depth analysis. However, given the practical simplicity of this solution, it seems like a viable option.

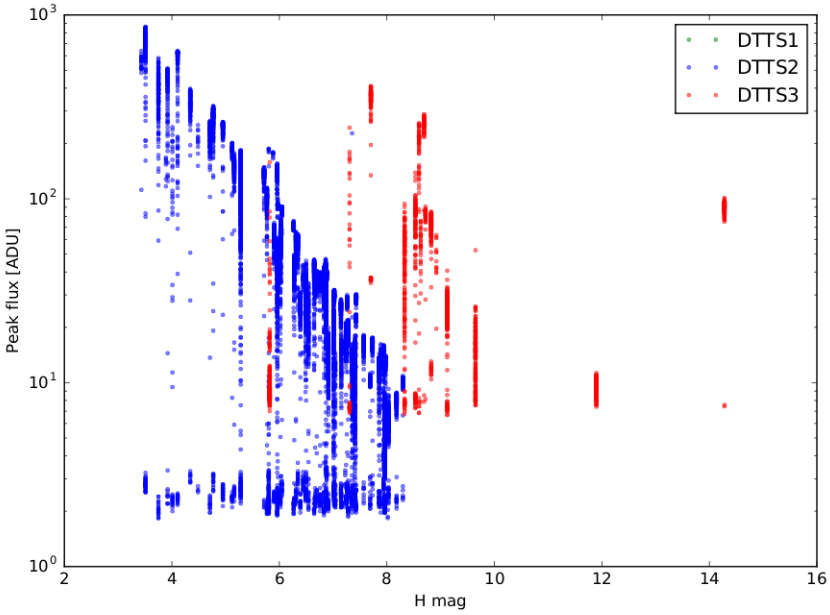

Figure 5.5: DTTS imager data, taken from SPHERE. The different colors correspond to different acquisition modes: blue points are taken in a mode optimized for bright stars while red points are suited for fainter stars; the green points represent an additional acquisition mode rarely used (and therefore explains the lack of points in this plot). The cloud of points around 2-3 ADU correspond to mis-detections, and we take this as the noise. Note: the values in this curve are subject to the inherent 20 nm PV focus on the DTTS imager, which results in a lower peak intensity than the true data shown here. After considering the noise floor and the data points adjusted for the 20 nm focus, we estimate a typical star has a SNR $\sim$ 70, and use this value for our analysis.

2. The convergence seems to break down because of a signal-to-noise issue, therefore it is worth exploring how a different type of diverse image can be used under these conditions. Introducting higher spatial modes, specifically cousins of the trefoil family (i.e. Z_{11}, Z_{21}, etc.), seem to work better in our simulations (in general). In particular, we consider introducing a Z_{66} aberration, because it is a relatively higher order mode as the diversity as opposed to just focus - which we find in general produces better phase estimates presumably because of the large diversity introduced to the PSF and it is not too high a spatial mode that it will be difficult to create with the SPHERE DM. Our simulation shows this mode always produces a better estimate of the phase (by a few nm RMS), and it converges faster than the focus-diversity case. We adopt 2 waves

(PV) of Z_{66} as our diversity and our simulation shows a Strehl increase from 0.47 to 0.91 (see bottom left image of Figure 5.6). This improvement is not as high as the previous example, but it is achieved with at a lower SNR. One problem may arise in realistically implementing this approach; high order phase speckles introduced from this diversity may be hard to disentangle from realistic AO phase residuals and high order, uncorrected NCPA. Furthermore, creating higher mode shapes such as Z_{66} will always have a higher residual fitting error compared with a low spatial mode such as focus.

3. Assume the object is known, which should be reasonable considering stars are effectively point sources, thereby simplifying the Phase Diversity algorithm. The immediate result is that the estimate is not as accurate (yielding a lower Strehl of 0.89 compared to the two aforementioned solutions), however it seems to converge must faster. Figure 5.6 shows results from our simulation using this method.

From all three of these scenarios we conclude:

- Under typical DTTS imaging conditions, 'Classic' Phase Diversity does not reliably work. If longer exposures do not contain adverse AO phase residuals, then using the classic Phase Diversity algorithm with long exposure images solves this issue.

- Alternatively, Phase Diversity can work with a higher order diversity, or with assuming a known object (using typical DTTS SNR values). In the former case the estimate is slightly more accurate, and in the latter the speed is considerably faster.

It is worth noting the diversity amplitudes adopted in this work were mainly chosen by convention. In the context of Phase Diversity and Phase Retrieval, the exploration of the amplitude of the induced diversity has been investigated by numerous groups; for example, Jurling & Fienup (2014) consider scenarios with up to +/- 8 waves of focus diversity. Therefore, we acknowledge that it is possible alternative diversities may be more desirable, but for the purposes of this work we do not further pursue this topic.

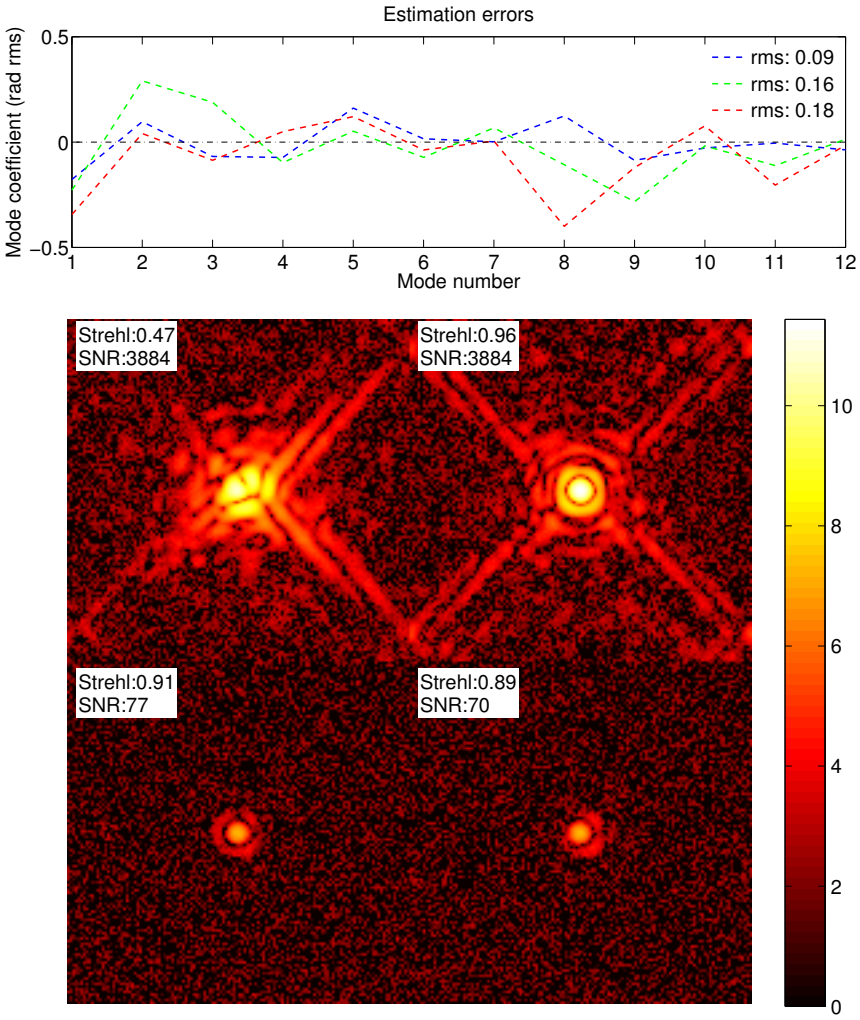

Figure 5.6: **Top:** residuals of LWE piston, tip, and tilt estimations from the actual modes, using Phase Diversity for 3 different scenarios (blue: long exposure object-estimation with focus diversity, green: object-estimation with higher diversity (Z_{66}), and red: focus-diversity assuming a point source). It can be seen the long exposure (blue) scenario performs the best, as indicated its RMS residual from the actual modes. **Bottom:** four panels of simulated VLT images, created from the phase projection of the estimated modes; they are described as follows: the upper two panels include no correction and long exposure Phase Diversity, respectively. The lower two panels include the higher diversity and assumed point source scenarios, respectively. The highest performance in terms of Strehl clearly uses the long exposure image. The bottom two images have diffraction rings that fall under the pedestal of the noise.

Focal Plane Sharpening

Given that FPS is not model dependent, (unlike our form of Phase Diversity), it is worth investigating its performance under the same conditions as our Phase Diversity analysis. In general, our simulations suggest FPS works with even lower SNR images than Phase Diversity. However, one obvious limiting factor of FPS is the number of iterations (i.e. images) taken, particularly for the application of measuring the LWE considering it can vary (over short time scales, i.e. tens of minutes; the LWE is actually observed to have time varying evolution over the course of several minutes, see Sauvage et al. 2015), and we arbitrarily choose a reasonable 'window' in which to quantify this effect as one minute. Therefore, we implement the constraint that FPS should contain no more than 60 iterations, given the fact that a typical DTTS exposure is ~ 1 second. In addition, we hypothesize that starting with an initial estimate from Phase Diversity may benefit from an improvement of FPS, based on its model independence. Furthermore, we hypothesize that the number of iterations (images) will be greatly reduced if using a starting point from Phase Diversity. Therefore we investigate 5 scenarios:

- Case-1: Apply Phase Diversity on a typical SNR DTTS image, taking the fastest solution - which is when the object is assumed to be a point source (i.e. scenario 3 from the previous section).
- Case-2: Focal Plane Sharpening on the same type of image, starting from the null position.
- Case-3: Focal Plane Sharpening starting from the solution from the Phase Diversity example.
- Case-4: Focal Plane Sharpening performed on the best solution from the Phase Diversity example to explore if it does indeed outperform the model dependent Phase Diversity.
- Case-5: Focal Plane Sharpening starting from the lowest SNR image possible.

Table 5.1 summarizes the results from the aforementioned cases. We note that global tip and tilt are removed from the residual wavefront. The residual wavefront is the known aberrated wavefront (LWE+NCPA) subtracted from that of the estimated wavefront. These residual wavefronts include 45 nm RMS NCPA and will therefore

be much larger than our target LWE estimation of 30 nm RMS. In case 4 and 5, FPS uses the PSF created from correcting the Phase Diversity estimate as input in addition to using the Phase Diversity estimated modes as a starting position. It is found FPS improves the Phase Diversity result when the object is assumed known. However, there is no clear improvement from FPS on the best case Phase Diversity from Section 5.3.2 (where we used a longer exposure and estimated the object). In other words, in the case where the Phase Diversity images have a lower SNR, FPS will always improve those images. We find the FPS improvement takes ~ 60 images when used with an initial Phase Diversity estimate, and for each image there is a very small computation time. Therefore we conclude this method would take between 1-2 minutes, which is slightly outside our prescribed time constraint of 1 minute.

Interestingly, we also find that FPS run by itself will converge on a solution much different than the original modal coefficients (see the RMS residual coefficients column of Table 5.1), and furthermore this solution is of comparable residual WFE to our other best scenarios. The number of iterations for this convergence was about 120 - about double the number of images that used an intial estimate from Phase Diversity. Perhaps even more intriguing was the performance of FPS when used with a low SNR image: it was found FPS could successfully converge on images with a SNR of 10, in about 120 iterations.

Regardless, we find the best estimate of the LWE requires Phase Diversity with object estimation. For the remainder of Section 3, we further expand this method to assess its feasibility to accommodate SPHERE's WFE requirements as outlined in 5.1. In addition, we consider an alternative Phase Diversity scenario that requires only the raw DTTS images.

Estimating the LWE from a single image

Considering the evolution between two sequential images acquired in a closed loop AO system (due to changing seeing and AO residuals), it is desirable to consider Phase Diversity using only one image. Single image Phase Diversity is analogous to Phase Diverse Phase Retrieval (Ellerbroek et al., 1997), and the image in question is subject to diversity; for the rest of this paper we will refer to this technique as 'single image Phase Diversity' instead of Phase Retrieval to stay consistent with nomenclature of the multiple image scenarios. Work has been done on-sky in the past showing the challenges involved with using two sequential Phase Diverse images (Jolissaint et al.,

Table 5.1: Phase Diversity and Focal Plane Sharpening results correcting for the Low Wind Effect.

Case	Method	Resid. coeff. RMS (rad)**	Resid. wavefront RMS (nm)***	Strehl (Marechal)	No. of images	Initial SNR
Case 1	PD-1 (assumed object)	0.17	89.4	89.1	2	70
Case 1	PD-2 (long exposure)*	0.09	55.3	95.7	2	3.8e4
Case 2	FPS	0.40	56.1	95.5	122	106
Case 3	FPS + PD-1	0.12	57.9	95.3	64+2	119
Case 4	FPS + PD-2	0.11	55.7	95.6	30+2	129
Case 5	FPS low SNR	0.28	75.4	92.1	121	10

*Shown for reference

***The RMS of the difference between the estimated and actual coefficients

****The *total* aberrated wavefront (LWE+NCPA) subtracted from the LWE estimate

2012). Furthermore, the DTTS has a natural focus amplitude of 20 nm RMS, providing a diverse image with no reference slope manipulation. We have found that when using a non-simple pupil - such as the case with the apodized VLT pupil considered here - that single image Phase Diversity works for this amplitude of natural focus. This approach assumes the object is known and is assumed a point source (which is not unreasonable considering we are simulating stars). In Chapter 4, we consider the limitations of single image Phase Diversity (i.e. for uniform, circular, symmetric pupils). However, for this paper we will not explore the technical background of this technique. It is worth noting similar work has been done investigating single image Phase Diversity (Meimon et al., 2010) in developing the LIFT technique, and it is not an entirely new concept. Furthermore, the concept of a non-simple pupil to facilitate phase estimation dates as far back as 1965 by C.L. Mehta (Mehta, 1965).

To validate the performance of single image Phase Diversity we consider 3 different scenarios of LWE estimation:

1. 'Classic Phase Diversity', in which case phase and object are simultaneously estimated from two images with 0 and +2 waves PV of focus.

2. Two image Phase Diversity with *no* object estimation, using images with -1 and +2 waves PV of focus.

3. One image Phase Diversity, using a single image subject to 20 nm RMS focus, similar to the actual DTTS images.

The images used in the above scenarios have a SNR of ~ 70 for an in-focus image to stay consistent with Section 5.3.2. In the case of Classic Phase Diversity, however, the solution did not converge with this value and a minimum SNR of ~ 700 was required. Figure 5.7 summarizes the results of each of these scenarios. The best estimation is achieved by Classic Phase Diversity; the residual between the phase estimate of the LWE and the actual injected LWE is 30 nm RMS (top right of the Figure). However, in the cases of ii) and iii) LWE estimations are marginally worse, with 50 and 62 nm RMS residuals (respectively). Two image Phase Diversity with no object estimation is considered here strictly as a comparison with single image Phase Diversity, where the only real difference between the two scenarios is a single image. From these results it appears single image Phase Diversity with the natural DTTS focus can reasonably estimate the LWE, although not at the same performance of Classic Phase Diversity.

5.3.3 Performance evaluation

Through consideration of both FPS and Phase Diversity, it appears the most viable form of LWE estimation (in terms of both speed and accuracy) is in some form of Phase Diversity. As mentioned in Section 5.1, 30 nm RMS WFE of the LWE is small enough to still achieve the target contrast of SPHERE and therefore a perfect correction from a Classic Phase Diversity estimate would achieve this requirement. We note here that the LWE in this simulation is representative of a larger-than-normal LWE night, therefore we expect better performance under less severe conditions. That being said, Classic Phase Diversity requires DTTS images with a higher SNR than those delivered by the operation of the sensor, and therefore would be subject to atmospheric residuals over the course of long exposures. Furthermore, the acquisition of diverse images would require reference slope manipulation; it is worth considering single image Phase Diversity requires no such manipulation when using the natural DTTS focus. Furthermore, the results shown here suggest the impact in LWE estimation is not terribly drastic between single image and Classic Phase Diversity (i.e. on the order of 5% Strehl loss using the Marechal approximation), and could be seriously considered for estimation/correction if the science does not require the full 10^{-6} contrast. Lamb et al. (in prep) are currently analyzing a sequence of DTTS images recently acquired at the VLT during a night subject to a strong LWE in order to better understand the feasibility of implementing single image Phase Diversity on VLT/SPHERE to measure the LWE. The results from this on-sky data will be discussed in Section 5.4.

5.4 Estimating the Low Wind Effect on SPHERE with bench and on-sky data

We now wish to quantify the LWE outside of the scope of simulation, therefore we turn our investigation to both an experimental bench and on-sky data. Showing the validity of our technique with on-sky data is essential prior to attempting any sort of real time estimation/correction. In addition, exploring the evolutionary effects over the course of a night subject to the LWE may lead to valuable insight in the approach taken to estimate this effect in real time. For example, if the effect is shown to have features which are relatively constant (i.e. on the order of minutes to hours) then developing an algorithm that needs to operate extremely quickly may not be

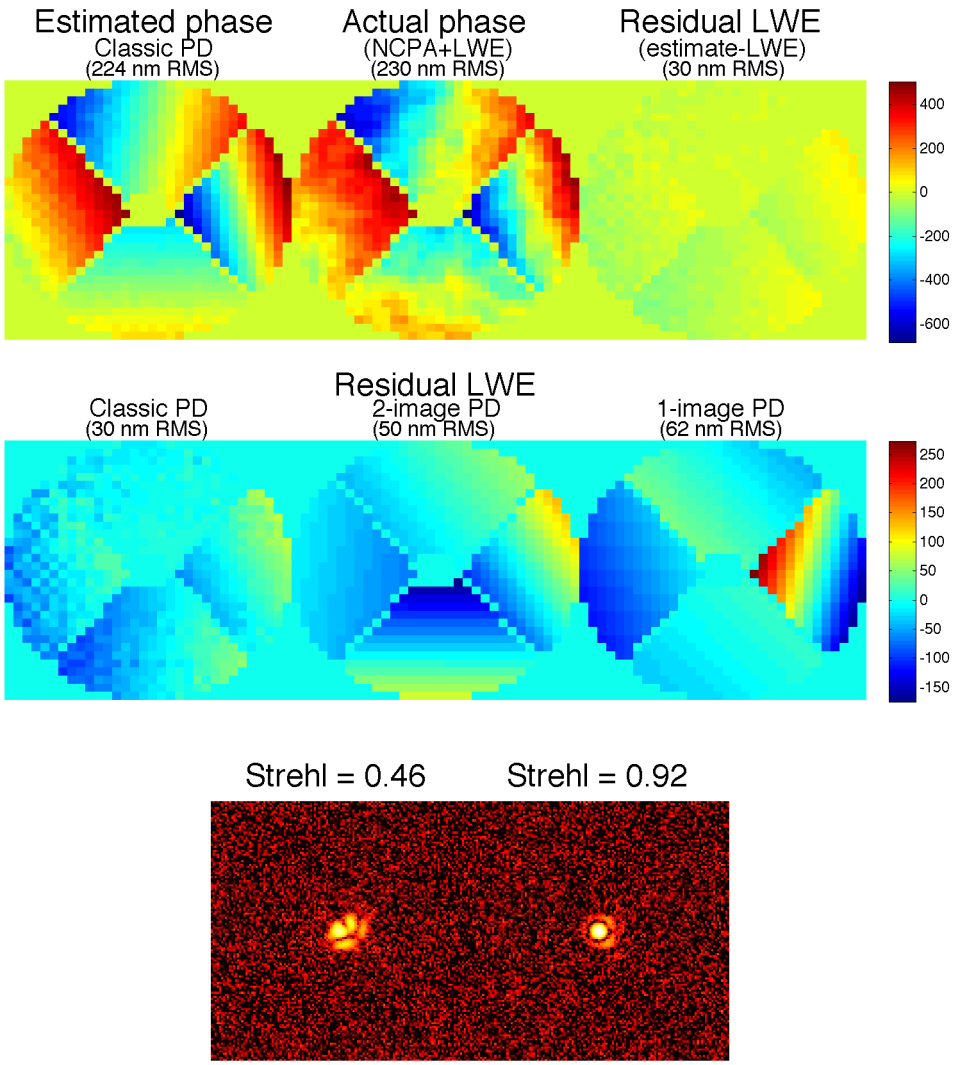

Figure 5.7: **Top:** Estimated LWE (left) from Classic Phase Diversity (phase and object estimation using images with 0 and +2 waves PV focus), actual phase injected (center), and residual phase between the estimate and actual LWE injection (right). The residual WFE reaches the desired 30 nm RMS, such that a perfect correction of this estimated phase would result in a contrast at least 10^{-6}. **Middle:** Residual phase maps for 2 image Phase Diversity with and without object estimation (left and center panels, respectively) and single image Phase Diversity (right panel, using a single image with the natural focus of the DTTS imager). These additional Phase Diversity scenarios do not meet the performance of Classic Phase Diversity, but are shown here for comparison. The case of the single image should be considered useful for its potential of both a quick LWE quantification and unobtrusiveness in image acquisition. **Bottom:** Simulated PSFs before and after (perfect) correction from the single image LWE estimate.

necessary. Therefore the scope of this Section is to: (i) first demonstrate the Phase Diversity techniques explored in Section 5.2 can effectively estimate that the LWE on an experimental bench; (ii) apply these techniques on a set of data acquired on SPHERE during a night subject to the LWE to try and quantify the effect; and (iii) explore the evolution of the effect over the course of the night. These three exercises will allow us to consider quantification at the telescope itself during a night with such an effect, and additionally provide insight as to how often one would need to measure the effect if they were to consider applying some sort of real-time correction (i.e. by providing offset slopes the AO system).

5.4.1 Methods and Observations

MITHIC Experimental Bench Observations

To validate our Phase Diversity technique we estimate the phase on an experimental bench with a known phase error. In particular, we consider two different scenarios on a high-contrast imaging experimental bench called MITHIC, located at Laboratoire d'Astrophysique de Marseille. On the bench we consider a phase map pertaining to 44 nm RMS WFE of 20 randomly oriented Zernike Polynomials injected into the system via a spatial light modulator (SLM), and a phase screen with 20 nm RMS WFE representative of the LWE phase. The phase screen in the latter case is described in detail in Vigan et al. (2016). Figure 5.8 displays the phase in each scenario: the left panel is the phase map introduced by the SLM while the right panel is a measurement of the phase screen taken with a ZELDA WFS (N'Diaye et al., 2013).

For each phase scenario five images were acquired with amplitudes of focus, corresponding to 0, 50, 75, 100, and 150 nm RMS. Figure 5.9 shows these images on a log-scale. This data will be utilized with Phase Diversity in Section 5.4.2 in an attempt to estimate the phase of each scenario.

On-Sky Data

On-sky data was acquired on the Differential Tip Tilt Sensor (DTTS) on the VLT SPHERE adaptive optics system during a night largely affected by the LWE in October 2016. A total of 13577 images were recorded every two seconds, spanning $\sim$4 hours of a night. Figure 5.10 displays DTTS images affected by the LWE at three different times throughout the course of this sequence. The images were acquired in

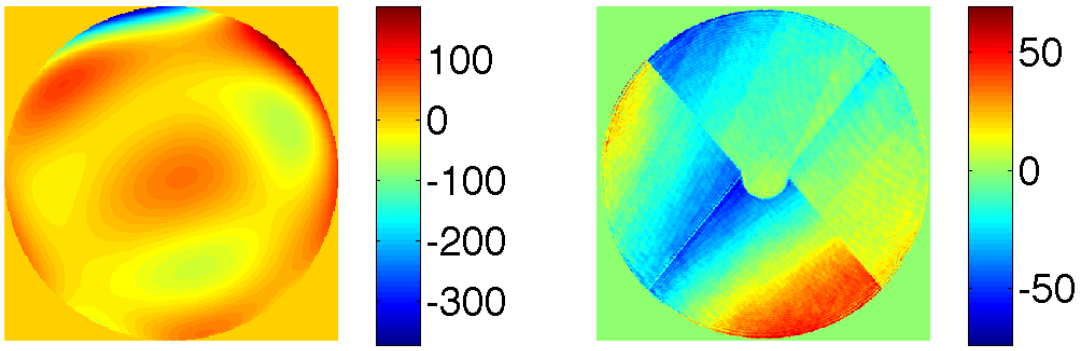

Figure 5.8: Phase maps representing each scenario considered on our experimental bench. Left: 44 nm rms WFE phase map resulting from random coefficients applied to the first 20 Zernike Polynomials; this phase map is projected into our system via a SLM. Right: phase screen with an imprint of a representation of the LWE (∼20 nm rms WFE), inserted in the pupil plane of the system.

H-band with a sampling of 3.46 pixels across the full width at half maximum. The size of the images are 32x32 pixels, resulting in PSF information-loss at the outer regions of the images; this lost information is less impactful on any focal-plane wavefront sensing due to the effect of pupil apodization, which already suppresses high spatial frequencies. Therefore if the PSF is properly modelled (i.e. correct pupil apodization, spider location, pixel scale, etc.), then Phase Diversity should have the capability to sense wavefront aberrations from DTTS images. In Section 5.4.3, we apply the techniques developed on the MITHIC bench in an attempt to estimate the LWE from the DTTS images and discuss our results.

5.4.2 Evaluating MITHIC Data

Classic Phase Diversity

We first employ 'Classic Phase Diversity' using data taken from the MITHIC experimental bench. We consider Classic Phase Diversity as the scenario similar to that originally put forth by Gonsalves (1982) and Paxman et al. (1992), specifically where an in-focus image and an out-of-focus image are used to estimate the coefficients of a modal basis representative of the phase error in question (identical to Section 5.3.2). This estimation is performed in two scenarios: with and without object esti-

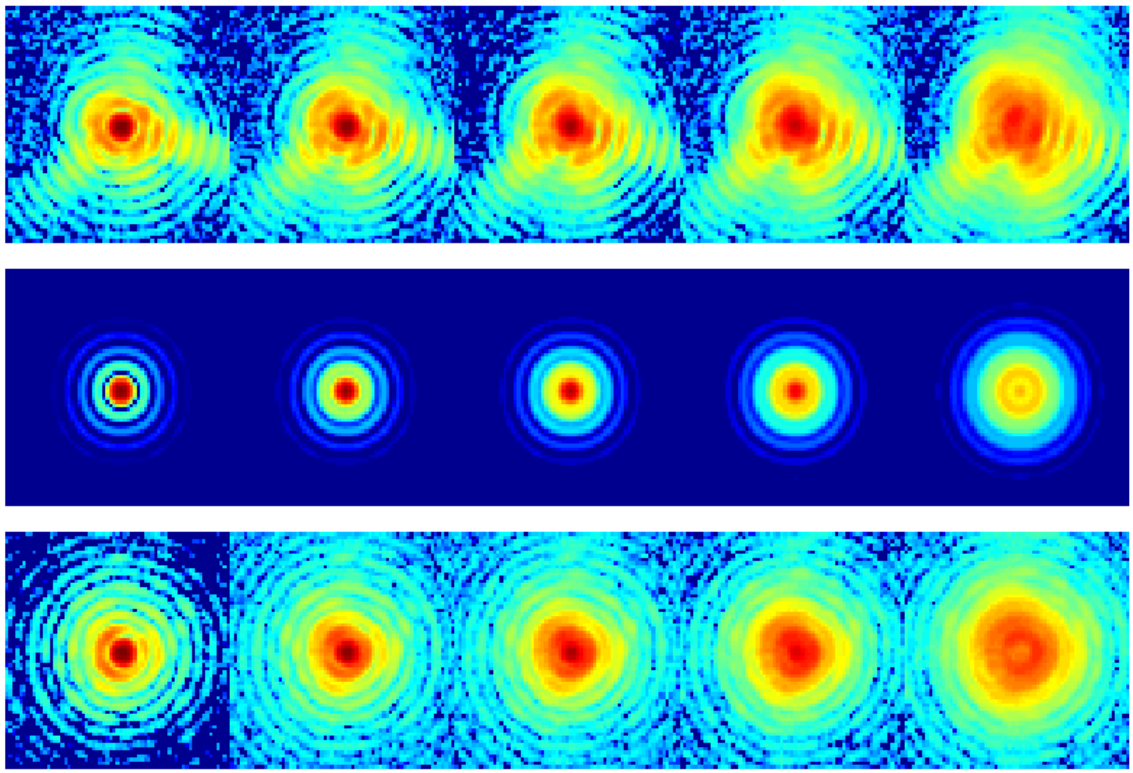

Figure 5.9: Top: images obtained at 5 different focal plane positions in the scenario where 44 nm rms WFE is injected from 20 random Zernike Polynomials; the focal positions are 0, 50, 75, 100 and 150 nm rms (from left to right). Middle: synthetic images created using the known bench parameters at the same focal positions. The real and synthetic images are used in the Phase Diversity algorithm to estimate the phase of the system. Bottom: images obtained in the same manner using the LWE phase screen. All images are shown here in log-scale. The images were created with a 677 nm fiber source.

mation. As previously shown in Chapter 4, Phase Diversity with object estimation is best achieved when one of the images is in-focus; conversely, we showed that Phase Diversity with no-object estimation (the object is assumed a point source) ideally uses diverse images away from the focal plane, because including an in-focus image degrades the phase estimation. In the following sections we employ Classic Phase Diversity with and without object estimation to quantify known phase errors injected into our system. We attempt to recover these known errors in order to validate our techniques, which will then be used to consider more complicated examples.

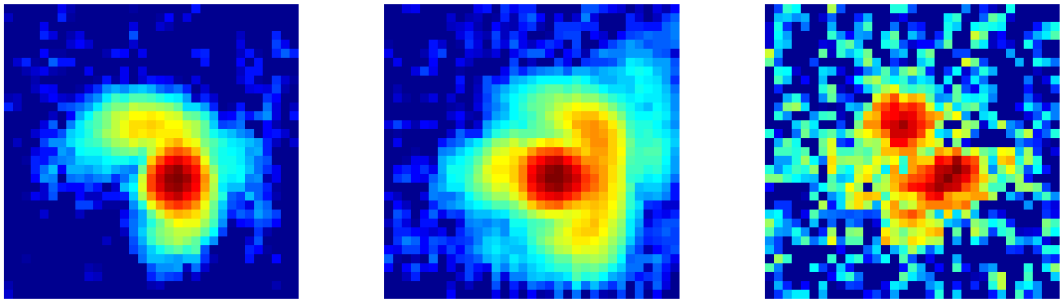

Figure 5.10: Images obtained by the DTTS on SPHERE at three different times affected by the LWE on this particular night.

Intrinsic NCPA: The intrinsic NCPA of the MITHIC bench must first be quantified so that its signature can be removed from future estimations where we estimate induced phase injections. The intrinsic NCPA are estimated with Phase Diversity in two scenarios: object estimation using an in-focus image and 150 nm rms focus image, and no object estimation (assuming a point-source) using the 100 and 150 nm rms focus images. The synthetic images created in the Phase Diversity algorithm here assume a uniform, circular pupil; in all future phase estimates using MITHIC data we continue to make this assumption. Figure 5.11 displays the phase estimated from the object-estimation scenario, along with a reconstructed PSF from this phase. Also shown is the in-focus PSF for comparison; visually the PSFs agree. The rms of the estimated intrinsic NCPA is 16 and 17 nm rms for the object and no-object estimation cases, respectively.

Estimating a Known Phase Injection

As previously discussed, the known phase injected (see Figure 5.8, left panel) produced the images shown in Figure 5.9 (top). We now use these images with the same Phase Diversity approach described in 5.4.2 to estimate this phase injection. We estimate coefficients for seven radial orders of Zernike Modes using both Phase Diversity scenarios (object/no-object estimation). The phase maps are reconstructed from the Zernike coefficients and the signature of the intrinsic NCPA is removed. Figure 5.12 shows our estimated phase for both scenarios, along with: the actual phase WFE, the SH-WFS phase WFE and the residual between our estimate and the actual. The residual phase maps are 10 nm RMS under both Phase Diversity scenarios. The reconstructed PSF from the object-estimation scenario is shown in Figure 5.13, which from visual inspection agrees with the actual in-focus PSF.

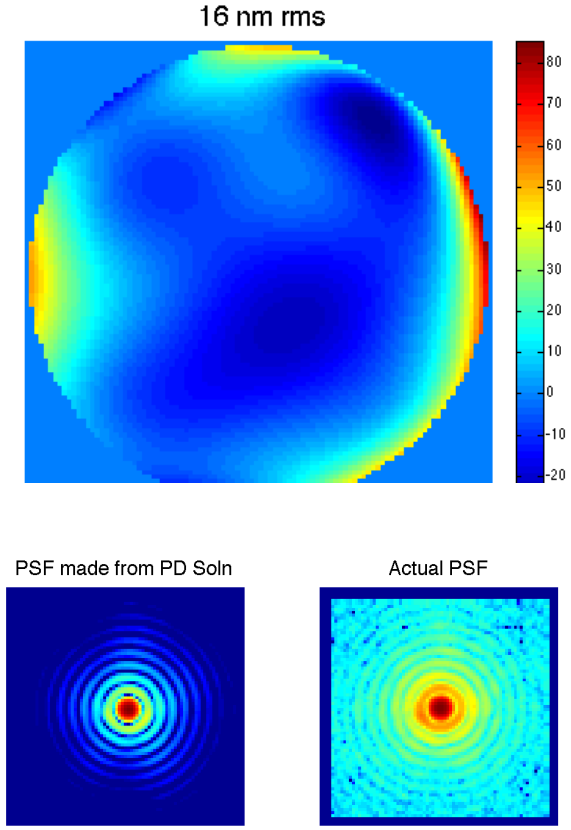

Figure 5.11: Top: Estimated intrinsic NCPA phase from the reconstruction of 7 radial orders of Zernike Polynomials; the Zerniikes were estimated employing classic Phase Diversity with two images: the in-focus and largest defocussed image. In this case the object was also jointly estimated. Bottom: reconstructed PSF using the estimated phase (left) and the actual in-focus PSF (right); visually the reconstructed PSF is nearly identical to the actual PSF. This estimate of the phase represents the intrinsic NCPA of the system and must be subtracted from any future scenario when trying to estimate a known phase injection.

LWE phase screen

We now utilize the same approach described in the previous Section to estimate the LWE phase, provided by a phase screen in the pupil plane. In this case we employ the basis described in Section 5.3 in lieu of Zernike Polynomials. The intrinsic NCPA are now estimated using this basis (following the same manner in Section 5.4.2) so that they can be removed from future LWE phase screen estimations using this basis. This ensures any contribution of the intrinsic NCPA to the estimated basis in the presence of the LWE phase screen will not be contaminated. The resulting basis coefficient

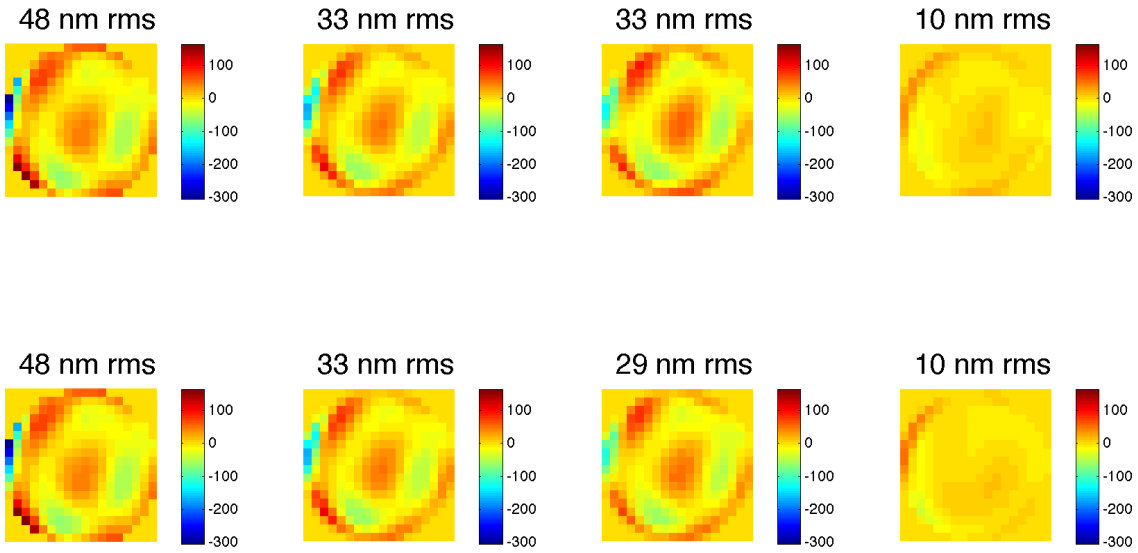

Figure 5.12: Top: estimation of the known phase-injection using Classic Phase Diversity with object estimation. Bottom: estimation of the same phase with no-object estimation (assuming a point source). From left to right: SH-WFS phase measurement, phase injected into system, estimated phase (via 7 radial orders of Zernikes), residual between the actual and estimate. The Phase Diversity described here used the 4 defocussed images from the sample, assuming a point source. For both cases the intrinsic NCPA were removed from the estimated phase. Note: the resolution of the phasemaps are restricted by that of the SH-WFS (18x18).

estimates from both Phase Diversity scenarios are reconstructed into phase maps (and removed for intrinsic NCPA) and shown in Figure 5.14. From inspection it can be seen the general trend of the actual phase (right) is reproduced in both of the estimates (left, middle), and the rms WFE is nearly identical. The residual between the estimated and actual phase of the top quadrant is on the order of a few nm rms, and a slight variation in tip/tilt can cause the visual discrepancy shown here. Figure 5.15 displays a reconstruction of the PSF from the phase estimated in one of the scenarios (left); it is nearly identical to the actual in-focus PSF (right). We conclude that we can make an accurate phase estimation of the LWE phase screen.

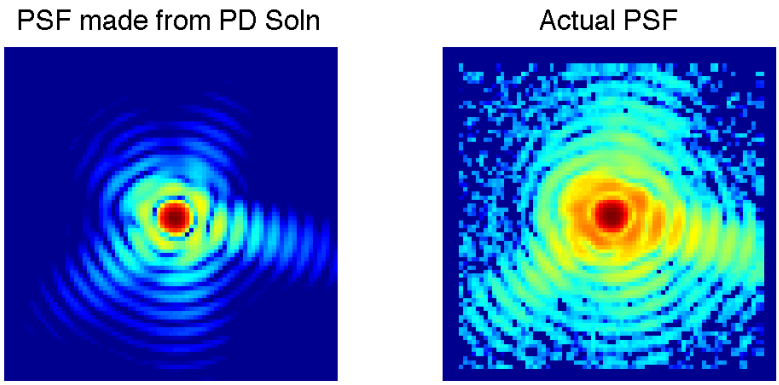

Figure 5.13: PSF comparison showing the reconstructed PSF from the estimated phase (left) with the actual in-focus PSF (right) for the images created from the 44 nm RMS phase map (injected by the SLM). The phase was estimated here using Classic Phase Diversity with object estimation. Visually the estimated PSF is very similar to the actual PSF.

Single image phase diversity

Employing Classic Phase Diversity on-sky has proved to be difficult in the past (i.e. Jolissaint et al. 2012). Quantifying the LWE from on-sky data using this approach will undoubtedly present equivalent difficulties, one of these difficulties being the fact that the evolution between two images on-sky (such as in and out of focus images used with Phase Diversity) can yield errors contaminating the true signal of the LWE. It is thus desirable to consider single image Phase Diversity, which can be achieved if the object is assumed a point-source and enough focus is used as the diversity. We follow the same procedure as Section 5.3.2, where we use the SPHERE/DTTS imager small focus error ($\sim$20 nm rms) as diversity. We explore here the possibility of estimating the wavefront from single images acquired by the DTTS during a night that exhibited the LWE. Prior to this, however, we aim to validate the technique of single image Phase Diversity on the experimental setup described here with the MITHIC bench.

A single image on the bench is considered using the largest focus diversity (150 nm rms) in both phase scenarios (known phase injection and LWE phase screen). We assume the object is a point source and estimate the phase in the exact same manner as Sections 5.4.2 and 5.4.2. Figure 5.16 displays the estimated phases for

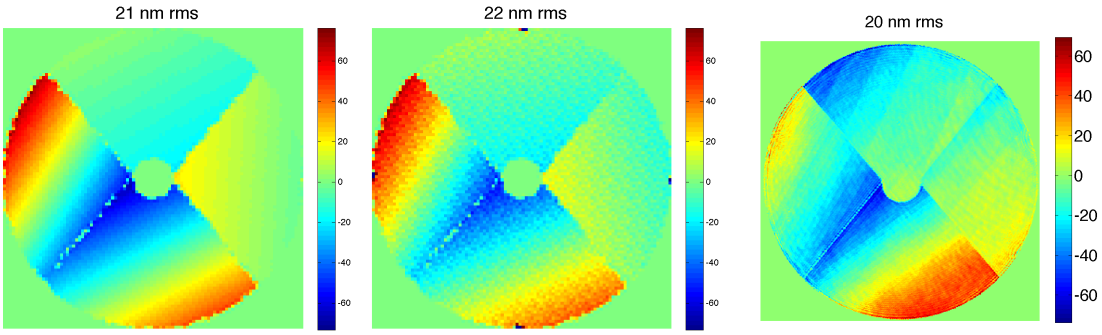

Figure 5.14: Phase estimates (no object estimation - left, object estimation - middle) compared with the actual phase (right). The general features in the estimation reproduce the known phase for three of the four segments. The rms WFE of the estimation is nearly identical to that of the phase screen.

each scenario: the known phase injection and LWE phase screen is estimated to almost the exact same degree as Classic Phase Diversity (shown in Figures 5.12 and 5.14), and the residual between the estimate of the phase screen and that measured by Zelda is ∼11 nm RMS (see Figure 5.17). From these results we are confident in the technique of single image Phase Diversity for other applications. In the following Sections we use this technique to estimate the LWE with single DTTS images on the SPHERE system during an active LWE night.

5.4.3 Evaluating On-Sky Data

Using the DTTS images discussed in Section 5.4.2 we employ single image Phase Diversity. The synthetic PSFs used in the algorithm are created from the known SPHERE apodization and VLT pupil, shown here in Figure 5.18. The DTTS imager is inherently subject to 20 nm RMS defocus inherent in the design of the DTTS, and we take advantage of this designed focus as diversity for our algorithm.

Basis selection

As previously discussed, the choice of basis for our estimation should reflect the nature in which the phase on the pupil is being manipulated during a LWE sequence. To ensure our custom piston/tip/tilt basis (shown in Figure 5.3) is a reasonable choice, we estimate the LWE on a strongly affected image using both a Zernike and piston/tip/tilt basis and compare. Figure 5.19 shows the estimation from Phase Diversity using both bases; the Zernike coefficients (estimated from 12 radial orders)

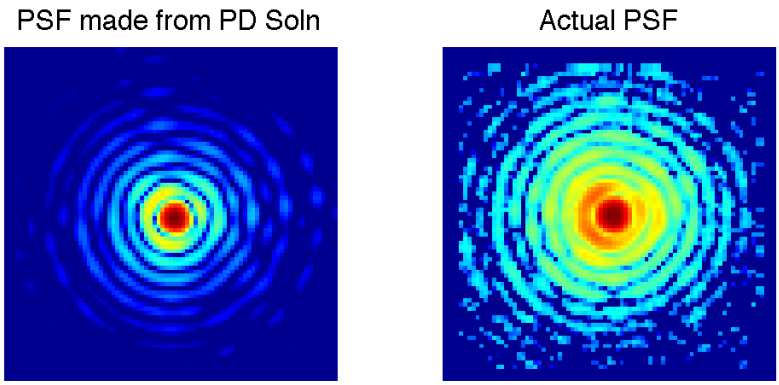

Figure 5.15: PSF comparison showing the reconstructed PSF from the estimated phase (left) with the actual in-focus PSF (right) using the LWE phase screen on the MITHIC bench. The phase was estimated here using Classic Phase Diversity with object estimation. Visually the estimated PSF is very similar to the actual PSF.

are clearly attempting to replicate a phase discontinuity defined by the pupil spiders as shown in the right panel of the Figure. This immediately suggests that part of the LWE is indeed due to the phase discontinuities originating from the secondary spiders. The left panel shows the piston/tip/tilt basis is a simplification of the effect and can naturally accommodate the pupil discontinuities. Furthermore, this twelve mode basis requires significantly less computation than when the large number of Zernike polynomials required to approximate these discontinuities are used. These results validate our choice to estimate the phase with a piston/tip/tilt basis, and we do so for the rest of this Section.

Estimation of a strong LWE sequence

We now turn to a one-minute sequence of images subject to a strong LWE to try and understand the evolution of this effect on short time scales. A strong motivation for this analysis is to assess the capability of this technique to quickly identify the error associated with the LWE when it happens, and understand how long of a 'window' exists for applying some sort of correction.

The LWE is estimated with Phase Diversity for thirty consecutive DTTS images, using the piston/tip/tilt basis. Figure 5.20 displays the observed DTTS images,

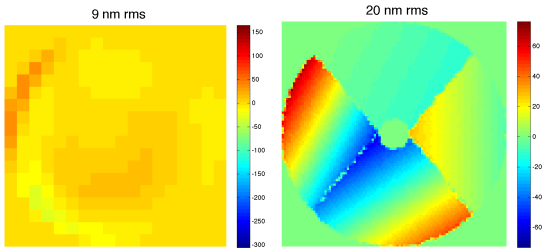

Figure 5.16: Single image Phase Diversity estimates of both the known phase injection (left, residual difference between estimate and actual shown) and the LWE phase screen (right). The residual phase in the known phase injection scenario is nearly identical to that estimated with Classic Phase Diversity (see Figure 5.12). Similarly, the LWE phase is nearly identical to its Classic Phase Diversity esimation counterpart (see Figure 5.14).

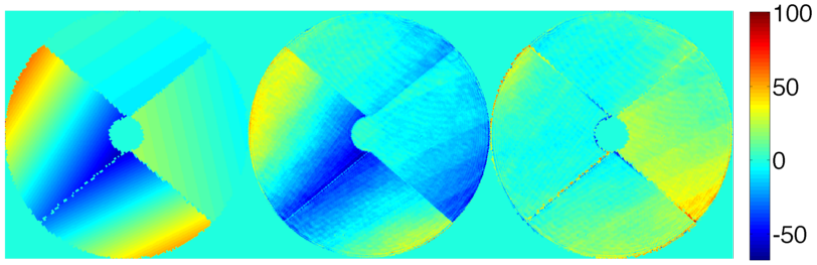

Figure 5.17: Single image Phase Diversity estimates of the LWE phase screen (left) and the actual phase screen (middle) as measured by Zelda. The residual between the two is shown on the right. The rms WFE of each phase map is 18, 20 and 12 nm, respectively.

along with PSFs reconstructed from the Phase Diversity estimation; this estimation is shown in Figure 5.21. The general PSF features over the course of one minute show some minor evolution, which can also be seen in the estimated phase maps. The average P-V WFE over the sequence is 474 nm while the standard deviation is 62 nm; the P-V phase estimates of the first and last DTTS image are 390 and 508 nm, respectively.

Evolution of the LWE over time

It is now worth considering how the LWE behaves on a time-scale much longer than the course of one minute to grasp its evolutionary behaviour. We consider a sequence of images obtained over a period of approximately one hour. The phase is estimated for each image in the sequence and its P-V WFE is plotted as a function of time (Figure 5.22). Upon inspection of this Figure, several interesting features become

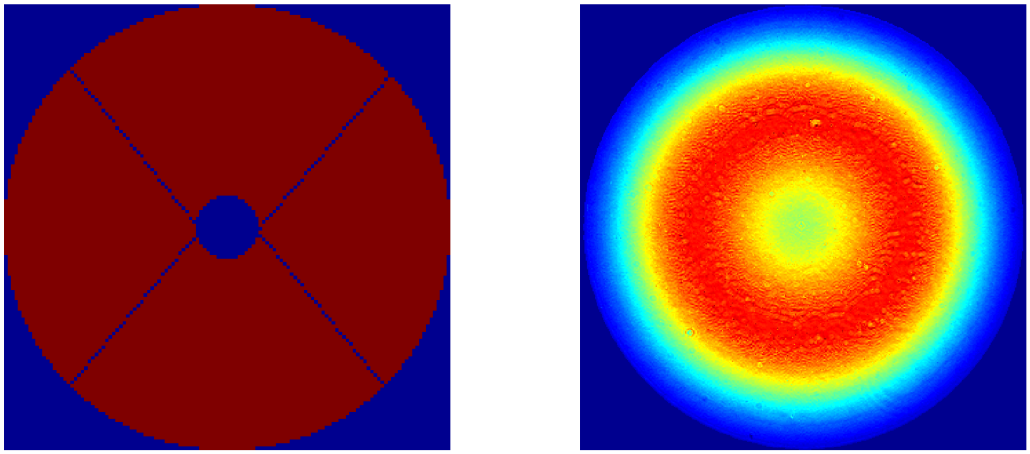

Figure 5.18: Pupil model (left) and apodization (right) used to model the synthetic PSFs used in the Phase Diversity determination of the LWE.

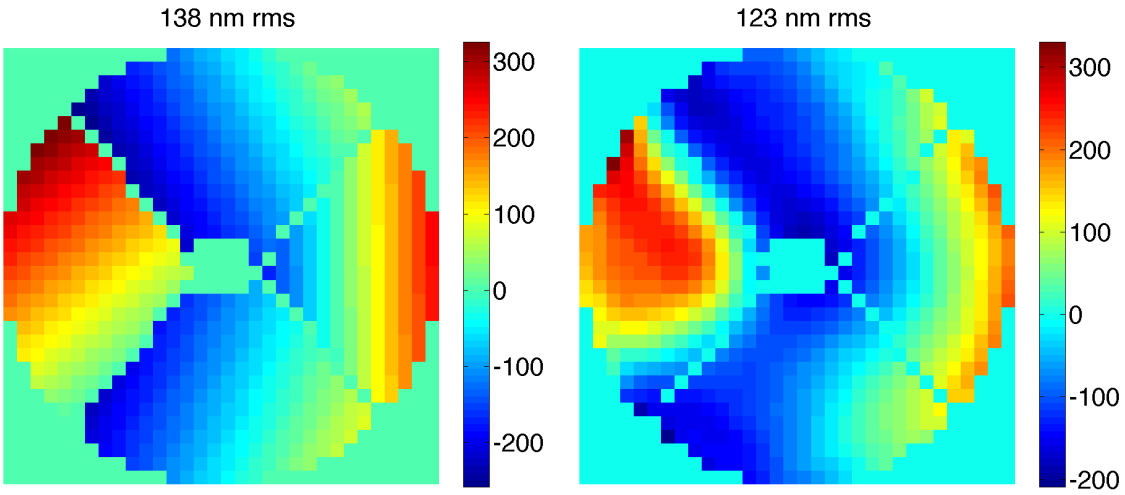

Figure 5.19: Phase estimated with Phase Diversity on the image shown in Figure 5.10 (middle) using the piston/tip/tilt basis (left) and 12 radial orders of Zernike polynomials (right). The phase appears to be well approximated with the piston/tip/tilt basis when compared with the Zernike estimate. Furthermore, the Zernike estimate reveals the phase is inherently split into the quadrants defined by the spiders in the pupil. This lends further support for using the piston/tip/tilt basis, which can facilitate the pupil discontinuities between two quadrants.

immediately apparent. First, there seems to be three distinct 'episodes' of the LWE, suggesting a particular event of some sort taking place at two different times over this sequence. Second, during each 'episode' (or event), the variation of the LWE is dif-

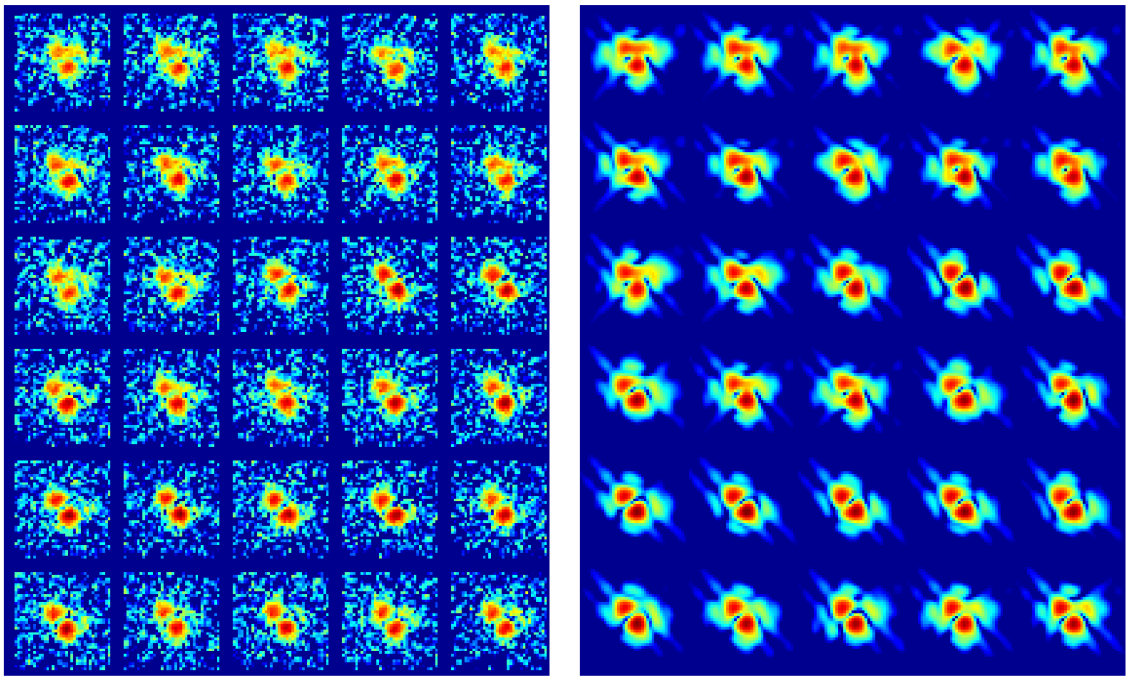

Figure 5.20: Left: a sequence of DTTS images taken during a particular sequence of the LWE during the night; the images are taken 2 seconds apart and span a total length of approximately one minute. Bottom: reconstructed images from the phase of the LWE estimated by Phase Diversity.

ferent. The first episode shows a very steady WFE, the second episode shows varying LWE strength between 0 and 400 nm (P-V), while finally the third episode contains the largest LWE variations with peak amplitudes of 2000 nm. Finally, throughout the latter two episodes, the LWE strength shows that there is an evolving trend (i.e. any measurement will be in relatively close proximity to an adjacent measurement, except in the case of an 'event'). The nature of these events are unclear and are discussed in Section 5.5.

5.5 Low Wind Effect Discussion

Simulated data

Segmented pupil error phase discontinuities were successfully estimated for a realistically simulated scenario on the VLT/SPHERE system. From this work we conclude:

- For SPHERE: typical DTTS imaging conditions make it difficult for 'Classic' Phase Diversity, and we propose 3 solutions that improve the estimation, which

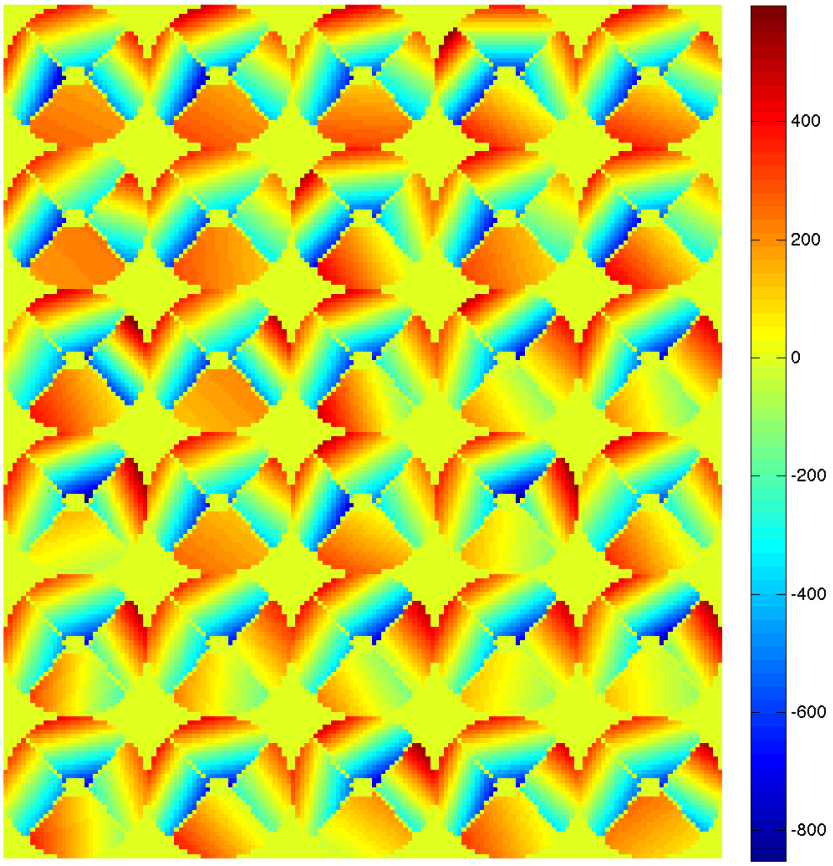

Figure 5.21: Phase estimates of the LWE during the sequence shown in Figure 5.20. The mean and standard deviation of the PV phase during this sequence is 474 and 62 nm, respectively. The total evolution of this sequence is about 60 seconds; the first and last PV phase measurements are 390 and 508 nm, respectively.

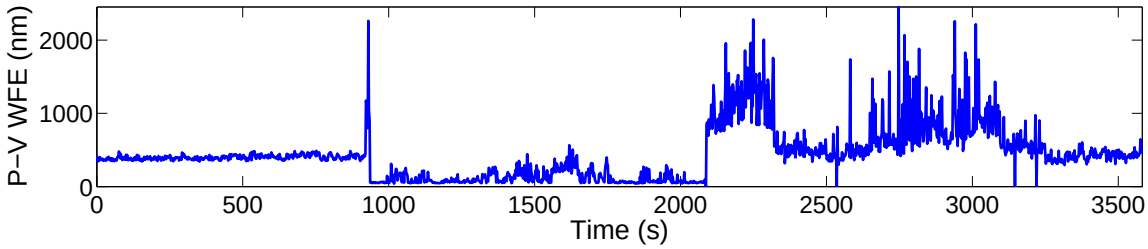

Figure 5.22: Peak-to-valley phase estimates plotted as function of time for a strong LWE sequence, taken over the course of approximately one hour. There appears to be three distinct episodes of the LWE, each with different strengths.

we show in simulation. The best phase estimation was achieved by using Phase Diversity with object estimation applied to long exposure images with higher

SNR than typical DTTS images. However, our simulation does not model the long exposure AO residual effects such as servo-lag, aliasing and fitting error which could degrade performance slightly in practice. If these AO residuals have a larger than desired impact on the Phase Diversity estimation, we can achieve a reasonably good LWE estimation by either using a higher diversity mode or leaving out the object estimation (and assuming a point-source). The latter method is less computationally expensive with respect to any phase plus object estimation.

- If using the non-object estimation method described in Section 5.3.3, then Focal Plane Sharpening will improve the image (on top of the Phase Diversity estimation) in around 60 iterations, which is around 1-2 minutes assuming each image takes ∼1 second to expose. However, if presented with the full aberration that induces the LWE, Focal Plane Sharpening can take more than twice this number of iterations. Note, however, that Focal Plane Sharpening can work on extremely low SNR (∼ 10) DTTS images.

- We find that running low SNR FPS on top of low SNR Phase Diversity yields roughly the same estimate as the best case Phase Diversity estimation, where a high SNR (i.e. long exposure) is required.

- Single image Phase Diversity is a useful technique for estimating the LWE. If using a single image with the natural focus on the DTTS imager, we find that this technique can estimate the LWE to almost the same accuracy as two images with no object estimation (using +1 and -2 waves of focus). However, two images *with* object estimation significantly improves the phase estimation, albeit higher SNR on the images is required. The single image approach could be useful considering sequential on-sky images will have evolution from one image to the next - an effect known to cause issues with Phase Diversity in the past (Jolissaint et al., 2012). Lamb et al. (in prep) are currently analyzing on-sky DTTS data taken during a LWE sequence to further explore the feasibility of single image Phase Diversity.

- To reach the target contrast of 10^{-6} for the SPHERE planet imager, the LWE must be estimated to within an error of 30 nm RMS, as discussed in Section 5.1. We find this goal can be achieved when using 'Classic' Phase Diversity (an in/out of focus image with object estimation), if the SNR of the in-focus

image is ∼700. The error on this estimation roughly doubles when we use Phase Diversity with a single DTTS image with a natural 20 nm RMS of focus on an image with a SNR 70. We conclude that at a small sacrifice in Strehl (∼ 4%) and therefore contrast, single DTTS images with no manipulation could be used to quantify the LWE.

- The correction of the LWE effect using the wavefront control capabilities of SPHERE is complex, and not studied in this work. The SPHERE system will benefit from a change of the spider coating in the near future, which could decrease the amplitude of the effect if it is indeed due to pupil temperature variations. Ideally the addition of this coating, combined with some sort of wavefront control scheme from the LWE estimation will be able to correct for the LWE that currently has a very negative impact on SPHERE performance. Some recent tests aim to prove that SPHERE wavefront control is able to produce the corresponding amplitude estimates of LWE (Sauvage et al. in prep.).

Bench and on-sky data

In the context of SPHERE, the LWE was estimated using single images on the DTTS imager on a night subject to a strong LWE. The techniques developed to do this were first validated on an experimental bench, and then subsequently applied to the DTTS data. The DTTS data consisted of ∼13000 images gathered over the course of the night at two second intervals; we estimated the LWE phase for each image and focus in particular on two subsets of this data: a strong LWE sequence over the course of one minute, and a strong LWE sequence over the course of one hour. The following statements below summarize our findings:

- Similar to our results in Section 5.3.2, single image phase diversity appears to be working using only the 20 nm rms focus as our diversity.

- The estimation algorithm *at minimum* is a tool available to monitor the LWE; at the very least for P-V observations but it seems a single image is enough to fully characterize the system. Of course, if this technique was used in situ at the telescope, it would be desirable to put some known focus on the image and use traditional phase diversity in order to confirm this.

- We present the evolution of the LWE over a one-minute sequence. The particular sequence chosen shows some of the strongest LWE aberrations of the night,

and even though we see a minor variation over the course of short timescales (i.e. one minute) this may not be reflective of all LWE cases. Considering the Peak-to-Valley WFE has a standard deviation of 62 nm over the one-minute squence, it seems if a correction were quantified every minute (with a corresponding update to the reference slopes with this estimate) then the LWE could be corrected to within this error.

- Evolution over a one-hour sequence: The 'episodic' nature of the LWE over the course of one hour further justifies the need for a quantification on the order of minutes as opposed to hours. The distinct nature of the three episodes shown in this work are not entirely known and may correspond to abrupt changes in wind direction (the wind speed is so slow that this is possible). However the determination of these features remains outside the scope of this work.

- Applying a correction: the algorithm requires only a few seconds to estimate the effect; as such an estimate and determination of offset slopes for the SHWFS is achievable many times per minute, and meets the requirements our suggestion of correcting at least once per minute be ideal.

- The applications Phase Diversity on high contrast imaging systems is an extremely desirable tool; as such we are exploring the capabilities of the technique developed here for the estimation of low order aberrations on the Gemini Planet Imager (GPI).

5.6 Estimating the segment piston errors on Keck in simulation

As mentioned in Section 5.1, significant low-order AO residuals in the Keck/NIRC2 system exist and may originate in the form of co-phasing errors of the primary mirror segments. We now consider estimating these segment-piston errors employing the same single image Phase Diversity approach that was used in quantifying the LWE in Section 5.3.3. The motivation for this approach is the desire to avoid unwanted evolutionary effects between two sequential images, as has been discovered with Classic Phase Diversity in the past (as previously mentioned in 5.3.2). We note that previous work has aimed at mitigating these effects by considering long exposure images with Phase Diversity, which average out the AO residuals and seeing effects (Mugnier

et al., 2008), however in this work we are interested in assessing the feasibility of using short exposure images. Since we are interested in avoiding evolutionary effects between sequential images, we do not consider Focal Plane Sharpening in this study.

A defocused NIRC2 image, subject to 153 nm RMS WFE co-phasing errors, is simulated as faithfully as possible (see Figure 5.23). The co-phasing error we adopt here was taken from a similar phasing-residual analysis that used different estimation algorithms (van Dam, 2016). The simulated images were created on a pupil with 32x32 sampling, and were subject to photon and read-noise errors. We adopted a read-noise of $60e^{-}$ (a single read-out NIRC2 image is closer to $40e^{-1}$, however we choose a larger value to be conservative). The images are generated with OOMAO in the environment of a simulated AO system with 21 actuators across the pupil (identical to the actual NIRC2 system). In addition to the co-phasing residuals, we also inject 60 nm RMS of astigmatism (a rough representation of the true non common path error), and 99 nm RMS of simulated AO residual errors (summarizing contributions from servo-lag, aliasing, and DM-fitting errors). Figure 5.23 shows phase maps representing these errors.

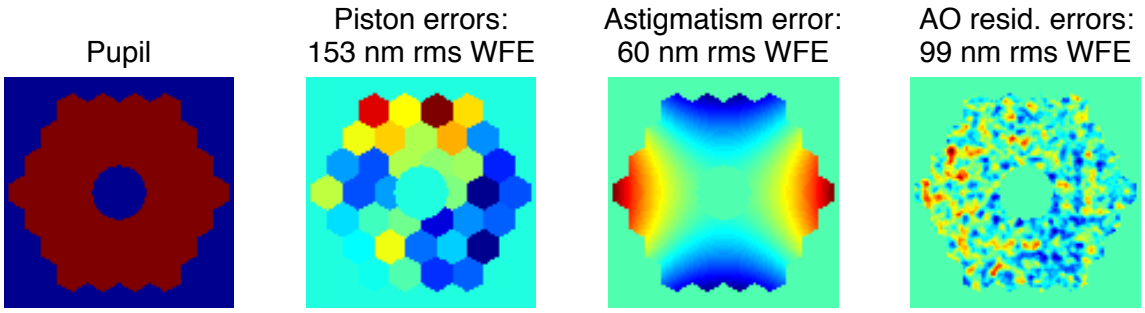

Figure 5.23: From left to right: Keck pupil, simulated piston phasing errors to be estimated, inherent astigmatism of NIRC2, AO phase errors (i.e. servo lag, aliasing, photon noise, fitting). The three phase maps on the right are used to create our simulated Keck images.

Assuming the object is a point source, the defocused NIRC2 image is estimated with our Phase Diversity algorithm. The amount of defocus is 1.5 waves (PV), and was chosen because larger values induced a focus pattern that crept into the uncorrected halo. The estimated basis modes are pure piston variations, defined by each mirror segment (therefore a 36 element basis), along with the first 10 Zernike modes. One of the goals of our estimation is to see if it can decouple the piston errors from

[1] http://www2.keck.hawaii.edu/inst/nirc2/Manual/ObserversManual.html#Section2.2

the astigmatism while under the influence of realistic AO residuals. Figure 5.24 summarizes our findings. The top panel of the figure shows the coefficients of the estimated piston plus Zernike basis in blue, overlaid on the actual modes injected into the system (red). The RMS residual difference between the actual and estimated modes is 0.1092 rad, which translates to 29 nm RMS. To visualize this estimation in terms of phase errors, the middle section of the figure displays the estimated phase (left), the actual NCPA plus segment error injection (middle), and residual phase of 29 nm RMS (right). Here the global tip and tilt is removed from both the estimated and actual phase prior to the subtraction. Hence the magnitude of the original 153 nm RMS co-phasing error has been reduced to 117 nm RMS; when this error is added to the 60 nm RMS of NCPA the final WFE is 99 nm RMS.

5.6.1 Performance evaluation

To evaluate the performance, we consider the situation where a perfect correction of the phase estimation can be achieved. The bottom of Figure 5.24 displays an image before and after such a correction, showing a Strehl improvement of $\sim 12\%$ (calculated directly from the images, using the ratio between the image OTFs and their diffraction limited counterpart). The signal to noise of a faint source increases proportionally to the Strehl ratio, therefore the exposure time is proportional to the square of the Strehl. In our example, achieving a perfect correction of the segment-piston estimation would decrease the exposure time of a faint object by a factor of $\sim$0.75 while achieving the same signal to noise without piston correction.

5.7 Estimation of segment piston errors on Keck with on-sky NIRC2 data

Recently, we were able to obtain on-sky data with NIRC2 subject to 'Low Order Residuals' (LOR), as described in Section 5.1. The data was acquired in October 2016 using NIRC2 to acquire a data set of in/out-of focus short-exposure images in K-band; the PIs responsible for the data are Sam Ragland and Marcos van Dam. Given our success in simulating an estimate of this effect, it is natural to apply the same technique to on-sky data.

The data was first analyzed with Phase Retreival and Phase Diversity by Marcos van Dam at *Flat Wavefronts*. The data was shared through private communication,

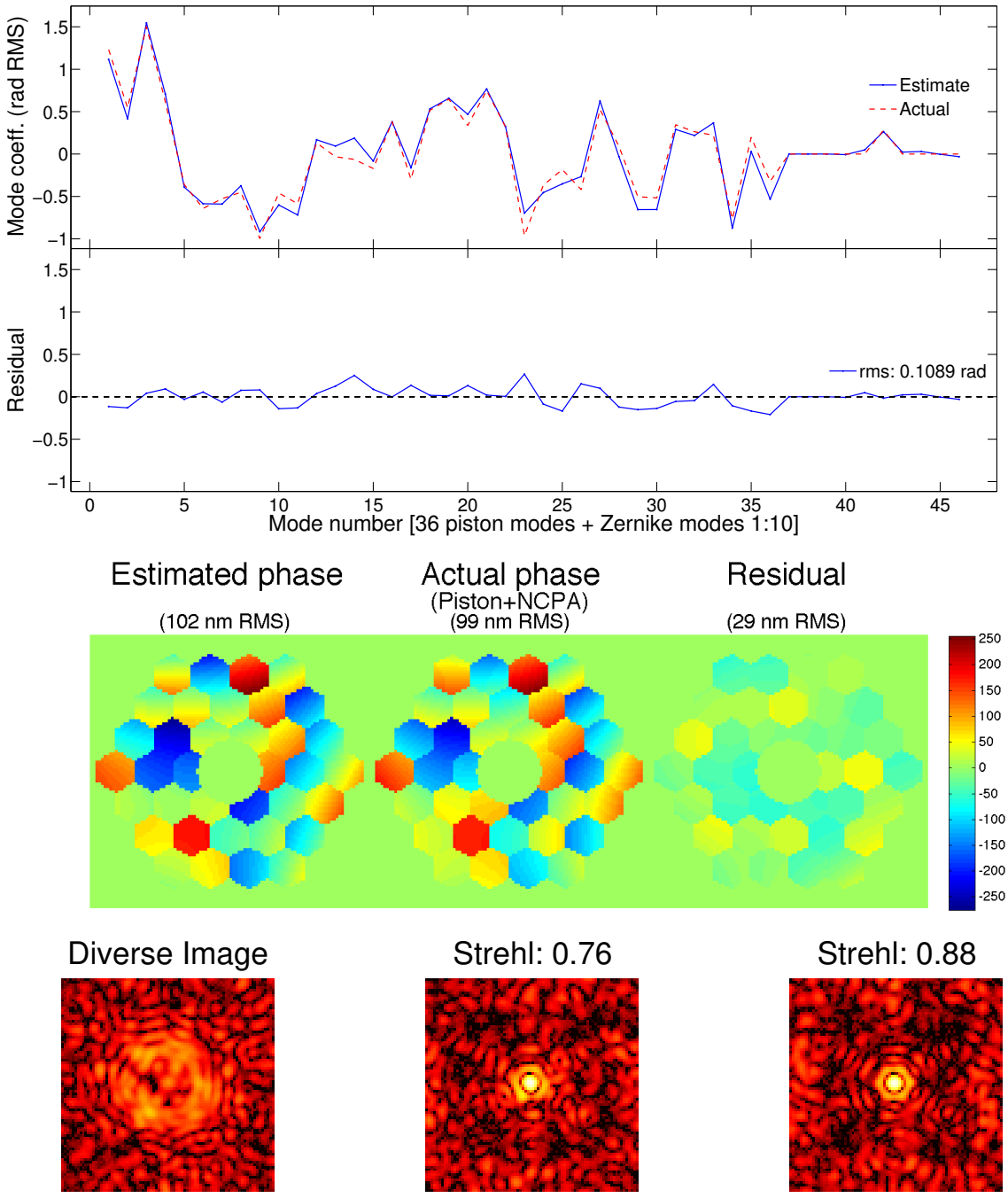

Figure 5.24: Estimation of both segment piston errors and NCPA (astigmatism) from a single diverse image of a simulated bright star (diverse image shown in bottom left). **Top:** Estimated modal coefficients of 36 piston modes and 10 Zernike modes (Z_1-Z_{10}). **Middle:** Phase reconstructed from the estimated modes (left) compared with the actual piston plus astigmatism phase (middle); the residual between the two is shown on the right with a WFE of 29 nm RMS. The global tip and tilt was removed from the estimated and actual phases, reducing the original co-phasing error from 153 to 117 nm RMS. **Bottom:** Simulated images of the initially aberrated system out of focus (left), in focus (middle) and the situation where the perfect correction of the estimated phase is applied (right).

from which I could use my Phase Diversity techniques successfully demonstrated in simulation to compare with the results of Marcos van Dam. I briefly describe here the outcome of this exercise.

A sequence of 50 short-exposure (8 millisecond), K-band, NIRC2 images of HIP 1602 were taken in closed loop. Another 50 image sequence was taken subject to +/- 500 nm RMS focus (with a slightly larger exposure time of 50 milliseconds). A sample in focus image is shown in Figure 5.25 (left), and compared with a perfect synthetic image for reference (right). The LOR impact on the PSF can clearly be seen, especially in the first diffraction ring. Figure 5.26 shows a sample of an image with 0, and +500 nm RMS focus (top) along with its synthetic counterpart for comparison (bottom).

As discussed in Section 5.1 and Ragland et al. (2016), the nature of the LOR is thought to be co-phasing errors of the mirror segments, however the phase in question can be estimated with any basis set. As such, the phase of these LOR was estimated by Marcos van Dam with Zernike polynomials; a sample of the phase estimation for an in/out of focus image pair is shown in Figure 5.27. The RMS WFE between our estimation and that of Marcos van Dam is nearly identical, and the same general features in the phase maps are observed (the wavefront map provided by M. van Dam did not match the same size as our estimated map, and therefore we could not show a direct residual here).

We now turn to estimating the phase of the LOR in terms of segment piston (instead of Zernike polynomials). It is reasonable to assume the mirror segments piston errors remain static throughout the observations, and that the main contribution of variation to the images is through residual AO correction errors. Therefore looking at the average phase estimation over the sequence of 50 images should lend insight as to the nature of these static errors. We now estimate the phase using the segment piston basis along with 50 in/out of focus image pairs. The pairs are chosen by using a single in focus image as a reference, and then pairing this image with 50 different +500 nm RMS focus images to obtain 50 different phase estimates. The average of these estimates is shown in Figure 5.28. If the LOR are indeed entirely due to co-phasing errors, this phase map is a reasonable representation of the static, co-phasing errors.

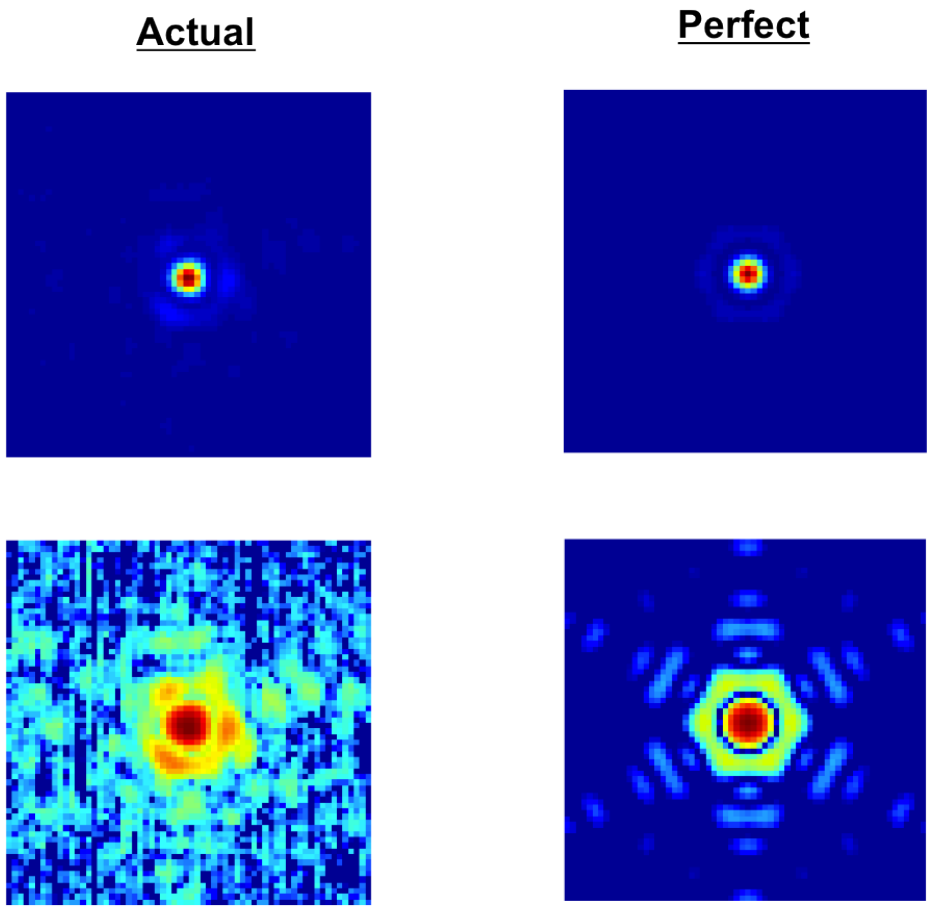

Figure 5.25: Left panels: a sample in-focus image taken in closed loop with NIRC2 at K-band (top is linear scale and bottom is log scale); the LOR impact on the PSF can clearly be seen in the first diffraction ring. Right panels: a synthetic image for comparison (top is linear scale and bottom is log scale).

5.8 Keck mirror segment error discussion

Simulated data

Phase segment piston errors were successfully estimated for Keck/NIRC2 simulated images with the assumption that images can be acquired nearly instantaneously (i.e. with 'frozen' turbulence). This assumption should not be too unreasonable considering the shutter speed of the detector is the only limitation (the availability of bright stars should not be an issue). We show the capability of using Phase Diversity with a single, diverse image; this technique avoids any significant evolution effects between

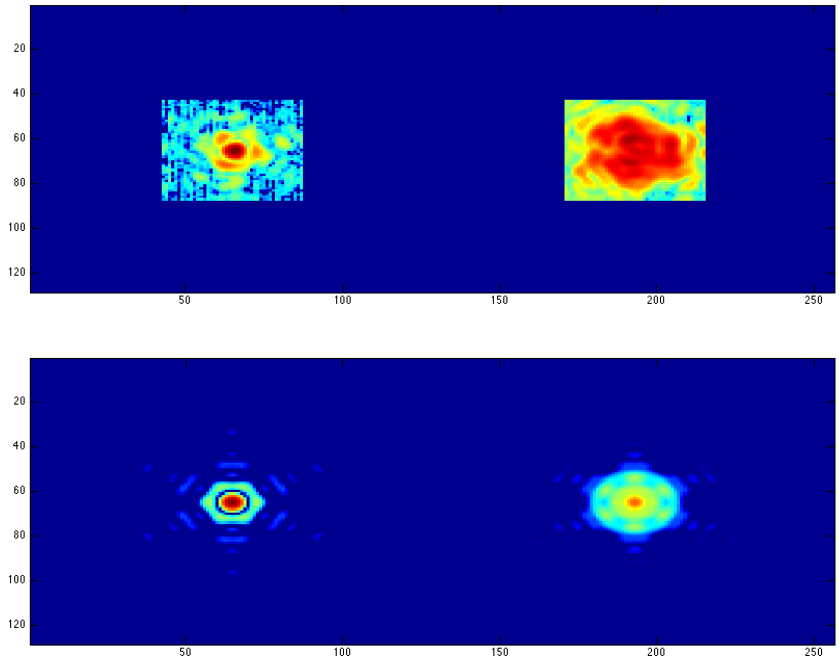

Figure 5.26: Top: images in-focus (left) and with +500 nm RMS focus (right) used with Phase Diversity to estimate the phase in this work. Bottom: synthetic images subject to the same focus values for comparison (with no phase error).

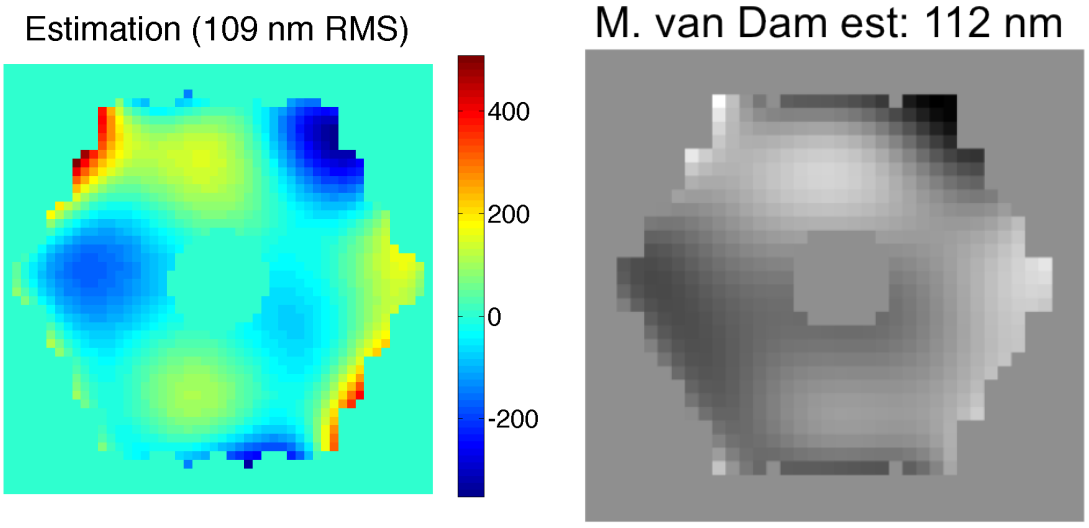

Figure 5.27: Left: the phase of the LOR estimated with the first 28 Zernike modes. Right: the phase estimation from the same images with the Phase Diversity algorithm of Marcos van Dam (private communication). The RMS WFE is nearly identical, and the estimated phase is very similar in features.

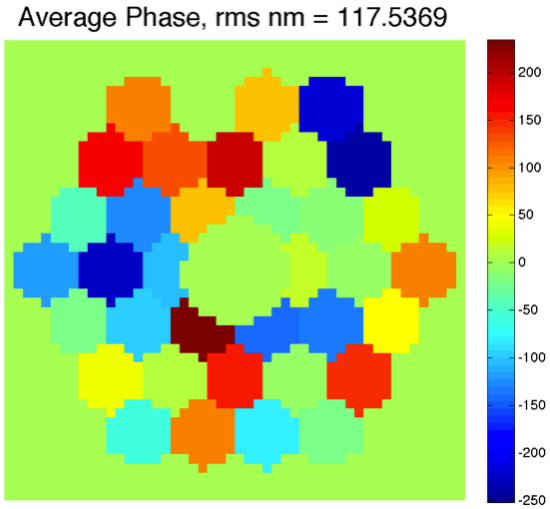

Figure 5.28: Segment piston error estimation average from 50 different image in/out of focus pairs. If the LOR are indeed entirely due to co-phasing errors, this phase map indicates the degree to which each segment is out of phase.

sequential images and would be a useful comparison to the complementary approach of using long exposure images for phase estimation (Mugnier et al., 2006). Given an aberrated image subject to 153 nm RMS WFE of simulated co-phasing errors, we can estimate the phase to within an 29 nm RMS. Assuming a perfect correction of this estimate can be applied to the mirror segments, this would result in a Strehl increase of 12% for our simulated NIRC2 images. A direct result of such a fix would decrease the exposure time on faint sources by a factor of 1.3 to achieve the same SNR if no fix was applied.

On-sky data

The Phase Diversity approach developed in simulation has been applied to on-sky Keck data to estimate the 'Low Order Residual' errors commonly seen in closed loop with the NIRC2 system. The results of our technique appear to be in reasonable agreement with an independent study conducted by Marcos van Dam. Our technique was then applied to estimate the average co-phasing error over the sequence of 50 in/out of focus image pairs, which should be a reasonable representation of the co-phasing error that night given these errors are static and that the variation seen in each phase estimation is the result of closed loop AO residuals. The average wavefront error found over the sequence of these 50 images was 118 nm RMS. The question

as to what the actual nature of the Low Order Residuals are still remains open. Disentangling potential co-phasing errors from the internal NCPA with on-sky data would be useful exercise. This could be achieved by pointing the telescope at a bright star and first acquiring in/out-of focus images, then subsequently using the internal calibration source of NIRC2 to acquire in/out-of focus images. Phase Diversity could then be used to estimate the intrinsic NCPA of NIRC2 from the calibration source, and then to estimate the co-phasing + NCPA errors from the on-sky source; the true co-phasing errors could be extracted from these two measurements.

5.9 Summary and Conclusions

In this chapter, the focal plane wavefront sensing methods put forth in Chapter 4 are applied to estimate the as yet uncorrectable wavefront errors of two major telescope AO systems: the LWE on SPHERE and the co-phasing errors on Keck. The methods are shown to be an effective quantifcation of these effects in simulation. The simulation is extended to an experimental bench and to on-sky data for the case of the LWE on SPHERE. Finally, we briefly apply the Keck LOR techniques developed in simulation in Section 5.6 to on-sky data acquired with Keck/NIRC2; the results show Phase Diversity could be a promising technique in identifying any co-phasing errors with the Keck mirror segments that could be used in the future to correct this issue.

Sections of this Chapter are modified from a publication recently submitted to JATIS (Lamb et al. 2017b, in prep.), which has now been through a second iteration with reviewers. The original submission to JATIS was very similar to a previous SPIE publication (Lamb et al., 2016b). The diversity parameters associated with Phase Diversity are unique to this application and explains why these parameters differ from those explored in Chapter 4.

Chapter 6

Conclusions

As outlined in the introduction, the goal of my thesis is to address the statements below:

- **(i)** Develop spectroscopic data-analysis techniques in the near-infrared (NIR), show they are robust, and use them to observe metal-poor stars in Milky Way globular clusters.
- **(ii)** Use these infrared techniques along with Adaptive Optics (AO) technology to observe metal-poor stars in the Galactic Centre.
- **(iii)** Develop and apply methods to correct the internal aberrations in the AO system used to make the aforementioned observations, and explore the applications of these methods to current and future AO systems.

I now summarize the findings in my thesis, and how they relate to the above statements.

6.1 Develop spectroscopic data-analysis techniques in the infrared, show they are robust, and use them to observe metal-poor stars in Milky Way globular clusters

In Section 2 a detailed chemical abundance analysis was performed for two RGB stars in NGC 5024 and three RGB stars in NGC 5466. In this analysis, we have found:

- The optical and infrared abundances are in good agreement for the elements Fe, Mg, Si, Ca, and Ti. There is a discrepancy in the oxygen abundances, which has been seen before in the literature. We favour our IR oxygen abundances, determined from several OH features.

- The neutron-capture elements are mildly enriched in s-process yields from metal-poor AGB stars.

- The stars in both clusters exhibit CNO mixing, as evidenced from the enhanced N, depleted C, and solar [(C+N)/Fe] ratios. One star NGC5466-9951 shows slight enhancements in Na and Al as well, which suggests it may be a member of a second generation population.

- Both globular clusters show element ratios that are similar to other Galactic clusters at this metallicity, however NGC5466 may have a larger spread in the iron abundances and a larger velocity distribution. This may be due to one star (NGC5466-10186) in a binary system, or it may represent a physical property of this cluster. Other clusters with metallicity and velocity dispersions similar to this include Omega Cen and M54, both accreted from the Sgr dwarf galaxy.

We conclude that abundances derived from both the optical and infrared regions complement each other in a stellar atmospheres analysis, and that NGC5024 and NGC5466 appear to be similar to the majority of Galactic globular clusters. Further spectroscopic analysis of NGC5466 is needed to confirm its apparent metallicity and velocity dispersion. The infrared techniques developed in this analysis are robust and can be confidently applied to other infrared spectroscopic data (such as the MOAO instrument RAVEN).

6.2 Using the Multi-Object Adaptive Optics system RAVEN to search for Metal-Poor stars in the Galactic Centre

Using the infrared techniques developed in statement **(i)**, a detailed chemical abundance analysis has been performed in Section 3 on the H band IR spectra for metal-poor stars in and towards the Galactic Centre. These spectra were taken with the

newly developed technology of MOAO, using the RAVEN science demonstrator and IRCS detector at the Subaru 8.2-m telescope. In this analysis, we have found:

- The technical feasibility of MOAO on an 8-m telescope has been a success for high resolution spectroscopy. We report the first use of MOAO with high resolution spectroscopy, which is a crucial step in the science demonstration of this technology for the future ELT era. We demonstrate the benefits of MOAO and GLAO on the uncorrected PSF, yielding an on-average improvement of 0.2" in seeing, along with a 2-3 times flux gain through the spectroscopic slit. We also demonstrate these observations are successful when observing dusty, crowded regions within the MW.

- Five metal-poor stars in and towards the Galactic Centre have been identified and their chemical abundances were derived for 12 elements. Two of these stars belong to the globular cluster M22, while three of these stars are currently situated in the bulge.

- The two M22 stars have metallicities and element abundance ratios in common with other spectroscopic analyses (Marino et al. (2011); Alves-Brito et al. (2012)). Our CNO abundances are in common with the more metal-poor subpopulation in M22 and CNO-mixing, although we suggest the initial abundances may have been slightly higher than scaled-solar.

- The three metal-poor bulge candidates in this paper are in a metallicity regime with little to no previous high-resolution measurements (-1 $<$ [Fe/H] $<$ -2.5 dex). One out of three of our bulge candidates (MA8) has an orbit that suggests its a transiting halo object; its chemistry shows some unique abundance characteristics that could imply it was captured from an accreted dwarf galaxy. Our two other stars (MA11 and MA14) may be bulge members based on both their kinematic and elemental properties. We note the large variation in orbit calculations when using two different proper motion catalogues. Future work on bulge members will benefit from the improved precision in the GAIA proper motions.

- The future of MOAO, and even GLAO, can benefit from the strategies developed for our observations, and from the lessons learned; we have summarized these strategies in order to facilitate the future use of this technology, which to date

has had very little to no documented use. We anticipate that in the coming ELT-era many interesting science cases will be developed specifically for the use of MOAO.

Therefore through the thesis statement **(i)**, thesis statement **(ii)** has been achieved, providing measurements of some of the most metal-poor stars observed to date in the Galactic Centre. This concludes the astronomically scientific portion of my thesis, and the final thesis statement regarding instrumentation will now be summarized. As previously mentioned, these observations could have conceivably been achieved using other AO facilities - such as Keck/NIRSPEC - and that the main purpose of these observations was to demonstrate the nascent technology of MOAO.

6.3 Develop and apply methods to correct the internal aberrations in the Adaptive Optics system used to make the aforementioned observations, and explore the applications of these methods to current and future Adaptive Optics systems

Through Chapters 4 and 5, I have developed and refined two techniques to quantify wavefront errors at the focal plane of an adaptive optics system. These techniques were shown in simulation that they will be effective in estimating the non-common path errors of the NFIRAOS adaptive optics system for the Thirty Meter Telescope. In addition to our experimental bench, these techniques were also used to estimate focal plane wavefront errors on the following AO systems: Subaru/RAVEN, HeNOS, VLT/SPHERE, and Keck/NIRC2. The summary of our findings directly address the thesis statement **(iii)**; their results from both simulation and real data are summarized for each Section below:

6.3.1 Characterization of NFIRAOS-like NCPA in simulation

Chapter 4, Section 4.1, the operational effects of Phase Diversity and Focal Plane Sharpening has been explored in simulation, and we draw the following conclusions:

- Single image Phase Diversity was shown to be effective in a noiseless scenario. We show the range of diversity over which the technique is successful. This technique is applied to realistic on-sky images in Section 5 to both successfully estimate the low wind effect on SPHERE and the low order segment piston errors on Keck.

- We explore the estimation of both Zernike modes and Disk Harmonics in a simple NCPA estimation scenario and show that both are comparable. This is important considering high order Disk Harmonic modes are more easily formed on a DM than their Zernike counterparts, thus leading us to conclude that if you can estimate Disk Harmonics to the same accuracy of Zernikes then they are a superior means to characterize the NCPA.

- We show that when estimating the first 13 radial orders of modes on a NFRIAOS-like system, we appear to achieve a threshold performance of the bases we are using where estimations using Disk Harmonics outperforms Zernike modes. Furthermore, estimating the object along with the phase yields the best results, however it takes a perhaps unrealistic amount of computation time on our machine. When considering the assumption of a point source and multiple diverse images, the performance is almost as comparable as the object-estimation case and runs in a much shorter amount of time; specifically for the case of estimating Disk Harmonics it took 26 times longer to estimate the object than to use use two diverse images and assume a point source. We explore a range of diversities and combination of images and conclude that using focus is the best choice, along with several images at asymmetric positions on either side of the focal plane. When these considerations are met the estimation is accurate regardless of the signal to noise. Finally, we find that estimating the first 11 radial orders with Phase Diversity and then the remaining 2 with Focal Plane Sharpening did not do as well as our best Phase Diversity cases. However, based on the visualization of the estimated modes (see Figure 4.5) it seems the best approach

might be to use FPS on the first 4 radial orders, and then follow up with Phase Diversity for the higher modes; this will be considered in future studies.

6.3.2 Characterization of NFIRAOS-like NCPA on an experimental bench

In Chapter 4, Section 4.2 we explore two focal plane wavefront sensing techniques and compare their abilities to estimate and correct NFIRAOS-like non-common path aberrations on an experimental bench. Using the SHWFS as a reference wavefront sensor, we conclude the following:

- Between the two methods, we found that Phase Diversity provides the best PSF correction to the phase screen, improving the Strehl ratio from ∼36% to ∼81%; Focal Plane Sharpening improves the Strehl to ∼75% while the SHWFS can achieve a Strehl of ∼ 85% in closed loop after appling an NCPA correction. It is worth noting that the SHWFS represents the ideal correction and could never realistically be applied as an NCPA estimator.

- When examining the first 10 radial orders (the maximum correctable modes by the DM), the wavefront of the phase screen (as measured by the SHWFS) is better characterized by Phase Diversity than Focal Plane Sharpening. We consider that Focal Plane Sharpening may work better in an AO system with smaller residual errors or in a reliable open loop scenario where the DM does not significantly drift in shape over time. Given the fact that Focal Plane Sharpening is not model dependent, unlike the Phase Diversity technique, it would be worth considering using Focal Plane Sharpening on a more stable AO system. However, if the signal to noise of the image is considerably poor, Focal Plane Sharpening may be the only viable option as was determined in simulation in Chapter 5.1.

- In the context of correcting the NFIRAOS NCPA, we recommend using at least two iterations of Phase Diversity based on the results of this work. In addition, we also find that multiple diverse images improve the estimation, where each is subject to at minimum *one* λ P-V focus error.

6.3.3 Characterizing the NCPA on two AO systems: RAVEN and HeNOS

From the techniques developed in Chapter 4, Sections 4.1 and 4.2, we were able to quantify the NCPA in two AO systems: RAVEN and HeNOS. From the analysis shown in Section 4.3 we conclude:

- The correction of NPCA on the RAVEN system allowed the on-axis PSF in one science channel to improve from 50% to 79% Strehl. The correction was achieved with Focal Plane Sharpening and was applied to almost every science observation taken throughout the three engineering runs. The correction led to a significant improvement in the performance of the AO system.
- Using Phase Diversity on the four HeNOS LGS stars, the off-axis NCPA were estimated for each star. The technique was applied every 15 minutes over the course of 14 hours in order to establish a relationship between the NCPA (in terms of individual Zernike modes) and bench temperature. A temperature drop of $\sim$ 1 degree Celsius resulted in a variation of up to 25 nm RMS in focus error, establishing a need for better temperature stabilization. The room has since been outfitted with an air conditioning unit.

6.3.4 Applications of Phase Diversity and Focal Plane Sharpening to VLT and Keck

VLT/SPHERE and the Low Wind Effect

In Chapter 5, Sections 5.1 - 5.5, segmented pupil error phase discontinuities representing the Low Wind Effect were estimated for the VLT/SPHERE system.

Simulated data: Segmented pupil error phase discontinuities were first successfully estimated for a realistically simulated scenario on the VLT/SPHERE system. From this work we conclude:

- For SPHERE: typical DTTS imaging conditions make it difficult for 'Classic' Phase Diversity, and we propose 3 solutions that improve the estimation, which we show in simulation. The best phase estimation was achieved by using Phase Diversity with object estimation applied to long exposure images with higher

SNR than typical DTTS images. However, our simulation does not model the long exposure AO residual effects such as servo-lag, aliasing and fitting error which could degrade performance slightly in practice. If these AO residuals have a larger than desired impact on the Phase Diversity estimation, we can achieve a reasonably good LWE estimation by either using a higher diversity mode or leaving out the object estimation (and assuming a point-source). The latter method is less computationally expensive with respect to any phase plus object estimation.

- If using the non-object estimation method described in Section 5.3.3, then Focal Plane Sharpening will improve the image (on top of the Phase Diversity estimation) in around 60 iterations, which is around 1-2 minutes assuming each image takes ∼1 second to expose. However, if presented with the full aberration that induces the LWE, Focal Plane Sharpening can take more than twice this number of iterations. Note, however, that Focal Plane Sharpening can work on extremely low SNR (∼ 10) DTTS images.

- We find that running low SNR FPS on top of low SNR Phase Diversity yields roughly the same estimate as the best case Phase Diversity estimation, where a high SNR (i.e. long exposure) is required.

- Single image Phase Diversity is a useful technique for estimating the LWE. If using a single image with the natural focus on the DTTS imager, we find that this technique can estimate the LWE to almost the same accuracy as two images with no object estimation (using +1 and -2 waves of focus). However, two images *with* object estimation significantly improves the phase estimation, albeit higher SNR on the images is required. The single image approach could be useful considering sequential on-sky images will have evolution from one image to the next - an effect known to cause issues with Phase Diversity in the past (Jolissaint et al., 2012). Lamb et al. (in prep) are currently analyzing on-sky DTTS data taken during a LWE sequence to further explore the feasibility of single image Phase Diversity.

- To reach the target contrast of 10^{-6} for the SPHERE planet imager, the LWE must be estimated to within an error of 30 nm RMS, as discussed in Section 5.1. We find this goal can be achieved when using 'Classic' Phase Diversity (an in/out of focus image with object estimation), if the SNR of the in-focus

image is ∼700. The error on this estimation roughly doubles when we use Phase Diversity with a single DTTS image with a natural 20 nm RMS of focus on an image with a SNR 70. We conclude that at a small sacrifice in Strehl (∼ 4%) and therefore contrast, single DTTS images with no manipulation could be used to quantify the LWE.

- The correction of the LWE effect using the wavefront control capabilities of SPHERE is complex, and not studied in this paper. The SPHERE system will benefit from a change of the spider coating in the near future, which could decrease the amplitude of the effect if it is indeed due to pupil temperature variations. Ideally the addition of this coating, combined with some sort of wavefront control scheme from the LWE estimation will be able to correct for the LWE that currently has a very negative impact on SPHERE performance. Some recent tests aim to prove that SPHERE wavefront control is able to produce the corresponding amplitude estimates of LWE (Sauvage et al. in prep.).

Bench and on-sky data: The LWE was estimated using single images on the SPHERE/DTTS imager on a night subject to a strong LWE. The techniques developed to do this were first validated on an experimental bench, and then subsequently applied to the DTTS data. The DTTS data consisted of ∼13000 images gathered over the course of the night at two second intervals; we estimated the LWE phase for each image and focus in particular on two subsets of this data: a strong LWE sequence over the course of one minute, and a strong LWE sequence over the course of one hour. The following statements below summarize our findings:

- Similar to our results in Section 5.3.2, single image phase diversity appears to be working using only the 20 nm RMS focus as our diversity.

- The estimation algorithm *at minimum* is a tool available to monitor the LWE; at the very least for P-V observations but it seems a single image is enough to fully characterize the system. Of course, if this technique was used in situ at the telescope, it would be desirable to put some known focus on the image an use traditional phase diversity in order to confirm this.

- We present the evolution of the LWE over a one-minute sequence. The particular sequence chosen shows some of the strongest LWE aberrations of the night, and even though we see a minor variation over the course of short timescales (i.e.

one minute) this may not be reflective of all LWE cases. Considering the Peak-to-Valley WFE has a standard deviation of 62 nm over the one-minute squence, it seems if a correction were quantified every minute (with a corresponding update to the reference slopes with this estimate) then the LWE could be corrected to within this error.

- Evolution over a one-hour sequence: The 'episodic' nature of the LWE over the course of one hour further justifies the need for a quantification on the order of minutes as opposed to hours. The distinct nature of the three episodes shown in this work are not entirely known and may correspond to abrupt changes in wind direction (the wind speed is so slow that this is possible). However the determination of these features remains outside the scope of this work.

- Applying a correction: the algorithm requires only a few seconds to estimate the effect; as such an estimate and determination of offset slopes for the SHWFS is achievable many times per minute, and meets the requirements our suggestion of correcting at least once per minute be ideal.

- The applications Phase Diversity on high contrast imaging systems is an extremely desirable tool; as such we are exploring the capabilities of the technique developed here for the estimation of low order aberrations on the Gemini Planet Imager (GPI).

Estimation of segment piston errors on Keck

In Chapter 5, Sections 5.6 - 5.8 we demonstrate the estimation of the Keck co-phasing errors using both simulated and on-sky data:

Simulated data: Phase segment piston errors were successfully estimated for Keck / NIRC2 simulated images with the assumption that images can be acquired nearly instantaneously (i.e. with 'frozen' turbulence). This assumption should not be too unreasonable considering the shutter speed of the detector is the only limitation (the availability of bright stars should not be an issue). We show the capability of using Phase Diversity with a single, diverse image; this technique avoids any significant evolution effects between sequential images and would be a useful comparison to the complementary approach of using long exposure images for phase estimation (Mugnier et al., 2006). Given an aberrated image subject to 153 nm RMS WFE of simulated

co-phasing errors, we can estimate the phase to within an 29 nm RMS. Assuming a perfect correction of this estimate can be applied to the mirror segments, this would result in a Strehl increase of 12% for our simulated NIRC2 images. A direct result of such a fix would decrease the exposure time on faint sources by a factor of 1.3 to achieve the same SNR if no fix was applied.

On-sky data: The Phase Diversity approach developed in simulation has been applied to on-sky Keck data to estimate the 'Low Order Residual' errors commonly seen in closed loop with the NIRC2 system. The results of our technique appear to be in reasonable agreement with an independent study conducted by Marcos van Dam. Our technique was then applied to estimate the average co-phasing error over the sequence of 50 in/out of focus image pairs, which should be a reasonable representation of the co-phasing error that night given these errors are static and that the variation seen in each phase estimation is the result of closed loop AO residuals. The average wavefront error found over the sequence of these 50 images was 118 nm RMS. The question as to what the actual nature of the Low Order Residuals are still remains open. Disentangling potential co-phasing errors from the internal NCPA with on-sky data would be useful exercise. This could be achieved by pointing the telescope at a bright star and first acquiring in/out-of focus images, then subsequently using the internal calibration source of NIRC2 to acquire in/out-of focus images. Phase Diversity could then be used to estimate the intrinsic NCPA of NIRC2 from the calibration source, and then to estimate the co-phasing + NCPA errors from the on-sky source; the true co-phasing errors could be extracted from these two measurements.

Appendix A

Additional Information

A.1 Derived log abundances

Table A.1: Atomic lines and derived log abundances

Element	Lambda (Å)	χ (eV)	log gf	M22-MA4	M22MA4.1	MA8	MA11	MA14	M15K341
FeI	15051.75	5.35	0.21	-	5.83	-	6.01	5.68	-
	15194.49	2.22	-4.76	-	-	-	-	5.58	-
	15207.53	5.39	0.17	5.32	5.43	-	5.91	5.38	4.97
	15219.62	5.59	-0.03	5.47	5.53	-	6.01	5.18	-
	15294.56	5.31	0.75	5.17	5.28	5.23	5.61	5.28	4.92
	15394.67	5.62	-0.23	-	5.48	-	5.91	5.38	-
	15395.72	5.62	-0.30	-	-	-	6.01	5.58	-
	15531.75	5.64	-0.54	-	-	-	-	5.58	-
	15588.26	6.37	0.32	-	-	-	5.91	-	-
	15591.50	6.36	0.95	5.37	5.63	5.53	6.06	5.33	-
	15604.22	6.24	0.44	5.52	5.68	-	6.06	5.23	
	15621.65	5.54	0.35	5.27	5.53	-	5.91	5.38	5.12
	15631.95	5.35	-0.02	5.42	5.48	-	6.16	5.38	5.42
	15648.51	5.43	-0.66	-	5.68	5.93	6.01	5.38	-
	15662.02	5.83	0.18	-	-	-	5.91	-	5.32
	15677.52	6.25	0.21	-	5.78	-	6.01	5.63	-
	15686.44	6.25	0.11	-	5.73	-	6.06	5.53	-
	15691.86	6.25	0.47	5.67	5.58	-	5.96	5.38	5.47
	15723.59	5.62	0.03	-	5.63	-	5.96	5.28	-
	15741.92	5.65	-0.40	-	-	-	6.11	5.58	5.77
	15769.42	5.54	-0.01	5.72	5.83	-	6.16	5.58	5.42
	15789.00	6.25	0.32	5.82	-	-	6.11	-	-
	15798.56	6.25	0.34	-	5.78	-	6.16	-	-
	15818.14	5.59	0.32	5.52	5.63	5.33	5.96	5.28	5.27
	15822.82	5.64	-0.10	5.67	5.73	5.83	5.96	-	-
	15835.17	6.30	0.67	-	5.58	5.33	5.86	5.68	5.57
	15837.65	6.30	0.16	-	5.98	-	5.96	5.78	-
	15868.52	5.59	-0.25	-	5.33	-	5.91	5.08	5.22
	15878.44	5.62	-0.48	-	-	-	-	5.83	-
	15895.23	6.26	0.28	-	-	-	6.16	-	-
	15906.04	5.62	-0.16	-	5.43	5.43	-	5.48	-
	15980.73	6.26	1.12	4.92	5.43	-	5.71	-	-
	16006.76	6.35	0.63	-	-	-	5.91	-	-
	16009.61	5.43	-0.53	5.87	5.58	5.38	6.06	-	5.52
	16040.66	5.87	0.12	-	5.63	-	6.11	-	-
	16042.71	6.26	0.02	-	-	-	6.01	-	-
	16102.41	5.87	0.26	5.47	-	5.68	5.96	5.58	-
	16115.97	6.39	0.32	-	-	5.83	5.96	-	-
	16125.90	6.35	0.69	5.27	5.73	5.23	5.91	5.73	5.32
	16153.25	5.35	-0.70	-	5.58	5.68	6.01	-	5.52
	16165.03	6.32	0.79	5.62	5.73	6.03	6.16	5.48	-
	16174.95	6.38	0.01	-	-	-	6.06	5.73	-
	16198.50	5.41	-0.49	5.47	5.63	-	5.81	-	-
	16231.65	6.38	0.51	5.57	-	-	-	-	-
	16316.32	6.28	1.12	5.42	5.23	5.78	5.86	5.08	4.92
	16324.45	5.39	-0.55	-	5.53	-	5.86	5.28	5.42
	16444.82	5.83	0.41	-	-	-	6.26	-	-
	16486.67	5.83	0.52	5.62	5.78	5.53	5.91	5.48	5.25
	16506.30	5.95	-0.37	-	-	-	-	5.53	-
	16517.23	6.29	0.56	5.62	5.38	5.53	6.11	5.43	-
	16524.47	6.34	0.64	-	5.63	-	6.06	-	-
	16541.43	5.95	-0.40	-	-	-	5.96	5.58	-
	16552.00	6.41	0.12	-	-	-	6.26	-	-
	16561.77	5.98	0.11	5.47	5.53	5.33	6.11	5.28	-
	16969.91	5.95	-0.20	-	-	-	5.81	5.59	-

Table A.2: Atomic lines and derived log abundances - continued

Element	Lambda (Å)	χ (eV)	log gf	M22-MA4	M22MA4.1	MA8	MA11	MA14	M15K341
Mg	15024.99	5.11	0.37	-	5.77	-	6.55	5.90	-
	15040.25	5.11	0.13	-	5.92	-	6.55	6.00	-
	15047.71	5.11	-0.37	-	5.77	-	6.30	5.90	-
	15740.72	5.93	-0.26	6.05	5.82	5.75	6.40	5.80	5.47
	15748.99	5.93	0.17	5.80	5.87	6.00	6.55	5.70	5.57
	15765.84	5.93	0.44	5.75	5.82	5.85	6.55	5.65	5.52
	15879.57	5.95	-1.30	6.25	-	-	6.45	-	-
	15886.18	5.95	-1.65	-	6.17	-	6.75	-	-
	16624.72	6.73	-1.48	-	-	-	6.85	-	-
	16632.02	6.73	-1.31	-	-	-	6.85	-	
Al	16718.96	4.09	0.29	4.04	4.26	4.49	5.14	3.99	4.06
	16750.56	4.09	0.55	4.24	4.21	4.24	5.24	4.09	3.96
	16763.36	4.09	-0.53	-	4.56	-	5.14	-	-
Si	15376.83	6.22	-0.58	6.07	5.99	-	6.28	5.87	-
	15557.78	5.96	-0.68	6.07	5.74	5.87	6.18	5.77	5.54
	15833.60	6.22	-0.17	6.22	5.69	5.62	6.20	5.52	5.24
	15884.45	5.95	-0.69	5.52	5.69	5.72	6.15	-	5.54
	15888.41	5.08	0.02	6.17	5.69	5.72	6.20	5.77	5.44
	16060.01	5.95	-0.48	5.82	5.79	5.92	6.25	5.77	5.44
	16094.79	5.96	-0.16	5.52	5.84	5.62	6.35	5.67	5.54
	16163.69	5.95	-0.94	5.82	5.94	5.82	6.45	5.87	5.64
	16215.67	5.95	-0.60	5.52	5.84	5.62	6.30	5.77	5.24
	16241.83	5.96	-0.77	5.82	5.79	5.52	6.30	5.72	5.24
	16434.93	5.96	-1.15		-	-	6.15	-	-
	16680.77	5.98	-0.06	5.12	5.74	5.72	6.35	5.67	5.24
	16828.16	5.98	-1.08	5.52	5.74	-	6.65	5.87	5.64
S	15403.72	8.70	-0.14	5.73	5.80	5.73	5.93	-	-
	15469.82	8.05	-0.15	6.08	-	5.88	6.13	-	-
	15478.48	8.05	0.08	5.48	5.60	-	-	-	-
Ca	16150.76	4.53	-0.17	-	4.55	4.38	5.08	4.43	-
	16155.24	4.53	-0.58	4.53	-	4.98	5.18	4.88	-
	16157.36	4.55	-0.14	4.63	4.65	4.78	5.13	-	-
	16197.08	4.54	0.16	4.63	4.15	-	5.08	4.48	-
Ti	15334.85	1.89	-1.00	3.61	3.48	3.11	-	-	-
	15543.76	1.88	-1.12	3.56	2.98	3.41	<3.66	<3.16	-
Mn	15159.14	4.89	-0.06	<3.66	<3.48	-	3.86	<3.31	<3.08
	15217.76	4.89	-0.19	-	-	-	3.86	-	-
	15262.50	4.89	-0.27	-	-	-	4.11	-	-
Ni	15555.42	5.49	0.10	4.47	4.64	5.02	-	-	-
	15605.68	5.30	-0.45	4.77	-	-	4.92	4.47	-
	15632.65	5.31	-0.04	4.22	-	-	4.72	4.17	-
	16136.16	5.49	-0.14	-	-	-	4.62	-	-
	16310.50	5.28	0.00	4.52	4.24	4.12	4.22	3.87	3.91
	16363.11	5.28	0.37	4.52	-	-	-	3.97	3.41
	16589.29	5.47	-0.55	-	-	-	-	-	4.51
	16673.71	6.03	0.39	-	-	-	4.92	-	-
	16996.27	5.30	0.34	-	4.29	-	4.72	4.17	-

Table A.3: Molecular features used to derive C, N, and O and their log abundances

Element	Lambda interval (Å)	M22-MA4	M22MA4.1	MA8	MA11	MA14	M15K341
C from CO lines	15582-15590	6.93	6.75	-	6.73	6.34	6.15
	15780-15788	-	6.85	6.68	6.93	5.94	6.15
	15977-15997	-	6.80	-	6.33	-	6.27
	16000-16018	5.98	-	-	6.53	5.89	-
	16182-16189	6.37	6.60	-	6.33	-	5.82
	16217-16229	-	-	-	-	-	-
	16304-16309	-	-	7.03	-	-	-
	16475-16485	-	-	6.68	-	6.14	-
	16609-16649	-	6.65	6.73	6.63	-	-
	16667-16679	-	6.95	7.23	-	-	-
	16690-16702	-	-	6.98	-	5.79	-
	16836-16851	-	-	6.63	-	-	-
O from OH lines	15002	7.50	7.32	-	7.80	7.55	-
	15004	-	-	-	7.40	7.45	-
	15021	-	7.72	-	7.55	7.45	-
	15023	-	-	-	7.40	7.40	-
	15129	-	7.02	-	-	7.30	6.82
	15131	-	-	-	7.40	7.40	7.07
	15145	-	7.32	-	7.50	7.35	6.82
	15148	-	-	-	-	-	6.87
	15237	-	-	-	7.30	7.15	-
	15266	-	7.22	7.50	7.20	7.30	6.97
	15279	7.60	7.17	7.90	-	7.35	7.02
	15281	7.35	-	7.60	-	7.30	7.02
	15392	-	-	7.75	7.10	7.25	6.72
	15409	-	7.32	7.55	-	7.30	6.92
	15422	-	7.22	7.45	7.55	7.35	6.97
	15560	-	7.42	7.55	-	-	6.92
	15569	-	7.32	7.50	-	7.30	6.82
	15572	-	7.22	-	7.50	7.35	7.07
	15627	-	7.02	7.40	-	7.30	7.09
	15652	-	7.42	7.40	7.50	7.30	7.07
	15654	-	7.42	7.50	7.45	7.35	7.07
	15719	-	7.22	7.65	7.45	7.25	-
	15726	7.50	-	7.90	7.40	7.30	7.02
	15755	-	-	7.70	-	-	6.92
	15756	7.20	7.37	-	7.60	7.25	6.62
	15893	-	-	7.40	-	7.35	-
	15911	7.20	7.12	7.85	7.60	7.35	6.97
	16037	-	7.42	-	7.40	7.15	6.87
	16039	-	7.22	7.70	-	-	6.97
	16052	-	7.12	7.80	7.75	7.30	6.92
	16061	-	7.12	7.65	-	-	6.77
	16065	-	7.27	7.60	-	-	-
	16069	-	6.92	7.35	-	-	6.92
	16074	-	7.22	7.50	-	-	-
	16190	-	-	-	-	7.15	-
	16192	-	-	-	-	7.05	-
	16248	-	-	-	-	-	6.92
	16252	-	7.22	7.45	-	-	6.97
	16255	-	7.12	7.65	-	-	6.92
	16260	-	7.22	7.00	-	-	6.92
	16313	7.10	7.37	7.70	7.55	7.15	-
	16346	-	7.72	7.50	-	-	-
	16348	-	7.02	-	-	-	-
	16352	-	7.12	7.75	-	-	6.72
	16354	-	7.42	7.35	-	-	6.97
	16368	-	-	-	-	7.20	-
	16448	-	7.37	-	7.60	7.25	-
	16450	7.20	7.32	-	7.75	7.10	-
	16456	-	7.37	-	6.90	7.30	-
	16523	-	7.17	-	7.40	7.25	-

Table A.4: Molecular features used to derive C, N, and O - continued

Molecular lines	Lambda interval (Å)	M22-MA4	M22MA4.1	MA8	MA11	MA14	M15K341
O from OH lines	16526	-	-	7.45	7.45	7.20	6.87
	16535	7.30	7.27	-	7.15	7.30	6.97
	16539	7.50		7.70	7.45	7.05	6.92
	16605	-	7.12	7.60	7.70	7.15	7.22
	16608	-	-	7.70	-	-	7.22
	16704	-	-	7.55	7.40	7.15	6.82
	16708	7.20	-	7.75	7.10	7.05	6.77
	16714	-	-	7.80	-	-	6.82
N from CN lines	15004	-	6.04	-	-	6.57	-
	15012	-	6.29	-	6.92	-	-
	15034-15036	-	-	-	-	6.87	-
	15048	-	-	-	6.92	-	-
	15052	-	-	-	7.02	-	-
	15106	-	-	-	7.02	-	-
	15118	-	-	-	6.87	6.67	-
	15128	-	-	-	-	7.07	-
	15134-15139	-	6.74	-	-	-	6.34
	15142	-	-	-	-	-	6.34
	15150-15166	-	6.34	-	-	6.67	6.34
	15184-15200	-	6.19	-	6.82	6.97	6.14
	15210	-	-	-	6.82	6.97	-
	15222	-	-	-	-	6.87	-
	15228	-	-	-	-	6.77	-
	15242	6.88	6.19	-	-	-	-
	15251-15254	-	6.19	-	6.77	6.62	6.29
	15284-15287	-	-	6.62	-	-	-
	15308-15323	6.23	-	6.27	6.92	6.82	6.09
	15328	-	-	-	-	-	6.09
	15351-15362	6.53	6.04	6.37	6.82	6.77	-
	15363	-	-	6.87	-	-	-
	15389	-	-	6.17	6.62	-	-
	15400	-	-	6.62	-	-	-
	15411	-	6.19	-	-	-	6.39
	15432	-	-	-	7.02	-	-
	15448	-	6.54	-	-	-	-
	15472	-	6.39	-	-	-	-
	15564	7.13	6.59	-	-	-	-
	15575	-	-	-	6.82	-	-
	15595	-	6.84	-	-	6.72	-
	15636	-	6.19	-	-	6.77	-
	15660	-	6.39	-	7.12	-	-
	15767-15775	-	-	6.12	-	-	-
	15825	-	-	7.02	-	-	-
	16180	-	-	6.52	-	-	-

Bibliography

Allen, C., Moreno, E., & Pichardo, B. 2006, 652, 1150

Alves-Brito, A., Meléndez, J., Asplund, M., Ramírez, I., & Yong, D. 2010, A&A, 513, A35

Alves-Brito, A., Yong, D., Meléndez, J., Vásquez, S., & Karakas, A. I. 2012, A&A, 540, A3

Amarsi, A. M., Asplund, M., Collet, R., & Leenaarts, J. 2016, MNRAS, 455, 3735

Andersen, D. R., Bradley, C., Gamroth, D., et al. 2014, in Proc. SPIE, Vol. 9148, Adaptive Optics Systems IV, 91485K

Anderson, J., Sarajedini, A., Bedin, L. R., et al. 2008, AJ, 135, 2055

Aoki, W., Beers, T. C., Christlieb, N., et al. 2007, ApJ, 655, 492

Arlandini, C., Käppeler, F., Wisshak, K., et al. 1999, ApJ, 525, 886

Asplund, M. 2005, ARAA, 43, 481

Asplund, M., Grevesse, N., Sauval, A. J., & Scott, P. 2009, ARAA, 47, 481

Babusiaux, C., Gómez, A., Hill, V., et al. 2010, A&A, 519, A77

Battaglia, G., Irwin, M., Tolstoy, E., et al. 2008, MNRAS, 383, 183

Beers, T. C., & Christlieb, N. 2005, ARAA, 43, 531

Bellazzini, M., Ferraro, F. R., & Ibata, R. 2003, AJ, 125, 188

Bellman, S., Briley, M. M., Smith, G. H., & Claver, C. F. 2001, PASP, 113, 326

Bensby, T., Feltzing, S., Johnson, J. A., et al. 2010, A&A, 512, A41

Bensby, T., Adén, D., Meléndez, J., et al. 2011, A&A, 533, A134

Bensby, T., Yee, J. C., Feltzing, S., et al. 2013, A&A, 549, A147

Bergemann, M. 2011, MNRAS, 413, 2184

Bergemann, M., & Cescutti, G. 2010, A&A, 522, A9

Bergemann, M., & Gehren, T. 2008, A&A, 492, 823

Bergemann, M., Lind, K., Collet, R., Magic, Z., & Asplund, M. 2012, MNRAS, 427, 27

Bergemann, M., Pickering, J. C., & Gehren, T. 2010, MNRAS, 401, 1334

Beuzit, J.-L., Feldt, M., Dohlen, K., et al. 2008, in Proc. SPIE, Vol. 7014, Ground-based and Airborne Instrumentation for Astronomy II, 701418

Bitenc, U., Bharmal, N. A., Morris, T. J., & Myers, R. M. 2014, Opt. Express, 22, 12438

Bland-Hawthorn, J., & Gerhard, O. 2016, ARAA, 54, 529

Booth, A. J., Shallis, M. J., & Wells, M. 1983, MNRAS, 205, 191

Bovy, J. 2015, ApJS, 216, 29

Burris, D. L., Pilachowski, C. A., Armandroff, T. E., et al. 2000, ApJ, 544, 302

Busso, M., Gallino, R., & Wasserburg, G. J. 1999, ARAA, 37, 239

Buzzoni, A., Patelli, L., Bellazzini, M., Pecci, F. F., & Oliva, E. 2010, MNRAS, 403, 1592

Carretta, E., Bragaglia, A., Gratton, R. G., et al. 2010, A&A, 516, A55

Carretta, E., Gratton, R. G., Lucatello, S., Bragaglia, A., & Bonifacio, P. 2005, A&A, 433, 597

Carretta, E., Bragaglia, A., Gratton, R. G., et al. 2009, A&A, 505, 117

Casey, A. R. 2016, ApJS, 223, 8

Casey, A. R., & Schlaufman, K. C. 2015, ApJ, 809, 110

Cayrel, R. 1988, in IAU Symposium, Vol. 132, The Impact of Very High S/N Spectroscopy on Stellar Physics, ed. G. Cayrel de Strobel & M. Spite, 345

Charbonnel, C. 1995, ApJL, 453, L41

Charbonnel, C., Brown, J. A., & Wallerstein, G. 1998, A&A, 332, 204

Chiappini, C., Frischknecht, U., Meynet, G., et al. 2011, Nat., 472, 454

Chun, M., Wilson, R., Avila, R., et al. 2009, MNRAS, 394, 1121

Chun, S.-H., Kim, J.-W., Sohn, S. T., et al. 2010, AJ, 139, 606

Cohen, J. G., Christlieb, N., McWilliam, A., et al. 2008, ApJ, 672, 320

Cohen, J. G., & Meléndez, J. 2005, AJ, 129, 303

Conan, R., & Correia, C. 2014, in Proc. SPIE, Vol. 9148, Adaptive Optics Systems IV, 91486C

Correia, C. M., Jackson, K., Véran, J.-P., et al. 2015, App. Opt., 54, 5281

Crain, R. A., Schaye, J., Bower, R. G., et al. 2015, MNRAS, 450, 1937

Cunha, K., Smith, V. V., Johnson, J. A., et al. 2015, ApJL, 798, L41

Da Costa, G. S., & Armandroff, T. E. 1995, 109, 2533

Davies, R., & Kasper, M. 2012, ARAA, 50, 305

Dékány, I., & Kovács, G. 2009, 507, 803

Denissenkov, P. A., & VandenBerg, D. A. 2003, ApJ, 593, 509

Diemand, J., Madau, P., & Moore, B. 2005, MNRAS, 364, 367

Dohlen, K., Wildi, F. P., Puget, P., Mouillet, D., & Beuzit, J.-L. 2011, in Second International Conference on Adaptive Optics for Extremely Large Telescopes. Online at ¡A href="http://ao4elt2.lesia.obspm.fr"¿http://ao4elt2.lesia.obspm.fr¡/A¿, id.75

Dotter, A., Sarajedini, A., & Anderson, J. 2011, 738, 74

Dotter, A., Sarajedini, A., Anderson, J., et al. 2010, ApJ, 708, 698

Ebstein, S. M. 1996, Opt. Lett., 21, 1454

Ekström, S., Meynet, G., Chiappini, C., Hirschi, R., & Maeder, A. 2008, A&A, 489, 685

Ellerbroek, B. L., Thelen, B. J., Lee, D. J., Carrara, D. A., & Paxman, R. G. 1997, in Proc. SPIE, Vol. 3126, Adaptive Optics and Applications, ed. R. K. Tyson & R. Q. Fugate, 307

Fattahi, A., Navarro, J. F., Sawala, T., et al. 2016, MNRAS, 457, 844

Fekadu, N., Sandquist, E. L., & Bolte, M. 2007, ApJ, 663, 277

Fienup, J. R., Marron, J. C., Schulz, T. J., & Seldin, J. H. 1993, Appl. Opt., 32, 1747

Finger, G., Baker, I., Dorn, R., et al. 2010, in Proc. SPIE, Vol. 7742, High Energy, Optical, and Infrared Detectors for Astronomy IV, 77421K

Forbes, D. A., & Bridges, T. 2010, 404, 1203

Frebel, A. 2010, Astronomische Nachrichten, 331, 474

Frebel, A., Simon, J. D., Geha, M., & Willman, B. 2010, 708, 560

Gallino, R., Busso, M., Picchio, G., & Raiteri, C. M. 1990, Nat., 348, 298

Gao, L., Theuns, T., Frenk, C. S., et al. 2010, MNRAS, 403, 1283

García Pérez, A. E., Asplund, M., Primas, F., Nissen, P. E., & Gustafsson, B. 2006, A&A, 451, 621

García Pérez, A. E., Cunha, K., Shetrone, M., et al. 2013, ApJL, 767, L9

García Pérez, A. E., Allende Prieto, C., Holtzman, J. A., et al. 2016, AJ, 151, 144

Gendron, E., Vidal, F., Brangier, M., et al. 2011, A&A, 529, L2

Girard, T. M., van Altena, W. F., Zacharias, N., et al. 2011, AJ, 142, 15

Gonsalves, R. A. 1982, Optical Engineering, 21, 215829

Gonzalez, O. A., Rejkuba, M., Zoccali, M., et al. 2011, A&A, 530, A54

Gratton, R., Sneden, C., & Carretta, E. 2004, ARAA, 42, 385

Gratton, R. G., Carretta, E., & Castelli, F. 1996, A&A, 314, 191

Grillmair, C. J., & Johnson, R. 2006, ApJL, 639, L17

Gustafsson, B., Bell, R. A., Eriksson, K., & Nordlund, A. 1975, A&A, 42, 407

Gustafsson, B., Edvardsson, B., Eriksson, K., et al. 2008, A&A, 486, 951

Harris, W. E. 1996, AJ, 112, 1487

Harris, W. E. 2001, Globular Cluster Systems, 223

Harris, W. E. 2010, ArXiv e-prints, arXiv:1012.3224

Hayano, Y., Takami, H., Oya, S., et al. 2010, in Proc. SPIE, Vol. 7736, Adaptive Optics Systems II, 77360N

Heiter, U., & Eriksson, K. 2006, A&A, 452, 1039

Herscovici-Schiller, O., Mugnier, L. M., & Sauvage, J.-F. 2017, Mon. Not. R. Astron. Soc. Lett., 467, L105

Hidalgo, S. L., Aparicio, A., Skillman, E., et al. 2011, 730, 14

Hidalgo, S. L., Monelli, M., Aparicio, A., et al. 2013, 778, 103

Hill, V., François, P., Spite, M., Primas, F., & Spite, F. 2000, A&A, 364, L19

Hill, V., Lecureur, A., Gómez, A., et al. 2011, A&A, 534, A80

Hinkle, K., & Wallace, L. 2005, in Astronomical Society of the Pacific Conference Series, Vol. 336, Cosmic Abundances as Records of Stellar Evolution and Nucleosynthesis, ed. T. G. Barnes, III & F. N. Bash, 321

Hogg, D. W., Blanton, M. R., Roweis, S. T., & Johnston, K. V. 2005, ApJ, 629, 268

Holtzman, J. A., Shetrone, M., Johnson, J. A., et al. 2015, AJ, 150, 148

Howes, L. M., Asplund, M., Casey, A. R., et al. 2014, MNRAS, 445, 4241

Howes, L. M., Casey, A. R., Asplund, M., et al. 2015, Nat., 527, 484

Howes, L. M., Asplund, M., Keller, S. C., et al. 2016, MNRAS, 460, 884

Israelian, G., Shchukina, N., Rebolo, R., et al. 2004, A&A, 419, 1095

Jablonka, P., North, P., Mashonkina, L., et al. 2015, A&A, 583, A67

Jackson, K., Correia, C., Lardière, O., et al. 2014, in Proc. SPIE, Vol. 9148, Adaptive Optics Systems IV, 91482K

Johnson, C. I., Rich, R. M., Kobayashi, C., Kunder, A., & Koch, A. 2014, AJ, 148, 67

Johnson, C. I., Rich, R. M., Kobayashi, C., et al. 2013, ApJ, 765, 157

Jolissaint, L., Mugnier, L. M., Neyman, C., Christou, J., & Wizinowich, P. 2012, in Proc. SPIE, Vol. 8447, Adaptive Optics Systems III, 844716

Jönsson, H., Ryde, N., Nissen, P. E., et al. 2011, A&A, 530, A144

Jordi, K., & Grebel, E. K. 2010, aa, 522, A71

Jurling, A. S., & Fienup, J. R. 2014, J. Opt. Soc. Am. A, 31, 661

Kacharov, N., Koch, A., Caffau, E., & Sbordone, L. 2015, A&A, 577, A18

Kirby, E. N., Guhathakurta, P., & Sneden, C. 2008, ApJ, 682, 1217

Kiselman, D. 1993, A&A, 275

Kobayashi, N., Tokunaga, A. T., Terada, H., et al. 2000, in Society of Photo-Optical Instrumentation Engineers (SPIE) Conference Series, Vol. 4008, Optical and IR Telescope Instrumentation and Detectors, ed. M. Iye & A. F. Moorwood, 1056–1066

Koch, A., McWilliam, A., Preston, G. W., & Thompson, I. B. 2016, A&A, 587, A124

Kopacki, G. 2000, A&A, 358, 547

Lagarias, J., Reeds, J. A., Wright, M. H., & Wright, P. E. 1998, "SIAM Journal of Optimization", 9, 112

Lamb, M., Andersen, D. R., Véran, J.-P., et al. 2014, in Proc. SPIE, Vol. 9148, Adaptive Optics Systems IV, 914857

Lamb, M., Correia, C., Sauvage, J.-F., Andersen, D., & Véran, J.-P. 2016a, in Proc. SPIE, Vol. 9909, Society of Photo-Optical Instrumentation Engineers (SPIE) Conference Series, 99096E

Lamb, M., Correia, C., Sauvage, J.-F., et al. 2016b, in Proc. SPIE, Vol. 9909, Society of Photo-Optical Instrumentation Engineers (SPIE) Conference Series, 99096D

Lamb, M., Venn, K., Andersen, D., et al. 2017, MNRAS, 465, 3536

Lamb, M. P., Venn, K. A., Shetrone, M. D., Sakari, C. M., & Pritzl, B. J. 2015, MNRAS, 448, 42

Lane, R. R., Kiss, L. L., Lewis, G. F., et al. 2011, A&A, 530, A31

Lardière, O., Andersen, D., Blain, C., et al. 2014, in Proc. SPIE, Vol. 9148, Adaptive Optics Systems IV, 91481G

Lawler, J. E., Bonvallet, G., & Sneden, C. 2001a, ApJ, 556, 452

Lawler, J. E., Wickliffe, M. E., den Hartog, E. A., & Sneden, C. 2001b, ApJ, 563, 1075

Leaman, R., VandenBerg, D. A., & Mendel, J. T. 2013, 436, 122

Lemasle, B., Hill, V., Tolstoy, E., et al. 2012, A&A, 538, A100

Letarte, B., Chapman, S. C., Collins, M., et al. 2009, MNRAS, 400, 1472

Letarte, B., Hill, V., Tolstoy, E., et al. 2010, A&A, 523, A17

Libralato, M., Bellini, A., Bedin, L. R., et al. 2014, A&A, 563, A80

Lind, K., Asplund, M., Barklem, P. S., & Belyaev, A. K. 2011, A&A, 528, A103

Lind, K., Bergemann, M., & Asplund, M. 2012, MNRAS, 427, 50

Mackey, A. D., & van den Bergh, S. 2005, 360, 631

Marino, A. F., Milone, A. P., Piotto, G., et al. 2009, A&A, 505, 1099

Marino, A. F., Sneden, C., Kraft, R. P., et al. 2011, A&A, 532, A8

Martell, S. L., Smith, G. H., & Briley, M. M. 2008, 120, 7

Martínez-Delgado, D., Gómez-Flechoso, M. Á., Aparicio, A., & Carrera, R. 2004, ApJ, 601, 242

Mateluna, R., Geisler, D., Villanova, S., et al. 2012, A&A, 548, A82

McCarthy, J. K., & Nemec, J. M. 1997, 482, 203

McWilliam, A. 1998, AJ, 115, 1640

McWilliam, A., Preston, G. W., Sneden, C., & Searle, L. 1995, AJ, 109, 2757

McWilliam, A., Wallerstein, G., & Mottini, M. 2013, 778, 149

Mehta, C. L. 1965, Il Nuovo Cimento, 36, 202

Meimon, S., Fusco, T., & Mugnier, L. M. 2010, 35, 3036

Meléndez, J., Asplund, M., Alves-Brito, A., et al. 2008, A&A, 484, L21

Mészáros, S., Allende Prieto, C., Edvardsson, B., et al. 2012, AJ, 144, 120

Mészáros, S., Martell, S. L., Shetrone, M., et al. 2015, AJ, 149, 153

Meynadier, L., Michau, V., Velluet, M.-T., et al. 1999, Appl. Opt., 38, 4967

Mishenina, T. V., Kovtyukh, V. V., Soubiran, C., Travaglio, C., & Busso, M. 2002, A&A, 396, 189

Miyamoto, M., & Nagai, R. 1975, PASJ, 27, 533

Monaco, L., Pancino, E., Ferraro, F. R., & Bellazzini, M. 2004, MNRAS, 349, 1278

Monet, D. G., Levine, S. E., Canzian, B., et al. 2003, AJ, 125, 984

Mottini, M., Wallerstein, G., & McWilliam, A. 2008, AJ, 136, 614

Mucciarelli, A., Lapenna, E., Massari, D., et al. 2015, ApJ, 809, 128

Mugnier, L. M., Blanc, A., & Idier, J. 2006, in Advances in Imaging and Electron Physics, ed. P. Hawkes, Vol. 141 (Elsevier), 1–76

Mugnier, L. M., Sauvage, J.-F., Fusco, T., Cornia, A., & Dandy, S. 2008, 16, 18406

Navarro, J. F., Frenk, C. S., & White, S. D. M. 1996, ApJ, 462, 563

N'Diaye, M., Dohlen, K., Fusco, T., & Paul, B. 2013, A&A, 555, A94

N'Diaye, M., Vigan, A., Dohlen, K., et al. 2016, A&A, 592, A79

Ness, M., Asplund, M., & Casey, A. R. 2014, MNRAS, 445, 2994

Ness, M., Freeman, K., Athanassoula, E., et al. 2013, MNRAS, 430, 836

Nissen, P. E., Akerman, C., Asplund, M., et al. 2007, A&A, 469, 319

Okamoto, S., Arimoto, N., Yamada, Y., & Onodera, M. 2012, 744, 96

Ono, Y. H., Correia, C. M., Lardière, O., et al. 2016, in Proc. SPIE, Vol. 9909, Adaptive Optics Systems V, 990910

Paul, B., Sauvage, J.-F., Mugnier, L. M., et al. 2014, Astron. Astrophys., 572, A32

Paxman, R. G., Schulz, T. J., & Fienup, J. R. 1992, Journal of the Optical Society of America A, 9, 1027

Perryman, M. 2012, European Physical Journal H, 37, 745

Pilachowski, C. A., Bothun, G. D., Olszewski, E. W., & Odell, A. 1983, 273, 187

Placco, V. M., Frebel, A., Beers, T. C., & Stancliffe, R. J. 2014, ApJ, 797, 21

Pritzl, B. J., Venn, K. A., & Irwin, M. 2005, AJ, 130, 2140

Prochaska, J. X., Naumov, S. O., Carney, B. W., McWilliam, A., & Wolfe, A. M. 2000, AJ, 120, 2513

Ragland, S., Jolissaint, L., Wizinowich, P., & Neyman, C. 2014, in Proc. SPIE, Vol. 9148, Adaptive Optics Systems IV, 91480S

Ragland, S., Jolissaint, L., Wizinowich, P., et al. 2016, in Proc. SPIE, Vol. 9909, Society of Photo-Optical Instrumentation Engineers (SPIE) Conference Series, 99091P

Ramírez, I., & Meléndez, J. 2005, ApJ, 626, 465

Rampy, R., Ragland, S., Wizinowich, P., & Campbell, R. 2014, in Proc. SPIE, Vol. 9148, Adaptive Optics Systems IV, 91485I

Reddy, B. E., Lambert, D. L., & Allende Prieto, C. 2006, MNRAS, 367, 1329

Robin, A. C., Marshall, D. J., Schultheis, M., & Reylé, C. 2012, A&A, 538, A106

Roddier, C., & Roddier, F. 1991, in Proc. SPIE, Vol. 1494, Space Astronomical Telescopes and Instruments, ed. P. Y. Bely & J. B. Breckinridge, 78–84

Roddier, C., & Roddier, F. 1993, Appl. Opt., 32, 2992

Roederer, I. U., Marino, A. F., & Sneden, C. 2011, ApJ, 742, 37

Roederer, I. U., Preston, G. W., Thompson, I. B., et al. 2014, AJ, 147, 136

Rosensteiner, M., Turri, P., Mieda, E., et al. 2016, in Proc. SPIE, Vol. 9909, Adaptive Optics Systems V, 990949

Rousselot, P., Lidman, C., Cuby, J.-G., Moreels, G., & Monnet, G. 2000, A&A, 354, 1134

Ruchti, G. R., Fulbright, J. P., Wyse, R. F. G., et al. 2010, ApJL, 721, L92

Ryde, N., Gustafsson, B., Edvardsson, B., et al. 2010, A&A, 509, A20

Sakari, C. M., Venn, K. A., Mackey, D., et al. 2015, MNRAS, 448, 1314

Salvadori, S., Ferrara, A., Schneider, R., Scannapieco, E., & Kawata, D. 2010, MNRAS, 401, L5

Salvadori, S., Schneider, R., & Ferrara, A. 2007, MNRAS, 381, 647

Sarajedini, A., Bedin, L. R., Chaboyer, B., et al. 2007, AJ, 133, 1658

Sauvage, J., Fusco, T., Guesalaga, A., et al. 2015, in AO4ELT4, Lake Arrowhead

Sauvage, J.-F., Fusco, T., Petit, C., et al. 2016a, JATIS, 2, 025003

Sauvage, J.-F., Fusco, T., Lamb, M., et al. 2016b, in Proc. SPIE, Vol. 9909, Society of Photo-Optical Instrumentation Engineers (SPIE) Conference Series, 990916

Sawala, T., Frenk, C. S., Fattahi, A., et al. 2016, MNRAS, 457, 1931

Schaye, J., Crain, R. A., Bower, R. G., et al. 2015, MNRAS, 446, 521

Schlegel, D. J., Finkbeiner, D. P., & Davis, M. 1998, ApJ, 500, 525

Schörck, T., Christlieb, N., Cohen, J. G., et al. 2009, A&A, 507, 817

Shetrone, M., Martell, S. L., Wilkerson, R., et al. 2010, 140, 1119

Shetrone, M., Venn, K. A., Tolstoy, E., et al. 2003, 125, 684

Shetrone, M., Bizyaev, D., Lawler, J. E., et al. 2015, ApJS, 221, 24

Shetrone, M. D., Bolte, M., & Stetson, P. B. 1998, 115, 1888

Shetrone, M. D., Côté, P., & Sargent, W. L. W. 2001, 548, 592

Skrutskie, M. F., Cutri, R. M., Stiening, R., et al. 2006, AJ, 131, 1163

Smith, G. H., & Briley, M. M. 2006, PASP, 118, 740

Smith, G. H., & Martell, S. L. 2003, PASP, 115, 1211

Smith, V. V., Cunha, K., Shetrone, M. D., et al. 2013, ApJ, 765, 16

Sneden, C., Kraft, R. P., Guhathakurta, P., Peterson, R. C., & Fulbright, J. P. 2004, AJ, 127, 2162

Sneden, C. A. 1973, PhD thesis, THE UNIVERSITY OF TEXAS AT AUSTIN.

Sobeck, J. S., Kraft, R. P., Sneden, C., et al. 2011, AJ, 141, 175

Stetson, P. B. 2000, PASP, 112, 925

Stetson, P. B., & Pancino, E. 2008, PASP, 120, 1332

Suntzeff, N. B., & Smith, V. V. 1991, ApJ, 381, 160

Sweigart, A. V., & Mengel, J. G. 1979, ApJ, 229, 624

Tafelmeyer, M., Jablonka, P., Hill, V., et al. 2010, A&A, 524, A58

Tolstoy, E., Hill, V., & Tosi, M. 2009, 47, 371

Tull, R. G., MacQueen, P. J., Good, J., Epps, H. W., & HET HRS Team. 1998, in Bulletin of the American Astronomical Society, Vol. 30, American Astronomical Society Meeting Abstracts, 1263

Tumlinson, J. 2010, ApJ, 708, 1398

van Dam, M. 2016, in Keck Adaptive Optics Note 1117

Venn, K. A., Irwin, M., Shetrone, M. D., et al. 2004, 128, 1177

Venn, K. A., Shetrone, M. D., Irwin, M. J., et al. 2012, ApJ, 751, 102

Verrall, S. C., & Kakarala, R. 1998, J. Opt. Soc. Am. A, 15, 389

Vigan, A., Postnikova, M., Caillat, A., et al. 2016, in Proc. SPIE, Vol. 9909, Society of Photo-Optical Instrumentation Engineers (SPIE) Conference Series, 99093F

Villanova, S., Geisler, D., Carraro, G., Moni Bidin, C., & Muñoz, C. 2013, ApJ, 778, 186

Weisz, D. R., Dolphin, A. E., Skillman, E. D., et al. 2014, 789, 148

Yong, D., Norris, J. E., Bessell, M. S., et al. 2013, ApJ, 762, 27

Zacharias, N., Finch, C. T., Girard, T. M., et al. 2012, VizieR Online Data Catalog, 1322